



# Pushing the physics of edge transport barriers towards the wall: how do boundary conditions impact confinement transitions in tokamaks?

Mathieu Peret

## ► To cite this version:

Mathieu Peret. Pushing the physics of edge transport barriers towards the wall: how do boundary conditions impact confinement transitions in tokamaks?. Plasma Physics [physics.plasm-ph]. Institut Polytechnique de Paris, 2022. English. NNT : 2022IPPA001 . tel-03681704

HAL Id: tel-03681704

<https://theses.hal.science/tel-03681704>

Submitted on 30 May 2022

**HAL** is a multi-disciplinary open access archive for the deposit and dissemination of scientific research documents, whether they are published or not. The documents may come from teaching and research institutions in France or abroad, or from public or private research centers.

L'archive ouverte pluridisciplinaire **HAL**, est destinée au dépôt et à la diffusion de documents scientifiques de niveau recherche, publiés ou non, émanant des établissements d'enseignement et de recherche français ou étrangers, des laboratoires publics ou privés.



INSTITUT  
POLYTECHNIQUE  
DE PARIS

NNT : 2022IPPA001

# Thèse de doctorat



# Pushing the physics of edge transport barriers towards the wall: how do boundary conditions impact confinement transitions in tokamaks?

Thèse de doctorat de l’Institut Polytechnique de Paris  
préparée à l’Ecole Polytechnique

École doctorale n°626 École doctorale de l’Institut Polytechnique  
de Paris (EDIPP)  
Spécialité de doctorat: Physique

Thèse présentée et soutenue à Saint-Paul-lez-Durance, le 1er février 2022, par

## MATHIEU PERET

Composition du Jury :

Mme Dominique FONTAINE	Examinateuse
Directrice de recherche, CNRS (LPP)	Présidente du jury
M. Ulrich STROTH	
Professeur, Université de Stuttgart and IPP	Examinateur
M. Yann CAMENEN	
Chargé de recherche, CNRS (PIIM)	Rapporteur
Mme Teresa ESTRADA	
Professeure, CIEMAT	Rapporteur
Mme Laure VERMARE	
Chargée de recherche CNRS (LPP)	Directrice de thèse
M. Nicolas FEDORCZAK	
Chargé de recherche, CEA (IRFM)	Superviseur CEA
M. Philippe GHENDRIH	
Directeur de recherche, CEA (IRFM)	Invité



# Remerciements

*Pour commencer, je tiens à remercier la direction de l’Institut de Recherche sur la Fusion par confinement Magnétique pour la confiance qu’ils m’ont accordé pour réaliser mon projet de thèse. Cette direction ainsi que les Task Force Leaders WEST m’ont permis de diriger une expérience dédiée sur le grand instrument qu’est le tokamak WEST. Cet aboutissement restera parmi les plus grandes choses que j’ai pu accomplir dans ma vie et pour cela, je serai toujours rempli d’une grande reconnaissance.*

*Je souhaiterais aussi remercier Yann Camenen et Teresa Estrada pour le temps et l’effort qu’ils ont investi dans leur tache de rapporteur de cette thèse. De plus, je remercie l’entièreté de mon jury de thèse pour l’attrait qu’ils ont porté à mon travail et leurs retours sur ce dernier. Je remercie plus particulièrement Dominique Fontaine d’avoir présidé ce jury.*

*J’aimerais aussi exprimer mon immense reconnaissance envers celui et celle sans qui tout ce travail n’aurais pas pu être possible à savoir mes deux encadrants Laure Vermare et Nicolas Fedorczak. Leur humanité et leur bienveillance m’ont permis de toujours rester au paroxysme de ma motivation et ce, même lors de moments difficiles. Leur patience et leurs conseils m’ont apporté beaucoup et ont permis à ce projet de se dérouler dans de parfaites conditions que ce soit d’un point vue scientifique ou personnel. Ces moments de partage resteront enracinés profondément dans ma mémoire et continueront d’éclaircir mes jours.*

*Je remercie aussi tous mes camarades de salle de pilotage, avec qui nous avons partagé des moments intenses de recherche d’accès au mode H, pour m’avoir tant appris sur l’exploitation d’un tokamak ainsi que sur le vaste monde qu’est celui des mesures dans un tel instrument. Je remercie plus particulièrement*

---

*Pascale Hennequin pour sa patience lorsqu'elle m'a encadré en terre allemande mais aussi pour nos discussions toujours enrichissantes à la porte d'un bureau ou dans un couloir. Un grand merci à tous ceux qui ont rendu mes journées de travail plus agréables. Mention spéciale pour ma voisine de bureau Corinne Desgranges pour son sourire solaire et ses conseils toujours plein d'espoir. Merci aussi au Docteur Gallo pour nos discussions toujours passionnantes. Il restera pour moi une source d'inspiration sans limites.*

*J'aimerais maintenant exprimer mon admiration à mes co-bureaux successifs Alexandre Gouin, Benjamin Luce, Nicolas Rivals et Yaakoub Boumendjel pour leur capacité à supporter mon humour ainsi que les moments aléatoires durant lesquels j'ai poussé la chansonnette.*

*Cette thèse aura aussi été l'occasion de rencontrer tous ces camarades de recherche, à savoir ces jeunes thésards, stagiaires et post-docs avec qui j'ai eu des discussions sérieuses des plus enrichissantes mais le plus souvent des discussions des moins sérieuses au détour d'un café, thé ou autour d'un repas. Parmi tous ces joyeux lurons, je voudrais distinguer deux énergumènes Robin Varennes et Eléonore Geulin qui m'ont apporté un soutien infini lors des mauvaises passes et des fou-rires en pagaille lors des bonnes.*

*Finalement, j'aimerais conclure ces remerciements en remerciant du fond du cœur le membres de ma famille qui m'ont soutenu : mes parents et beaux-parents pour les sacrifices et les efforts qu'ils ont fait pour me permettre d'en arriver au titre de docteur. Merci aussi à mon frère, mes soeurs, mes cousins, Jeep et Masha pour leur soutien. J'exprime un immense merci à mes grands-parents pour leur aide incommensurable sans laquelle je ne serais jamais arrivé aussi loin. Une admiration particulière à ma copine pour être restée avec moi même après avoir supporté ces interminables session vouées à l'écriture du manuscrit et à la préparation de ma soutenance. Merci à Christine pour son hospitalité et sa bienveillance.*

*Enfin, je conclurai en dédiant ce travail à un frère parti trop tôt.*

# Résumé élargi

## La fusion thermonucléaire

De nos jours, la question de la production d'énergie électrique est au cœur des priorités de l'humanité dû aux enjeux économiques, écologiques et sociaux qu'elle soulève. La recherche d'une source d'énergie abondante et à faible rejet de gaz à effet de serre est donc nécessaire. La fusion thermonucléaire vise à s'inscrire comme solution à cette problématique. En effet, la fusion de deux noyaux atomiques légers donnant un noyau plus lourd peut présenter un défaut de masse dans le bilan de réaction convertissant cette énergie en énergie cinétique pour les produits de la réaction de fusion. Dans le cas de la réaction retenue pour les réacteurs de premières générations, la réaction envisagée est la réaction Deutérium-Tritium donnant un noyau d'Hélium et un neutron ayant respectivement une énergie cinétique de 3.5MeV et 14.1MeV. Pour maximiser le taux de réaction de ce processus, la température des réactifs doit avoisiner les 10keV, les portant ainsi dans l'état de plasma. Ces conditions extrêmes sont directement responsables de l'efficacité d'un réacteur qui peut être quantifier par un bilan de puissance. De ce bilan résulte le critère de Lawson donnant une valeur minimale au triple produit de la température  $T$ , de la densité  $n$  et du temps de confinement de l'énergie  $\tau_E$  :  $nT\tau_E \geq 3 \times 10^{21} m^{-3}.keV.s$ . Le contrôle du confinement de la matière et de l'énergie est donc primordial pour augmenter l'efficacité des réacteurs à fusion. Pour atteindre ces conditions, deux moyens principaux de confiner le plasma de réactifs sont à l'étude : la fusion inertielle et la fusion magnétique. Dans le cadre de cette étude, nous nous focaliserons sur la fusion par confinement magnétique dans des enceintes toroïdales nommées tokamaks.

## Le confinement dans les tokamaks

Le confinement magnétique du plasma repose sur le mouvement de précession des particules chargées autour des lignes de champs magnétique. Ce confinement orthogonal au champ n'est pas suffisant pour confiner totalement les particules car elles sont libres de s'échapper dans la direction parallèle aux lignes de champ. Ce problème peut être résolu par une fermeture toroïdale du système permettant de boucler les lignes de champ et ainsi confiner parallèlement les particules. Cette forme toroïdale induit une décroissance de l'amplitude du champ magnétique toroïdal avec le grand rayon de la machine. Cette inhomogénéité du champ magnétique est à l'origine de dérives verticales et opposées des ions et des électrons engendrant ainsi un champ électrique vertical et donc une dérive d'ensemble des particules dans la direction du grand rayon de la machine. Pour pallier ces pertes importantes de particules, un champ magnétique poloïdal est utilisé pour enrouler hélicoïdalement les lignes de champ et court-circuiter la séparation de charge. Pour cela, dans les tokamaks, un courant toroïdal est induit dans le plasma. Un équilibre entre plasma et champ magnétique est décrit par la magnétohydrodynamique (MHD) et résulte alors en une organisation des lignes de champs sur des surfaces toriques enboîtées sur lesquelles la pression plasma est uniforme.

L'évolution radiale de cette pression plasma dans les surfaces magnétiques fermées est dictée par l'équilibre entre le transport radial et les sources de particule et de chaleur contrôlé durant l'opération du tokamak. Une précision volontaire est faite ici sur le caractère fermé des surfaces magnétiques considérées qui se distinguent des surfaces ouvertes qui interceptent le mur de l'enceinte. En effet, il est impossible de créer un plasma qui ne touche pas le mur ou qui lui est tangent en tout point. Au niveau de la surface du mur qui est en contact avec le plasma, une gaine électrostatique se forme imposant alors une contrainte sur la dynamique parallèle du transport de particule et d'énergie. L'évolution radiale du profil de pression dans ce volume de plasma interceptant le mur résulte alors de l'équilibre entre le transport radial, les sources et le transport parallèle.

Cette surface "mouillée" du mur va servir de zone d'évacuation de la chaleur qui sera ensuite utilisée pour produire l'énergie électrique. Elle délimite un volume

de plasma communément appelé scrape-off layer. Une attention particulière doit être portée à la largeur d'impact du flux de chaleur sur le mur. Si elle est trop fine, l'intensité du flux de chaleur va engendrer des dommages conséquents au mur de l'enceinte. La géométrie du plasma peut être modifiée dans l'optique de mieux contrôler l'impact du plasma sur le mur. La géométrie limitée vise à asseoir des plasmas circulaires (ou élongués) sur le mur. Cette méthode permet l'introduction d'impuretés directement dans le cœur qui peuvent avoir des conséquences dramatiques sur les propriétés du confinement en rayonnant une partie de l'énergie thermique contenue mais aussi diluer les réactifs de fusion et diminuer le rendement d'un réacteur. Cette géométrie a été à l'étude dans le tokamak Tore Supra qui sera étudié au cours de projet de doctorat. Pour pallier le problème de contamination, une solution a été apportée en appuyant le plasma sur deux jambes reposant sur des zones cibles du mur. Ces deux jambes se rejoignent alors en un point appelé point-X qui marque l'entrée dans le plasma confiné. Cette géométrie présente l'avantage de diviser le flux de chaleur allant vers le mur en deux parties. Malheureusement, il est observé dans l'expérience que la largeur d'impact du flux de chaleur est diminuée dans cette géométrie appelée configuration diverteur. Le tokamak Tore Supra a évolué vers cette géométrie pour donner le tokamak WEST. Cette géométrie est celle prévue pour les futurs tokamaks comme le tokamak ITER qui vise à montrer la faisabilité d'atteinte de conditions propices à la production d'énergie par la fusion nucléaire. Nous avons vu que la géométrie magnétique a un impact direct sur le transport dans les surfaces magnétiques ouvertes du plasma. L'importance de comprendre la mise en place du transport radial dans les tokamaks est donc de première importance pour à la fois contrôler le confinement et l'efficacité du réacteur mais aussi sa capacité à extraire la chaleur de manière sûre pour les composants.

## Transport radial dans les tokamaks

Ce transport radial est dû à deux contributions : une contribution dite néoclassique et une contribution turbulente. La première est due aux collisions entre les particules au sein du plasma. Ces particules peuvent être passantes ou piégées. Les particules piégées ont des trajectoires présentant des points de rebroussement à cause des inhomogénéités du champ magnétique.

La deuxième contribution vient des différentes instabilités qui peuvent apparaître au sein du plasma. En effet les forts gradients de quantités thermodynamiques (densité, pression, température), placent le plasma de tokamak dans un état hors équilibre thermodynamique. La turbulence peut alors se développer en puisant l'énergie libre de ces gradients. En particulier, une instabilité responsable de transport dans les plasmas de tokamak sera au cœur de l'étude menée durant ce doctorat, à savoir l'instabilité d'interchange. Cette instabilité se caractérise par un échange local entre des zones de valeurs de forte pression vers des zones de plus faible pression, donc le long du profil décroissant de la pression. Plusieurs instabilités de type interchange peuvent se développer dans le plasma tirant leur nom du nom du gradient de la quantité qui les déstabilisent (Ion Temperature Gradient, Electron Temperature Gradient).

Dans le bord du plasma, la turbulence est caractérisée par des filaments intermittents allongés dans la direction parallèle aux lignes de champ. La dynamique, l'intermittence et l'amplitude de ces filaments ont été beaucoup étudiés à la fois expérimentalement et théoriquement mais ne sont toujours pas totalement décrites de manière analytique. Ce point est un point central de cette étude.

## Barrière de transport externe

En 1982, il a été observé pour la première fois une augmentation significative et spontanée du confinement lorsque la puissance additionnelle injectée au plasma a atteint un seuil. Cette augmentation du confinement est associée à la mise en place d'un écoulement très cisaillé au bord du plasma caractérisé par le fort creusement d'un puit dans le profil radial de la rotation perpendiculaire (quasi-poloïdale). Cet écoulement cisaillé induit une mitigation locale de la turbulence caractérisant une barrière de transport. Cet effet localisé à la périphérie du plasma confiné engendre une forte augmentation du confinement global. Ce mode de haut confinement ou mode H (en opposition au mode de confinement classique mode L) est le mode de confinement envisagé pour les futurs réacteurs de fusion.

Il a aussi été observé que la géométrie du plasma a un fort impact sur la mise en place de ce régime de haut confinement. Premièrement, l'accès au

---

mode H est bien plus difficile en géométrie limitée qu'en configuration diverteur. Deuxièmement, la position du point-X impacte fortement le niveau de puissance injectée nécessaire à la transition. Lorsque la dérive diamagnétique ionique pointe vers le point-X la puissance à injecter est moindre que dans la configuration opposée. Ce phénomène a donné le nom de configuration favorable et défavorable à ces configurations magnétiques.

## Contexte et objectifs de la thèse

L'absence de description analytique du transport turbulent dans les plasmas de tokamaks a conduit à deux manières de prédire les niveaux de confinement et les largeurs d'impact du flux de chaleur sur le mur. Le premier est l'utilisation de simulations numériques premiers principes qui sont très coûteuses en temps et difficile à interpréter. Deuxièmement, l'utilisation de base de données de mesures a permis de déduire des lois d'échelles en fonction de puissance des différents paramètres de contrôle. Malheureusement, la mise en place de l'écoulement cisaillé et l'impact de la géométrie sur cette mise en place ne sont pas non plus décrit analytiquement, ce qui a mené aux mêmes approches pour prédire ces propriétés pour les futurs machines comme ITER.

Dans ce travail de thèse, nous proposons une approche basée sur la réduction de modèle pour décrire le transport induit par la turbulence ainsi que son interaction avec un écoulement cisaillé. Ce modèle se base sur une approche spectrale des équations fluides isothermes à partir de laquelle nous pouvons prédire le flux radial de matière ainsi que le tenseur de Reynolds induisant de la rotation. Nous y incluons l'effet du cisaillement de l'écoulement de fond ainsi que l'effet de la géométrie magnétique au travers du cisaillement magnétique caractérisant l'inhomogénéité radiale de l'enroulement des lignes de champ.

Ce modèle est ensuite vérifié en utilisant des simulations 2D non-linéaires pilotées par le flux. Ensuite, un travail expérimental en 2 étapes permettra de mettre en regard expériences et prédictions du modèle. En effet, une caractérisation de la turbulence à partir de mesure de sondes dans les plasmas de Tore Supra et du torsatron TJL ainsi que des mesures de rotation au bord du plasma employant la réflectométrie Doppler ont été menées.

Enfin, un travail d'inclusion d'effets plus fins tels que l'impact de la géométrie sur la turbulence ou encore l'impact de la résistivité du plasma sur la dynamique parallèle a été réalisé montrant des pistes pour expliquer des phénomènes tels que l'épaule en densité ou encore la réduction de la largeur d'impact du flux de chaleur sur le mur en configuration diverteur.

## **Mesures de turbulence et d'écoulement dans le plasma de bord**

L'emploi de sondes de Langmuir pour la caractérisation des plasmas en interaction avec le mur dans les tokamaks est très commun. Ce diagnostic est utilisé dans cette étude principalement dans le tokamak Tore Supra pour construire deux bases de données mesurées dans des conditions plasmas variées et contenant suffisamment de statistiques pour la validation du modèle développer en parallèle. La première base de données sera constituée de mesure de largeur de profils de densité dans la SOL. L'équilibre entre le flux parallèle et le flux radial dans la SOL résulte en profils exponentiellement décroissants. La longueur de décroissance de ces profils étant directement liée au transport radial turbulent, une caractérisation de la turbulence est nécessaire pour comprendre la mise en place des profils. Cette caractérisation fera l'objet de la seconde base de données de mesures contenant les propriétés d'événements intermittents dans la SOL telles que leur longueur de corrélation poloïdale, leur vitesse de convection électrostatique radiale ainsi que les niveaux de fluctuations qui leur sont associés. Enfin, l'utilisation d'un réseau poloïdal de sonde dans le torsatron TJ-K permettra d'extraire des spectres turbulents qui seront comparables aux prédictions directes du modèle.

La deuxième partie du travail expérimental réalisé durant ce doctorat consiste en la caractérisation des écoulements de bord dans le tokamak WEST via l'utilisation du réflectomètre Doppler DIFDOP du LPP. Cette caractérisation sera décomposée en deux approches. La première est basée sur une approche statistique. Une base de donnée d'environ 300 profils a été constituée dans des conditions plasmas très variables en terme de courant plasma, densité, géométrie magnétique

ou encore puissance injectée durant 3 campagnes d'opération du tokamak. La profondeur du puit de rotation est utilisé comme un proxy du cisaillement de ces profils. Une tentative de mise en lumière de tendance de l'évolution de cette profondeur de puit avec les différents paramètres plasma n'a montré aucune tendance globale claire. La corrélation entre les différents impacts des paramètres de contrôle semble trop forte. Pour mieux comprendre l'impact d'un paramètre isolé sur la mise en place du profil radial de rotation, une approche basée sur des expériences dédiées apparaît alors plus indiquée. Cette seconde approche employée durant cette thèse a permis la mise en lumière des effets du chauffage injecté, de l'injection de matière, du courant plasma et de la géométrie magnétique sur la rotation. Ces deux derniers constituent notamment le résultat principal de cette étude. En effet, à faible courant plasma ( $500kA$ ), la rotation en configuration favorable présente un puit alors que la configuration symétrique non. En revanche, lorsque le courant plasma augmente cette différence s'estompe et la rotation en configuration défavorable devient même plus profonde. Ce point sera ensuite comparé aux prédictions analytiques du modèle développé en parallèle de ce travail expérimental.

Finalement, les premières mesures de rotation en mode H sur WEST ont été réalisées dans le cadre de ce doctorat montrant des propriétés singulières de la rotation dans ce tokamak. En effet, la transition vers le mode de confinement amélioré dans les deux configurations, favorable et défavorable, s'est fait à puissance injectée équivalente. Il en résulte que la rotation au bord du plasma en configuration défavorable présente une profondeur de puit et cisaillement plus importants que dans la configuration opposée, ce qui semble contre-intuitif. En revanche, le confinement semble meilleur en configuration favorable malgré le cisaillement plus faible.

## **Un modèle pour prédire le transport turbulent et les profils de rotation**

Le modèle développé durant ce doctorat est basé sur une approche spectrale des équations 2D et isothermes de conservation de la vorticité et de la densité dans la SOL. Ces équations ont été moyennées dans la direction parallèle. Ces équations contiennent des termes non-linéaires qui sont ici approximées

par des approches heuristiques. L'idée proposée est basée sur l'interaction des modes poloïdaux turbulents avec un mode dominant. Cette interaction va mener à un phénomène de saturation de l'amplitude des fluctuations en densité et en potentiel qui va s'ajouter à la saturation due aux pertes parallèles dans la gaine. Nous pouvons donc déduire des spectres poloïdaux de turbulence. A partir de ces spectres, il est possible de prédire les niveaux de fluctuations ainsi que le flux radial de matière. Dans la SOL, l'équilibre de ce flux radial avec le flux parallèle nous donne la longueur de décroissance des profils en densité. Premièrement, le modèle a été développé en l'absence d'un cisaillement de fond. Il a ensuite été comparé aux résultats de simulations constituant une base de données d'une dizaine réalisées durant ce doctorat. Cette comparaison a permis de vérifier les prédictions du modèle pour les spectres, les niveaux de fluctuations ainsi que la longueur de décroissance des profils de densité. Ces prédictions ont ensuite montré un accord quantitatif avec les mesures de sondes dans le tokamak WEST mais aussi avec les données obtenues dans TJ-K.

Dans un second temps, l'inclusion d'un écoulement de fond cisaillé de manière homogène a permis de comprendre l'impact du cisaillement sur les spectres turbulents. L'inclinaison des modes, c'est-à-dire la création d'un vecteur d'onde radial par les effets de cisaillement dus à l'écoulement sont quantifiés par un modèle faisant l'équilibre entre la création d'inclinaison et une force de rappel propre à l'interchange. Nous incluons aussi la création de vecteur d'onde radial par le cisaillement magnétique. A partir des spectres ainsi obtenus, nous pouvons quantifier l'impact du cisaillement sur la turbulence mais aussi prédire la génération d'écoulement par la turbulence via la prédiction du tenseur de Reynolds. L'impact de l'écoulement cisaillé sur les prédictions des spectres, des niveaux de fluctuations et de la longueur de décroissance du profil de densité est ensuite comparé aux résultats de 16 simulations avec des paramètres de contrôle de la turbulence et de niveaux de cisaillements différents menant à une vérification complète du modèle.

Enfin, un modèle prédisant la mise en place de la rotation poloïdale basé sur l'équilibre entre la génération d'écoulement par la turbulence et la force de rappel vers la vitesse néoclassique est développé. Des effets fins tels que l'impact de la géométrie sur le cisaillement magnétique ou les largeurs de cisaillement finies

sont aussi inclus au modèle. Ses prédictions sont comparées avec les mesures de rotation caractérisant l'impact de la géométrie et du courant plasma. Les prédictions permettent de retrouver à la fois la tendance du creusement du profil de rotation avec le courant plasma mais aussi la présence ou l'absence de puit dans le profil suivant la nature de la géométrie magnétique.

## Perspectives et limitations du modèle

La dernière partie de ce travail de thèse consiste en l'étude des limitations du modèle et des perspectives atteignables à partir de ce dernier. En effet, le modèle de transport turbulent a été validé en le comparant à des mesures en géométrie limitée. En le comparant à des mesures de largeurs de SOL en mode L sur WEST en géométrie diverteur ou à des lois d'échelle expérimentales en modes L et H, un accord est trouvé pour les dépendances paramétriques mais l'amplitude est sur-évaluée par le modèle. En incluant des effets comme les impacts du cisaillement et de la géométrie magnétique sur les paramètres de contrôle de la turbulence, on retrouve une diminution de l'amplitude du transport turbulent observé dans l'expérience en mode L.

Le modèle présenté ici ne tient pas non plus compte de la resistivité du plasma dans la SOL. Cette quantité peut avoir un fort impact lorsque le plasma est très dense. Une inclusion de la résistivité dans les jambes du plasma dans le paramètre de contrôle du modèle caractérisant la dynamique parallèle permet de retrouver des observations expérimentales telles que l'épaule en densité. Un effort reste à faire sur la description de la dynamique parallèle dans les surfaces magnétiques fermées. En effet des effets de résonance et de resistivité plasma sont à prendre en compte pour pouvoir employer le modèle dans les surfaces magnétiques fermées. Ce point est un des principaux points de discussion sur les résultats de la comparaison du modèle avec les observations de la rotation dans WEST.

Enfin, l'inclusion de ce modèle de transport turbulent et de génération d'écoulement dans un système d'équations de transport de matière, d'énergie et de conservation du moment poloïdal a été entamée dans l'optique de faire un modèle simple 1D pour prédire les propriétés macroscopiques du plasmas. Il en résulte le

code 1DCIS (1D Code for Interchange and Shear) qui permet d'étudier l'impact du chauffage et des paramètres de contrôle du plasma comme la géométrie ou le courant plasma sur les profils de densité, température et rotation poloïdale. Encore une fois, une extension du modèle en surface de flux fermées reste à peaufiner. De plus, le modèle considéré est électrostatique et isotherme et ne tient donc pas compte des fluctuations de température et champ magnétique. Les fluctuations de température sont très importantes notamment dans le transport de chaleur. Néanmoins, nous pouvons nous attendre à ce que la nature du transport reste de type interchange et soit comparable en terme de dépendances paramétriques aux prédictions du modèle.

# Contents

<b>1</b>	<b>Introduction</b>	<b>1</b>
1.1	The fusion energy to provide for humankind needs . . . . .	2
1.2	From a single particle motion to the tokamak principles . . . . .	4
1.2.1	Motion of a particle subject to the Lorentz force . . . . .	4
1.2.2	The tokamak magnetic configuration . . . . .	6
1.3	Transverse transport in closed field lines: classical, neoclassical and anomalous transport . . . . .	9
1.3.1	Collisional transport . . . . .	10
1.3.2	Turbulent transport . . . . .	11
1.4	Modelling of the equilibrium in opened field lines : plasma-wall interaction and balance equations . . . . .	14
1.4.1	Plasma wall interaction : sheath boundary conditions . . . . .	15
1.4.1.1	<i>The Bohm boundary condition</i> . . . . .	16
1.4.1.2	<i>The potential drop at the wall</i> . . . . .	18
1.4.2	An edge turbulent transport model : TOKAM2D . . . . .	19
1.4.2.1	<i>Continuity equation</i> . . . . .	20
1.4.2.2	<i>Total charge conservation : the vorticity conservation equation</i> . . . . .	20
1.4.2.3	<i>Field line average</i> . . . . .	21

<b>1.5 Power exhaust control : limiter and divertor configurations . . . . .</b>	<b>22</b>
<b>1.6 From Tore Supra and WEST to ITER . . . . .</b>	<b>24</b>
<b>1.7 Confinement regimes and transport barriers . . . . .</b>	<b>25</b>
1.7.1 What are the H-mode and the transport barriers? . . . . .	25
1.7.2 Impact of the density and the magnetic topology on the L-H transition threshold . . . . .	27
1.7.3 The other confinement regimes . . . . .	29
<b>1.8 Edge rotation profile establishment . . . . .</b>	<b>29</b>
<b>1.9 Context and objectives of the thesis . . . . .</b>	<b>32</b>
 <b>2 Experimental characterisation of edge turbulent transport and flows : Langmuir probes and Doppler Reflectometry data</b>	 <b>35</b>
<b>2.1 Langmuir probe measurements in Tore Supra : an experimental database of SOL turbulent features for model validation . . . . .</b>	<b>36</b>
2.1.1 Principle of Langmuir probes measurements . . . . .	36
2.1.2 SOL background profiles measurement in Tore Supra . . . . .	39
2.1.3 Turbulent transport characterisation . . . . .	41
2.1.3.1 <i>The rake probe system implemented in Tore Supra</i> . . . . .	41
2.1.3.2 <i>Discussion on the ability of probes to measure turbulence features</i> . . . . .	42
2.1.3.3 <i>Saturation current and floating potential time traces</i> . . . . .	43
2.1.3.4 <i>Data treatment and database build-up</i> . . . . .	45
<b>2.2 Experimental characterisation of edge flows : use of a Doppler Back Scattering (DBS) system . . . . .</b>	<b>47</b>

2.2.1	Reflectometry principle : the collective scattering . . . . .	48
2.2.2	Local velocity measurement using the Doppler shift . . . . .	49
2.2.3	Propagation of an electromagnetic wave through the edge plasma . . . . .	51
2.2.4	Doppler reflectometry in WEST : system and data treatment	54
2.2.4.1	<i>The DBS system in WEST : DIFDOP</i> . . . . .	54
2.2.4.2	<i>Edge rotation profile reconstruction</i> . . . . .	55
2.2.4.3	<i>Discussion on fundamental hypotheses and uncertainty sources</i> . . . . .	59
2.2.5	Understanding the correlation between edge rotation and plasma parameters . . . . .	63
2.2.5.1	<i>Build-up of a wide database of edge rotation profile to study global trends</i> . . . . .	64
2.2.5.2	<i>Impacts of heating power, density and magnetic geometry on edge rotation in WEST</i> . . . . .	66
2.2.6	Assessment of increased confinement discharges in WEST : high injected power experiments . . . . .	75
2.2.6.1	<i>H-mode assessment in WEST</i> . . . . .	76
2.2.6.2	<i>Observations of L-H transition in LSN</i> . . . . .	77
2.2.6.3	<i>Observations of L-H transition in USN</i> . . . . .	82
<b>3</b>	<b>A model of edge turbulence interplay with sheared flows</b>	<b>89</b>
3.1	<b>State of the art on the characterisation of edge turbulent transport</b> . . . . .	90
3.2	<b>A transport model of interchange turbulence in a sheared flow</b>	94

3.2.1	The Sheared Spectral Filament (SSF) model paradigm . . . . .	94
3.2.2	The Sheared Spectral Filament model . . . . .	95
3.2.2.1	<i>From isolated filaments to a description of non-linear terms : the Isolated Filament model</i> . . . . .	97
3.2.2.2	<i>The mixing length rule for the density spectrum</i> . . . . .	99
3.2.2.3	<i>A model of turbulence without background shear : the Spectral Filament model</i> . . . . .	100
3.2.2.4	<i>A model of turbulence in a homogeneous background shear : the Sheared Spectral Filament model</i> . . . . .	103
3.2.2.5	<i>Effect of non homogeneous shears</i> . . . . .	105
3.2.2.6	<i>From the spectra to the transport observable predictions</i> . . . . .	106
3.2.2.7	<i>Flux conservation in the scrape-off layer : predictions of the density decay length</i> . . . . .	108
3.2.3	Poloidal momentum conservation . . . . .	110
3.2.3.1	<i>Field line average of magnetic shear tilt</i> . . . . .	111
3.2.3.2	<i>A 1D transport code with sheared flows : 1DCIS (1D Code for Interchange and Shear)</i> . . . . .	112
3.3	<b>Verification of the model with TOKAM2D simulations</b> . . . . .	116
3.3.1	Databases from TOKAM2D simulations . . . . .	116
3.3.2	Comparison of the model predictions with the simulation results . . . . .	118
3.3.2.1	<i>Database without sheared flows against SF model predictions</i> . . . . .	118

3.3.2.2 <i>Database with homogeneous background sheared flows against SSF model predictions</i> . . . . .	119
<b>3.4 Validation of the SSF model against experimental measurements</b> . . . . .	123
3.4.1 Expressions of the control parameters ( $g, \sigma_{\parallel}$ ) as functions of plasma parameters . . . . .	124
3.4.2 Validation of the spectral model against TJ-K probe measurements . . . . .	125
3.4.3 Validation of the turbulence features and transport observables predictions against Tore Supra probe measurement .	128
3.4.4 Validation of the flow generation predictions against WEST DBS measurement . . . . .	130
<b>4 Discussions about the perspectives and the limits of the model</b> . . . . .	135
4.1 Model predictions against SOL width measurements in diverted plasma . . . . .	136
4.2 Impact of the density on the parallel dynamics description . .	140
4.3 Impact of the phase shift between potential and density fluctuations on the model predictions . . . . .	152
4.4 Impact of the geometry on the curvature drive coefficient $g$ . .	153
4.5 Impact of the plasma shaping on the structure tilt . . . . .	156
4.6 Impact of the electromagnetic effects on the SOL transport amplitude . . . . .	158
4.7 Global confinement features from a generic flux model . . . .	159
4.8 The link between the spectral model and blob description . .	160

4.9 Towards a 0D model for main confinement features . . . . .	161
<b>5 Conclusion</b>	<b>163</b>
<b>Appendices</b>	<b>167</b>
<b>A Flux divergence ordering</b>	<b>169</b>
<b>B Curvature parameter <math>G</math> derivation in circular geometry</b>	<b>171</b>
<b>C Study of the impact of the viscous and diffusive parameters on the TOKAM2D simulations for the model verification</b>	<b>173</b>
<b>D Extracting turbulence features and transport observables from the simulation results</b>	<b>175</b>
D.1 Electrostatic potential, density and particle flux radial profiles	175
D.2 Poloidal spectra of the density and electrostatic potential . . .	178
D.3 Structure tilt characterisation . . . . .	179
D.4 Fluctuation levels measurement . . . . .	182
<b>E Ion and electron radial profiles reconstruction</b>	<b>183</b>
<b>Bibliography</b>	<b>185</b>

# Chapter 1

## Introduction

### Content

---

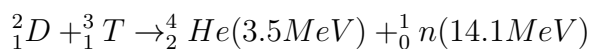
We introduce here the main plasma physics principles that will be used in this manuscript. Starting from the single particle motion in an electromagnetic field, we develop until the description of the tokamak principle. A discussion on the radial transport of particle and energy in tokamak discharges is included illustrating the difference between the confined region and the region of plasma-wall interaction. The impact of the plasma shaping on the heat and particle flux deposition widths will then be presented emphasising the need to understand the underlying physics of the widening of these widths in the quest of the power and particle exhaust without wall damaging. In order to situate the starting point of the theoretical development of this thesis which aims at predicting such width, we present the fluid description of the transport in the edge region. Then, the concept of transport barrier establishing at the periphery of the confined plasma is detailed showing the importance of understanding the establishment of the edge region rotation profile. Finally, we will conclude on the context and the motivations of this thesis consisting in the objective of palliating to the lack of knowledge of the impact of the edge plasma conditions on the edge particle transport and rotation profiles behaviour.

---

## 1.1 The fusion energy to provide for humankind needs

Nowadays, the question of the energy is one of the Humankind's priorities for its survival. This context is linked to economical, societal and ecological issues. First, the demographic growth induces an increase of energy needs. Then, the current energy mix is mostly based on fossil energies which are huge greenhouse gas producers. This last point is one of the main contributors to the global warming. The need of an abundant, zero-carbon rejecting energy source is of the utmost importance and a few candidates are proposed to answer this issue : 1) renewable energies, 2) nuclear fission and 3) nuclear fusion. Renewable energies presents 2 main issues : the intermittency (of the Sun, of the wind, ...) leading to the question of electric energy storage and the floor area needed to produce a megawatt of energy ( $1\text{km}^2$  for  $1\text{MW}$ ). Nuclear fission is exempt from these issues but generates long-life radioactive wastes which have to be stored. It also needs non-abundant resources and could be victim of catastrophic accidents. The nuclear fusion relies on a process which does not create directly heavy radioactive nuclei and so palliates the issue of radioactive waste storage. Moreover, as for nuclear fission, the power plants doesn't need wide floor areas to produce electric energies of the order of the gigawatt.

This later candidate aims at getting back the mass defect energy of a fusion reaction of light nuclei towards a more stable element. Hydrogen isotopes are the perfect candidates for such reactions because they are abundant (Deuterium is abundant in oceans), and their fusion cross sections are higher than the ones for other reactions at lower temperature making it able to be reached in terrestrial reactors (see figure 1.1). The chosen reaction is the following because of its high reaction rate for temperatures of  $1 - 10\text{keV}$ .



Nevertheless, a huge constraint has to be taken account : Deuterium and Tritium nuclei are positively charged and consequently repels themselves. To reach temperatures high enough to allow the fusion reactions, we have to heat the

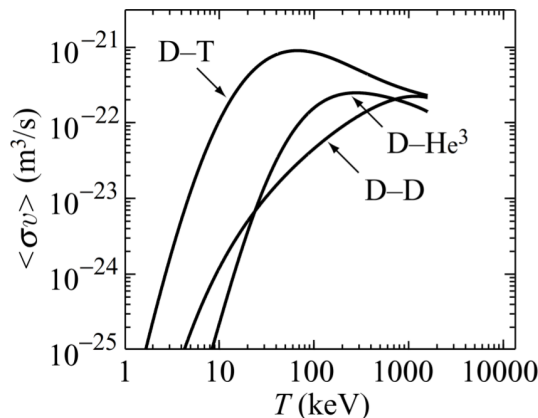


Figure 1.1: Reaction rates of fusion reactions for the different hydrogen isotopes function of the thermal energy [1]

reactants in a plasma state and then highly confine it. This process is naturally maintained in stars where the gravitational force confines hot dense plasmas in the stars core and allows fusion reactions. In fusion reactors, we have to find ways to confine such plasmas to generate sufficiently energy to be profitable. To quantify the profitability of such devices, we built the ratio  $Q$  between the fusion energy over the injected one called amplification factor :

$$Q = \frac{P_{fus}}{P_{in}}$$

To increase this ratio, we have to get closer to the ignition criterion corresponding to the phenomenon where the fusion reactions heat the surrounding medium and help other reactions to occur (very high  $Q$ ). One can translate the point where the reactor becomes profitable ( $Q = 1$ ) as a criterion called Lawson's criterion [2] :

$$n_i T_i \tau_E >= \frac{3 \times 10^{21} \text{keV s}}{m^{-3}}$$

where  $n_i$  and  $T_i$  are respectively the ion density and temperature and  $\tau_E$  is the energy confinement time. To reach this criterion, two main opposite ways have been explored. The inertial fusion consists in confining plasmas with high intensity lasers shooting uniformly on spherical fuel targets during a very short time ( $10^{-11} \text{s}$ ) to reach densities of  $10^{31} \text{m}^{-3}$  at temperatures of  $10 \text{keV}$ . The second attempt is the magnetic fusion, involving lower densities ( $10^{20} - 10^{21} \text{m}^{-3}$ ) at similar temperatures but for longer confinement time of the order of the second. These

conditions are reached confining plasmas with strong magnetic fields ( $1 - 10T$ ). The record for magnetic fusion efficiency has been observed in the tokamak JET (Joint European Torus) in 1997 with  $Q = 0.62$  [3]. This is a step towards the assessment of the building of a fusion reactor. One of main future steps is the start of the operation of the ITER tokamak [4]. This device currently under construction will be operated to demonstrate the feasibility of nuclear fusion reactors as a reliable energy source by reaching an amplification factor of 10. From the research experience accumulated during the last decades, we understood that in order to increase this amplification factor, a large heating injection, high magnetic fields as well as a large plasma size are needed, leading to the features of the ITER tokamak. All these points represent engineering and research challenges. Moreover, a few other points have to be controlled, such as the core plasma dilution by the Helium wastes of the fusion reactions, the wall contamination by the radioactive Tritium, ... This fusion solution to the energetic crisis currently encountered will be at the centre of the study presented in this manuscript.

## 1.2 From a single particle motion to the tokamak principles

As mentioned in the previous section, all the work presented here will take place in the context of the tokamak physics [5]. We will introduce the tokamak principles in this section starting from the magnetic mirror phenomenon to the magnetic equilibrium obtained in a tokamak.

### 1.2.1 Motion of a particle subject to the Lorentz force

The motion of a non-relativistic charged particle of charge  $q$  and mass  $m$  subject to an electromagnetic field  $(\vec{E}(\vec{r}, t), \vec{B}(\vec{r}, t))$  can be deduced from Newton's principle :

$$m \frac{d\vec{v}}{dt} = q \left( \vec{E}(\vec{r}, t) + \vec{v} \times \vec{B}(\vec{r}, t) \right) \quad (1.1)$$

As it is often done in tokamak physics, one can decompose the motion in two components: one parallel to the magnetic vector (of director vector  $\vec{b} = \frac{\vec{B}}{|\vec{B}|}$ ) and one perpendicular to  $\vec{b}$ . We will consider a system with a static magnetic field.

For example, a particle plunged in magnetic field generated by two parallel coils. In this case, the particle will have a motion composed of a free motion along the field lines with a rotation around this field lines called Larmor precession. This perpendicular rotation is observed at the cyclotron frequency  $\omega = \frac{qB}{m}$  where  $B$  is the magnetic field amplitude, with a radius of  $\rho_l = \frac{v_\perp}{\omega}$  called Larmor radius. This perpendicular confinement is the main idea considered in magnetic fusion devices. In the case of the two coils system, the magnetic field amplitude is varying between the two coils. Indeed, the magnetic field amplitude is higher close to the coils. The magnetic field being divergence free ( $\vec{\nabla} \cdot \vec{B} = 0$ ) and the Lorentz force work being null, the total energy and the magnetic momentum of the system have to be conserved. So when, the particle approaches the coils, it will experiment a higher magnetic field leading to a higher perpendicular velocity because of the magnetic momentum  $\mu = \frac{mv_\perp^2}{2B}$  conservation. In consequence, the particle parallel velocity will decrease until the particle bounces back. This is the magnetic mirror principle [6].

In the case of a fusion device, we have to consider a system with much more particles. These particles will collide and will spread in the velocity space with a Gaussian distribution function. The high velocity particles will be able to go through the coils and a loss of particles will be observed. This point led to toroidal designs for magnetic devices in order to palliate these losses by closing the field lines on themselves (see figure 1.2). This toroidal shape induces a toroidal magnetic field proportional to the current in the coils with an amplitude decreasing with the increase of the major radius  $R$ :

$$\vec{B} = \frac{\mu_0 I_{tor} \vec{e}_\varphi}{2\pi R}$$

This magnetic field amplitude gradient will lead to the well-known "grad-B" drift (or  $\nabla B$  drift). On the point of view of the particle, its orbits around field lines will be of larger radii where the magnetic field amplitude is lower. It induces a drift of the motion guiding centre perpendicular to the magnetic field and to its gradient :

$$\vec{v}_{\nabla B} = \frac{1}{2} \rho_l v_\perp \frac{\vec{B} \times \vec{\nabla} B}{B^2} = \frac{1}{2} m v_\perp^2 \frac{\vec{B} \times \vec{\nabla} B}{q B^3} \quad (1.2)$$

A second drift is due to the magnetic field line curvature itself. It is equivalent to

a centrifugal-like force and is called "curvature drift". Its expression is :

$$\vec{v}_{curv} = mv_{\parallel}^2 \frac{\vec{R} \times \vec{B}}{qB^2 R^2} = mv_{\parallel}^2 \frac{\vec{B} \times \vec{\nabla} B}{qB^3} \quad (1.3)$$

These two last drifts are in the same direction and their sum depends on the sign of the charge of the particle. It is responsible of a charge separation on spatial scale of the order of the minor radius  $a$  of the machine. This charge separation generates a vertical electric field perpendicular to the toroidal magnetic field. This impacts the particle motion through a third drift velocity called  $E \times B$  drift:

$$\vec{v}_{E \times B} = \frac{\vec{E} \times \vec{B}}{B^2} \quad (1.4)$$

As one can see in the last expression the  $E \times B$  drift does not depend on the charge of the particle. Consequently, it cannot generate current or charge separation.

These drifts are obtained in the case of a single particle system but in the case of tokamak plasmas, pressure  $p$  and density  $n$  profiles decaying from the magnetic axis to the edge occur. Locally, in presence of this background pressure gradient, the particle Larmor orbits of the particles up in the pressure gradient will encounter the ones of particles down in the pressure gradient. It will lead to a local non-zero average velocity called the *diamagnetic drift*.

$$\vec{v}_* = \frac{\vec{B} \times \vec{\nabla} p}{nqB^2} \quad (1.5)$$

Finally, fluctuations of electrostatic potential  $\Phi$  will lead to fluctuations of electric field. These fluctuations will induce a polarisation drift function of the time evolution of the guide-center velocity of the particle  $\vec{v}_d$ .

$$\vec{v}_{pol} = \frac{\vec{B}}{B^2} \times \frac{m}{q} d_t \vec{v}_d \quad (1.6)$$

## 1.2.2 The tokamak magnetic configuration

The  $E \times B$  drift pushes away all the particles along the major radius axis and all these particles are lost. A way to avoid this loss phenomenon consists in adding

a poloidal magnetic field  $B_\theta$  in the azimuthal direction  $\theta$  to short-circuit the charge separation caused by the drifts. Two main designs for magnetic devices have been considered : the tokamak and the stellarator.

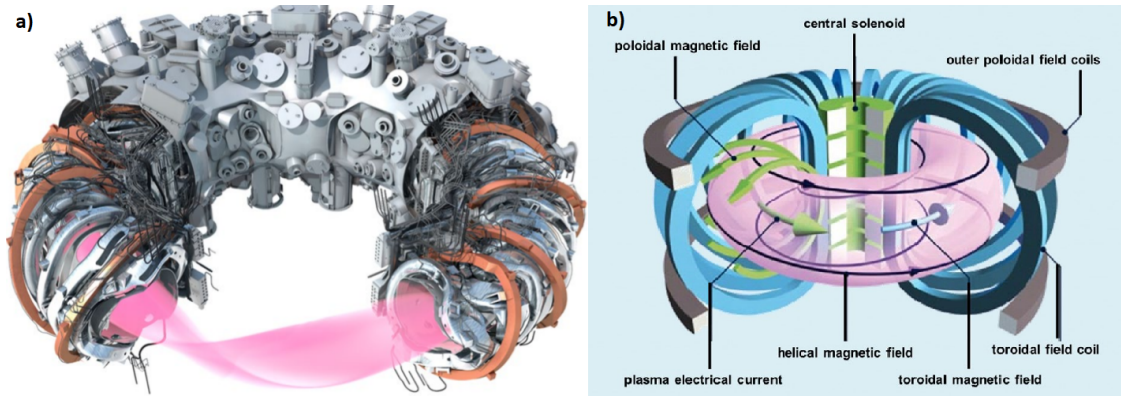


Figure 1.2: Designs of the magnetic devices : a) a stellarator (Wendelstein 7-X) [7] and b) a tokamak [4]

In a stellarator the magnetic coils are designed in order to generate a 3D magnetic field without toroidal symmetry. In the case of a tokamak, a toroidal current  $I_P$  is induced in the plasma through induction thanks to a central solenoid, electromagnetic waves or even injecting particles with a toroidal momentum (Neutral Beam Injection systems, NBI), generating the expected poloidal magnetic field. Generally, the amplitude of this poloidal magnetic field is one order of magnitude lower than the toroidal one. This poloidal magnetic field leads to an increase of the confinement time of 2 orders of magnitude compared to the case without it (from  $1ms$  to  $100ms$ ) but it is still not enough to access ignition.

The complete description of the magnetic field in a tokamak has to take into account the retro-action of the currents generated by the plasma itself on the magnetic field. It can be done through the magnetohydrodynamics theory (MHD) [8]. These calculations are reduced in the well known Grad-Shafranov equations. Resolving these equations gives us the shape of the magnetic surfaces which are organising as layers. The centre of these surfaces is slightly shifted towards the higher major radii due to the so-called Shafranov-shift. The plasma pressure is conserved on flux surfaces. The resulting magnetic equilibrium is summarised in the fig.1.3.

The total magnetic field being non-fully toroidal, the field lines are no longer toroidal loops but become inclined compared to the toroidal axis. This angle called *pitch angle* is determined by the geometry of the plasma and by the ratio

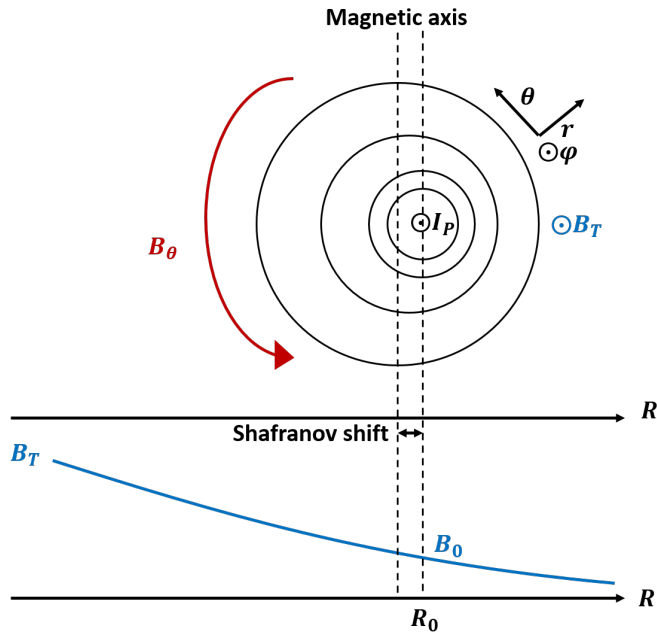


Figure 1.3: Poloidal section of the magnetic equilibrium in a tokamak

of the poloidal and toroidal magnetic fields amplitudes. An important quantity in the tokamak physics is the helicity of the field lines characterised by the so-called *safety factor* represented by the number of toroidal turns in one poloidal turn. This name comes from the importance of this term in the stabilisation of MHD turbulence. To calculate it, one needs to take into account the spatial variation of magnetic field amplitude on the path of a poloidal turn. This is represented by an integral over a poloidal path coordinate  $l_\theta$ .

$$q = \frac{1}{2\pi} \oint \frac{B_\varphi}{RB_\theta} dl_\theta \quad (1.7)$$

Neglecting the contribution of the poloidal magnetic field, one can estimate the length of a field line  $L_{FL}$  as :

$$L_{FL} \approx 2\pi qR \quad (1.8)$$

The safety factor is also a function of the minor radius  $r$  because of the dependency of the poloidal magnetic field with the radial distribution of the plasma current (Ampere's law). One can approximate the safety factor in the case where the major radius  $R$  is much larger than the minor radius  $r$  (or equivalently, if the

inverse aspect ratio  $\epsilon = r/R$  is much lower than 1) as:

$$q(r) \approx \frac{rB_\varphi}{RB_\theta} \quad (1.9)$$

The radial variation of the safety factor induces a shear, called *magnetic shear* calculated from the logarithmic derivative of the safety factor.

$$s = \frac{r}{q(r)} \frac{dq(r)}{dr} \quad (1.10)$$

Magnetic shear and parallel length are key players in the work presented in this manuscript because of their impact on the transport perpendicular to the flux surfaces [9, 10, 11, 12]. This perpendicular transport of particle towards the plasma boundary will balance with the particle sources coming from the ionisation of neutrals leading to the establishment of a density profile. The same equilibrium is assessed for the energy by the balance between heat transport, heating power injection and radiated power. The radiated power is resulting from different processes such as the ionisation. It results in density and temperature profiles which radially decays (see figure 1.10). Typically the density decreases from  $0.1 - 5 \times 10^{20} m^{-3}$  in the core to  $0.1 - 5 \times 10^{19} m^{-3}$  at the Last Closed Flux Surface (LCFS) and the temperature decreases from  $1 - 10 keV$  in the core to  $10 - 100 eV$  at the plasma boundary. Therefore, the perpendicular transport is directly responsible of the efficiency of fusion reactors. In consequence, its description is one of the key questions of the research domain. This will be addressed in the next sections.

### 1.3 Transverse transport in closed field lines: classical, neoclassical and anomalous transport

The *transverse transport processes* can be decomposed in two contributions. The first one comes from collisional mechanisms and is called *neoclassical*. On the other hand, strong spatial gradients of the thermodynamic quantities (temperatures varying of 3 – 4 orders of magnitude on a distance of the order of the meter) make these plasmas out of thermodynamic equilibrium. This imbalance is responsible for a perpendicular transport through different turbulent mechanisms pumping their energy from the free energy contained in these gradients.

### 1.3.1 Collisional transport

Historically, the first phenomenon considered to explain the transverse transport is due to the coulombian interactions between particles. If two field lines are close enough, the particles of each line can interact through the coulombian repulsion and create a random diffusive process by making these particles moving from a field line to another. This is the *classical* transport. As this transport is a random diffusive one, it can be characterised by a simple diffusive radial flux proportional to the density gradient with a diffusive coefficient  $D_{\perp}^{(c)}$ . This diffusion is done on a collision time  $\nu_c^{-1}$  on a distance of the order of a Larmor radius :

$$D_{\perp}^{(c)} \approx \rho_l^2 \nu_c \quad (1.11)$$

The collision frequency is proportional to  $n T_e^{-3/2}$  while the Larmor radius is proportional to  $T_e^{1/2}$  so the diffusive coefficient is inversely proportional to the square root of the temperature. For a typical Deuterium discharge, this diffusive coefficient is of the order of  $10^{-4} - 10^{-2} m^2 s^{-1}$ .

Tokamak being toroidal devices, the radial variation of magnetic field induces other diffusion processes responsible of transverse transport [13, 14]. This is the *neoclassical transport*. A particle making a poloidal turn will experience different values of magnetic field (stronger for low major radii and lower for high major radii). It can give birth to magnetic mirror phenomena for low velocity particles. These particles will slow down approaching their bouncing point when they go towards lower major radii. In a poloidal cross section it will be characterised by *banana-like* trajectories. Such particles are called *trapped* in opposition to the *passing* ones. These particles can collide with other particles and be detrapped. The characteristic radial step of such diffusive mechanism is of the order of the banana trajectory width  $\delta_b \approx 10\rho_l$ . It characterises the diffusion regime at low collisionalities which is stronger than the classical diffusion (one to two orders of magnitude higher). Another collisional mechanism comes from the curvature drift and affects the passing particles. Collisions of particles at the top of the plasma will lead to slight drifts towards the increasing minor radii and conversely, towards the decreasing minor radii at the bottom of the plasma. The collisionality increasing with the minor radius, this phenomenon occurs more often for the higher radii leading to an effective outward flux. This phenomenon becomes dominant for high collisionality regimes and is called *Pfirsch-Schlüter* regime. It

leads to diffusion coefficient higher than the classical one by two or three orders of magnitude. Finally, at intermediate collisionalities, the trapped particles do not have the time to complete their orbit before colliding leading to a saturation of the diffusion coefficient with the collisionality. This is the *plateau* regime. All of these regimes are summarised in figure 1.4.

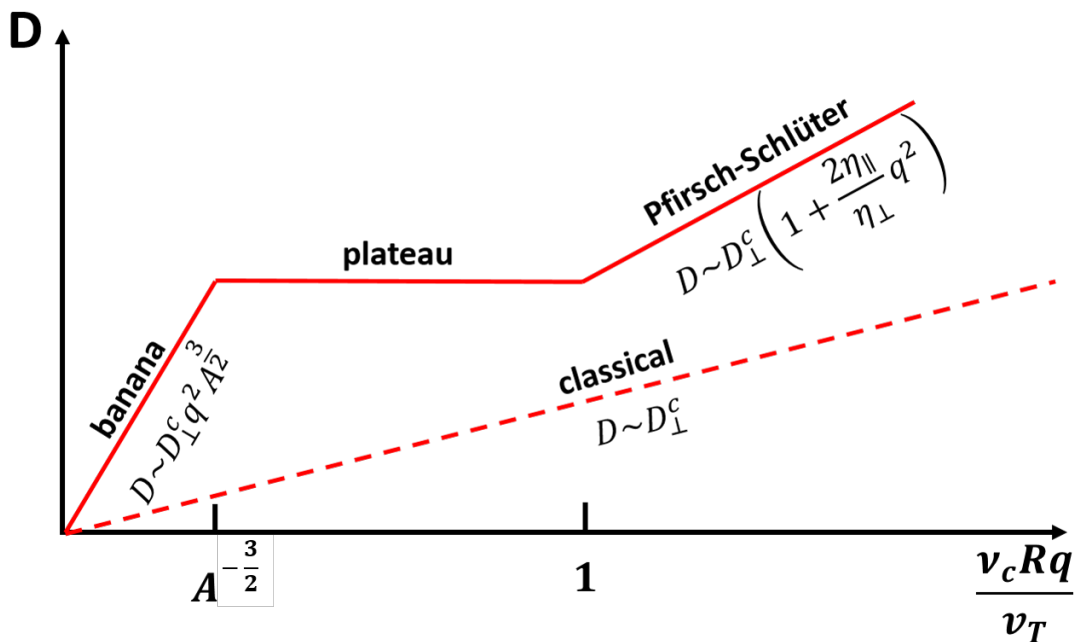


Figure 1.4: Diffusion coefficient evolution with collisionality : different neoclassical regimes

Moreover, in a tokamak, the number of toroidal coils is finite. It leads to toroidal variations of the magnetic field named *ripple*. It creates toroidal mirrors leading to local trapping. This last phenomenon can also affect the transverse transport.

### 1.3.2 Turbulent transport

Experimentally, measuring the gradients of the main quantities, one can estimate the effective diffusion coefficient in a discharge. Such measurements showed that the experimental diffusion coefficients are a few orders of magnitude higher than the predicted ones from neoclassical considerations. This higher transport level was for this reason named *anomalous transport* [15]. It is also called *turbulent transport* since it is attributed to a turbulent contribution [16] which dominates the energy and particle transport as well in the core plasma as in the edge. It represents one of the research topics on the community because of its

large impact on the degradation of the confinement time.

As mentioned above, the plasma is out of a thermodynamic equilibrium. The free energy contained in the thermodynamics quantities gradients is pumped by the turbulence to develop and transport matter and energy on large spatial distances. Indeed, temperatures, densities, electrostatic potentials and magnetic potentials can fluctuate and these fluctuations can lead to large radial transport levels through transverse convective-like phenomena. The resulting convective flux is proportional to the convolution of density/temperature ( $\tilde{n}/\tilde{T}$ ) fluctuations with their velocity fluctuations ( $\tilde{U}$ )  $\langle \tilde{n}\tilde{U} \rangle$  (or  $\langle \tilde{T}\tilde{U} \rangle$ ). This velocity being mainly an  $E \times B$  drift, it depends on the electrostatic fluctuations  $\tilde{\Phi}$  [17]. Hence, we can rewrite the flux as  $\langle \tilde{n}\tilde{\Phi} \sin(\varphi) \rangle$ . The phase shift  $\varphi$  between the density (or temperature) and electrostatic potential fluctuations is at the origin of the turbulent transport.

In this section, we describe the basics of the physics underlying two instabilities which can be a source of transport across the whole plasma minor radius and especially in the plasma edge. More particularly, we detail the destabilisation of the instabilities as well as the establishment of the phase shift between the density (temperature) and potential fluctuations. The first instability is based on the principle of drift waves (DW). We consider a density perturbation with a finite wavenumber  $k_{\parallel}$  in the direction parallel to the magnetic field. The low inertia of electrons will induce an electric field in the opposite direction to these density parallel gradients. This hypothesis of low inertia for the electrons named adiabatic electrons, induces density fluctuations in phase with the potential ones. The electrostatic potential fluctuations imply a poloidal perturbation of the electric field directed in the direction opposite to the background density gradient (see figure 1.5). This induces a drift in the radial direction leading to an enhancement of the density in the slightly outward surface on which the density is lower and a lowering of the density on the slightly inward surface. This phenomenon is responsible of the time oscillation of this wave characterising its poloidal drift and leading to the name of Drift Wave. This simple description of the drift waves is stable and does not imply any radial transport. Different mechanisms can induce an unstable behaviour such as the collisions. In the case of a resistive plasma, the electrons are no longer adiabatic and their response to the potential

fluctuations is slowed. It results in a low phase shift between the potential and density fluctuations which induces a radial transport of over-densities due to a radial  $E \times B$  drift towards the plasma boundary. In presence of a background density gradient, this phenomenon is unstable. This is the so-called Resistive Drift Wave instability (RDW).

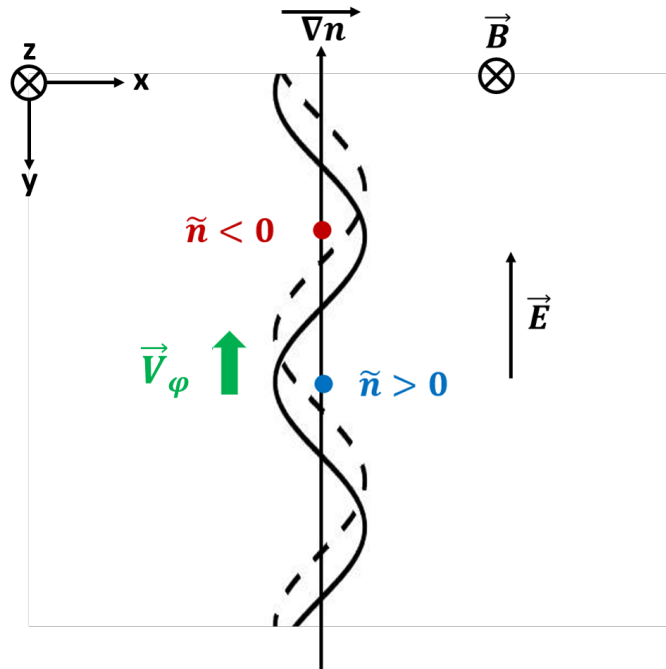


Figure 1.5: Movement of the constant density surface representing the electron drift wave. The full line represents the initial state and the dashed line a later time [5].

Another source of phase shift between density (temperature) fluctuations and electrostatic ones is the interchange mechanism. This mechanism induces a phase-shift maximising the transport  $\varphi = \frac{\pi}{2}$ . In order to understand the interchange instability, we will consider a poloidally periodic fluctuation of the electrostatic potential (see figure 1.6). These fluctuations will induce convective cells or vortices around their positive and negative values as indicated by the black arrows on the figure 1.6. These vortices introduce low-density regions in the denser part of the local density gradient and inversely. These over and under densities correspond to the B and A areas respectively on the figure 1.6. This phenomenon induces poloidal fluctuations of the density (temperature) in the poloidal direction. First, one can consider the case with curvature and diamagnetic drifts in the direction opposite to the gradient of density fluctuations. This

situation appears in the plasma Low Field Side (LFS), when the density gradient is in the same direction than the magnetic field gradient (corresponding to the case represented in figure 1.6). In a region where the potential is negative, the electronic current due to curvature drift going from an over-density towards a low-density one is higher than the ionic current going in the opposite direction. This induces an accumulation of local negative charge. This current divergence is compensated by the polarisation current. Consequently, this charge accumulation leads to a lowering of the potential. The same phenomenon happens in the positively charged regions leading to an unstable process. In the opposite case, ie the magnetic field gradient in the opposite direction to the density gradient (in the plasma High Field Side, HFS), the system is stable. This difference between HFS and LFS leads to an asymmetry characterised by a localisation of the instability around the LFS mid-plane. This is the origin of the so-called ballooning feature of the instability. In the end, this instability leads to exchanges between areas with different densities leading to the name of interchange. This instability is unstable in the ideal case and does not need any collisionality to be unstable in opposition to the RDW instability. In the case described in this section, we consider the influence of the density gradient but it is also true for other gradients such as the ion temperature gradient leading to the so-called Ion Temperature Gradient instability (ITG). This instability is characterised by fluctuations of width of a few tens of ion Larmor radii. The case of Electron Temperature Gradient (ETG) also exists with fluctuations of sizes of a few tens of electronic Larmor radii.

## 1.4 Modelling of the equilibrium in opened field lines : plasma-wall interaction and balance equations

One of the main issue in magnetic fusion devices is the interaction between the plasma and the internal wall of the vacuum vessel. Indeed, it is impossible to keep the plasma away from the wall. Moreover, it is not possible to keep the field lines tangential to the wall everywhere. Consequently, a flux of heat and particle is flowing along the field lines impacting the wall leading to a particle and heat exhaust. The wetted area represents the boundary of a plasma volume called *scrape-off layer* (SOL). Examples of a magnetic equilibria showing the shapes

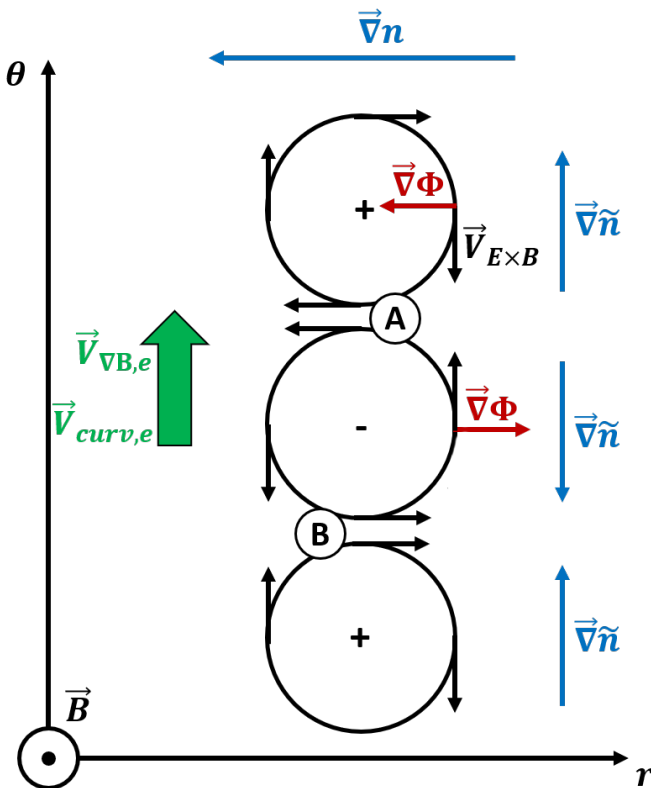


Figure 1.6: Scheme of the interchange mechanism [18].

of the open and closed field lines are given in figures 1.8 and 1.9. The fluxes impacting the wall are responsible for sputtering and damaging phenomena on the impacted areas [19]. Consequently, in this region, the equilibrium radial profiles of temperature and density result from the balance between the perpendicular transport, the volume sources and sinks and the parallel transport. The description of both parallel dynamics and transverse transport will be detailed in this section.

#### 1.4.1 Plasma wall interaction : sheath boundary conditions

The difference between the closed and opened field lines regions is the impact of the interaction of the plasma with the targets. This interaction will drive the parallel dynamics in the SOL.

Both electrons and ions are flowing along the field lines towards the targets. Nevertheless, electrons mobility is larger than the ions one, due to their lower mass, getting them first at the targets. This will polarise negatively the target, creating a positive electric field leading to two effects : ions are accelerated and

the target will repel the electrons not having enough kinetic energy to overcome the electrostatic potential. This phenomenon is a shielding-like effect on the target and occurs on a small spatial scale of the order of the Debye length defined as :

$$\lambda_D = \sqrt{\frac{\epsilon_0 k_B T_e}{n_e e^2}} \quad (1.12)$$

where  $k_B = 1.38 \times 10^{-23} J.K^{-1}$  is the Boltzmann constant. This spatial region is named *plasma sheath region* and is schemed on figure 1.7.

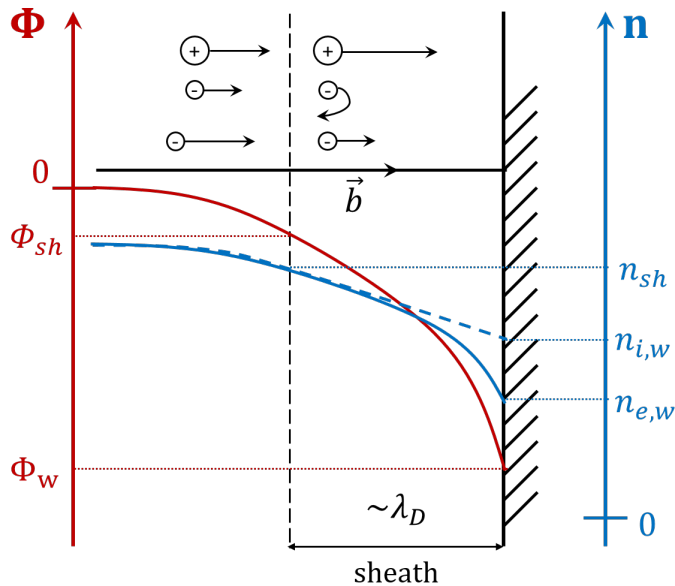


Figure 1.7: Sketch of the plasma sheath region with the associated density and electrostatic potential evolutions

#### 1.4.1.1 The Bohm boundary condition

The electric field build-up ends in an equilibrium when the ion and electron fluxes become equal at the sheath entrance. This steady-state can be determined considering a quasi-null potential on the field line far from the sheath [19]. We will follow the notation of fig.1.7 : *sh* indexes stands for sheath properties and *w* for wall properties. Let's consider a Boltzmann distribution function for the electrons entering the sheath region :

$$n_e = n_{e,sh} \exp\left(\frac{e(\Phi - \Phi_{sh})}{k_B T_e}\right) \quad (1.13)$$

For typical tokamaks SOL :  $n \approx 10^{19} m^{-3}$ ,  $T \approx 10 eV$  leading to  $\lambda_D \approx 1 - 10 \mu m$ . This is much lower than the field line connexion length  $L_{\parallel} \approx \pi q R \approx 10 - 100 m$ . This order difference allows to consider quasi-neutrality all along the field line until plasma reaches the sheath region. This condition is no longer valid in the sheath region and we have to consider the Poisson's equation :

$$\frac{d^2\Phi}{dx_{\parallel}^2} = -\frac{e}{\epsilon_0}(n_e - n_i) \quad (1.14)$$

Considering cold ions, the energy conservation equation for ions and the ion flux conservation along the field line (this is possible neglecting the ionisation in the sheath due to collision mean free path much larger than the sheath width), one can express the ion density in terms of sheath ion density and potential expressions.

$$n_i = n_{i,sh} \sqrt{\frac{\Phi_{sh}}{\Phi}} \quad (1.15)$$

Substituting (1.13) and (1.15) in (1.14) and considering quasi-neutrality at the sheath entrance ( $n_{i,sh} = n_{e,sh} = n_{sh}$ , we obtain an equation for the potential  $\Phi$ .

$$\frac{d^2\Phi}{dx_{\parallel}^2} = -en_{sh} \left( \sqrt{\frac{\Phi_{sh}}{\Phi}} - \exp \left( \frac{e(\Phi - \Phi_{sh})}{k_B T_e} \right) \right) \quad (1.16)$$

Introducing the potential difference  $\Delta\Phi = \Phi_{sh} - \Phi > 0$ , we can approximate the right hand side terms as :

$$\sqrt{\frac{\Phi_{sh}}{\Phi}} \approx 1 + \frac{1}{2} \frac{\Delta\Phi}{\Phi_{sh}} = 1 - \frac{1}{2} \frac{\Delta\Phi}{|\Phi_{sh}|} \quad (1.17)$$

$$\exp \left( \frac{e(\Phi - \Phi_{sh})}{k_B T_e} \right) \approx 1 - \frac{e\Delta\Phi}{k_B T_e} \quad (1.18)$$

The potential difference equation rewrites :

$$\frac{d^2\Delta\Phi}{dx_{\parallel}^2} = \frac{e\Delta\Phi n_{sh}}{\epsilon_0 k_B T_e} \left( 1 - \frac{k_B T_e}{2e|\Phi_{sh}|} \right) \quad (1.19)$$

The non oscillatory solution is an exponentially decaying function with an e-folding length corresponding to the Debye length and exists only if  $|e\Phi_{sh}| \geq \frac{k_B T_e}{2}$ . Using ion energy conservation  $\frac{1}{2}m_i u_i^2 = -e\Phi$ , we obtain the *Bohm boundary*

*condition :*

$$u_{i,sh} \geq C_s \quad (1.20)$$

where  $C_s = \sqrt{\frac{k_B T_e}{m_i}}$  is the sound speed. This sound speed is different from the neutral one because of the difference of collision nature. Indeed, in neutral gases, mechanical collisions occur whereas in the case considered here, electrostatic collisions are considered. This last result can be generalised in an isothermal and non-cold ion approximation leading to :

$$C_s = \sqrt{\frac{k_B (T_e + T_i)}{m_i}} \quad (1.21)$$

Another notation of the Bohm boundary condition can be encountered defining the Mach number  $M = \frac{u_i}{C_s}$  as :

$$M_{sh} \geq 1 \quad (1.22)$$

#### 1.4.1.2 The potential drop at the wall

Still considering no ionisation source in the sheath, the ion particle flux is conserved. Consequently, the flux impacting the wall is the same as the one entering the sheath :  $\Gamma_{i,sh} = \Gamma_{i,w} = n_{i,sh} C_s$ .

To determine the electron flux in the sheath, we assume a constant electron temperature through the sheath such as the electrons keep a constant parallel velocity. Assuming also the electrons as following a Maxwellian distribution function, we determine the electron average velocity by integrating this distribution function in the velocity space :

$$\bar{v}_{e,w} = \frac{1}{n_{e,w} (\sqrt{2\pi v_{e,th}})^3} \int_{-\infty}^{+\infty} dv_x \int_{-\infty}^{+\infty} dv_y \int_0^{+\infty} dv_{e,\parallel} n_{e,w} v_{e,\parallel} \exp\left(-\frac{v_{e,\parallel}^2}{2v_{e,th}^2}\right) = \frac{v_{e,th}}{\sqrt{2\pi}} \quad (1.23)$$

Using Boltzmann's equation to determine the electron density at the wall, we

thus obtain the electron flux on the wall :

$$\Gamma_{e,w} = n_{e,sh} \frac{v_{e,th}}{\sqrt{2\pi}} \exp\left(\frac{e(\Phi_w - \Phi_{sh})}{k_B T_e}\right) \quad (1.24)$$

We can now write the total parallel current at the wall :

$$j_{\parallel,w} = e (\Gamma_{i,w} - \Gamma_{e,w}) \quad (1.25)$$

$$= e n_{sh} C_s \left( 1 - \frac{v_{e,th}}{C_s \sqrt{2\pi}} \exp\left(\frac{e(\Phi_w - \Phi_{sh})}{k_B T_e}\right) \right) \quad (1.26)$$

We define the sheath floating potential  $\Lambda$  as :

$$\Lambda = \log\left(\frac{v_{e,th}}{C_s \sqrt{2\pi}}\right) = \frac{-1}{2} \log\left(2\pi \frac{m_e}{m_i} \left(1 + \frac{T_i}{T_e}\right)\right) \quad (1.27)$$

Considering a null parallel current at the wall and a wall at the floating potential ( $\Phi_w = 0$ ), we obtain the sheath potential as :

$$\Phi_{sh} = \Lambda T_e [eV] \quad (1.28)$$

The radial profile of sheath potential will then follow the electron temperature's one. For deuterium and considering equality for electron and ion temperatures,  $\Lambda \approx 2.8$ . To be more precise, a lower potential drop is occurring in the *pre-sheath region* of  $0.7T_e [eV]$ . The electrostatic potential radial profile remains proportional to the electron temperature's one. Other effects, such as second electron emissions in the sheath due to particle (photons, ions, neutrals and electrons) impacting the wall will add contributions to the parallel total current impacting the wall through the charge balance. It leads to slight lowering of  $\Lambda$  value [19].

#### 1.4.2 An edge turbulent transport model : TOKAM2D

Plasma particle behaviours is determined by Vlasov equation taking into account the collisions between the particles. Taking the different order momenta of this equation leads to the conservation laws for mean quantities such as the density or the energy. In the plasma edge, we can consider that the collisionality between particles is high and that no significant fast particle population are contributing to the distribution functions. Hence, we can assume that the plasma description by the mean quantity is a good approximation. This description re-

sults in considering a fluid approach. The edge plasma description we use in this work is based on this fluid description in 2 dimensions : radial and poloidal by applying a field line average on 3D fluid equations. We will focus on an isothermal model of the density and vorticity conservation [20, 21].

### 1.4.2.1 Continuity equation

The matter conservation equation in the SOL simply balances the parallel and perpendicular fluxes due to particle drifts with a source term  $S_n$ . We also include collisional transport through the diffusive term  $D_n \nabla_{\perp}^2 n$ . This term will help to stabilise the behaviour under the Larmor radius scale during the numerical resolutions. Here, we consider electron continuity equation :

$$\partial_t n - D_n \nabla_{\perp}^2 n + \nabla_{\parallel} j_{\parallel} + \nabla_{\perp} j_{\perp} = S_n \quad (1.29)$$

We recall the  $s$  particle fluid drift velocity as the sum of the  $E \times B$ , the diamagnetic and the polarisation drift [22] velocities.

$$j_{s,\perp} = n (v_{s,E \times B} + v_{s,*} + v_{s,pol}) \quad (1.30)$$

It is possible to show that, in the low  $\beta$  limit ( $\beta = \frac{2\mu_0 p}{B^2}$  is the ratio of the plasma pressure  $p$  over the magnetic one  $B^2/2\mu_0$ ), the divergence of the perpendicular particle flux can be approximated by the density advection due to the  $E \times B$  drift velocity (see Appendix A).

$$\partial_t n - D_n \nabla_{\perp}^2 n + \nabla_{\parallel} j_{\parallel} - \frac{1}{B} [U, n] = S_n \quad (1.31)$$

The  $E \times B$  advection of the density gradient is rewritten as a Poisson bracket  $\frac{1}{B} [U, n] = \frac{1}{B} (\partial_x U \partial_y n - \partial_y U \partial_x n)$  where  $U$  is the electrostatic potential.

### 1.4.2.2 Total charge conservation : the vorticity conservation equation

We will now consider the total charge equation as the difference between the continuity equation for electrons and ions. This results in the relation  $\vec{\nabla} \cdot \vec{j} = 0$  by assuming electro-neutrality. The  $E \times B$  drift being not able to carry current, the diamagnetic and polarisation drift velocities are no longer negligible. The total charge conservation equation can be simplified assuming the cold ions limit ( $T_i = 0$  so  $\vec{v}_{i,*} = 0$ ) and the mass difference between ions and electrons to

neglect electron polarisation drift.

$$\vec{\nabla}_{\perp} \cdot (-\vec{j}_{e,*} + \vec{j}_{i,pol}) + \nabla_{\parallel} j_{\parallel} = 0 \quad (1.32)$$

The divergence of the electronic diamagnetic flux can be rewritten considering a constant electron temperature as a Poisson's bracket containing the physical information of the impact of the magnetic field curvature.

$$\vec{\nabla}_{\perp} \cdot (-\vec{j}_{e,*}) = \vec{\nabla}_{\perp} \cdot (-n_e e \vec{v}_{e,*}) = T_e \vec{\nabla}_{\perp} \cdot \frac{\vec{b} \times \vec{\nabla}_{\perp} n}{B} = T_e [n, B^{-1}] \quad (1.33)$$

The second flux perpendicular divergence contains more terms. In this work we will only consider first order terms in perturbation. We will also neglect the pressure gradient non linearities lower in magnitude and the curvature terms considering that the diamagnetic flux divergence contains the underlying physics of the impact of the curvature.

$$\vec{\nabla}_{\perp} \cdot (-\vec{j}_{i,pol}) \approx \frac{-m_i n}{B^2} \left( \partial_t + \vec{v}_{i,E \times B} \cdot \vec{\nabla}_{\perp} \right) \Delta_{\perp} U \quad (1.34)$$

$$= \frac{-m_i n}{B^2} \left( \partial_t \Delta_{\perp} U + \frac{1}{B} [U, \Delta_{\perp} U] \right) \quad (1.35)$$

The vorticity equation finally stands in :

$$\frac{m_i n}{B^2} \left( \partial_t \Delta_{\perp} U + \frac{1}{B} [U, \Delta_{\perp} U] \right) - T_e [n, B^{-1}] - \nabla_{\parallel} j_{\parallel} = 0 \quad (1.36)$$

This system dictates the temporal and spatial evolutions of the density and the potential. To completely determine these evolutions, the parallel dynamics has to be expressed.

#### 1.4.2.3 Field line average

In order to reduce the model to two dimensions, an average of the equations (1.31) and (1.36) over a field line is made. The field line average is defined in terms of the parallel reconnection length  $L_{\parallel} \propto \pi q R$  as  $\langle \dots \rangle_{FL} = \frac{1}{2L_{\parallel}} \int_{-L_{\parallel}}^{+L_{\parallel}} \dots dl_{\parallel}$ . We will assume that the electrostatic potential, the density and its gradient are constant along the field line. After this consideration, only two terms have to be treated : the parallel dynamics term and the curvature one in the vorticity

equation. The first one is the parallel integral of a parallel divergence of the parallel current resulting in the difference between the parallel currents at the boundaries of the integral. This difference is derived from the Bohm condition and the sheath model giving  $j_{i,\parallel} = neC_s$  and  $j_{e,\parallel} = neC_s e^{(AT_e/e-U)/T_e}$ . Then the last term to be averaged is the curvature term which can be rewritten as  $\langle [n, B^{-1}] \rangle = \frac{G_0}{BRr} \partial_\theta n$  in circular geometry. Introducing the normalised potential  $\Phi = \frac{eU}{T_e}$ , the normalised radial coordinate  $x = \frac{r-a}{\rho_s}$  (where  $\rho_s \frac{1.5}{B} \sqrt{\frac{AmpT_e(1+T_i/T_e)}{Ze}}$  is the sonic Larmor radius), the normalised poloidal coordinate  $y = \frac{a\theta}{\rho_s}$  and the time normalised to the cyclotron frequency  $t = t\omega$ , the parallel damping rate  $\sigma_\parallel = \rho_s/L_\parallel$ , the curvature drive coefficient  $g = \rho_s G_0/R$  and a viscosity term  $\nu \Delta_\perp \Delta_\perp \Phi$  coming from the interaction with the small turbulent scales the equations (1.31) and (1.36) become the system with all the derivative expressed in the new coordinate system :

$$(\partial_t - D_n \Delta_\perp) n - [\Phi, n] = S_n - \sigma_\parallel n e^{\Lambda-\Phi} \quad (1.37)$$

$$(\partial_t - \nu \Delta_\perp) \Delta_\perp \Phi - [\Phi, \Delta_\perp \Phi] = -g \frac{\partial_y n}{n} + \sigma_\parallel (1 - e^{\Lambda-\Phi}) \quad (1.38)$$

It is worth noticing that the viscous coefficient  $\nu$  and the diffusive one  $D_n$  are used to stabilise numerical resolutions of the system. From equations (1.37) and (1.38), we can see that there is a competition between the curvature driving and the parallel damping. This will be the starting point of the model derived in this work in the last chapter of the manuscript.

## 1.5 Power exhaust control : limiter and divertor configurations

In order to control the wall damages and the particle and heat exhaust through the wall, dedicated areas are added in the device by inserting plasma facing components as targets. Two main concepts were studied : toroidal *limiters* and *divertor* plates. The first one consists in putting a target component toroidally symmetric in the chamber (see fig.1.8).

The field lines intercepting the limiter are named *open field lines* in opposition to the ones non-intercepting the wall. Equivalently, we differentiate the open and closed flux surfaces which are separated by the *Last Closed Flux Surface* (LCFS) or *separatrix*.

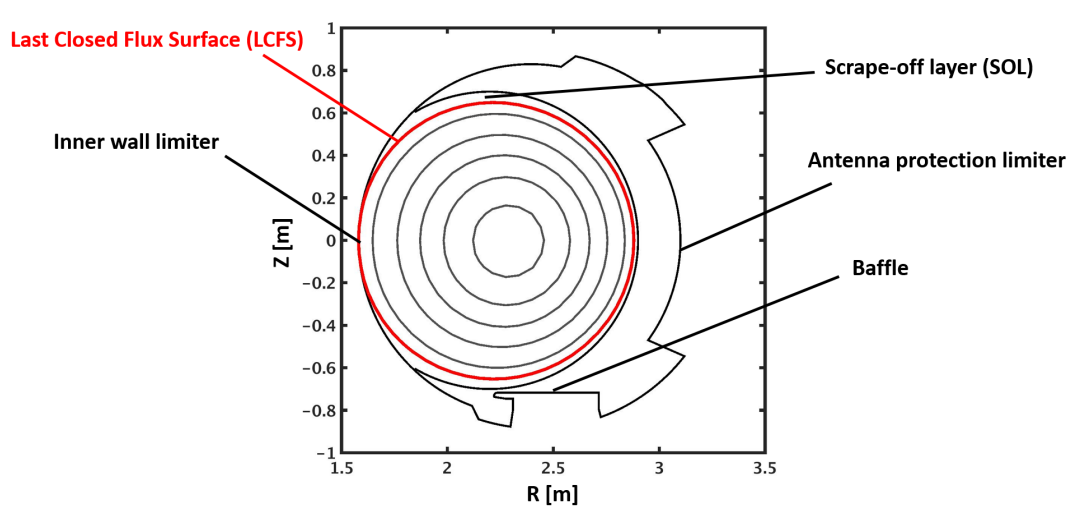


Figure 1.8: Poloidal cross section of a plasma in a limiter configuration (Tore Supra shot #44537)

As we can see on fig.1.8, the wall is in contact with the confined plasma through the LCFS. Neutrals sputtered on the limiter will go directly in the core and will radiate or dilute the fusion reagents. To palliate this contamination, coils were added close to the targets to created legs to the plasma equilibrium. This new configuration is the so-called *diverted configuration*. It is characterised by a fully toroidal field line where the poloidal magnetic field is none. This line intercepts a poloidal cross section in a point named *X-point* (see fig.1.9).

This second configuration has a few other advantages : 1) the neutrals from the targets will be ionised in the legs and won't pollute much the confined plasma, 2) the fluxes are deposited on two targets and not on a single one, helping for limiting wall damaging and 3) the flux expansion  $f_x$  due to the divertor coils leads to larger deposition areas. On the other hand, experimental observations showed heat flux deposition area widths narrower in diverted configurations. For a typical ITER test discharge, the heat power coming from the confined plasma  $P_{SOL}$  is of the order of  $100MW$ . The parallel heat flux  $q_{||}$  on the targets will be given by :

$$q_{||} = \frac{P_{SOL}}{2 \times 2\pi R f_x \lambda_q} \quad (1.39)$$

where  $\lambda_q$  is the characteristic radial heat flux deposition length at the low field side mid-plane. Materials are able to sustain heat flux up to almost  $10MW/m^2$ . Consequently, for ITER ( $R = 6.2m$ ,  $f_x \approx 10$  and  $P_{SOL} \approx 100MW$ ) we need a

width of heat flux deposition of the order of a few centimetres or millimetres.

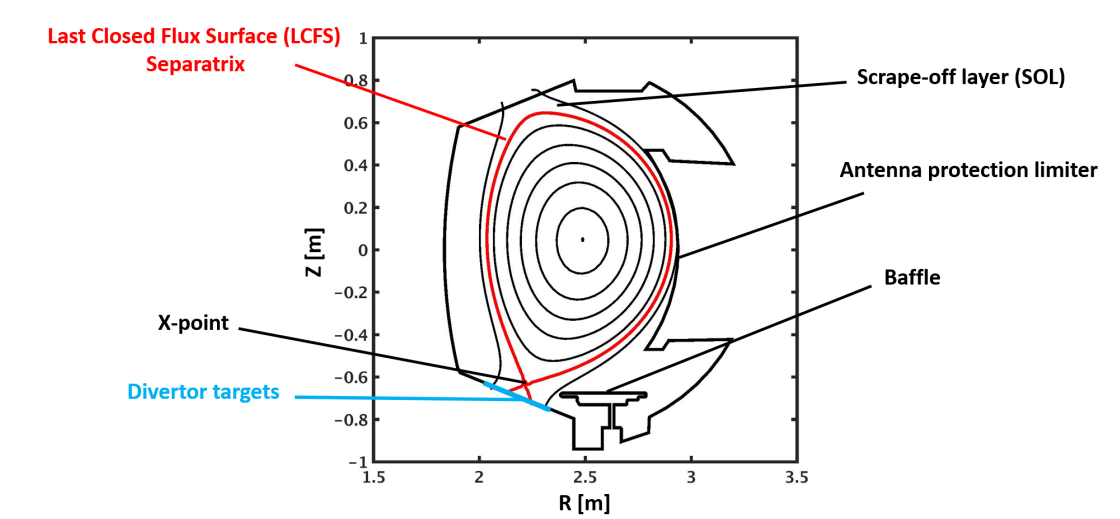


Figure 1.9: Poloidal cross section of a plasma in a divertor configuration (WEST shot #55732)

Nowadays, the main tokamaks sustain diverted discharges as it will be the case for ITER. Nevertheless, the plasma in the early phase of the discharges generated in ITER will be in inner-wall limited geometry [23]. Consequently, both configurations have to be studied in order to prepare future devices operation. Moreover, some more exotic configurations are studied such as *Snowflake* where multiple X-points are considered [24, 25] or *X-divertor* with a high flux expansion at the targets [26].

## 1.6 From Tore Supra and WEST to ITER

This thesis is based on experimental observations and their use to validate theoretical investigations. It aims at giving a theoretical and experimental background to prepare the ITER tokamak operation. These observations are made on the device situated here in the CEA centre of Cadarache. Initially, this device called **Tore Supra** operated limited discharges with Electron and Ion Cyclotron Resonance Heating (ECRH and ICRH) and Lower Hybrid (LH) heating systems in a carbon-wall vessel. Then, it has been upgraded towards the **WEST** tokamak with a full Tungsten vessel wall able to sustain discharges in diverted configuration. The characteristic quantities of these devices are summarised in table 1.1. The change in magnetic topology in the device offers an opportunity to study the

impact of the geometry on edge transport. Indeed, in WEST, two divertors are installed : one at the top of the vessel and another one at the bottom. The conditions around these divertors are not completely the same. The volume around bottom divertor is closed with a baffle increasing the neutral compression in this region. A pumping system situated close to this divertor is used to pump a part of this neutral pressure. Both baffle and pumping system are absent at the top of the vessel leading to a discrepancy between the divertor conditions. Moreover, the aspect ratio  $R/a$  is of the order of 5 in WEST which is unique in the frame of the current devices. This also allows to study the impact of this parameter on tokamak operation and confinement properties.

Tokamak	Tore Supra	WEST	ITER
Major radius $R[m]$	2.5	2.5	6.2
Minor radius $a[m]$	0.7	0.5	2
Elongation $\kappa$	1	1.4	1.8
Plasma volume $V[m^3]$	25	15	850
Toroidal magnetic field amplitude $B_T[T]$	3.8	3.7	5.3
Plasma current $I_p[MA]$	1.5	0.5-1	15
Neutral Beam Injection (NBI) power [MW]	0.5	0	33-50
Ion Cyclotron Resonance Heating power [MW]	12	9	20-40
Lower Hybrid power [MW]	7	7	0
Electron Cyclotron Resonance Heating power [MW]	0.8	0	20-40
Magnetic configuration	Limited	Diverted	Diverted

Table 1.1: Table of the plasma parameter ranges of the Tore Supra, WEST and ITER tokamaks

## 1.7 Confinement regimes and transport barriers

### 1.7.1 What are the H-mode and the transport barriers?

The main goal of tokamak research consisting in increasing confinement, a lowering of transport level is needed. Fortunately, in the 80's in the ASDEX tokamak in Germany, a spontaneous increase of confinement has been experimentally

observed [27]. This higher confinement is characterised by a local steepening of the pressure profile associated to a reduction of the transport. This is the so-called *transport barrier*. This high confinement regime or *H-mode* (in opposition to the usual low confinement L-mode) is due to an increase of the radial gradient of the pressure in a thin radial region close to the separatrix which is called the *pedestal* (see fig.1.10). Some attempts to build-up transport barriers in the plasma core have also been managed such as in Tore Supra [28] or in JET [29].

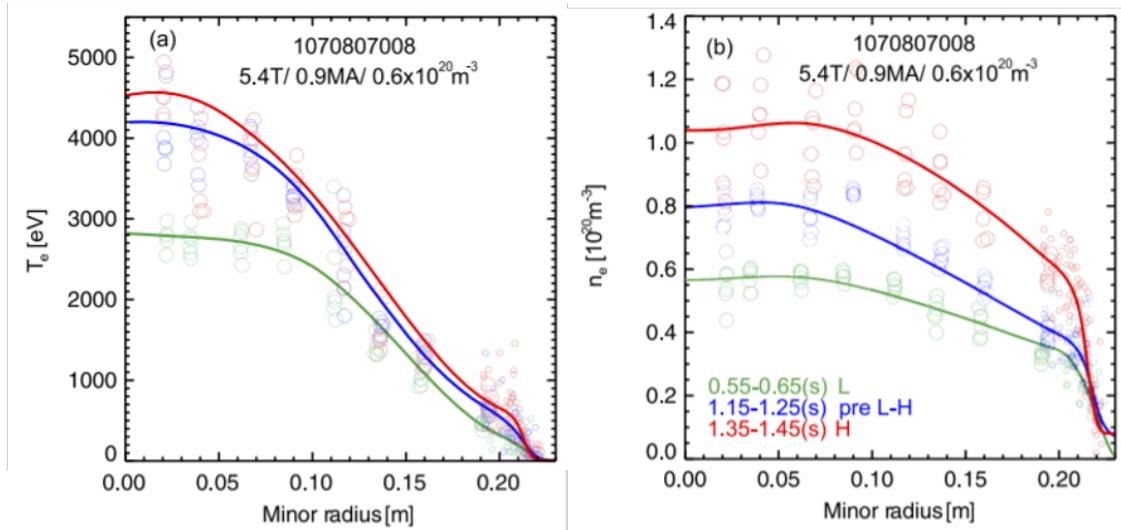


Figure 1.10: Profiles of a) electron temperature and b) electron density in L-mode (green), pre H-mode (blue) and H-mode (red) in the Alcator C-mod tokamak [30]

The apparition of the transport barrier has been attributed to a strong local shear of velocity (almost poloidal velocity) which is shearing the turbulent eddies and decorrelate them [31, 32] (see figure 1.11). This key point will be at the core of the work presented in this manuscript.

The velocity being mostly due to the  $E \times B$  drift, this shear is associated to the radial electric field  $E_r$ . As shown by figure 1.12, the difference between the L-mode radial electric field profile and the H-mode one is strongly visible in the very edge of the plasma (normalised radius equal to 1).

This confinement regime offers an opportunity to reach ignition conditions but it shows intrinsic issues. Indeed, when the edge transport is reduced, the heat deposition width on the targets reduces leading to wall damaging risks. Moreover, other instabilities are triggered in the pedestal, the so-called *Edge Localised Modes* (ELMs). These instabilities are characterised by a frequency from 10

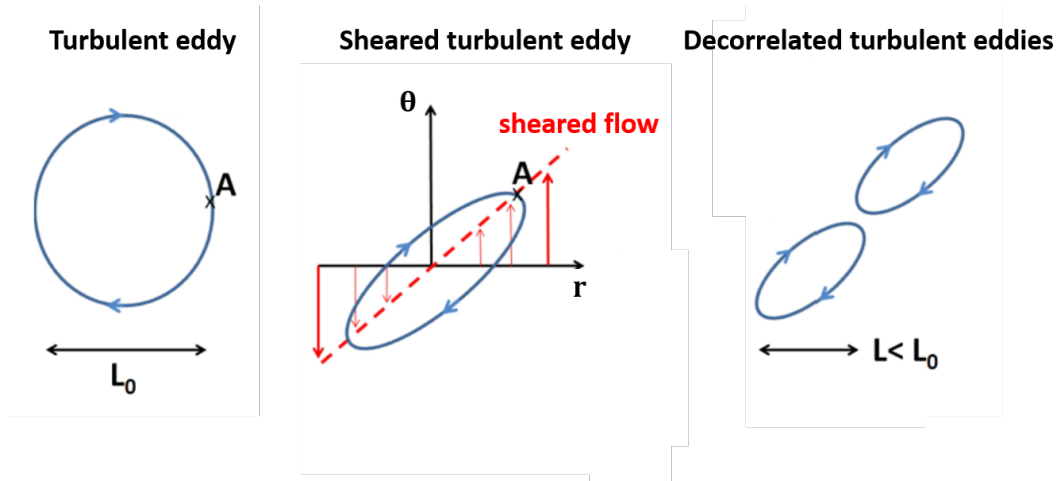


Figure 1.11: Representation of the turbulence decorrelation by a background sheared flow.

to 1000 kHz and by important heat loads going to the SOL. As soon as this regime is the chosen one for future reactors, controlling these high heat loads is a key point in managing the heat exhaust. Furthermore, the transition from L-mode to H-mode (the *L-H transition*) happens when the injected power reaches a threshold which is not yet fully explained[34]. This lack of knowledge led to the establishment of an experimental scaling law of this power threshold [34] quasi proportional to the plasma surface  $S$ , the toroidal magnetic field amplitude and the electron density  $n_e$ .

$$P_{L-H} = 0.049 n_e^{0.72} B_T^{0.8} S^{0.94} \quad (1.40)$$

Unfortunately, this scaling law carries large uncertainties. Indeed, the L-H transition threshold have been obtained reaching values of power crossing the separatrix going from half to a few times the predictions of this scaling. Moreover, even if this scaling gives us a global trend of this power threshold with the main plasma quantities, it is not able to capture impacts of plasma conditions on experimental observations.

### 1.7.2 Impact of the density and the magnetic topology on the L-H transition threshold

As mentioned above, some experimental observations remain non recovered by the experimental scaling law of the power threshold to reach the L-H transition. Experimental and numerical efforts have been managed in order to understand

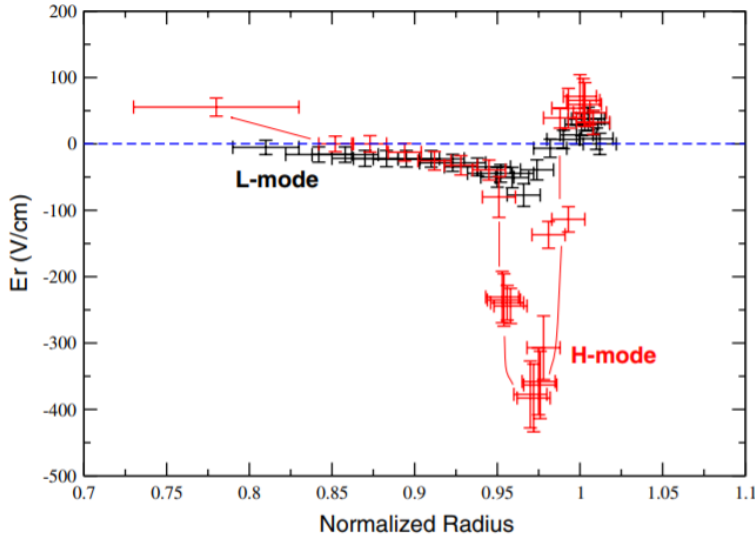


Figure 1.12: Radial profile of radial electric field in L-mode (black) and H-mode (red) in the ASDEX-Upgrade tokamak [33]

such discrepancies [35]. Interestingly, the power threshold scaling decreases when the density decreases as observed from the scaling. Nevertheless, at some point a minimum is reached and under this density threshold, the power threshold increases when the density decreases. Experimental observations [36, 37] showed that this discrepancy comes from the energy transfer to the ion channel. Indeed, when the plasma is heated by the electron channel, the energy transfer to the ions is only carried by the collisions with the electrons. When the density is low enough, the collisions are more rare and the heat transfer from the electrons to the ions is less efficient. This explains why the L-H power threshold reaches a minimum at a given density.

A second feature which is not recovered by the scaling law is the impact of the geometry on the power threshold. Two main effects were highlighted from experimental observations : 1) when the X-point is closer to the targets the threshold is lower [38, 39] and 2) the X-point position, namely at the top or the bottom of the plasma, strongly impacts the power threshold. This latter point results in the observation of a lower power threshold when the ion diamagnetic drift is directed towards the X-point [40]. This observation gave birth to a nomenclature of the symmetric configurations consisting in a *favourable* (to the transition) and an *unfavourable* configuration. A lot of theoretical, experimental and numerical investigations are managed in order to understand the impact of the geometry

on the L-H transition assessment. Moreover, experimental observations in exotic configurations with a negative triangularity showed increased confinement properties in L-mode which are comparable to H-mode ones, demonstrating again the importance of the plasma shaping [41].

### 1.7.3 The other confinement regimes

As mentioned above, the H-mode is characterised the presence of strong heat and particle bursts in the plasma edges (ELMs). These loads represent a danger for future reactor plasma facing components. This is why the avoidance of such events is crucial for future devices. It motivated current investigations on other confinement regimes characterised by the absence or the reduction of ELMs activity.

One of the main ways is favoured by the unfavourable configuration. Indeed, the power threshold to assess the H-mode being higher, it opens a window in the parameter space in which a confinement regime can be reached, the so-called I-mode (for Improved confinement mode). This I-mode presents a pedestal in temperature but not in density. The absence of ELMS lets appear its signature : the *Weak Coherent Mode* (WCM) [42, 43, 44]. This WCM is thought to be responsible of the transport in the temperature pedestal leading to the absence of a density pedestal. This confinement regime could be an opportunity for future reactors because of its wider heat deposition on the targets and its lower and continuous transport in the edge. Unfortunately, the parameter space to assess this regime seems to be narrower than the one to assess the H-mode.

Recently, some regimes have been discovered presenting advantages such as the *quiescent H-mode* in which no ELM activity is observed. The parameter spaces of these regimes have not been yet well established and an experimental investigation aims at palliating this lack of knowledge [45].

## 1.8 Edge rotation profile establishment

Understanding the H-mode assessment relies on the modelling of the establishment of the rotation profiles at the periphery of the confined plasma which is responsible of the turbulence mitigation. We distinguish three regions of interest.

The first one is the core plasma (radii under 80% on the plasma minor radius) where, in absence of torque injection, the rotation is imposed by an equilibrium between the pressure gradient [46, 47] and turbulent momentum transport. The second one is the scrape-off layer in which the electrostatic potential is imposed by the sheath and consequently the resulting  $E \times B$  drift is given by the temperature gradient  $v_\theta = -\frac{\Lambda \partial_r T_e}{ZB}$ . The last one is the confined plasma boundary (from 80% to 100 % of the minor radius) across which the edge transport barriers establishes. The rotation profile behaviour in this region as well as the impact of plasma parameter such as the magnetic topology on this behaviour are still not fully understood.

The rotation profile induced by the  $E \times B$  drift in perpendicular direction is the consequence of the establishment of the radial electric field profile. This electric field results from non-ambipolar currents formation in the plasma [48]. Indeed, it aims at short-circuiting the resulting charge separation. Two main contributors to the radial current can be distinguished : 1) the phenomena induced by a difference of trajectories between electrons and ions and 2) the currents induced by the turbulence activity. The first category includes the neoclassical bulk viscosity leading to an excess of ion current [48]:

$$J_r^{BV} = -enD_p \left[ \frac{\partial_r n}{n} + \gamma_j \frac{\partial_r T}{T} - \frac{e}{T} (E_r - B_\theta V_{||}) \right] e^{\left(\frac{e\rho_p E_r}{T}\right)^2}$$

Another example of phenomenon coming from the particle trajectories inducing a radial electric field is the ion orbit loss mechanism [49, 50, 51]. Trapped ions can have trajectories crossing the separatrix. When the particle moves through the SOL, collisions can detrap the particle or even collisions with the wall can lead to a charge loss on the flux surface corresponding to the one of the centre of the banana orbit. This phenomenon can be associated to a fraction of the phase space in which the particles can be lost. This effect impacts mainly the ions because of their wider banana orbit width leading to a negative effective charge of the flux surface. It results in the creation of a radial current  $J_r^{IOL}$  and consequently, to a negative radial electric field in the closed flux surfaces close to the separatrix.

The second main contribution to the radial electric field profile establishment is

the turbulent one induced by the turbulent Reynolds tensor  $\Pi_{r\theta}$ :

$$J_r^{turb} = -\frac{en}{r\omega} \frac{\partial r \Pi_{r\theta}}{\partial r}$$

where  $\omega$  is the ion cyclotron frequency. This last term is very important in the models of predator-prey aiming at describing the interaction between sheared flow and turbulence. Indeed, this predator-prey approach is based on two phenomena : 1) the turbulence generates a local sheared flow through the contribution of the Reynolds stress and 2) the damping of the turbulence intensity by the sheared flow [52, 53]. From the sum of the different contributions to the radial current, we can deduce the time evolution of the radial electric field with the relation :

$$-\epsilon_{\perp} \epsilon_0 \partial_t E_r = J_{BV} + J_r^{turb} + J_r^{others} \quad (1.41)$$

where  $\epsilon_{\perp}$  is the dielectric constant of the plasma. The electric field will evolve in order to compensate the currents.

This approach can also be seen from the point of view based on the poloidal momentum conservation equation in which the rotation is resulting from the balance between a flow generation due to the turbulent Reynolds tensor  $\Pi$  and a neoclassical force  $f = -\nu n (v_{E \times B} - K_{\theta} v_{dia})$  recalling the  $E \times B$  drift towards the opposite of the diamagnetic one. Expressions of the  $\nu$  and  $K_{\theta}$  coefficients can be found in [13, 54, 55]. The balance between the flow generation by the turbulent Reynolds tensor and the neoclassical force will be a key point of the work presented here. We also consider a viscous term of momentum characterised by a viscosity coefficient  $\chi_{diff}$  representing rotation breaking by small scale physics. The poloidal momentum conservation results in :

$$\partial_t n v_{\theta} + \nabla_r (n \Pi_{r\theta}) = -(\nu - \chi_{diff} \partial_r^2) n (v_{\theta} - K_{\theta} v_{*}) \quad (1.42)$$

It is worth noting that the inclusion of a friction force with neutrals would lead to a recalling term similar to the one invoked by the neoclassical recall force. This last point is invoked in the explanation of experimental observations showing that in H-mode the edge rotation is given by the neoclassical prediction [56].

Finally, the radial momentum conservation or force balance can be seen as a closure equation linking the radial electric field, the pressure gradient, the poloidal

and parallel velocities.

$$E_r = \frac{\nabla_r p_i}{Z_{en_i}} + v_\varphi B_\theta - v_\theta B_\varphi \quad (1.43)$$

Note that this expression alone is not able to predict both radial electric field and toroidal velocity in axisymmetric devices. These degenerated quantities can be separated invoking breaking of this axisymmetry such as with the toroidal ripple of the magnetic field amplitude due to the finite number of coils [57].

## 1.9 Context and objectives of the thesis

Nowadays, the turbulence is known to be the main contributor to the radial transport across the whole plasma. In the edge, this turbulent transport is responsible for the particle and heat flux going through the separatrix. Then, this flux will flow along the field lines reaching the targets leading to possible damages. The edge turbulence is a current topic of research. Indeed, this turbulence is simultaneously across the confined plasma and the open field lines where the parallel dynamics is different. Moreover, linear and quasi-linear models are applied to closed flux surfaces [58] whereas the flux in the SOL is described by intermittent structures represented by mean characteristics [59] or statistically with distribution functions [60]. The equilibrium between transverse and parallel dynamics leads to the deposition width on the target for both particles and heat. Some models allow to make predictions [61, 62] for deposition width to compare with experimental scalings [63, 64, 65] used because of the lack of knowledge. However, these approaches are at least partially based on experimental observations and are not able to recover all of the SOL features. In particular, the parallel dynamics is not fully included in such models and should be important especially when the edge density increases [66, 67]. The change in plasma geometry should also be taken into account in the parallel dynamics description [12].

The edge turbulent transport is also involved in the confinement time of both energy and particles. Experimental observations of higher confinement regimes gave hopes for reaching Lawson criteria high enough for future reactors. These regimes are linked to turbulence reduction or suppression in the edge plasma by a thin shear layer. Nowadays, the origin of this shear layer and its impact on the turbulence are not fully understood but are of primary interest. Shear impact on

turbulence and shear flow generation are the two key ingredients involved in this complex system.

Recently, experimental data showed a correlation between core confinement and heat flux deposition width on the target [68]. This link seems to be comparable through all the confinement regimes. This point indicates that the edge physics has to be fully understood in order to predict confinement and power exhaust properties for future devices.

The passage from limited to diverted configurations lead to a change in the edge properties. Indeed, the SOL width is reduced by a factor 2 to 10 from limited discharges to diverted ones [63, 69]. Also, plasma shaping can be used as an actuator to vary this width [70, 71]. The analytical models are not able to reproduce such effects. Another unexplained experimental feature is the formation of a shoulder in SOL density radial profiles. This appears when the plasma density increases. Moreover, geometry showed impacts on the L-H transition threshold. First, the access to H-mode has been demonstrated in almost all the diverted geometry devices in the world while in limited geometry only a few H-mode have been observed so far [72]. Even in diverted geometry, the direction of the ion diamagnetic drift compared to the position of the principal X-point showed an importance in the value of the H-mode power threshold. When the ion diamagnetic drift points towards the principal X-point, the power threshold appears lower than in the opposite configuration. This difference can be significant and is not fully understood.

All of the points presented in this section are studied experimentally, theoretically and numerically. The phenomena involved in turbulent transport being non-linear, theory encounters difficulties to model analytically all the features of this transport. It's possible to make numerical simulations to solve the turbulence equations and determine transport levels but this method is very time consuming and somehow hard to interpret. In addition, if one wants to model the ion turbulence, a precision of the order of the ion Larmor radii is needed to recover all the turbulence feature. This would lead to a high number of spatial points to model a plasma volume of a few cubic meters which is above the current simulation capabilities ( $\rho_l \approx 10^{-3}$  so  $10^{10}$  points are needed for the ion turbulence it is even higher for the electron one because  $\rho_l^i \approx 40\rho_l^e$ ). Nevertheless, simple 2D models showed the ability to recover SOL features such as both turbulence properties and radial transport levels [73, 74, 75]. A way to palliate the issues encountered by numerical simulations is the model reduction as using quasi-linear methods

[58]. It can lead to analytical estimations of transport coefficient which can be used in simple diffusive or convective transport models [76].

The objective of this thesis is to study the impact of edge plasma conditions such as the geometry on the transport level and the transport barrier establishment. Starting from a simple 2D model TOKAM-2D [21], a model reduction will be applied in order to quantify the transport by determining the edge turbulence properties. The inclusion of complex effects in the model control parameters will attempt to take into account of the geometry and parallel dynamics effects. An experimental study of the impact of the geometry and plasma parameters on the edge velocity profiles is also included in this manuscript. For that, measurements in the WEST tokamak were managed in different magnetic configurations with different edge safety factors. Then, a reduced model of interplay between turbulence and shear flows is the next step towards the understanding of the edge shear flow generation and turbulence mitigation. Both model, with and without interplay with shear flows, are verified against 2D simulations and validated against experimental observations from Langmuir probes measurement in the Tore Supra tokamak and the TJ-K stellerator.

# **Chapter 2**

## **Experimental characterisation of edge turbulent transport and flows : Langmuir probes and Doppler Reflectometry data**

### **Content**

---

This chapter is dedicated to the experimental characterisation of edge turbulent transport and rotation profiles. We will introduce the physics principle involved in Langmuir probes and Doppler reflectometry measurements. Points on data treatment from both diagnostics are developed leading to the building of databases. Correlation between confinement properties and edge rotation is showed. A study with dedicated experiment on impacts of magnetic geometry, plasma current and density on edge rotation is presented and discussed. Finally, the assessment of an increased confinement regime in WEST is documented in terms of edge sheared flow profiles.

---

## 2.1 Langmuir probe measurements in Tore Supra : an experimental database of SOL turbulent features for model validation

In this section, the physics underlying probe measurements is introduced. Afterwards, we detail the data processing used to characterise turbulent transport in Tore Supra scrape-off layers supported by a discussion on physical limitations. Finally, the experimental system and the Tore Supra plasmas considered are presented as well as the database which is used to validate turbulent transport models in the next chapter (see section 3.4.3).

### 2.1.1 Principle of Langmuir probes measurements

An intrusive way to measure local plasma quantities consists in introducing small electrostatic collectors in the plasma. These collectors interact with the local plasma through the same phenomena as the ones presented in the introduction on plasma-wall interactions (section 1.4.1). Assuming that the probe size  $a_p$  is very small compared to typical SOL sizes (parallel reconnection lengths), we can fairly consider that the whole SOL physics will not be perturbed such as the perturbation induced by the presence of the probe is very local. Nevertheless, the collection area of a probe is larger than the collector's one due to the sheath formation and momentum transfer close to the probe [77]. The presence of the collector causes a wake extending its collection area in the parallel direction. This perturbation area would replace the collection one. Estimations of this collection size go from a few centimeters to a few meters which are still lower than the SOL size ( $\approx 100m$ ).

Langmuir probes can be located at different positions in order to study tokamak plasma edges : some are included in the targets where the plasma wets the wall and others are mounted on isolating heads and plunged directly in the SOL. Usual Langmuir probes can measure three plasma quantities : the electron density (ions one also considering quasineutrality), the electron temperature and the electrostatic potential. To this end, the probes are polarised with different potential to determine the potential-current curve as one can measure for an electronic component (diodes). Starting from very negative polarisations of the

collector, the electrons will be repealed and only the ion channel will be probed. This measurement will directly give the so called saturation current, proportional to plasma density. Gradually increasing the voltage applied to the probe will lead to a progressive collection of a part of the distribution function of the electrons. The trend obtained by this method is directly linked to the electron temperature as long as we consider the electrons behaviour governed by a Boltzmann equation. In a steady-state, the current measured by the probe  $j_p$  will be simply the sum of the ion and electrons one. It can be written in terms of the potential  $\Phi_p$  at the sheath entrance, the current at the sheath entrance given by the saturation one  $j_{SAT} = Zn_eaeC_s$ , the reference potential  $\Phi_0$ , the potential drop in the sheath  $\Delta\Phi$  and an attenuation factor  $\alpha$  due to a slight drop of the density at the pre-sheath entrance. Models of conservation in the pre-sheath region of local quantities such as the total pressure can lead to estimations of this coefficient.

$$j_p = j_{SAT} \left( 1 - \exp \left( \frac{e(\Phi_p - \Phi_0 - \Delta\Phi)}{k_B T_e} \right) \right) \quad (2.1)$$

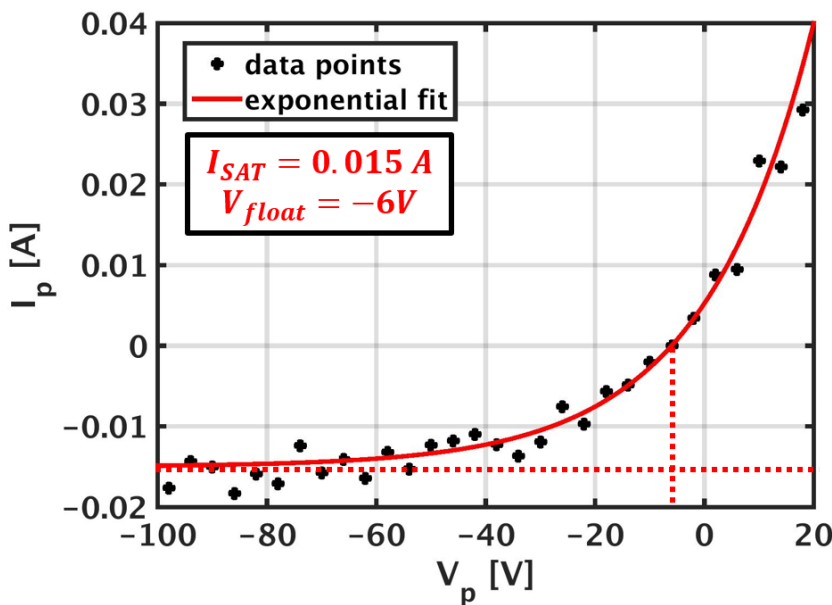


Figure 2.1: Example of a typical potential-current profile of a Langmuir probe measurement

A typical evolution of the current measured by a Langmuir probe when its polarisation is varied is shown on figure 2.1. From this plot, one can recover the explanations on the particle fluxes collected introduced earlier. Following this, three regimes of operation are indicated :

- **saturation regime** : The polarisation of the probe is maintained strongly negative ( $\approx 200V$ ). Only the **ion saturation current** is measured. This is used to measure saturation current fluctuations which are associated to the density fluctuations.
- **floating regime** : The current in the probe is imposed to zero allowing the measurement of the **floating potential**  $V_p = V_0 + \Delta V$  (equivalent to  $\Phi_p = \Phi_0 + \Delta \Phi$ ). This regime allows to measure the electrostatic potential fluctuations.
- **characteristics** : The potential imposed to the probe is swept in order to change the polarisation and describe the potential-current curve presented earlier. Applying an exponential fit to the obtained curve gives access to the three important plasma local quantities : **the saturation current**  $j_{SAT}$ , **the floating potential**  $V_0 + \Delta V$  and **the electron temperature**  $T_e$ . The characteristic time of acquisition of such systems is limited by the electronic capabilities and is of the order of a few tens of microseconds. This acquisition time keeps one from measuring turbulent fluctuations. Thus, this method is used for time averaged measurements. Nevertheless, it is not possible to determine the ratio between ion and electron temperature. An assumption is usually done to estimate the sound speed  $C_s$  approximating this ratio by a value of 2 in the SOL ( $\frac{T_i}{T_e} \approx 2$ ). Indeed, experimentally, it has been observed in a few tokamaks, including Tore Supra, that this ratio is about 2 at the separatrix [78]. It gives an evaluation of the sound speed and gives access to the electron density dividing the saturation current by this sound speed. This method is based on a strong assumption : the electron temperature is well described by the wings of the distribution function. Indeed, the electrons captured by the collectors are on the wings of the distribution function. It supposes that the distribution function is a pure Maxwellian with a width corresponding to the thermal velocity of the electrons. If a fast population of electrons is present at the probing position, the electron behaviour cannot be fully described by a fluid model and this assumption can be discussed.

The evolution of both turbulence and background profiles are inseparable. Consequently, the use of these three regimes is necessary to fully characterise edge transport features.

## 2.1.2 SOL background profiles measurement in Tore Supra

In order to understand the interplay between intermittent turbulence and averaged profiles, one has to measure both turbulence properties and background profiles. Moreover, if one tries to validate model predictions comparing it against measurement, will need local plasma quantities to evaluate the parameters of control of the model. First, we will focus on the background electron density and temperature profile measurement leading to the built of a database for the model validation.

In Tore Supra, a plunging probe system situated in the top part of the device measured the electron temperatures and densities in the SOL (see figure 2.2). Plunging a probe in the plasma can be responsible of a overheating of the probe. In consequence, the plunge has to be very quick. The system used in Tore Supra consists in a probe head mounted on a hydraulic piston able to move back and forth the probe from the wall to the LCFS and to the wall again in less than 200 ms. This travelling time is short enough to avoid damages but constrains the time sampling of the acquisition system in order to obtain precise radial profiles. Besides, we consider that this dive of the probe is fast compared to the plasma equilibrium evolution. It results in a consideration of a steady-state plasma measurement. In other words, the obtained profiles does describe the local plasma state. The position of the probe is known in the absolute space ( $R, Z, \varphi$ ) but not in the plasma coordinates ( $\Psi, \theta, \varphi$ ) where  $\Psi$  is the poloidal magnetic field flux coordinate,  $\theta$  is the poloidal angle from the low field side mid-plane and  $\varphi$  is the toroidal angle [5]. The coordinate transform is given by the equilibrium reconstruction from the magnetic measurements and pressure profiles across the confined plasma. Conveniently, the profiles are plotted in function of the distance from the LCFS. Also using the equilibrium reconstruction, the flux tube envelope can be described allowing to extrapolate the profiles to the outboard mid-plane, as it is usually done.

Characteristics curves (potential-current plot) are made at different positions of the probe. Fitting the obtained points as shown in figure 2.1, gives access to the local electron temperature leading to the reconstruction of the radial temperature profile (see figure 2.2 b)).

Then, measuring the saturation current  $j_{SAT}$ , one can deduce the electron density assuming the ion to electron temperature ratio. An example of density

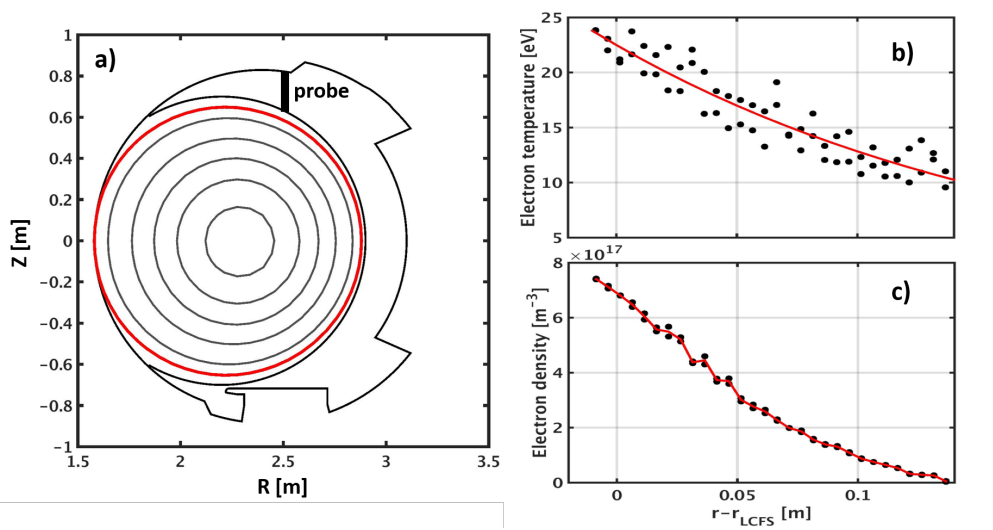


Figure 2.2: a) Poloidal section of a Tore Supra plasma indicating the Langmuir probe position, b) and c) are typical electron temperature and density profiles measured by the Langmuir probe system (Tore Supra #44600)

profile reconstructed from Tore Supra measurement is given in figure 2.2 c). We observe exponentially decaying profiles for both electron density and temperature as expected for a simple balance equilibrium between parallel and radial flow. Exponential fit of these profiles using the expression  $n_e = n_{e,sep} e^{\frac{-(r-r_{sep})}{\lambda_n}}$  (and  $T_e = T_{e,sep} e^{\frac{-(r-r_{sep})}{\lambda_T}}$  for the temperature) give values for the electron density and temperature at the LCFS and for the e-folding lengths of these quantities (see figure 2.3) showing high regression coefficients ( $R^2 > 0.85$ ) in all the parameter range explored in this database. Note that fluctuations are observed on the experimental data due to measurement uncertainties and turbulence. These values constitute the database used to validate the model of transport which will be presented in the next chapter (section 3.4.3).

In addition, the plasma electrostatic potential is proportional to the temperature. This will be used to estimate the local radial shearing rate via the expression of the poloidal  $E \times B$  drift velocity :  $\gamma_{E \times B} = \frac{-\partial_r E_r}{B} \propto \partial_r^2 T_e \propto \lambda_T^{-2}$ . The database will also include all the plasma parameters needed to apply the model on :  $I_p$  the plasma current,  $B$  the magnetic field amplitude at the magnetic axis,  $R$  the major radius of the plasma,  $a$  the minor radius of the plasma,  $q_{cyl}$  the cylindrical safety factor at the LCFS and  $T_{e,sep}$  the electron temperature measured at the LCFS. The range of these parameters used in this study is given in table 2.1.

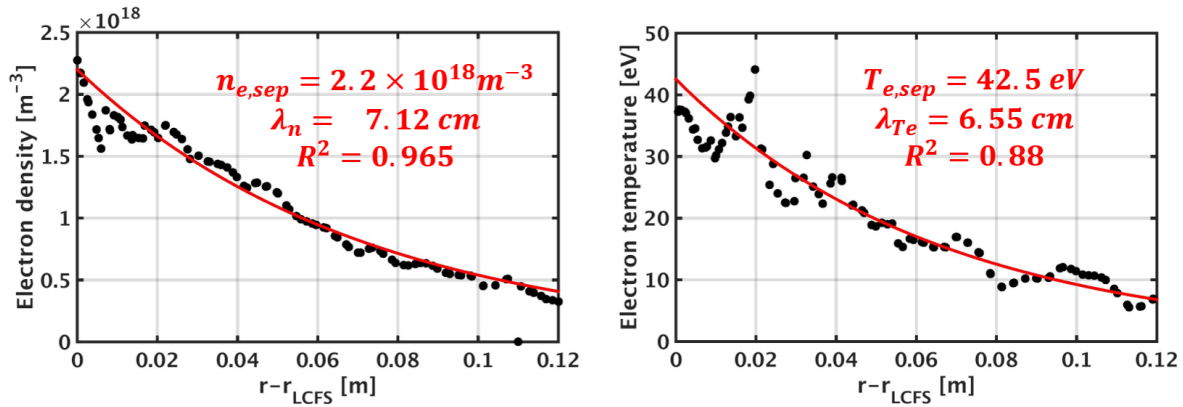


Figure 2.3: Radial profiles of electron density (left) and electron temperature (right) measured by the Langmuir probe system (Tore Supra #44584). In red are represented the exponential fit leading to the measure of LCFS conditions and e-folding lengths evaluation

Database	number of points	$R$ [m]	$a$ [m]	$B$ [T]	$I_p$ [kA]	$q_{cyl}$	$T_{e,sep}$ [eV]
mean profiles	133	2.4	0.65	2.6 - 4.1	400 - 1300	3.4 - 11.5	17 - 81

Table 2.1: Table of the plasma parameter ranges of the mean profiles

## 2.1.3 Turbulent transport characterisation

### 2.1.3.1 The rake probe system implemented in Tore Supra

In order to characterise turbulence in the SOL plasma, we need a diagnostic with an accurate time resolution. The use of probes in saturation and floating regimes seems to be indicated. Indeed, no potential sweep is needed in these regimes leading to a very accurate measurement of the time evolution of the local plasma quantities including their fluctuations. The diagnostic installed on Tore Supra consists in a rake of 6 stainless steel pine designed to be aligned with flux surfaces (see figure 2.4). Each collector has a diameter of 1.27 mm and are separated from their neighbour by 3 mm. The stainless steel has been chosen for sake of good electric conduction and resistance to erosion by the plasma flow. These probes can operate in both saturation and floating regimes. The system is also composed of two other probes on both sides to measure Mach numbers but will not be studied in this work. The acquisition is made at 1 MHz with an anti-aliasing filter (at 250 kHz).

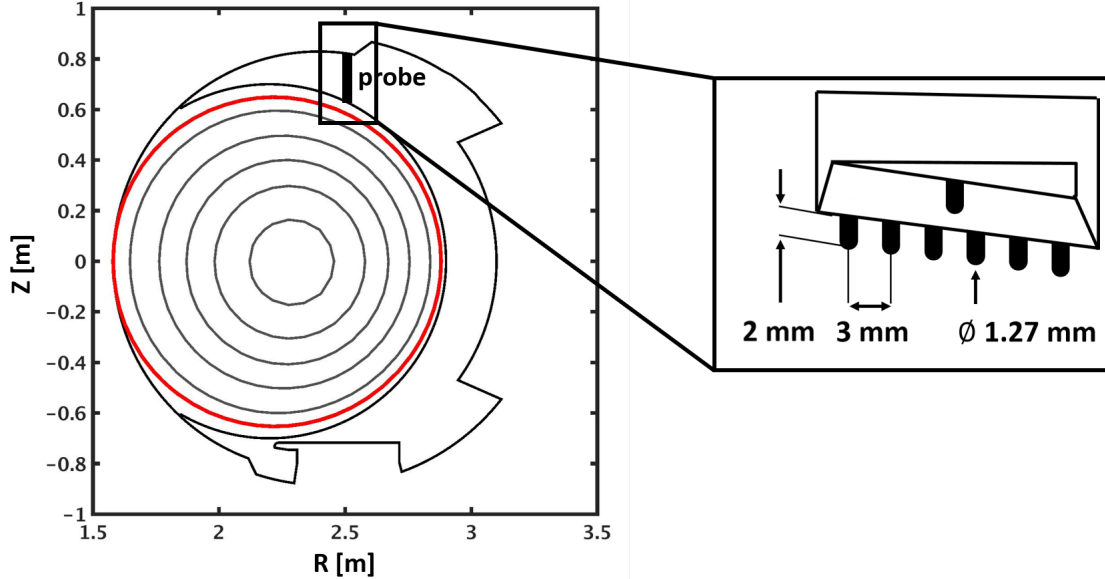


Figure 2.4: Poloidal section of a Tore Supra plasma indicating the rake probe system position with a zoom detailing the shape of the diagnostic

### 2.1.3.2 Discussion on the ability of probes to measure turbulence features

The non-perturbation of the plasma by the probe dive is still questionable. What is more, the system has to be very accurate to measure small fluctuations. A study to understand the perturbation of both fluxes and fluctuations due to the probe has been managed in order to determine the optimal geometry [79]. Moreover, the uncertainty on the collection area being important, one has to evaluate the impact of this unknown on the measurement. The typical time scale on which the plasma flows from the pre-sheath entrance to the probe is evaluated to a value slightly lower than  $1\mu\text{s}$ . Consequently, the use of the rake probe system in order to measure saturation current fluctuation can be considered as valid for fluctuations of frequency lower than the mega-hertz. In the case of edge turbulence, the fluctuation frequencies are of the order of  $10 - 100\text{kHz}$ . One can assume that the system described here is adapted. Furthermore, a calibration has been done in order to be able to analyse the data considering these sources of uncertainties [80]. The saturation current fluctuations can also be due to the electron temperature fluctuations. It has been shown that in Tore Supra, the dependence in electron temperature of the saturation current is cancelled by the dependence of the collection area

for the mean quantities [80]. Nevertheless, it has not been demonstrated for fluctuations.

Concerning the floating potential measurement, the collection area of the probe is different for electrons and ions leading to a probable overestimation of the floating potential. No model is able to predict this overestimation but we will assume that the probe geometry induces the minimum of disturbance with respect to the floating potential measurement. Recalling the floating potential expression :  $V_f \approx V_{plasma} - \Lambda T_e$ , one can see that the floating potential fluctuations can come from both plasma electrostatic potential fluctuations and electron temperature fluctuations. These latter ones are usually not measured and no robust model is able to predict the contribution of these fluctuations in the total floating potential. Experimentally, it has been observed that temperature fluctuations are in phase with density [81, 82] or electric field ones [83]. Thus, we can pragmatically consider that these fluctuations are contributing to the saturation current ones. Finally, the measured potential perturbations can come from both plasma potential and electron temperature ones. These potential perturbations are used to predict perturbations of the electric field. This electric field perturbations is used to determine the turbulent particle flux  $\Gamma = <\tilde{n}\tilde{E}_\theta>$ . This flux depends on the cross-phase between the density and the electric field perturbations. The temperature fluctuations being in phase with the density ones, the electric field perturbations they generate will be in phase opposition with the density ones and somehow, their contribution should vanish.

### 2.1.3.3 Saturation current and floating potential time traces

Keeping in mind all of these limitations and hypotheses on the ability to interpret the measurement, one can use the rake probe system to measure turbulence features.

An example of the time trace of the measured saturation current obtained by such method is shown in figure 2.5. We observe a bursty signal due to the presence of turbulence intermittency. Strikingly, these fluctuations appear asymmetric. The positive fluctuations are more plentiful than the negative ones. This is due to positive density perturbations lasting a few tens of microseconds attributed to the filaments in the SOL plasma. Furthermore, we can see

that the fluctuation level is very high. Indeed the mean value of the profile is  $\langle I_{SAT} \rangle = 33 \times 10^{-3} A$  and the standard deviation is  $\sigma_I = 5.8 \times 10^{-3} A$  corresponding to a relative fluctuation level  $\sigma_I / \langle I_{SAT} \rangle \approx 18\%$ . This fluctuation level can be seen as a proxy of the density fluctuation level. Some violent event amplitudes can even reach a few times the standard deviation.

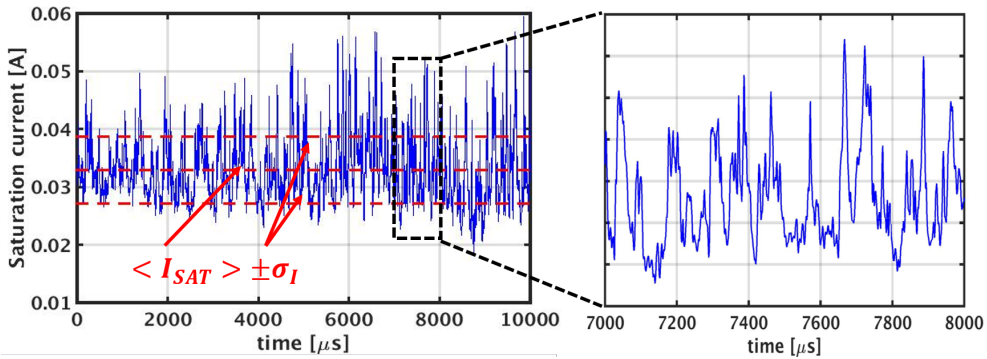


Figure 2.5: Time trace of the saturation current measured by the rake probe in Tore Supra (shot #41628). Red lines corresponds to the mean of the signal and standard deviations from this mean

The floating potential time traces exhibit a similar behaviour in terms of bursty signal properties and living time of the structures (see figure 2.6). Nevertheless, no asymmetry is observed concerning the sign of these fluctuations as it would be expected from interchange origin of the fluctuations. Such observations are common in magnetically confined plasmas.

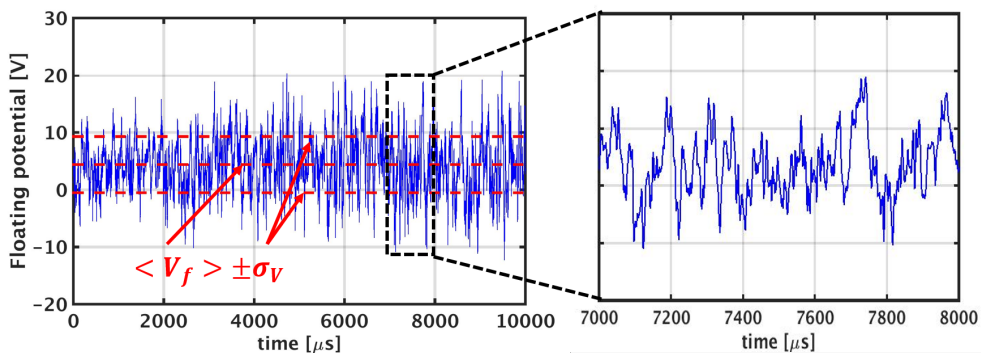


Figure 2.6: Time trace of the floating potential measured by the rake probe in Tore Supra (shot #41628). Red lines corresponds to the mean of the signal and standard deviations from this mean

### 2.1.3.4 Data treatment and database build-up

Similarly to the database of background density profiles, we built a database of turbulent features. The measurement of these features will be detailed in the following. This database is built in a set of bottom-limited ohmic discharges in various plasma conditions as indicated by the table 2.2.

Database	number of points	$R$ [m]	$a$ [m]	$B$ [T]	$I_p$ [kA]	$q_{cyl}$	$T_{e,sep}$ [eV]
fluctuation features	6820	2.4	0.65	3.2 - 3.8	800 - 1400	3 - 5.25	5 - 36

Table 2.2: Table of the plasma parameter ranges of the turbulence features database

In order to compare to the model predictions, we included in the database of fluctuation features which are time averaged over time windows of 5ms. The measurement we considered are :

- **the fluctuation levels** of the density  $\sigma_n / \langle n \rangle$  assumed to be the same as the ion saturation current ones  $\sigma_I / \langle I_{sat} \rangle$  and of the potential normalised to the electron temperature  $e\sigma_\Phi / \langle T_e \rangle$  measured as presented in the subsection 2.1.3.3.
- **the poloidal correlation length** of the density (ion saturation current) and potential structures. These are evaluated polarising all the pins in saturation or floating configuration respectively. Then, we calculated the poloidal cross correlation function  $C_{i,j,\theta}$  of the signals  $s_n^{(i)}$  and  $s_n^{(j)}$  measured by probes  $i$  and  $j$  integrated on time.

$$C_{i,j,\theta}(l_\theta) = \int_{-\infty}^{+\infty} s_n^{(i)}(t - t') s_n^{(j)}(t')' dt' \quad (2.2)$$

where  $s_n^{(i)} = \frac{s_n^{(i)} - \langle s_n^{(i)} \rangle}{\sigma_{s,i}}$  is the normalised fluctuating signal of the probe  $i$ . This function is exponentially decaying with an e-folding length  $\delta_\theta$  corresponding to the mean poloidal correlation length of the structures. This correlation length can be associated to the poloidal structure size and will be compared with model predictions in the next chapter.

- **average blobs features** are reconstructed from signals measured by the pins. Half of the probes are polarised in saturation regime and the others

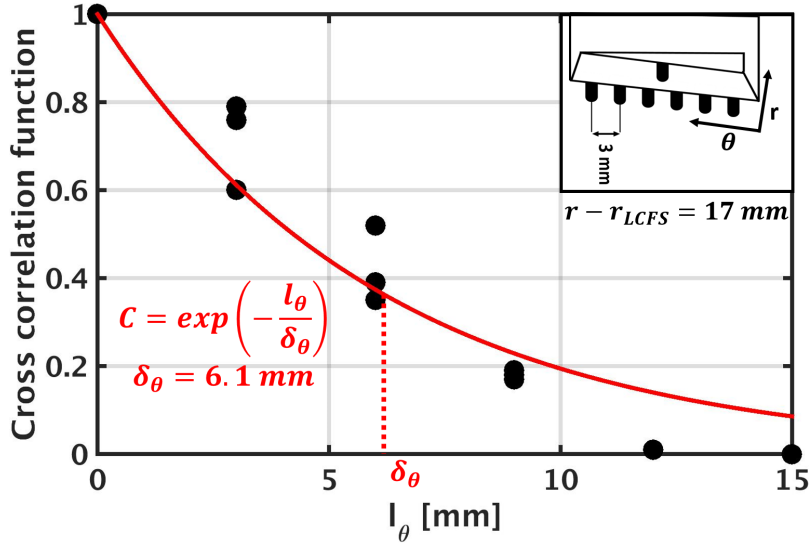


Figure 2.7: Cross correlation function of saturation current signals measured by the rake probe system (TS #42973,  $B = 3.9T$  /  $I_p = 1MA$ )

in floating regime (see figure 2.8). Blobs are identified as structures with lasting time greater than  $10\mu s$ . Considering cosinus shapes for blobs one can determine their wavelength or wavenumber.

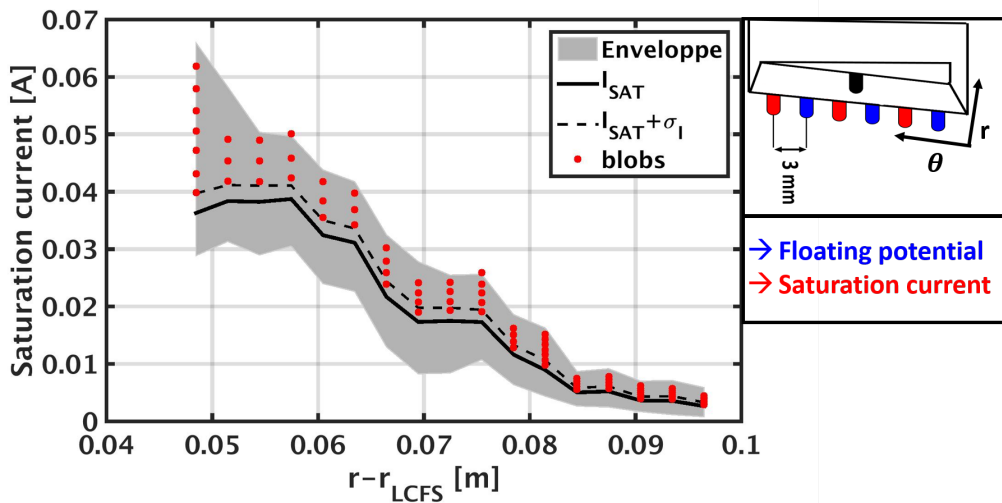


Figure 2.8: Left : Radial profile of Saturation current measured by the rake probe system (TS #44635). The red dots corresponds to the considered blobs. Right : Rake probe configuration : half saturaton regime and half floating regime alternatively

Then, a radial velocity is associated to these structures using the 2 neighbour probes which are polarised in floating configuration. The poloidal electric field  $\tilde{E}_\theta$  created by the structures will be calculated by making the

difference of the potential between two probes  $i$  and  $j$  separated by the distance  $d_{i,j}$  :  $E_\theta = \frac{\Phi^{(j)} - \Phi^{(i)}}{d_{i,j}}$ . This poloidal electric field induces a radial  $E \times B$  drift of the structures  $\tilde{V}_r = \tilde{E}_\theta/B$  which will be compared to model predictions in the next chapter. All the details of the data treatment used to study the average blobs can be found in [75].

The turbulence studied here is responsible of edge transport and consequently of the physical quantities profile shapes. This transport can be strongly impacted by edge sheared flows through the mitigation of the turbulence. These flows are of utmost interest in the quest of high efficiency reactors and will be the topic of the next section.

## 2.2 Experimental characterisation of edge flows : use of a Doppler Back Scattering (DBS) system

Reflectometry diagnostics are used to characterise edge density profiles and turbulence in magnetically confined plasmas thanks to the reflection of an electromagnetic wave on a cut-off layer. These methods provide local measurements with a high enough temporal resolution to describe density fluctuation features. Two reflectometry systems are considered in fusion devices : one measuring turbulent features and background density profiles [84, 85] and one relying on the Doppler shifting of the electromagnetic wave by the density fluctuations to measure the local rotation [86, 87, 88, 89]. This edge rotation is thought to be responsible of the turbulence mitigation and, consequently, of the local lowering of transport. Accordingly, in this work, we will focus on the Doppler reflectometry system implemented in WEST : **DIFDOP** and its use to characterise edge rotation profiles.

In this section, we first detail the operation of Doppler Back-Scattering systems (DBS) and present the signal processing managed to reconstruct radial profiles of edge rotation. Also, the error sources and the hypotheses behind the estimation of the local velocity are discussed. Then, the database of edge rotation profiles built during this work by these processes is presented. Dedicated experiments on the impact of power injection, edge density, plasma current and geometry on the rotation profiles are described and the resulting observations are discussed. Finally, a characterisation of an increased confinement regime

observed in WEST is laid out showing the strong shear layer appearing at the plasma edge.

### 2.2.1 Reflectometry principle : the collective scattering

Reflectometry systems rely on the local scattering of a wave by turbulent structures. Considering a monochromatic plane wave  $E_i(\vec{r}, t) = E_{i,0}e^{i(\vec{k}_i \cdot \vec{r} - \omega_i t)}$  at the position  $\vec{r}$  propagating towards an assembly of turbulent structures at the position  $\vec{r}_j$  with  $j$  the index of the structure  $j$ . These structures will then act as second emitters of spherical waves. We will interest in the scattered wave  $E_s(\vec{r}', t)$  at the position  $\vec{r}'$  with a wavenumber  $\vec{k}_s$  propagating towards an observer pointed by the direction  $\vec{n}'$  and far from the scattering structures (see figure 2.9).

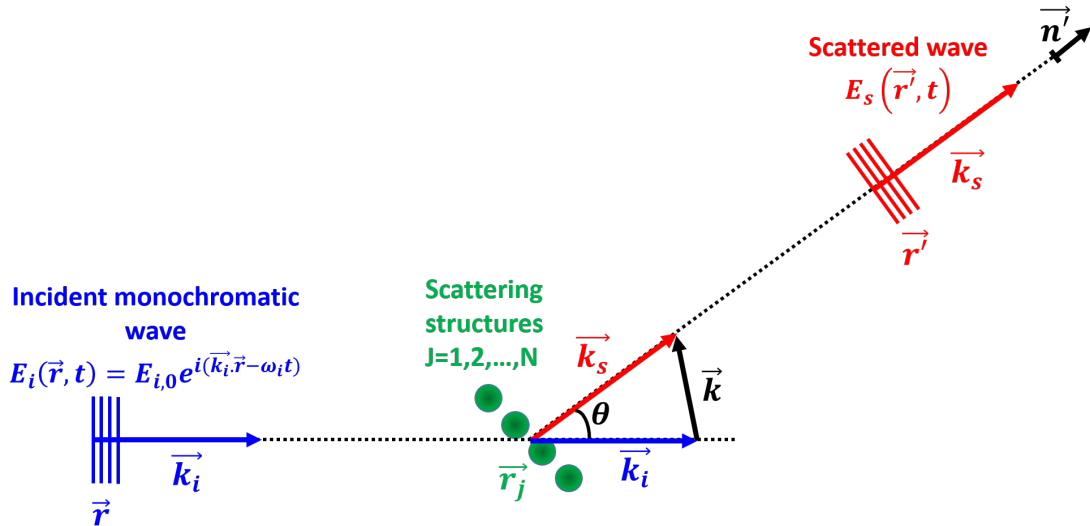


Figure 2.9: Scheme of a monochromatic plane wave collectively scattered by turbulent structures

The wavenumber amplitude is conserved during the scattering ( $\vec{k}_s = k_i \vec{n}'$ ). The scattered wave is the sum of the waves produced by each structure and can be written as :

$$E_s(\vec{r}', t) \propto \sum_{j=1}^N e^{i(\vec{k}_i \cdot \vec{r}_j + \vec{k}_s \cdot (\vec{r}' - \vec{r}_j) - \omega_i t)} \quad (2.3)$$

Considering the scattering wave number  $\vec{k} = \vec{k}_s - \vec{k}_i$ , the amplitude of the scattered wave will be maximum if the sum of the phases is constructive. It corresponds to the situation in which the structures are spread in the perpendicular plane to the scattered wavenumber  $\vec{k}$  separated by equal distances of  $\lambda = \frac{2\pi}{|\vec{k}|}$ .

This wavelength is depending of the scattering angle  $\theta$  as :

$$\lambda = \frac{1}{2 \sin(\theta/2)} \frac{2\pi}{k_i} \quad (2.4)$$

This condition is known as the Bragg's relation and lead in the case of DBS measurement to  $k = k_{turb} = -2k_i$ .

## 2.2.2 Local velocity measurement using the Doppler shift

The scattered wave can be separated in two contributions : a plane wave  $e^{i(\vec{k}_s \cdot \vec{r} - \omega_i t)}$  times a scattered signal  $s(\vec{k}, t) = \sum_{j=1}^N e^{-i\vec{k} \cdot \vec{r}_j(t)}$ . This second contribution will contain the information on the features of the scattering structures. In the case of an magnetically confined fusion plasma, the turbulent structure velocities  $\vec{v}_s$  are the sum of the instability phase velocity  $\vec{v}_\phi$  and of the background plasma velocity. In general, the first contribution is neglected and the second one is usually associated to the  $E \times B$  drift.

$$\vec{v}_s = \vec{v}_\phi + \vec{v}_{plasma} \approx \vec{v}_{E \times B} = \frac{\vec{E} \times \vec{B}}{B^2} \quad (2.5)$$

Nevertheless, experiments in Tore Supra showed that at low collisionality the measured velocity is depending on the probing wavenumber at a same position [90]. This can be explained only by the phase velocity dependency on the wavenumber. This work is based on measurement at 80% of the minor radius, slightly inner than the area of interest of the PhD thesis. In this work, the phase velocity will be neglected and dedicated measures have been performed in WEST at the boundary of the confined plasma to check this assumption. This will be discussed later in this manuscript.

Taking into account the structures velocity, we can decompose their position as the sum of a static position and a drifting contribution :  $\vec{r}_j(t) = \vec{r}_j(0) + \vec{v}_{E \times B t}$ . The scattered signal is then composed of a constant part due to the amplitude of the fluctuations  $s(\vec{k}, 0) = e^{-i\vec{k} \cdot \vec{r}_j(0)}$  and a time depending second part  $e^{-i\vec{k} \cdot \vec{v}_{E \times B t}}$ . This second contribution contains the information of the local velocity. In order to extract this information from the measured signal, we can apply a Fourier

transform to the auto-correlation function in time of the signal :

$$S(\vec{k}, f) = \int_{-\infty}^{+\infty} d\tau \frac{1}{N} \langle s^*(\vec{k}, t)s(\vec{k}, t + \tau) \rangle \quad (2.6)$$

$$= \frac{1}{N} \left| s(\vec{k}, 0) \right|^2 \int_{-\infty}^{+\infty} d\tau e^{i(2\pi f - \vec{v}_{E \times B} \cdot \vec{k})\tau} \quad (2.7)$$

$$= \frac{1}{N} \left| s(\vec{k}, 0) \right|^2 \delta(f - \frac{1}{2\pi} \vec{v}_{E \times B} \cdot \vec{k}) \quad (2.8)$$

In the case of the monochromatic plane wave, it results in a Dirac function centred on the Doppler frequency  $f_D = \frac{1}{2\pi} \vec{v}_{E \times B} \cdot \vec{k}$ . In the case of edge plasma turbulence the structure velocities are following a probability function and the spectrum of the signal becomes broader. An example of a spectrum measured in WEST is given in figure 2.10.

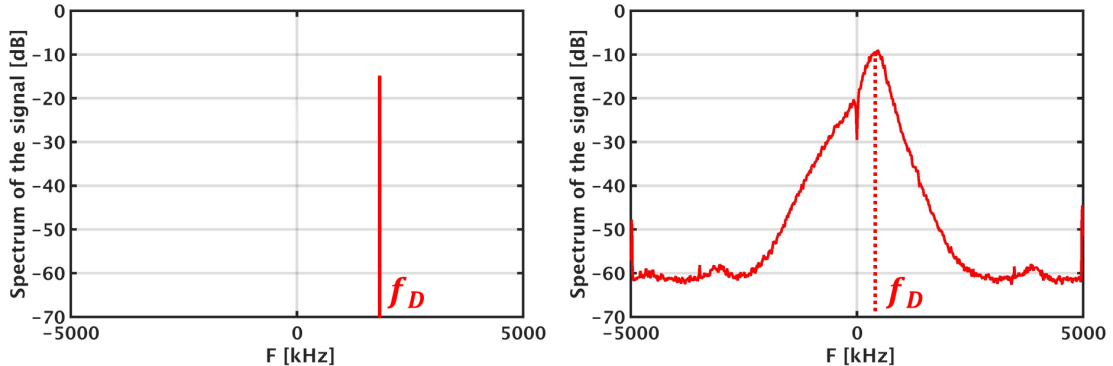


Figure 2.10: *Left* : Example of a spectrum measured from a single velocity population of structure. *Right* : Example of spectrum measured in WEST by the DBS system (WEST #54732 @t=4.6s)

The aim of the method applied here is to measure the velocity profile. More precisely, we want to measure radial profiles of binormal velocity. The probed velocity is composed of the perpendicular and of the parallel (to the magnetic field lines) velocities. The second contribution is neglected. Three key ingredients are needed to reconstruct a poloidal velocity radial profile : the Doppler shift  $f_D$ , the probing wave number  $k$  and the position of probing. The first one is obtained by the process detailed in this subsection. The two others need to determine the path of the electromagnetic wave through the plasma. This is the point of the next subsection.

### 2.2.3 Propagation of an electromagnetic wave through the edge plasma

Doppler reflectometers consists in systems launching a probing wave through an antenna towards the plasma. This wave will propagate until it reaches a point where it will be reflected by the magnetised plasma known as the cut-off layer where the propagation index is null. Because of the presence of a helical magnetic field lines, the wave has to be launched with an angle allowing to obtain a propagation of the wave perpendicularly to the magnetic field at the reflection point ( $\xi = 90^\circ$  in figure 2.11).

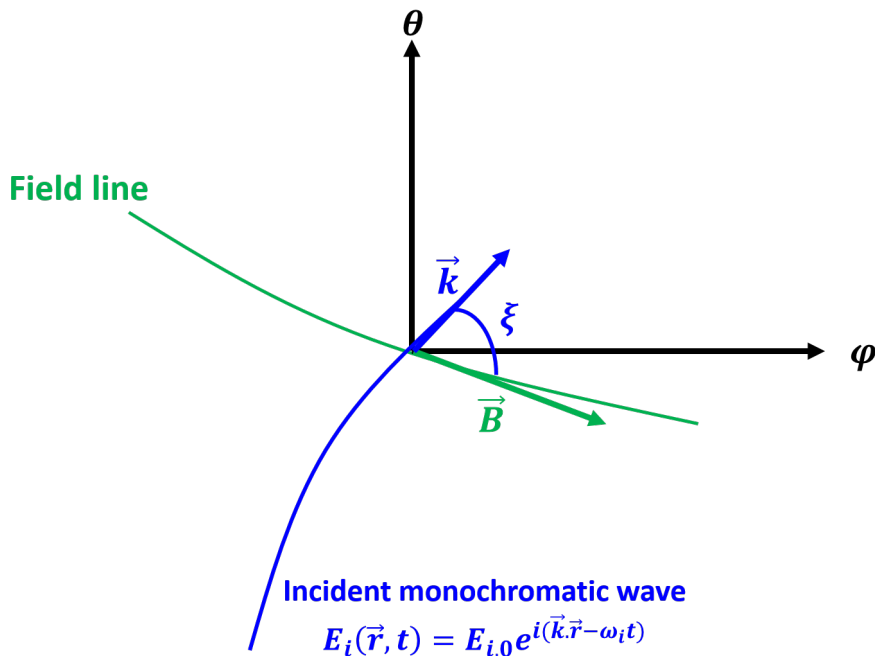


Figure 2.11: Scheme of the propagation and the reflection of the wave on a field line

In order to determine the position of the reflection of the electromagnetic wave as well as the corresponding local wavenumber, one has to find the position where the local refractive index reaches a null value. We will consider a monochromatic plane wave of pulsation  $\omega_i$ , wavenumber  $\vec{k}$  and amplitude  $E_{i,0}$   $E_i(\vec{r}, t) = E_{i,0} e^{i(\vec{k} \cdot \vec{r} - \omega_i t)}$  to represent the beam launched by the system antenna. This wave will propagate through the plasma. To describe this propagation, we call on the Maxwell equations to characterise the beam behaviour and the Ohm's

law for the plasma medium. This leads to the dispersion relation for the wave :

$$\vec{k} \times \vec{k} \times \vec{E}_i + \bar{\epsilon} \frac{\omega_i^2}{c^2} \vec{E}_i = \vec{0} \quad (2.9)$$

with the dielectric tensor :

$$\bar{\epsilon} = \bar{I} + \frac{i\bar{\sigma}}{\epsilon_0 \omega_i} \quad (2.10)$$

where  $\bar{I}$  is the identity tensor,  $\epsilon_0$  the void permittivity and  $\bar{\sigma}$  the plasma resistivity tensor. This equation can be rewritten in terms of the refractive index  $n^2$  and of the angle between the magnetic field line and the propagation direction  $\xi$  introducing the electronic plasma frequency  $\omega_{p,e} = \sqrt{\left(\frac{e^2 n_e}{\epsilon_0 n_e}\right)}$  and the cyclotron frequency  $\omega_c = \frac{eB}{m_e}$  [91, 92].

$$(A \sin \xi^2 + B \cos \xi^2) n^4 - (CD \sin \xi^2 + AB (1 + \cos \xi^2) n^2) + BCD = 0 \quad (2.11)$$

with :

$$A = \frac{1}{2}(C + D) \quad (2.12)$$

$$B = 1 - \frac{\omega_{p,e}^2}{\omega_i^2} \quad (2.13)$$

$$C = 1 - \frac{\omega_{p,e}^2}{\omega_i (\omega_i + \omega_c)} \quad (2.14)$$

$$D = 1 - \frac{\omega_{p,e}^2}{\omega_i (\omega_i - \omega_c)} \quad (2.15)$$

Hence, in the case of the perpendicular propagation the refractive index is given by :

$$n_{\pm}^2 = \frac{CD + AB \pm |CD - AB|}{2A} \quad (2.16)$$

In the limit of low frequencies compared to the electron cyclotron one ( $\omega < \omega_c$ ), we obtain two possible waves : the ordinary one (O-mode with a polarisation parallel to the magnetic field) with a refractive index  $n_O^2 = 1 - \frac{\omega_{p,e}^2}{\omega_i^2}$  and the extraordinary one (X-mode with a polarisation perpendicular to the magnetic field) with a refractive index  $n_X^2 = 2 \frac{CD}{C+D}$ . The radial evolution of the corresponding

cutoff frequencies in a typical WEST discharge is given in figure 2.12.

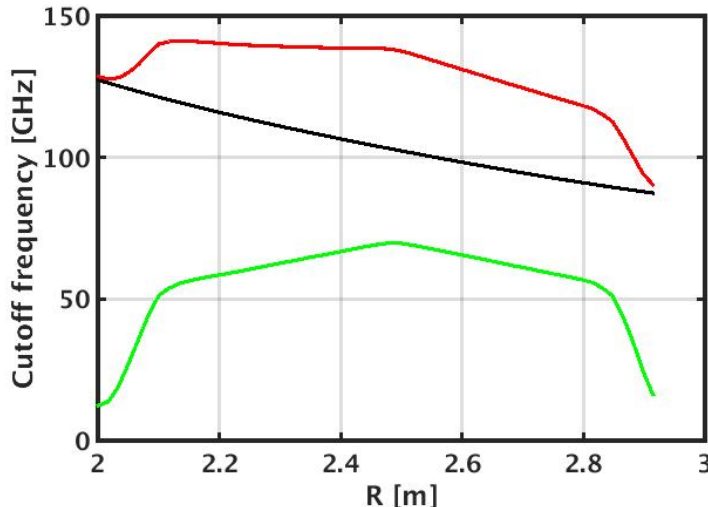


Figure 2.12: Radial profile of the cutoff frequencies in WEST (WEST #55732 @t=5.1s). The curves corresponds to the electron cyclotron frequency in black, the plasma frequency (O-mode cutoff) in green and the cutoff frequency of the X-mode in red.

Usually, frequencies used to probe tokamak edge plasmas are in the microwave range (30 – 150GHz). In order to measure edge profiles in WEST, we can see from figure 2.12 that we need to use the X-polarisation at high frequencies 75 – 110GHz to probe the very edge, SOL included, and the O-polarisation to probe further towards the plasma core in the range of 50 – 75GHz.

These cutoff calculations were made in the framework of a wave incoming perpendicularly to the plasma. In the case of DBS probing in tokamak discharges, this is not the case since the incidence angle is not perpendicular and more complex methods have to be considered [91, 93] to describe the cut-off layer position and the probed wavenumber. To model the path of the beam in a realistically described plasma, the resolution of the dispersion relation along the propagation has to be done numerically. The entries of the code are the magnetic equilibrium 2D map, the electron density profile, the antenna properties (position and inclination) and the wave features (frequency  $\omega$  and polarisation). Consequently, the DBS data processing necessitates other diagnostic measurements for the density profile and the magnetic equilibrium reconstruction. From these data and considering the simple cutoff model described above, we can reconstruct a 2D map of the cutoff frequencies indicating approximatively the probing positions in terms of the launched frequencies and polarisations (see figure 2.13).

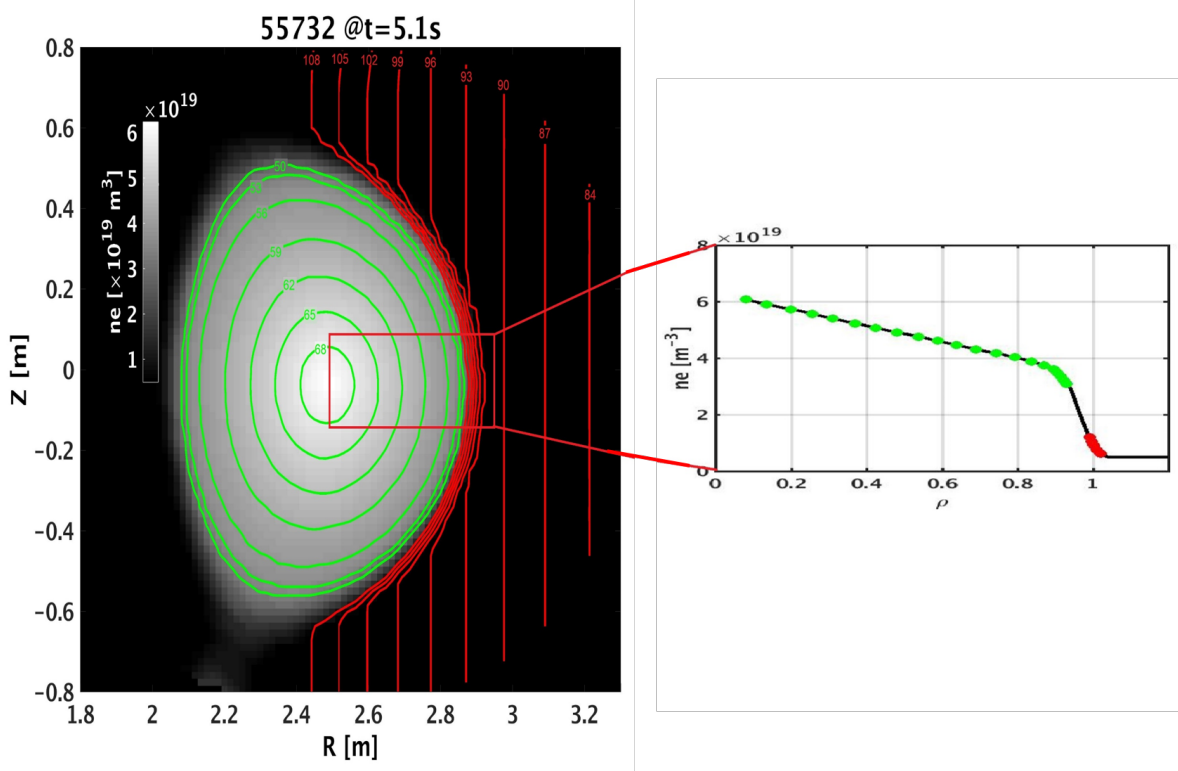


Figure 2.13: *Left* : 2D map of the plasma density in WEST (colormap, WEST #55732 @ $t=5.1\text{s}$ ). The cut off frequencies are over-plotted for the different polarisation of the wave : O-mode in green and X-mode in red. *Right* : radial profile of the density at the midplane. Dots corresponds to the cutoff position for the different wave propagation : O-mode in green and X-mode in red.

## 2.2.4 Doppler reflectometry in WEST : system and data treatment

### 2.2.4.1 The DBS system in WEST : DIFDOP

The Doppler reflectometry system in WEST is composed of a gaussian antenna positioned in the low field side of the device. The diagnostic was already present in Tore Supra and a more detailed description can be found in [94]. The inclination of the antenna can be changed remotely. This is useful to probe on different wavenumbers on the same magnetic flux surface. The system uses two independent systems to generate signals which can be used simultaneously to probe the plasma edge structures. The first system uses synthesizers to generate frequencies which are multiplied (four times) to shift in the V-band range ( $50 - 75\text{GHz}$ ). This wave is polarised in O-mode. The second one generates frequencies in the W-band range ( $75 - 110\text{GHz}$ ) through

a higher multiplication (6 times) and is polarised in X-mode probing the confined plasma boundary and the SOL. These ranges have been chosen considering the density and magnetic field profiles in magnetically confined plasmas in order to probe the plasma edge such as explained in the previous subsection (see figure 2.12).

In order to probe at different radial position, the frequencies of the beam is varied step by step with steps of around  $5 - 10ms$ . Usually to build a profile, the system describes 10 – 20 steps in frequency depending on the wanted radial precision. In the end, this sequence lasts almost  $100ms$  and is repeated at different time during the plasma discharge in order to study the time evolution of the perpendicular velocity profiles. The triggering of the probing sequences has to be careful because of the time acquisition of the system which is about  $300ms$ .

After the sent of the beam in the plasma, the back-scattered signal is then detected by the antenna and separated in a cosine and a sine components in order to reconstruct the complex signal. The acquisition system has a variable storing frequency but the one usually used is  $10MHz$ . During the PhD, this system has been upgraded in order to have a continuous acquisition during the discharge (between WEST C4 and C5 campaigns).

#### 2.2.4.2 Edge rotation profile reconstruction

We will now detail the data processing applied to the signals aiming at determining the edge perpendicular velocity radial profile. Two steps are necessary to reconstruct the profiles : estimate the Doppler shift and then simulate the path of the beam in the plasma edge to determine its probing position and wavenumber. We will discuss on the uncertainty sources appearing from the measurement to the end of the data processing.

- **Doppler shift measurement :** Once the complex signal reconstructed, it can be studied to determine the Doppler shift of the back-scattered wave. The signal is cut in time windows corresponding to each frequency step giving signals of around 50000 points. A temporal Fourier transform is then applied on samples of 1024 points. Finally, an average of this spectra gives access to a low-noised spectrum (see figure 2.14). Usually, this

spectrum is composed of a non shifted Gaussian contribution coming from reflections of the beam by the wall or the plasma itself and a shifted contribution containing the physical information on the Doppler shift induced by the drifting structures.

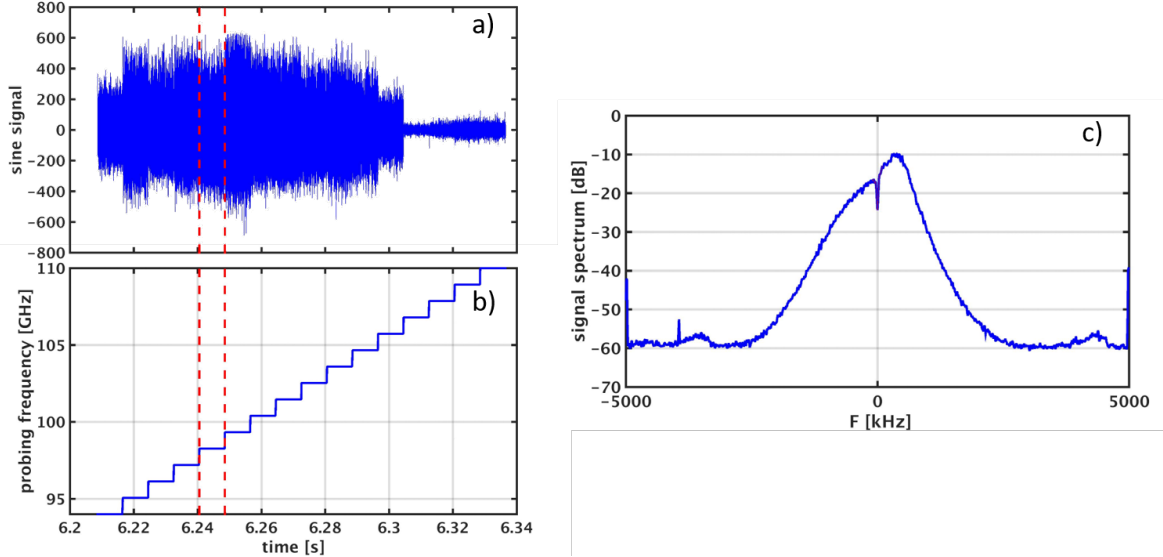


Figure 2.14: a) time trace of the sine part of the measured signal, b) time trace of the probing frequency and c) spectrum extracted for the fifth frequency ( $f = 98.3\text{GHz}$ ) in the time window delimited by the red dashed lines. (WEST #55732 trigger 4 @ $t = 6.2\text{s}$ )

Fitting this spectrum allows to estimate the Doppler shift frequency. Commonly, three mathematical functions are considered to fit these spectra : a Lorentzian function, a Gaussian function and a Voigt function which is the convolution product of a Gaussian and a Lorenzian function. The Lorentzian function shows a high accuracy to extract the position of the maximum of the spectrum whereas it is not able to fit the shape. On the other hand the Gaussian function allows to fit the shape of the spectrum with a slightly lower accuracy on the maximum position. Consequently, the use of the convolution of these function is a powerful tool to fit both maximum position and spectral shape. These three fitting functions lead to similar values with a deviation of the order of the percent (see figure 2.15).

This method is applicable in most of the edge plasma measurement. During this PhD, high power injection scenario were studied in order to access high confinement regimes. In such discharges a fluctuation

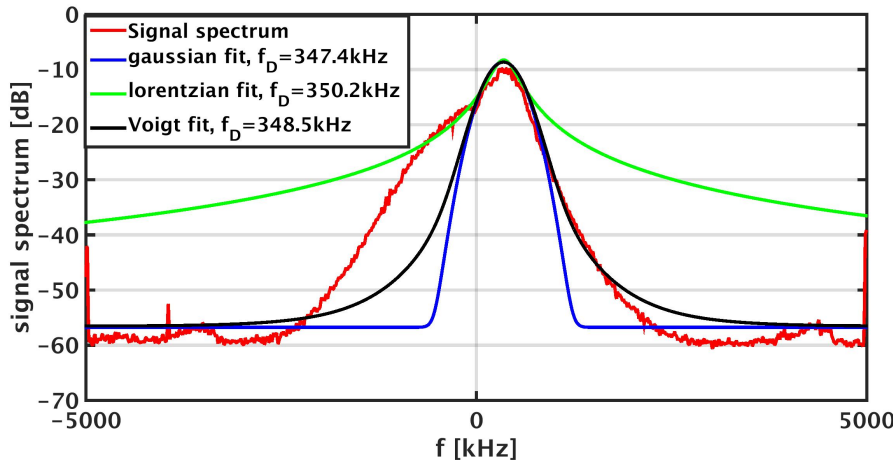


Figure 2.15: Fit of the signal spectrum to extract the Doppler shift frequency. (WEST #55732 trigger 4 @ $t = 6.2s$ )

of the signal amplitude has been encountered leading to time variation of the Doppler shift during a probing frequency step. These particular cases will be detailed later in this section. Another method has been developed in order to estimate the Doppler shift in these oscillatory phases allowing to describe the dynamics of the signal. It consists in determining the dominant frequency in time windows using the **pmusic** function in MATLAB based on the MUSIC algorithm [95]. This has already been used to study oscillatory phases in presence of Geodesic Acoustic Modes (GAM) in Tore Supra [96]. This algorithm extracts eigenvectors from the auto-correlation matrix of the signal. These eigenvectors are sorted in decreasing. The larger eigenvalues correspond to the signal components whereas the lower ones are equal and correspond to the noise contributions. This technique can be applied to time windows thin enough to study the Doppler shift dynamics. The resulting Doppler shift values are slightly lower than measured with the fit method (15% lower) but allows to have a look to the dominant frequency even in oscillatory phases of the signal amplitudes. Figure 2.16 shows the temporal dynamics of this dominant frequency for a standard mode discharge and for the oscillating regime. In this second regime the dominant frequency varies with a standard deviation of about 35%. This method allows to automate the Doppler shift measurement with a good enough accuracy. Both methods lead to shifts amplitude of the order of a few hundreds of kilohertz to a few megahertz.

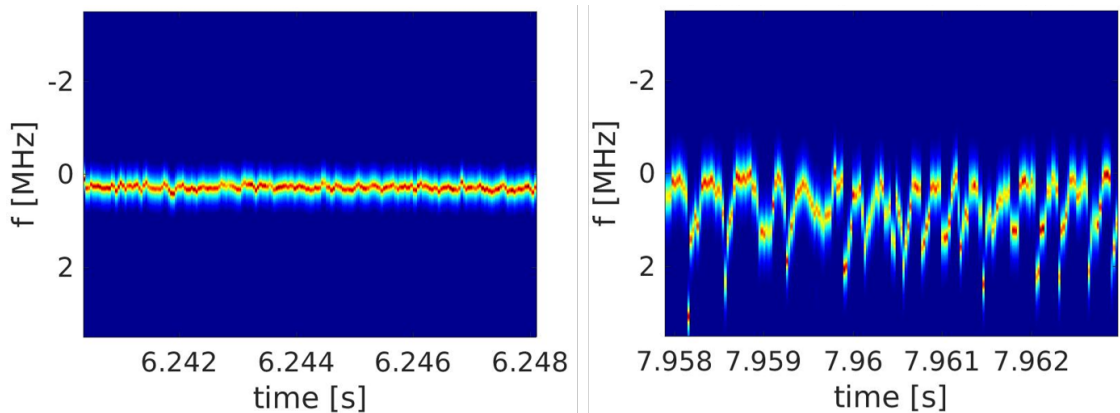


Figure 2.16: Colormap of the dominant frequency extracted from signal with **pmusic**. *Left* Usual signal in L-mode (WEST #55732 trigger 4 @ $t = 6.2s$ , probing frequency  $f = 98.3GHz$ ). *Right* Oscillatory regime (WEST #55562 trigger 8 @ $t = 7.9s$ , probing frequency  $f = 104.5GHz$ )

- **Probed position and wavenumber calculation with a beam tracing code** The probing position and wavenumber are determined using a beam tracing code following the principles detailed in sec.2.2.3. This code, fully described in [91], solves the propagation equations of the beam in the WKB approximation and in three dimensions taking into account the ripple of the magnetic field. To that end, the code needs to have access to the magnetic equilibrium and the electron density profile to represent the plasma medium, the antenna position and inclination and all the features of the probing wave (frequency, polarisation). This is summarised in table 2.3. In order to evaluate the beam propagation, 4 other beams corresponding to an intensity lowering of two times its Gaussian width are considered.

Inputs	Outputs
Electron density profile	Cutoff coordinates ( $r$ )
Magnetic equilibrium	Cutoff wavenumber
Antenna position ( $R, Z, \varphi$ )	
Antenna inclination (poloidal & toroidal)	
Probing wave features (frequency & polarisation)	

Table 2.3: Table compiling the inputs and outputs of the beam tracing code

The electron density profiles used by the code are measured either by the interferopolarimetry system or by the fast sweep reflectometer in WEST [84]. The first one is reconstructing profiles from tomography using line of

sight crossing the plasma. Unfortunately, only one (during C3 campaign) or two (during C4 and C5 campaigns) lines of sight are passing through the plasma edge and it leads to a bad constraint of the plasma edge density profile shape. Usually, the profiles from the reflectometry system are the ones input into the code.

The beam tracing code has been developed during Tore Supra operation and is using an analytical equilibrium consisting in an elongated circular geometry. The plasma equilibrium in WEST being in diverted geometry, the magnetic field profile and the elongation from the equilibrium reconstruction are input in the code(see figure 2.17). An effort is currently made in order to use real equilibria for the beam path reconstruction.

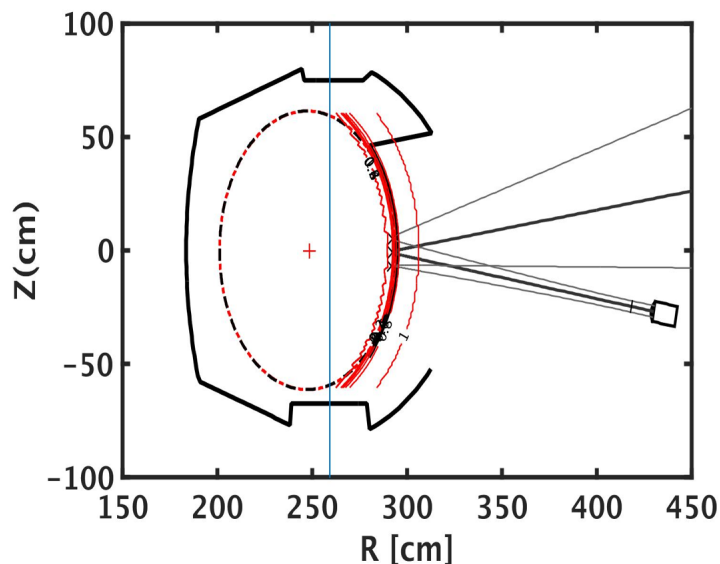


Figure 2.17: Beam tracing code results for the WEST discharge #55732 trigger 4 @ $t = 6.2s$  (probing frequency  $f = 98.3GHz$ )

The obtained probing wavenumbers are of the order of the inverse of a fraction of centimetre. and are increasing with the antenna inclination as it can be seen figure 2.18. It leads to perpendicular velocities of a few kilometers per second.

#### 2.2.4.3 Discussion on fundamental hypotheses and uncertainty sources

The estimate of the error bars on both radial position and amplitude of the velocity measures is not trivial since uncertainties comes from both Doppler

shift measurement and beam tracing reconstruction. Either the signal or the inputs of the beam tracing code as well as the data processing can induce errors. This section will present a discussion on the approximations used in the reconstruction and the corresponding error sources in order to give an ordering of the error bars.

First of all, as explained earlier, the measured velocity is the sum of the contribution of the background drift and the phase velocity of the probed turbulence. Neglecting this last one is a common point in DBS studies but it can be a mistake. A way to address this key point consists in varying the antenna poloidal inclination at a constant probing frequency during a steady-state phase. This method allows to vary the probing wavenumber without changing the measurement radial location. If the velocity varies with the wavenumber at a same radial position, it can indicate a domination of the phase velocity contribution. Indeed, only this contribution will depend on the wavenumber. A dedicated measurement has been managed in USN and LSN ohmic discharges in WEST in order to validate this assumption. Figure 2.18 summarises the results of this experiment showing a non dependency on the probing wavenumber. We can consider that the probed velocity corresponds to the local background  $E \times B$  drift. It is worth keeping in mind that it is not a proof of null phase velocity. It only shows a non dependency of the probed measurement on the phase velocity which can come either from a small value of the phase velocity compared to the background flow or from an inverse dependency of the phase velocity with the wavenumber.

The uncertainties on the measured data have also to be considered. These uncertainties can come from the Doppler shift estimate and the beam path reconstruction. The uncertainties from the first contribution is discussed in this paragraph. The reflections of the signal on the wall or on cut-off layers on the path of the beam can lead to a non shifted Gaussian contribution to the Doppler spectra of the signals. This contribution overlaps the Doppler contribution in the case of low rotation  $V_{\perp} \leq 1 km.s^{-1}$ . This induces an inability to extract the Doppler shift even applying the data processing using **pmusic**. When the velocity is marginally above these values, the fitting function allows to remove a part of the spectrum before applying the fit on the data. It increases the accuracy but the uncertainty can be of the order of a few percents.

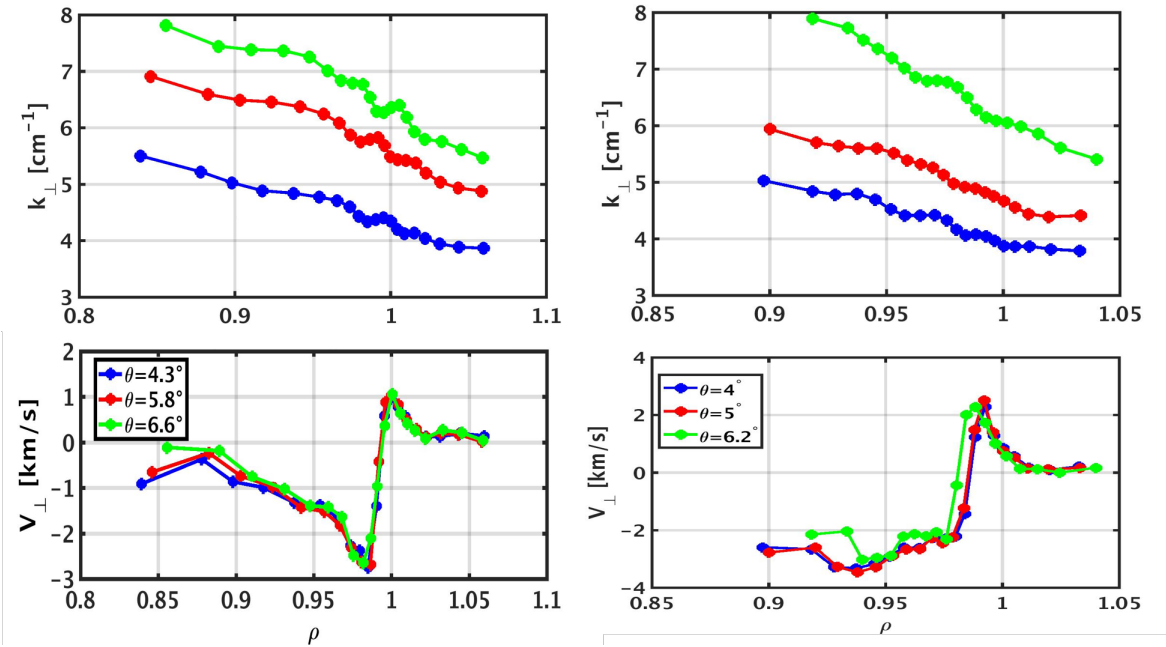


Figure 2.18: Radial profiles of probing wavenumber (top) and perpendicular velocity (bottom) in LSN configuration (left) and USN configuration (right) (respectively WEST#56710 & #56714)

The major contribution to the errors in the profile reconstruction comes from the determination of the probed position and wavenumber. For X-mode polarisation, the radial shape and position of probing will strongly depend on the density profile and the magnetic equilibrium reconstruction. The latter can lead to an uncertainty on the flux surface positions at the low field side mid-plane which will be of the order of a few millimetres. However, the density profiles from the reflectometry can encounter some difficulties to reconstruct the edge density profile. Reflections on the wall or light emission by suprathermal electrons can disturb the reflected signal and keep one from finding the initial point of the profile. This will lead to uncertainties on the profile position of the order of the centimetre. Moreover, during one probing frequency step, the density profiles may vary. Generally, the profile used by the beam tracing code is the time average of the profiles measured during the frequency step. Taking the standard deviation of the profile at each radial position gives an estimate of the shift of the profile. Inputting the mean profile and the ones at plus and minus the standard deviation gives an estimate of the radial position uncertainty of each measuring point of the order of a centimetre as shown figure 2.19. This is the major contribution and it will be the one retained in this work. This point illustrates the difficulty to interpret the radial shape of the profiles in order to

estimate the shear from the velocity profiles.

In the case of a probing which is non perfectly perpendicular to the magnetic field lines, a contribution to the measured velocity can come from the parallel velocity. Fortunately, the parallel wavenumbers are very low compared to the perpendicular ones leading to the assumption of neglecting the parallel contribution to the measured velocity.

Finally, the uncertainty on the poloidal angle of the antenna can lead to an uncertainty on the probing wavenumber and on the radial probing position. The second one is very low but the first one can be significant. The error on the antenna poloidal inclination should be of the order of  $0.1^\circ$ . In order to take into account all the effects of the inputs of the ray tracing simulations on the perpendicular wavenumber, we simulated the beam path in the edge plasma with angles varying from minus to plus  $0.5^\circ$  which is high compared to the measured one ( $5^\circ$ ). It results in an error of the order of  $5 - 10\%$  on the wavenumber and, consequently, on the perpendicular velocity. This is shown in figure 2.19 representing the radial profiles of perpendicular velocity. The  $\rho$  coordinate is the poloidal normalised coordinate  $\rho = \sqrt{\frac{\Psi(r) - \Psi(r=0)}{\Psi(r=a) - \Psi(r=0)}}$ .

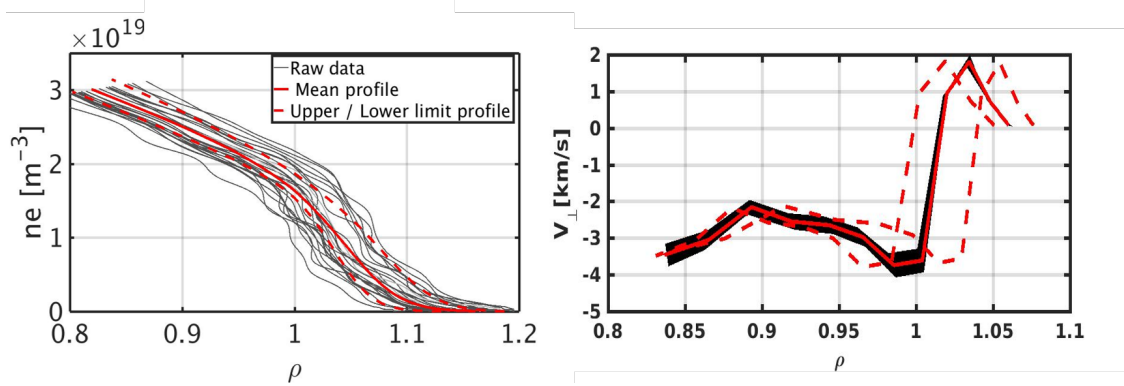


Figure 2.19: *Left* : Radial profiles of edge density measured by fast sweep reflectometry. *Right* : Radial profile of perpendicular rotation measured by DBS reflectometry. Full red line are the rotation profile reconstructed using the mean density profile. The red dashed lines corresponds to the profiles reconstructed from the uncertainties estimated on the density profiles (in red dashed lines also). The black area corresponds to the error bars from the uncertainty on the antenna angle as mentioned in this section.

Even if the interpretation of the radial shape of the rotation profiles is ques-

tionable, the depth of the rotation profile well can be considered as a robust measure. This depth and the width of the well are the contributors to the edge rotation shear which is assumed to be responsible of the turbulence mitigation. Indeed, it is not known if it is whether the shape or the depth of the rotation well which is responsible of the shear amplitude and, in consequence, of the turbulence mitigation. It is worth noting that a combination of both amplitude and shape can lead to the establishment of a strong turbulence shearing. In order to investigate this point, a database of profile depth has been built in this work and will be the point of the next section.

### **2.2.5 Understanding the correlation between edge rotation and plasma parameters**

In most of the experimental observations, the establishment of transport barriers is the key point of assessing increased confinement regimes in tokamak operation. These barriers being due to the establishment of a strong shear layer in the plasma edge, one has to understand how the edge rotation is impacted by the different plasma parameters to determine the parameter space of the increased confinement regime. The number of operational parameters as well as the high wideness of the range of their values prevent from fully scanning the parameter space. Nevertheless, two complementary approaches can help to fill our lacks of knowledge. The first one consists in building wide databases aiming at establishing global trends or building scaling laws. This way has been followed in order to characterise global features such as energy confinement time. The development of Artificial Intelligence (A.I.) and neural networks offers a promising point of view in this sense. The second approach is based on dedicated experiment in which a minimum of parameters is varied. Thus, one can point out the specific effect of the varied quantities. Nevertheless, this approach can only give information in precise regimes or domain of parameters. Moreover, in experiment, it is often difficult to vary only one parameter due to cross correlations and then, it can be difficult to separate their impacts. In this work, both approaches have been considered and will be detailed in this section. First, we will describe the parameters of interest used in this work as well as the method used to extract the minimum value of edge rotation from the profiles built with the DBS system. Then, we will discuss the global trends appearing from the database built during the C3b and C4 campaigns. Finally, specific studies of impact of plasma param-

eters, injected heating power and magnetic geometry will be detailed showing some clear dependencies of the edge velocity well depth.

### 2.2.5.1 Build-up of a wide database of edge rotation profile to study global trends

During the C3b and C4 campaigns of operation in the WEST tokamak, a wide range of the operational parameter space has been investigated. It offered an opportunity to make correlation between the edge rotation and control parameters such as the plasma density, the injected power or the magnetic geometry. In this framework, we managed a data processing of the Doppler reflectometer system leading to the build up of almost 400 perpendicular velocity radial profiles. From these profiles, we extracted the position and the depth of the velocity well fitting the well with polynomials. The fifth degree polynomials appeared to be the more precise one to recover shapes and depth of the wells. As it can be seen on figure 2.18, the Upper Single Null configuration doesn't show a well in the edge rotation profile. Hence, the database of velocity wells is finally reduced to the profiles in Lower Single Null configuration which are well fitted by the polynomials (see figure 2.20). The points retained for this study will also be filtered in terms of MHD activity. Only the measurement at low MHD activity are used. In the end, this database contains 263 profiles in various conditions regarding the plasma parameters values : integrated density  $n_l$  averaged on an interferometry line of sight crossing the plasma core, plasma current  $I_p$ , injected heating with both LH and ICRH ( $P_{LH}$  and  $P_{ICRH}$ ), Greenwald fraction  $f_G = \frac{n_l[10^{20}m^{-3}\pi a^2]}{I_p[MA]}$ , X-point height  $h_X$  and radiated power fraction  $f_{rad} = \frac{P_{rad}^{bulk}}{P_{TOT}}$ . The table 2.4 summarises the range of values of the database.

number of points	$R$ [m]	$a$ [m]	$B$ [T]	$I_p$ [MA]	$n_l$ $[10^{20}m^{-3}]$	$f_G$	$P_{inj}$ [MW]	$f_{rad}$ [%]
263	2.5	0.45	3.7	0.43 - 1	0.2 - 0.63	0.3 - 0.7	0 - 6.2	20 - 80

Table 2.4: Table of the plasma parameter ranges of the rotation profile depth database

First we tried to correlate the perpendicular velocity well depth with global confinement features. For that we included two quantities in the database : the stored energy  $W_{MHD}$  and the neutron rate produced by the fusion reaction, sign

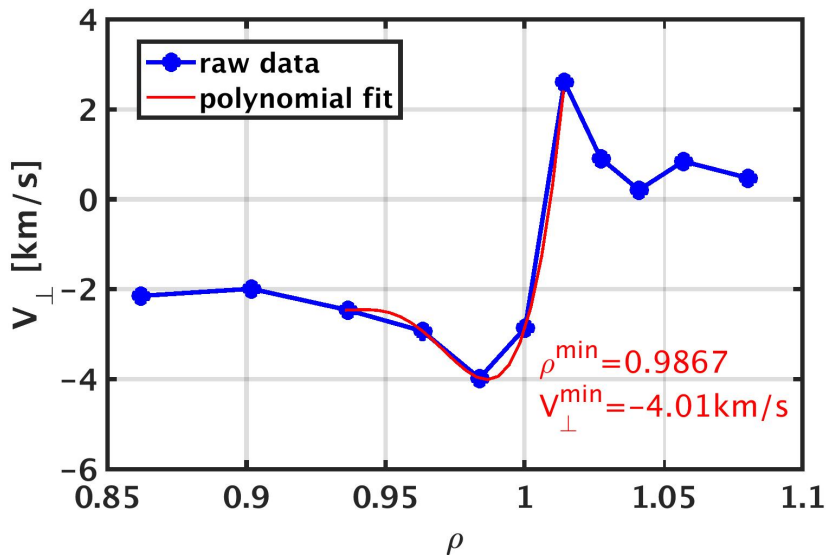


Figure 2.20: Edge perpendicular rotation profile measured by Doppler reflectometry (in blue) fitted by a polynomial of degree 5 in order to determine the well position and depth (WEST #54810 @ $t = 6.7s$ )

of a good core confinement. Looking at the evolution of these quantities with the profile depth in the overall database doesn't show a clear trend (see figure 2.21 a)). A more precise way to try to point out trends is considering reduced databases such as filtering density ranges in the overall database. Figure 2.21 b) & c) represents the same comparison as in a) but with a low and high density range respectively. It underlines that at low densities confinement and edge rotation seems to be correlated whereas in the high density range it does not seem to. At this point, the interpretation of this result is impossible. At low density, the transport looks correlated with the edge rotation but we can't know if the transport is lowered by the turbulence mitigation or if the rotation is enhanced by stronger gradients across the separatrix.

Unfortunately, this trend is the only one appearing clearly in the database. As it can be observed in figure 2.22, the profiles depth is clamped between 3 and 4 kilometres per second in almost every conditions. We can conclude that the approach is not adapted to isolate effects of plasma parameters on the profiles. More precise studies have to be done on the variation of unique parameters to point out trends. We then focused of the comparison of similar discharges to understand the effects of control parameters on edge rotation. This will be the point of the next section.

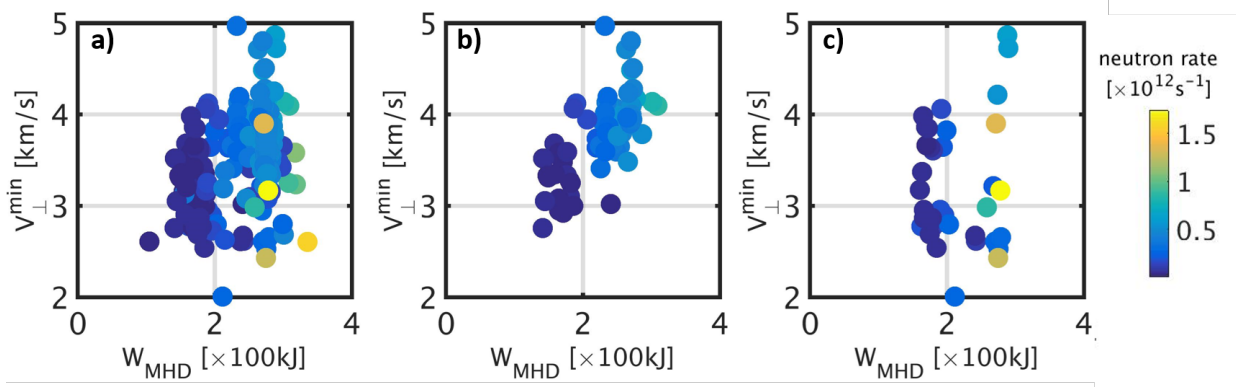


Figure 2.21: Evolution of the edge rotation well depth with neutron production and stored energy in a) the whole database, b) the low density cases ( $n_l < 3.5 \times 10^{19} m^{-2}$ ) and c) the high density cases ( $n_l > 4 \times 10^{19} m^{-2}$ )

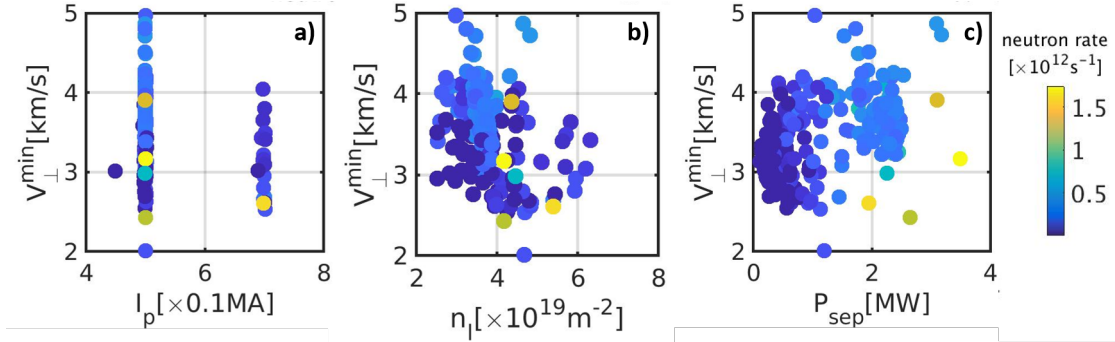


Figure 2.22: Evolution of the edge rotation well depth with neutron production and a) plasma current, b) line averaged density and c) power crossing the separatrix.

### 2.2.5.2 Impacts of heating power, density and magnetic geometry on edge rotation in WEST

In order to understand how the edge rotation profiles behaves with relevant control parameters evolution, we selected measured times in comparable conditions with only one parameter varying. It pointed 3 main parameters impacting the perpendicular velocity profiles : the heating power injection, the density and the magnetic configuration (X-point height and position). These three parameters are known to be actuators of L-H transition. Consequently, the study of their impact on edge rotation is of utmost importance in the quest of the understanding of high confinement assessment. Moreover, the heating channel showed strong impacts on rotation (toroidal rotation) in Tore Supra [97, 98]. We tried to dissociate Lower Hybrid power  $P_{LH}$  and ICRH power  $P_{ICRH}$  to investigate if the way to heat had an impact on the deepening of the profiles.

- **Lower Hybrid power injection :** The question of the origin of the power threshold to access increased confinement regime is usually addressed making a step by step increase of injected power. In this work, we interested in such discharge to better understand the impact of power increase on the edge rotation. The evolution of the edge rotation with the injected power in a typical discharge in WEST at a plasma current of  $500kA$  is represented on figure 2.23. The profile measured during the early phase is obtained in a low density regime and appears different from the others. Nevertheless, we clearly observe a deepening of the profile when we start the injection and, then, a clamping of the profile with the increase of injected power, even doubling the power. This clamping is not attributed to an increase of radiated power equivalent to the one of the injected power. An explanation to this phenomenon could be the impact of the magnetic field ripple on the fast particles. The ripple can be responsible of losses of fast particles leading to a polarisation and so to a radial electric field. In the case of LH heated discharges, we expect the loss of fast electrons leading to a positive contribution to the rotation. This will opposite to the deepening of the profiles which could be consistent with the observations. Ripple regimes are characterised by a proportionality between the rotation and the pressure gradient profiles. The electron density profiles are similar during the injected power increase phase which could be consistent with this hypothesis, at least for the density gradient contribution to the pressure gradient. Experiments dedicated to this key point have been managed and have to be further studied. In parallel, huge theoretical effort is carried to understand the impact of ripple on magnetically confined plasma rotation [99] especially in Tore Supra and WEST presenting large values of ripple amplitude.
- **Ion Cyclotron Resonant Heating power injection :** We investigated also the impact of ICRH heating injection on edge rotation applying the same methods than for the LH heating impact study at the same plasma current  $500kA$ . We observed a non deepening of the rotation profile with the increase of injected power but the internal branch (profile part at lower radii than the well) deepens when the ICRH power increases (see figure 2.24). This could be attributed to two effects : a steepening of the ion

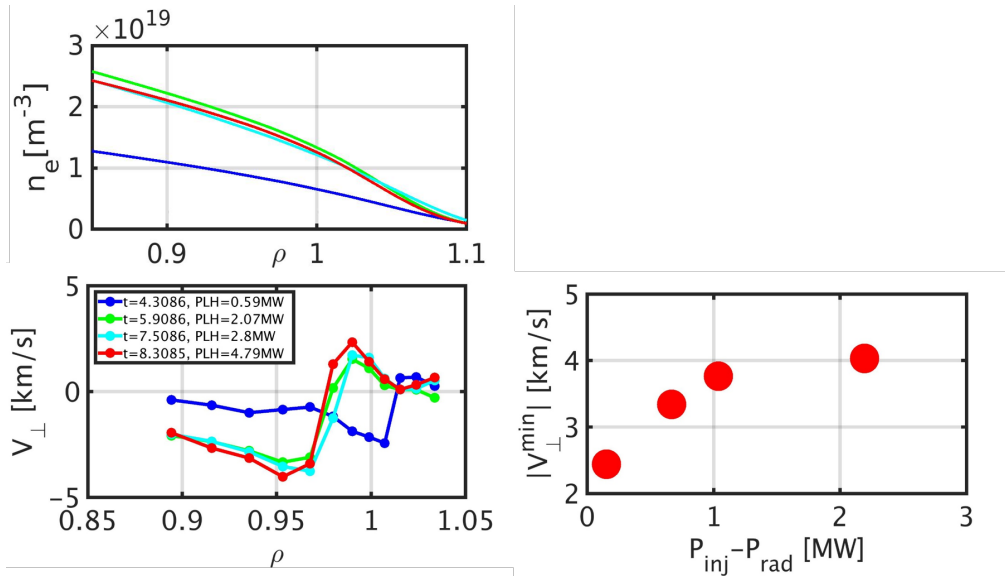


Figure 2.23: *Left* : Evolution of the edge electron density (top) and rotation (bottom) radial profile with the increase of Lower Hybrid heating power injection (WEST #53905). *Right* : Saturation of well depth with the increase of LH injected power.

pressure profile leading to an increase of the neoclassical rotation or a fast ion loss in the core leading to a polarisation and a deepening of the radial electric field profile. Without measurement of ion temperature radial profiles, we could not conclude on which was the explanation but looking at the electron density profiles, we clearly see a steepening of the gradient in the inner branch region in agreement with the local deepening of the rotation. Specific effects of LH and ICRH heating have been studied here for moderate heating power amplitudes. These observations should be deeper investigated through more dedicated experiment. A dedicated study to high injected power discharges aiming at assessing increased confinement regimes will be presented in the next section.

- **Magnetic geometry :** Finally, the most striking result of our observations during the C3b campaign in WEST is the impact of the position of the X-point on the edge rotation at  $I_P = 500kA$ . Indeed, as we can see on figure 2.25, both the amplitude and the shape of the profiles are different between the two symmetric LSN and USN geometries while the electron density profiles are similar. This observation indicates that the neoclassical predictions are not sufficient to explain the edge rotation at the confined plasma boundary.

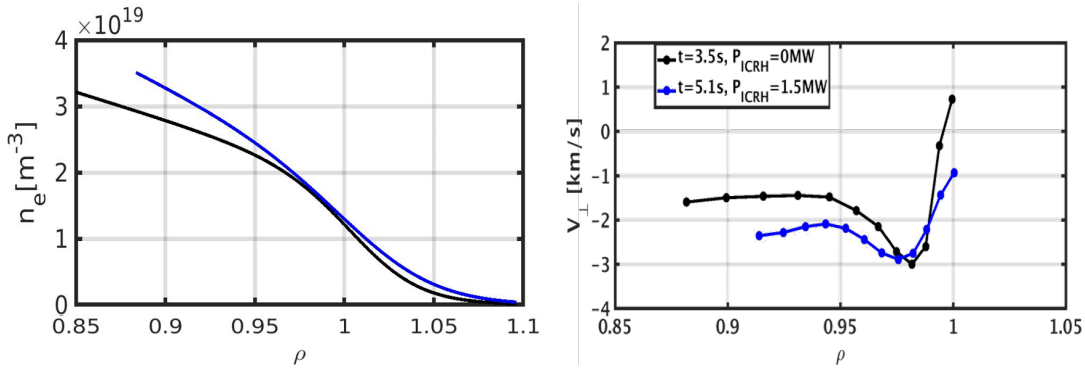


Figure 2.24: Evolution of the edge rotation radial profile with the increase of ICRH power injection (WEST #54449).

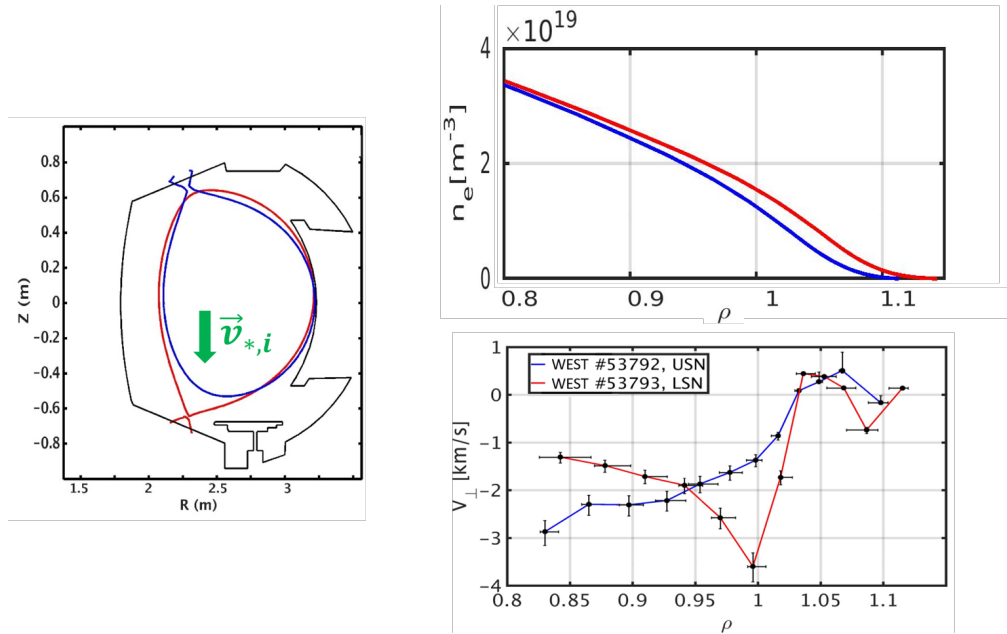


Figure 2.25: Comparison of edge electron density (top) and rotation (bottom) radial profiles at a plasma current of 500kA in LSN (red line, WEST #53793) and USN (blue line, WEST #53792). Left panel represents the magnetic geometries of the discharges illustrating the favourable and favourable configurations.

Increasing the plasma current leads to a vanishing of this difference. At currents above 700kA, both profiles exhibits a flattening of the internal branch at the same well depth (see figure 2.26). The electron density profiles are also similar in both configurations indicating that the phenomenon responsible of the profile discrepancy at 500kA seems to be mitigated at higher plasma current. Interestingly this flattening trend is comparable to

the observations in Tore Supra. Moreover, dedicated experiment changing the position of contact point of the plasma with the antenna protection limiter of Tore Supra as well as changing the plasma current value led to comparable trends in the edge rotation profile shape variation [100].

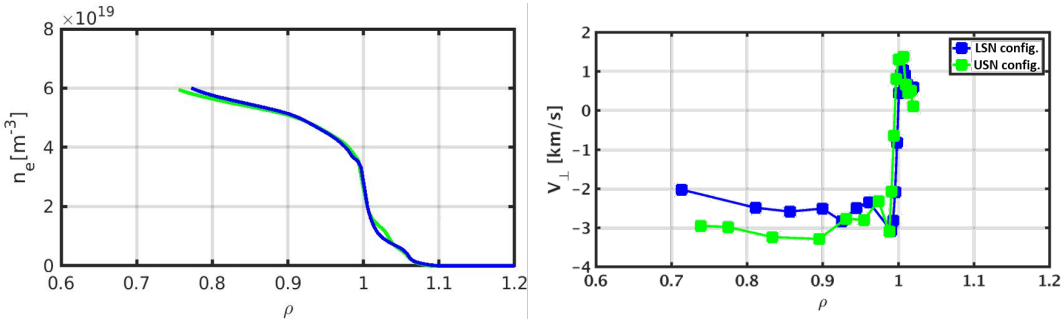


Figure 2.26: Comparison of edge electron density (left) and rotation (right) radial profiles at a plasma current of 700kA in LSN (blue line, WEST #55169) and USN (green line, WEST #55170)

All of these observations motivated a dedicated experiment to deeper study the impact of geometry and plasma current on edge rotation during the WEST C4 campaign. To that end, we realised discharges in symmetric configurations with a plasma current variation aiming at determining the impact of the reconnection length, the edge safety factor and the geometry on the perpendicular velocity profiles. The magnetic field is maintained at  $3.7T$  and the line averaged density at  $3.9 \times 10^{19} \text{ m}^{-2}$ . The edge safety factor varied in the range of  $[3.3 - 5.8]$  in LSN and  $[2.85 - 4.7]$  in USN with comparable radial profiles. We recovered the same trend both with geometry and plasma current as previously observed (see figure 2.27). More importantly, at high plasma currents, the USN configuration exhibits deeper profiles with a 'well-like' shape while the density profiles remains similar between both configurations. This feature is not a common observation in tokamak plasma edges and is counter-intuitive in the framework of the favourable and unfavourable configurations. A theoretical investigation based on magnetic shear induction of turbulent Reynolds stress has been managed during this work to understand this phenomenon aiming at emphasising the importance of the flow generation by the turbulence. This will be presented in the next chapter (see section 3.4.4).

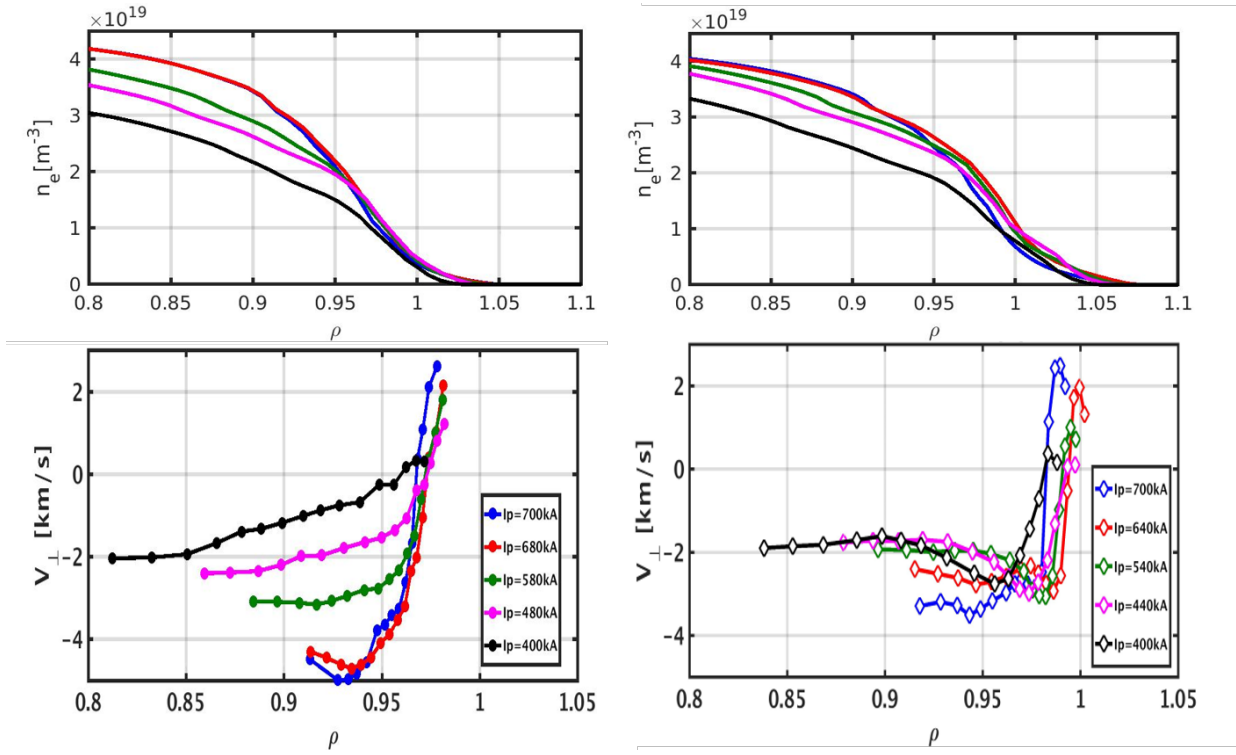


Figure 2.27: Comparison of edge electron density (top) and rotation (bottom) radial profiles at different plasma current in USN configuration (left, WEST #55622) and LSN configuration (right, WEST #55732)

- **X-point height :** As mentioned in the introduction of this manuscript, the X-point height impacts the L-H transition power threshold. It has been observed that a low X-point height is favourable to access H-mode in DIII-D and JET tokamaks [38, 39]. In order to understand its impact on edge rotation, we studied perpendicular velocity profiles evolution during X-point height sweep experiment in both ohmic and ICRH heated discharges at plasma currents of 500 kA. The profiles remain identical for all the X-point heights and are only affected by the injected power (see figure 2.28). This impact of the ICRH heating is the same as the one detailed in the paragraph on the impact of this heating on the inner branch. The density profiles are slightly steepening in the inner branch according to the same discussion. However, the well of the rotation profiles and the density profiles are not impacted by the X-point height as well as in the SOL. The fact that we do not observe changes in the rotation profile is not necessarily in contradiction with the L-H transition observations. The impact of the X-point height can occur when the injected power is high enough to approach the transition. The scan in height realised in the

study presented here may be not enough to highlight an effect. Further experiment is needed to fill this lack of knowledge.

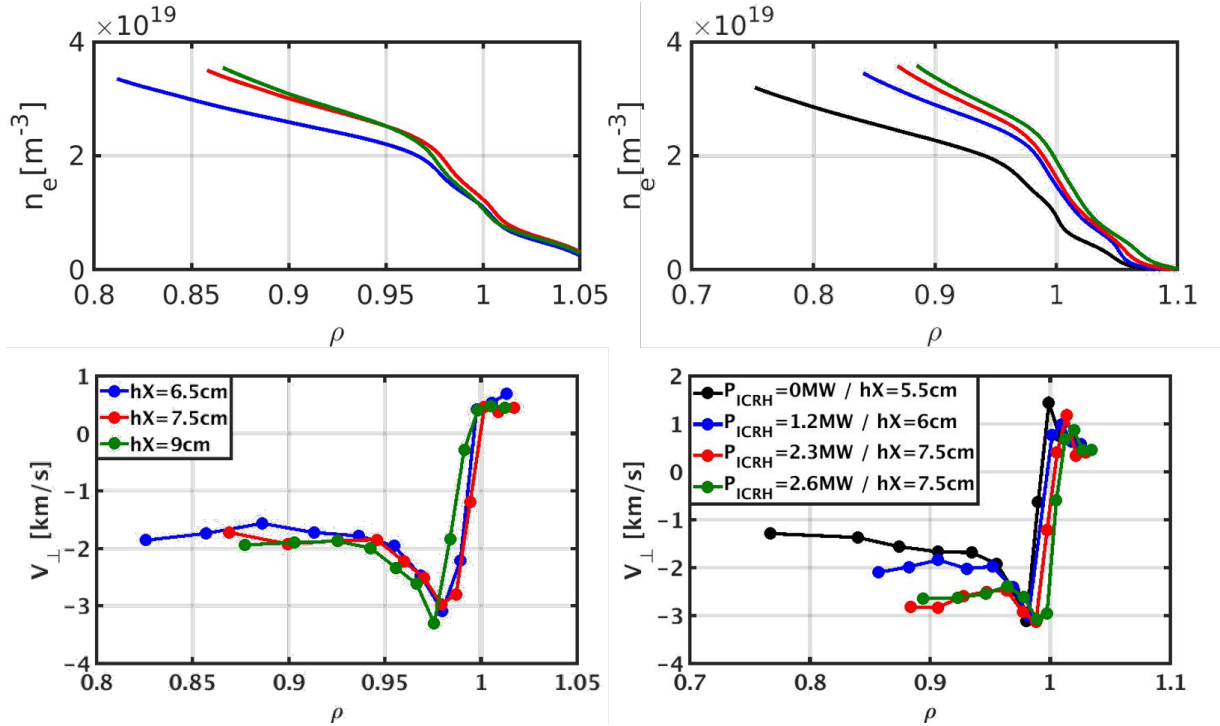


Figure 2.28: Evolution of the edge electron density (top) and rotation (bottom) during a X-point height sweep in an ohmic case (left, WEST #55013) and an ICRH heated case (right, WEST #55015).

- **Impact of density control in LSN configuration :** It has been observed experimentally and extracted from the scaling laws that the density is a key player in the quest of L-H transition [34, 35]. In WEST, plasma fuelling can be controlled by two systems, the gas puffing system fuelling gas in the chamber and the pellet injection. Impact of both fuelling methods have been studied in this work at plasma currents of 500 kA. Two main results have been obtained. First of all, the diverted configuration offers the ability to pump the gas close to the targets. Injecting gas in this region could help to increase the local pressure and modify the target conditions maybe assessing partial or full detachment. The study of the impact of the location of the gas puffing in the machine showed the invariance of the edge rotation profile with this location (see figure 2.29). Interestingly, above a threshold in density close to  $n_l = 5.5 \times 10^{19} m^{-3}$ , the perpendicular velocity profile changes with both fuelling valve positions.

The exponential shape of the profile in the SOL vanishes. The high spatial resolution of the DBS system used in these experiments allows to highlight clearly this effect. This variation in radial trend corresponds to the predictions of Chankin *et al.* basing the model on the neutral pressure dynamics at the targets [101]. Moreover, the profiles measured when the plasma is fuelled by the divertor valve presents a slightly deeper well when the SOL behaviour changes. This effect is not visible when the fuelling was made in the main chamber due to the lack of points to resolve the well shape. Other experiments and investigations based on numerical fluid simulations with the SOLEDGE code coupled with a neutral dynamics solver EIRENE would be the next step to understand this feature [76, 102].

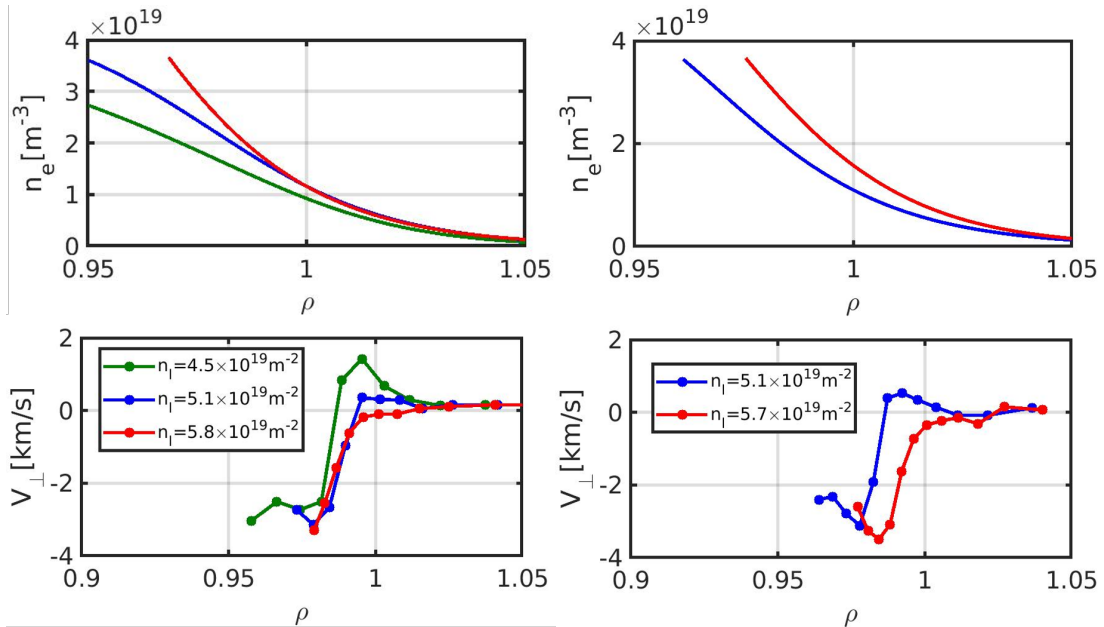


Figure 2.29: Evolution of the edge electron density (top) and rotation (bottom) profiles with the fuelling intensity (density of the plasma). *Left* : Plasma fuelled by the main chamber valve (WEST #54481). *Right* : Plasma fuelled by the divertor valve (WEST #54496).

- **Density control with pellet injection :** We also observed this change of trend during pellet injection experiment at the plasma current. On figure 2.30, we see this change when the pellet deposits the matter in the plasma before recovering the initial state when the density recovers its previous amplitude. The density profile measured right after the pellet injection appears slightly shifted inwards probably due to plasma perturbation and difficulties to reconstruct the equilibrium in this case. Nevertheless, the

edge density profile keeps its amplitude and shape while the rotation is changing. This would indicate again a contribution of thin effects not taken into account in the neoclassical prediction of the edge velocity such as particle sources from ionisation or turbulent momentum transport.

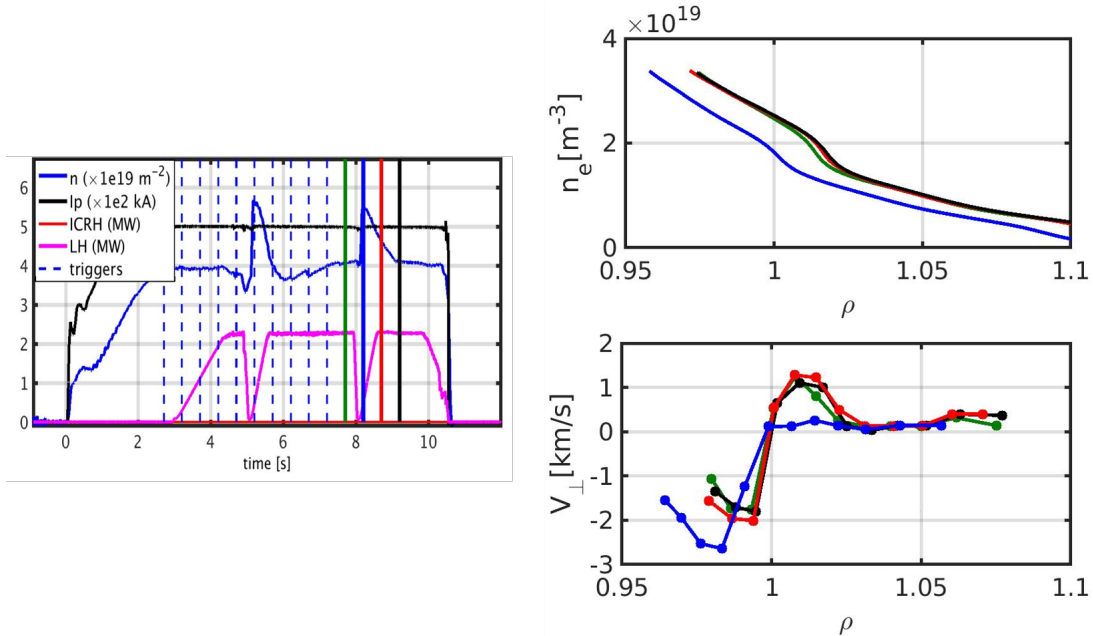


Figure 2.30: Evolution of the edge rotation during a pellet injection. *Left* : Time traces of the principal signals of the plasma discharge WEST #54680. *Right* : Electron density (top) and perpendicular velocity (bottom) profiles before (green), at (blue), right after (red) and well after (black) the pellet injection.

- **Impact of density in USN configuration :** Another interesting observation is the appearance of a well in USN configuration when the density is increased above  $n_l = 4 \times 10^{19} \text{ m}^{-3}$  at a plasma current of  $500 \text{ kA}$  (see figure 2.31). This observation is different from the one in LSN because of 1) the lower threshold in density, 2) the non vanishing of the exponential feature of the rotation profile in the SOL and 3) the formation of the well is associated to a local steepening of the density profiles. A way to explain this later point is considering that the density profile steepens increasing the pressure gradient and consequently the edge rotation. This explanation leads to another question which is why the density gradient locally steepens. Another way to explain it is the mitigation of the turbulent transport by the local increase of the shearing rate leading to a steepening of the density profile. This second point calls another question : why does the rotation

profile deepen ? The model developed in this work proposes an explanation based on the competition between the neoclassical recall force of the rotation towards the diamagnetic one and the Reynolds stress contribution to the rotation tending to smooth the profile. Increasing the density leads to an increase of the edge collisionality leading to an increase of the recalling force contribution which pushes the edge profile to recover the pressure gradient trend exhibiting a well at the confined plasma boundary. This will be discussed in the next chapter. Another striking point on this figure is the fact that the internal branch tends to the same asymptote even if the density gradient is varying. Plotting the radial evolution of the normalised density gradient  $\frac{\partial \rho n_e}{n_e}$  shows that the contribution of the density gradient to the neoclassical rotation prediction is in agreement with the global shape of the profiles leading to the same inner branch asymptote. This indicates that even if the overall radial profile shape is in agreement with neoclassical predictions, thin effects induced by local density changing can be non negligible.

## 2.2.6 Assessment of increased confinement discharges in WEST : high injected power experiments

This section treats the H-mode assessment experimental observation in WEST. Dedicated experiments have been performed in order to study the increase of confinement in a large aspect ratio device. A development of scenarios of high injection of power have been managed reaching 8MW of total input power in discharge #55799. An increase of confinement has been observed in both Lower Single Null and Upper Single Null configurations. A comparison of the results in these symmetric geometries is detailed presenting the rotation and density profiles. It is worth recalling that the two divertor configurations are not exactly the same since a pumping system and a baffle are present at the bottom of the vessel. Nevertheless, the baffle and the pumping system having opposite impacts on the neutral pressure in the divertor volume, one could expect comparable conditions at the upper and lower targets. Then, observations of discharges which do not transit to H-mode with higher injected power is discussed in terms of impurity contamination.

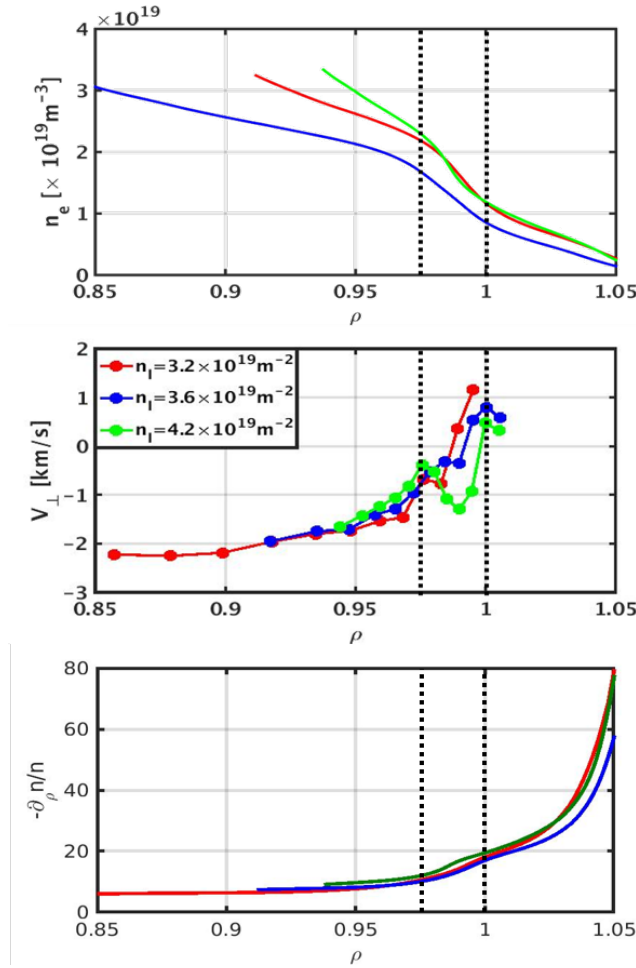


Figure 2.31: *Top* : Evolution of the edge electron density profile with the increase of the density in USN configuration. *Middle* : Evolution of edge rotation radial profiles at different densities in USN configuration). *Bottom* : Radial profiles of the normalised radial gradient of the edge electron density at different densities in USN configuration (WEST #54896). Dashed lines delimits the rotation well and the associated steeper density gradient.

### 2.2.6.1 H-mode assessment in WEST

H-mode assessment has been observed in WEST during discharges after fresh boronization. This latter condition allows to operate with low radiated power fraction (almost 40%) and consequently high power crossing the separatrix reaching values above multi-machine scaling laws of H-mode power threshold [34]. Figure 2.32 shows the parameter space in power crossing the separatrix and line average density of the C4 campaign emphasising the high confinement discharges. The evolution of the power threshold scaling law is over-plotted showing that the transiting discharges are slightly under or above the scaling.

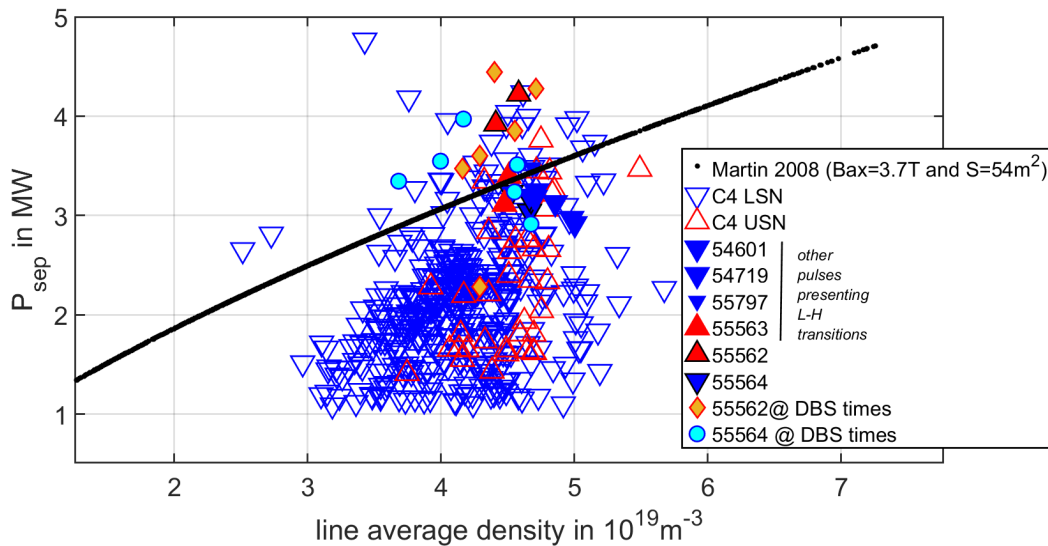


Figure 2.32: Space parameter of WEST C4 campaign in terms of power crossing the separatrix and line average density. H-mode discharges are highlighted and the Martin scaling law for H-mode power threshold is over-plotted in black.

### 2.2.6.2 Observations of L-H transition in LSN

Strikingly, these high confinement plasmas do not exhibit usual markers such as ELMs [103]. This leads to difficulties to identify the transitions [104]. Nevertheless, the time traces of both SOL and core allowed to clearly point out L-H transitions. An example of these time traces measured in favourable configuration (Lower Single Null) is given in figure 2.33 (WEST #55564). This discharge was operated in typical plasma parameters :  $B = 3.7T$ ,  $I_P = 500kA$ ,  $q_{95} = 4.5$  with both *LH* and *ICRH* power injection reaching power crossing the separatrix values of  $3.8MW$ .

A transition is observed at  $t=6.45s$ . This is deduced from a decrease of the plasma inductance (sign of an increase of edge bootstrap current) and the increase of stored energy and neutron rate even if we do not observe a lowering of the heat flux and the  $D - \alpha$  emission on the divertor. It is worth noticing that the increase of stored energy is low (20%) compared to usual transitions. In the same time, the core density increases while the edge one decreases indicating a pedestal formation or, at least, a steepening of the edge density gradient. Unfortunately, the observation of an equivalent edge temperature pedestal formation, typical of H-mode assessment, is impossible due to suprathermal electron generation by LH heating leading to perturbation of edge ECE electron

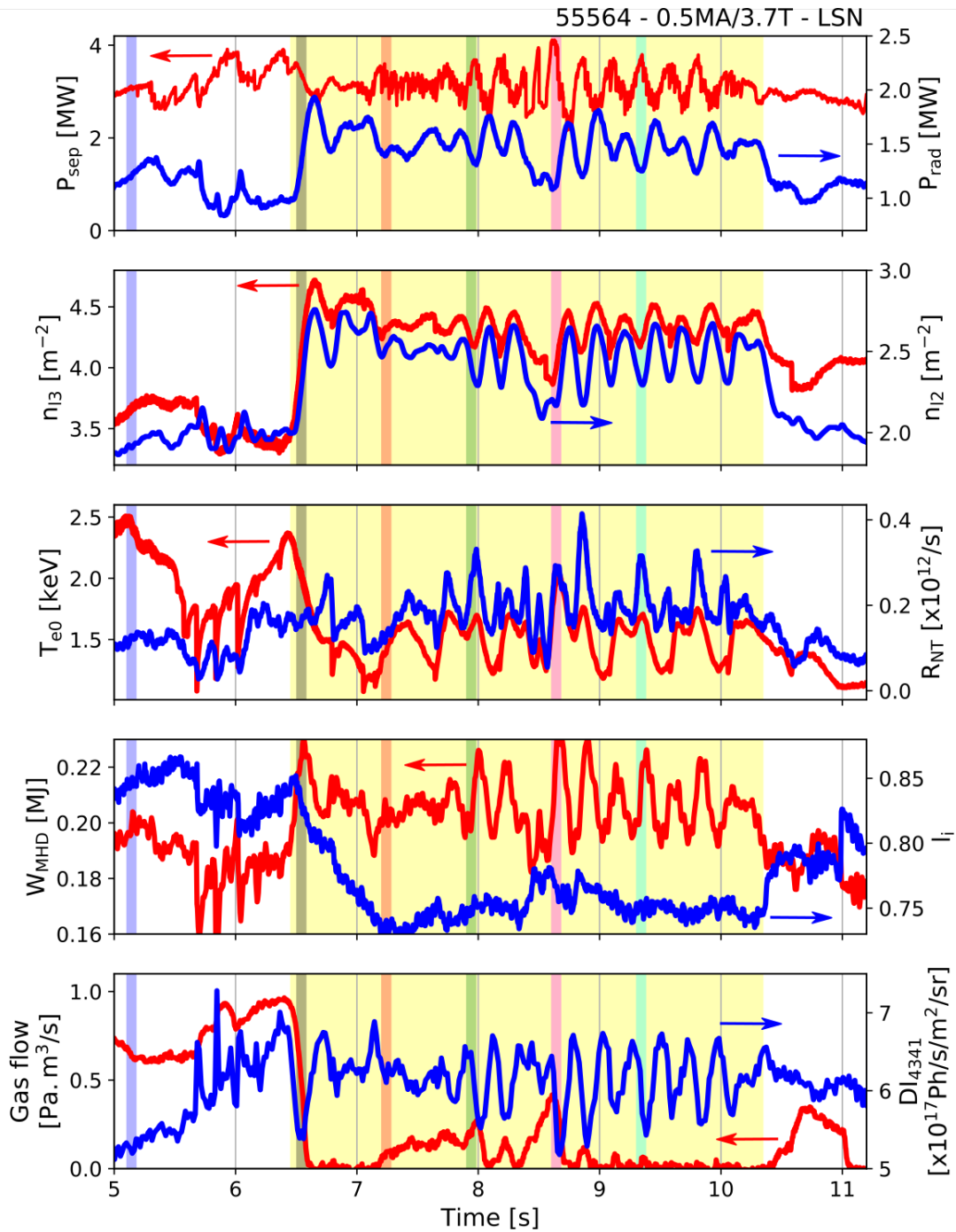


Figure 2.33: Time traces of from the top to the bottom : power crossing the separatrix  $P_{sep}$  and radiated power  $P_{rad}$ , core  $n_{l3}$  and edge  $n_{l2}$  line average densities, core temperature  $T_{e0}$  and neutron rate  $R_{NT}$ , stored energy  $W_{MHD}$  and plasma inductance  $l_i$ , gas puff rate and  $D-\alpha$  emission. Vertical colour lines corresponds to the DBS probing times. (WEST #55564)

temperature measurement. Another indicator of changing in behaviour of the plasma during the discharge is a strong deepening of the edge rotation profiles as it will be discussed further. Then, an oscillatory phase builds-up.

This is due to the increase of density and radiated power which is lowering the power crossing the separatrix leading to a back transition and consequently a lowering of the density and the radiated power. This lowering leads to a rise of the power crossing the separatrix reaching the H-mode again. This oscillatory phase of L-H transitions and H-L back-transitions has been observed in ASDEX-Upgrade in the case of discharges well after wall conditioning by boronization [105]. Interestingly, the four LSN discharges in WEST reaching the H-mode are occurring at power crossing the separatrix close to the Martin scaling giving a first step towards the validation of this scaling in the case of a large aspect ratio device. In these specific cases of high hybrid power injection, the suprathermal electron creation leads to emissions in the frequency range of the fast sweep reflectometer. This point makes difficult the initialisation of the first profile point and consequently induces shifts in the reconstructed profiles [106]. In order to make readable the comparison between LSN and USN profiles, a choice was made in the position of the principal inflection point of the time averaged electron density profile placed at the separatrix one. We recall that this shift in density profile impacts also the rotation profile reconstruction by impacting the probing position estimated by the ray tracing code.

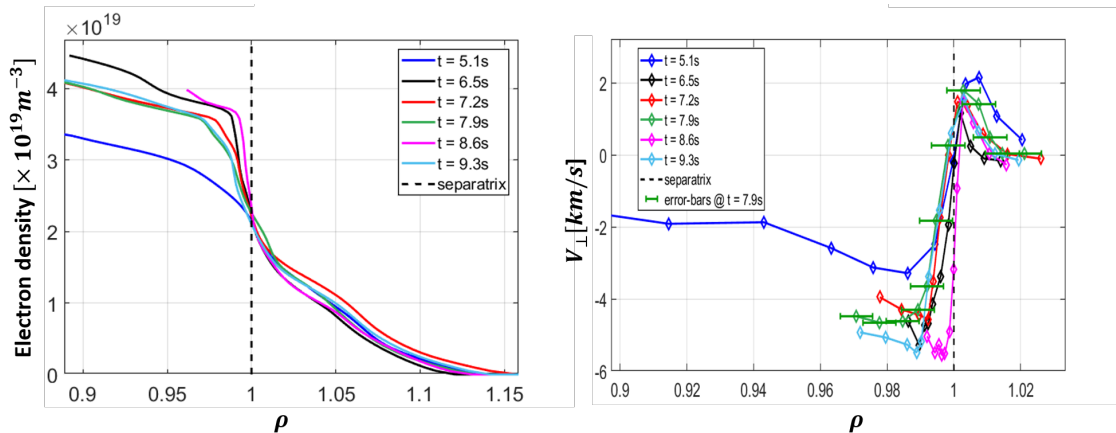


Figure 2.34: *Left* : Electron density profiles at different DBS measuring time. *Right* : Perpendicular velocity profiles at different DBS measuring time. Colours correspond to the probing times of figure 2.33.(WEST #55564)

The pedestal formation expected from the time traces of the interferometry chords measurements is recovered by the profiles measured by the fast sweep reflectometry system as show figure 2.34. This steepening of the edge electron density happens simultaneously with a deepening of the local rotation. This

steepening remains all along the oscillatory phase, at least at the Doppler Back Scattering system probing times. These probing times correspond to the phase prior the transition, right after and during the oscillatory phase at different trends of the oscillations. The pedestal top density increases and decreases slightly with the increments of power. Unfortunately, full variations of density and rotation profiles during the oscillatory phase is blurred since times measured by the DBS system do not cover a full cycle of oscillations. As mentioned earlier in this manuscript the error bars on the profiles are obtained using the shift of the electron density profiles. In this case during a DBS profile measurement, almost  $80\text{ms}$ , the profile radial positions oscillate much and lead to the error bars of figure 2.34. On the other hand, edge rotation profile depth also slightly varies during the oscillatory phase. These deepenings are consistent with the increases of the edge density radial gradient as expected from neoclassical considerations.

Aiming at characterising the pedestal properties, a modified hyperbolic tangent fit is applied to the profiles, as it is usually done in such studies [107]. From the fit, we can mainly measure the top pedestal density  $N_{e,ped}$ , the pedestal width  $\Delta\rho_{ped}$  and the local density gradient at the middle of the pedestal. Furthermore, commonly, the confinement quality is quantified by the enhancement factor  $H_{98y}$ . It is worth noticing that the application of the scaling law of the energy confinement time to the WEST case is questionable even if it has been showed that the L-mode ohmic scalings are respected by WEST discharge confinement features [108]. The time evolution of all these features are reported by figure 2.35. This figure illustrates the previous visual observations from the density profiles and stored energy time variations. Nevertheless, the values of enhancement factors in the discharge is of the order of 60% which is well below the values expected for an H-mode (almost 1). This has already been observed in strongly radiating discharges in Alcator C-mod [109]. An attempt to decorrelate the impact of the radiated power is to subtract it to the input power. This consideration taken into account, we estimated enhancement factors closer to usually observed ones in other devices.

After, these marginal transitions, scenarios with even higher injected power were developed reaching the WEST record value of  $8\text{MW}$  during the #55799 discharge. This discharge presented a high radiated fraction around 50% leading to power crossing the separatrix of about  $3.9\text{MW}$ . This value is 25% higher than

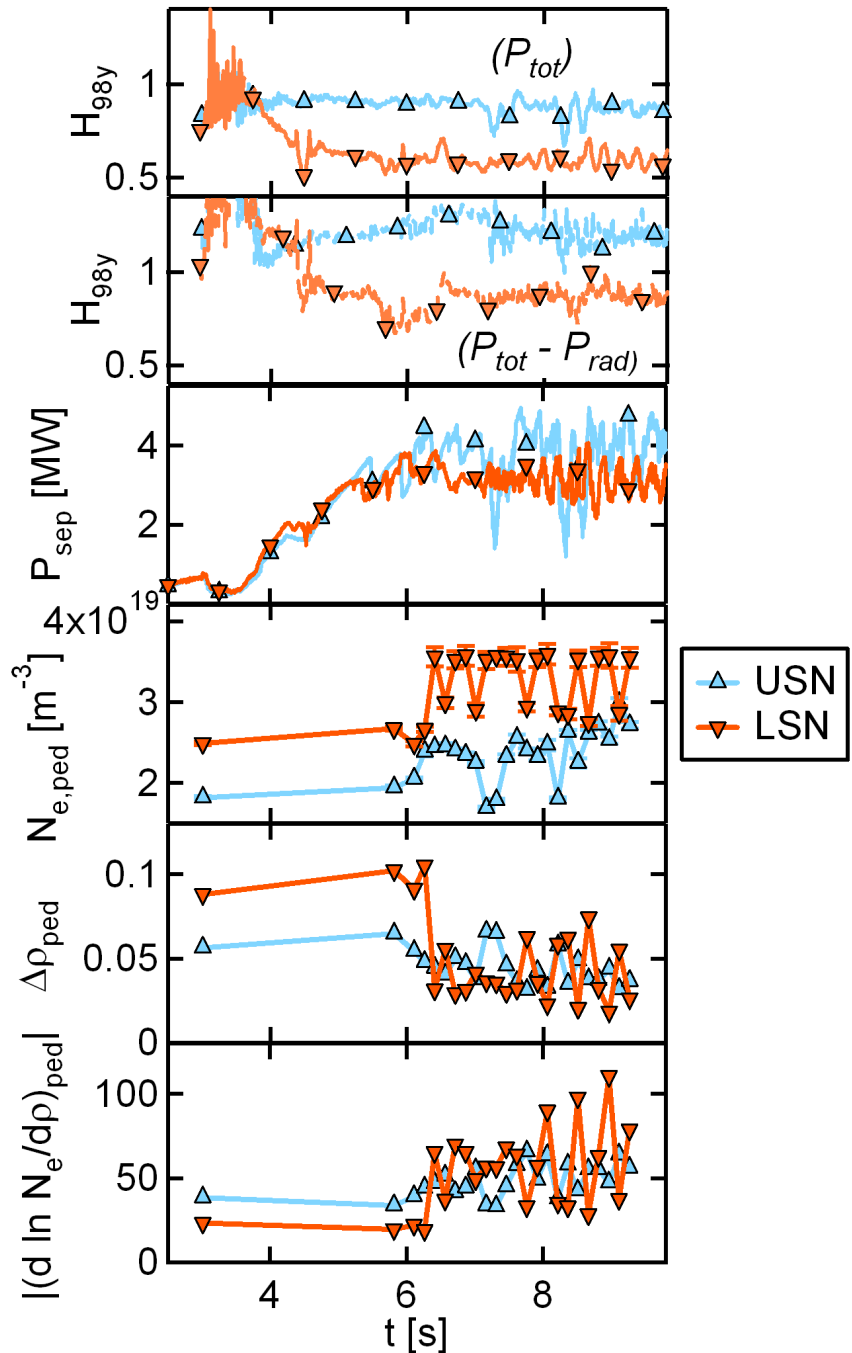


Figure 2.35: From the top to the bottom : Time evolutions of enhancement factors  $H_{98y}$  considering total injected power and power crossing the separatrix, power crossing the separatrix  $P_{sep}$ , top pedestal density  $N_{e,ped}$ , pedestal width  $\Delta\rho_{ped}$  and maximum pedestal density gradient. Blue colour dots stand for USN (WEST #55562) measurement whereas red ones stand for LSN measurements (#55564).

the threshold prediction scaling but, unfortunately, the discharge did not transit towards an increased confinement regime (see figure 2.37).

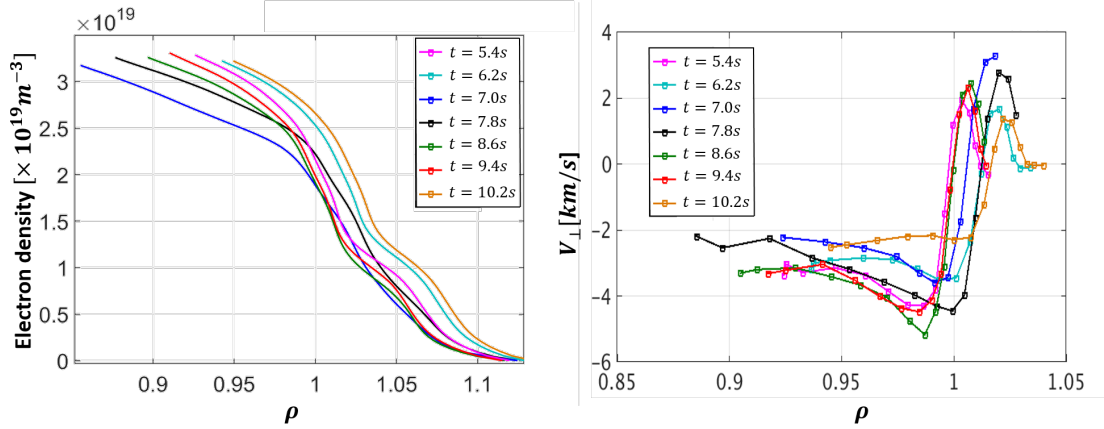


Figure 2.36: *Left* : Electron density profiles at different DBS measuring time. *Right* : Perpendicular velocity profiles at different DBS measuring time. (WEST #55799)

Interestingly, the deep wells observed in the edge rotation profile reaches  $5 \text{ km/s}$  comparable to the one observed in #55564 during which a transition occurred. Moreover, no pedestal formation is observed on the electron density profiles (see figure 2.36). At this point, the impact of the effective ionisation degree is proposed as the origin of this non-transition. Indeed, this discharge was realised well after a boronisation and we expect enough impurity content to increase the  $Z_{eff}$ . This latter exhibited strong impact on H-mode access in previous experiment [110]. Even if the discharge did not transit, the achievement of  $8 \text{ MW}$  of injected power is a key milestone towards stationary H-mode assessment in WEST.

### 2.2.6.3 Observations of L-H transition in USN

The assessment of an increased confinement regime has also been achieved in WEST in USN (WEST #55562). Interestingly, this transition happening in the unfavourable configuration exhibits similar behaviours in terms of absence of ELMs and in time evolution of the hints of L-H transition (see figure 2.38). The stored energy increment in this configuration remains lower than in the favourable one. Strikingly, the time traces do not present the oscillatory phases. This point can be explained by another difference with the transition in LSN : the electron density pedestal is less pronounced (see figure 2.35). Indeed, the density less increases in this discharge leading to a non high enough increase

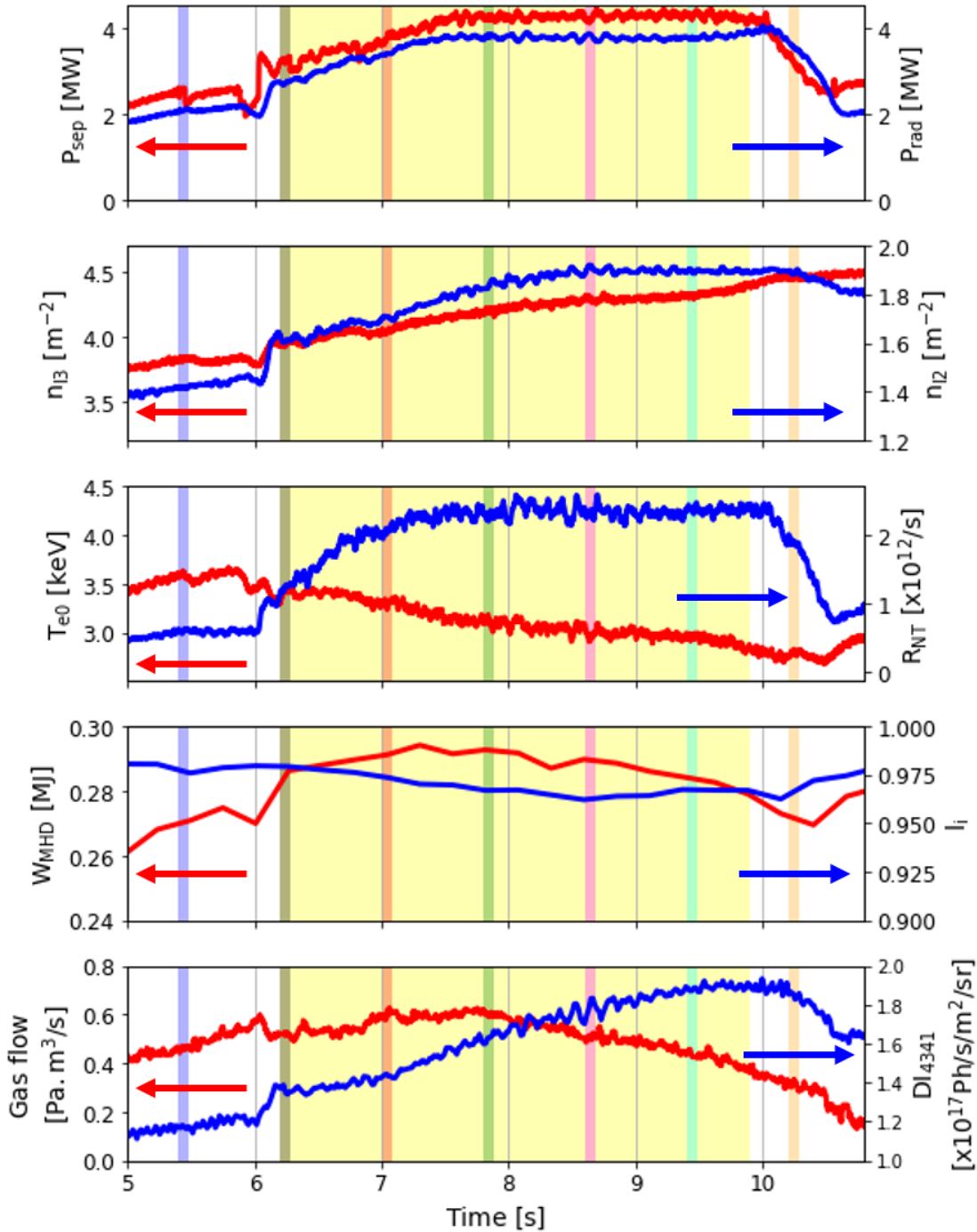


Figure 2.37: Time traces of from the top to the bottom : power crossing the separatrix  $P_{sep}$  and radiated power  $P_{rad}$ , core  $n_{l3}$  and edge  $n_{l2}$  line average densities, core temperature  $T_{e0}$  and neutron rate  $R_{NT}$ , stored energy  $W_{MHD}$  and plasma inductance  $l_i$ , gas puff rate and  $D-\alpha$  emission. Vertical colour lines corresponds to the DBS probing times. (WEST #55799)

of the radiated power to enter the oscillatory phase. On the other hand, the power crossing the separatrix and the enhancement factor are higher in this

configuration.

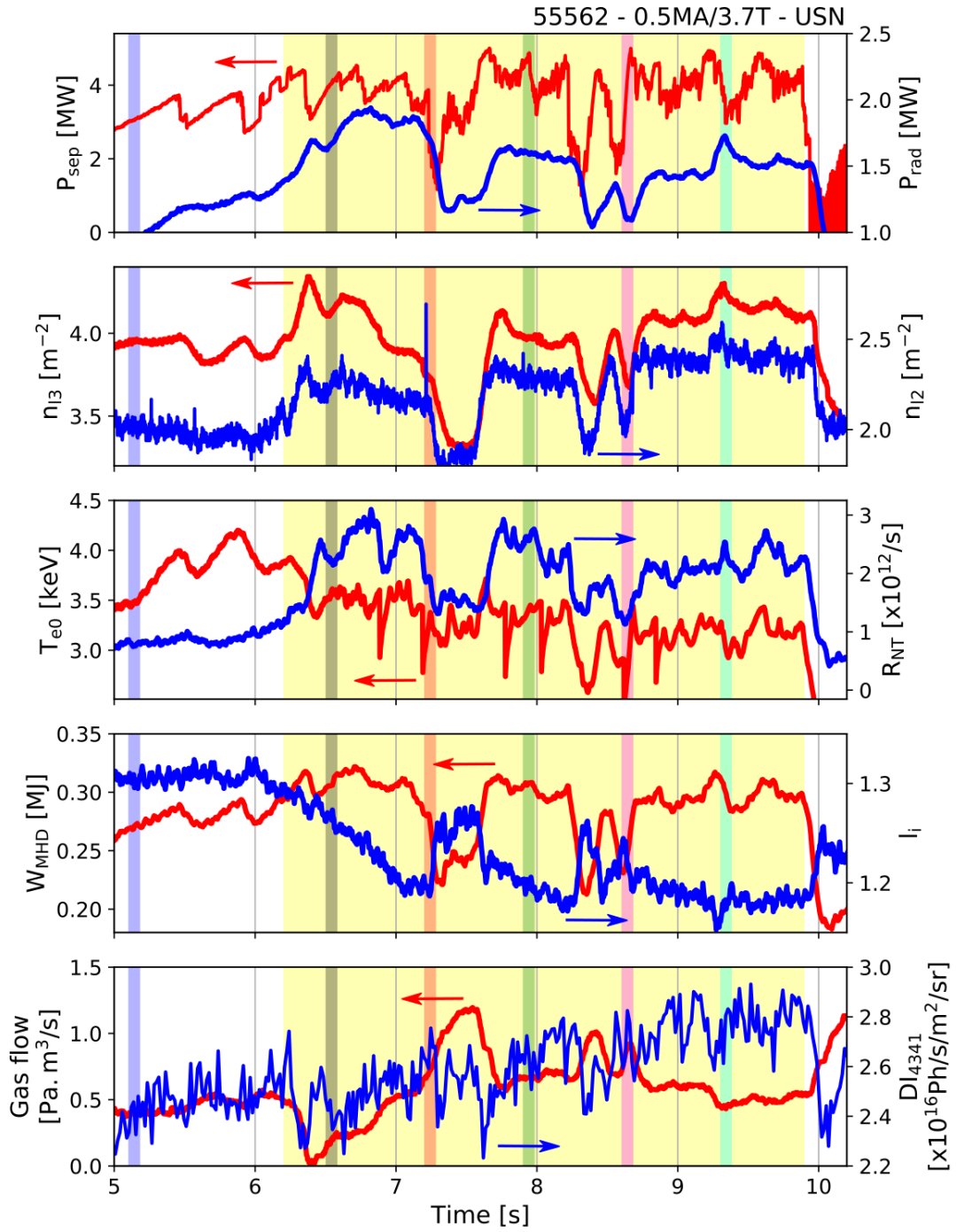


Figure 2.38: Time traces of from the top to the bottom : power crossing the separatrix  $P_{sep}$  and radiated power  $P_{rad}$ , core  $n_{l1}$  and edge  $n_{l2}$  line average densities, core temperature  $T_{e0}$  and neutron rate  $R_{NT}$ , stored energy  $W_{MHD}$  and plasma inductance  $l_i$ , gas puff rate and  $D-\alpha$  emission. Vertical colour lines corresponds to the DBS probing times. (WEST #55562)

The rotation profiles in this configuration present also an interesting behaviour.

First, after the transition the profile exhibits a well similarly to the LSN configuration whereas it does not in L-mode. Second, due to lowering of the injected power, the H-mode is lost at  $t=7.3\text{s}$  and then recovered at  $t=7.55\text{s}$ . It happens a second time at  $t=8.6\text{s}$  and finally after a quieter phase in terms of injected heating power the density increases again. Just before the first loss of high confinement, the perpendicular velocity well depth reaches the record value in WEST, namely  $-11\text{km/s}$ , which is almost twice the one obtained in LSN. This observation becomes even more puzzling looking at the edge density gradient behaviour. This latter is less pronounced than in the symmetric configuration for a deeper rotation well. This emphasises the unknown on the impact of the edge density gradient contribution to the velocity. This would suggest the formation of pedestal formation in temperature such as in I-mode. Moreover, the high magnetic field operation of WEST ( $B = 3.7T$ ) offers a wide operation parameter space to enter this confinement regime [111]. Unfortunately, no measurements of the temperature at the edge are available to verify it. However no clear signs of a Weakly Coherent Mode, considered as the signature of I-mode, is reported on fast sweeping reflectometry.

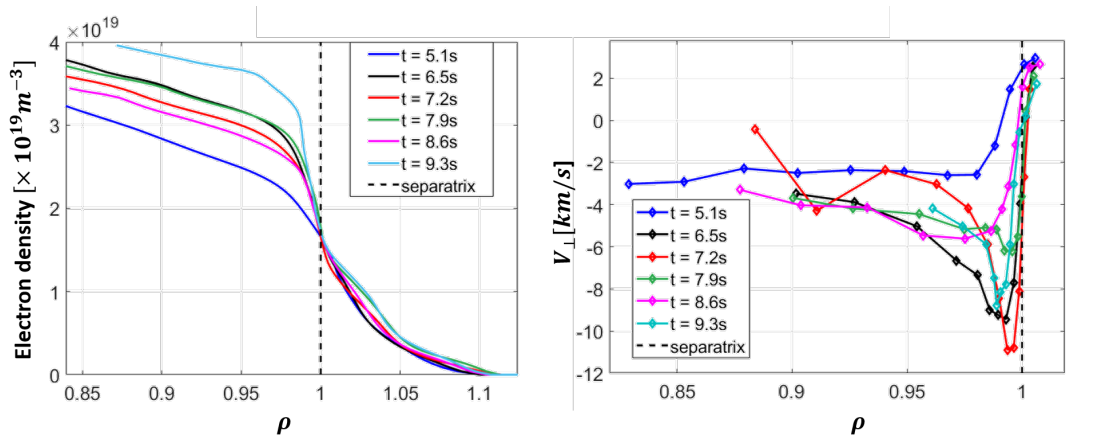


Figure 2.39: *Left* : Electron density profiles at different DBS measuring time.  
*Right* : Perpendicular velocity profiles at different DBS measuring time. Colours correspond to the probing times of figure 2.33.(WEST #55562)

Looking at the profile at  $t=8.6\text{s}$ , after the back transition, the profile recovers usual L-mode features with an absence of well. Finally, the profile at  $t=7.9\text{s}$  exhibits a strange behaviour with a low depth well while the power crossing the separatrix is higher than the Martin scaling. Having a look to the measured raw signals helps to find the origin of the phenomenon. The Doppler shift temporal

dynamics exhibits bursts with an occurring frequency of  $f = 3.8\text{kHz}$  associated to amplitude intermittency of the raw signals in the well and further in (see figure 2.41). These oscillations could be interpreted as a Limit Cycle Oscillations (LCO) marker, corresponding to an oscillation between low and high confinement regimes. In fact, the oscillation frequency does not correspond to the usual observations in such phases [112, 113, 114]. The oscillatory feature of the signal is observed at different probing positions. This could indicate MHD mode activity. The spectrogram of the discharge does not exhibit an edge localised mode in the probed region (see figure 2.40). Another explanation to the observations could be the presence of an electromagnetic mode perturbing locally the magnetic equilibrium leading to perturbations of the beam path. It is to be noted that this behaviour has also been observed in another discharge in LSN : #54601.

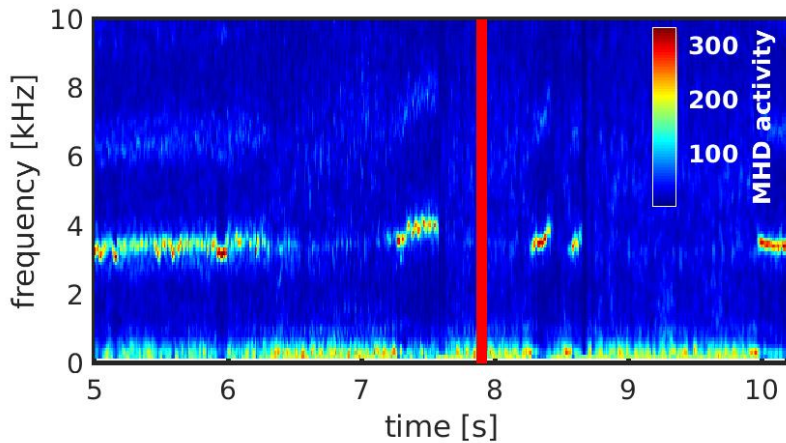


Figure 2.40: Time evolution of the MHD activity in the discharge #55562 in WEST. Red vertical line corresponds to the DBS probing time exhibiting oscillatory phases.

The dynamics of the Doppler shift being well described by the pmusic technique, a method based on conditional averaging could be developed to reconstruct a profile. Indeed, the conditional averaging approach seems legitimate since we consider that we can only measure the local drift velocity when we probe on structures. In the case of the figure 2.41, the time average of the Doppler shift during these intermittent phases is almost twice lower than the average of the values at the bursts only. The resulting value of shift in the well multiplied by the perpendicular wavenumber gives a perpendicular velocity higher than the values measured at the other triggers during the H-mode phase of this discharge as it can be observed figure 2.42.

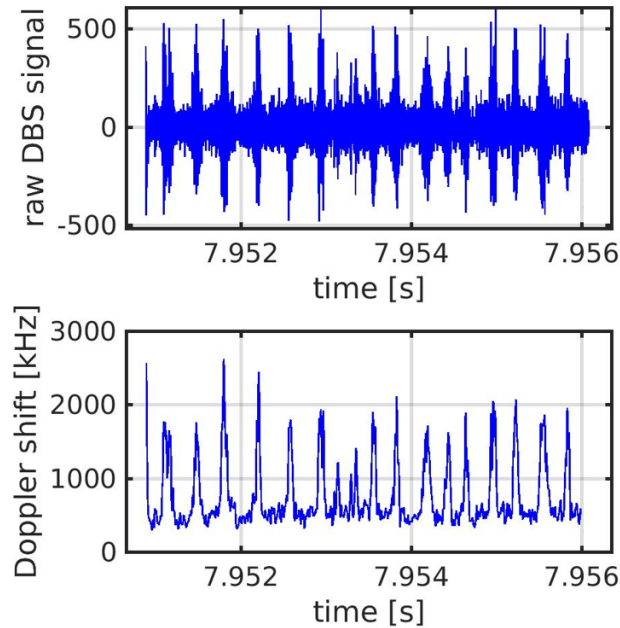


Figure 2.41: Time evolution of the DBS signal amplitude (top) and the Doppler shift (bottom) in the rotation well exhibiting oscillations (WEST #55562)

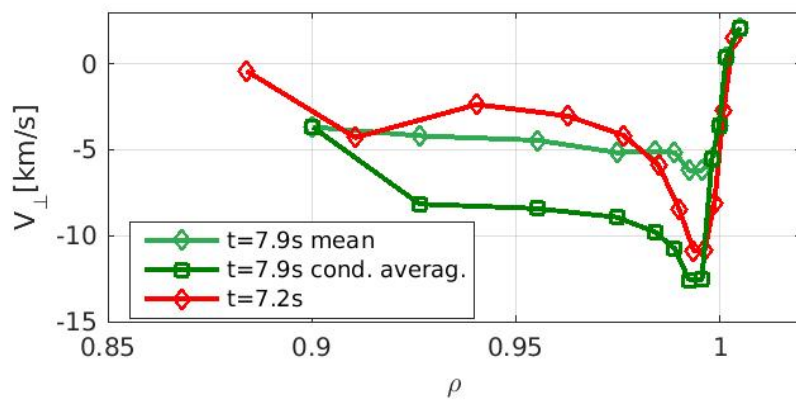


Figure 2.42: Edge rotation profiles at different probing time during the WEST discharge #55562. The square dots corresponds to the measure of the Doppler shift using a conditional averaging method and the diamond ones correspond to usual time averaging methods.



# **Chapter 3**

## **A model of edge turbulence interplay with sheared flows**

### **Content**

---

This chapter is dedicated to the presentation of the development and the validation of a model of interplay between turbulence and sheared flows. We first make a state of the art of theoretical, experimental and numerical characterisation of the edge turbulent transport. This state of the art also includes a discussion on the models of impact of sheared flows on turbulence and their involvement in L-H transition modelling. Then, we develop a spectral model of interchange turbulence interacting with sheared flows which describes the turbulence behaviour, the radial particle flux and the poloidal flows that it generates. A section about the numerical verification of the reduced model will detail the numerical experiment plan leading to a complete verification of the model predictions. A comparison of the model predictions with experimental data from Langmuir probes will exhibit a sound quantitative agreement with turbulent spectra measured in the TJ-K torsatron and with turbulence and background features in the SOL of Tore Supra. Furthermore, a study of magnetic topology impact on the edge rotation will be presented recovering experimental observations in WEST. The chapter will end on a discussion on the model generic nature and the inclusion of more complex effects such as edge density or geometric on the control parameter in the model showing the limits and perspectives of the model.

---

### **3.1 State of the art on the characterisation of edge turbulent transport**

This section is a summary of the state of the art concerning the description of the edge turbulent transport emphasising the context and the motivations of theoretical development derived in this work. We will consider two spatial regions of interest. The first one is the edge region located at the boundary of the confined plasma. The turbulence in this region converts the thermodynamic free energy from the gradients to macroscopic transport. Ion temperature gradient modes (ITG) are driven by the ion temperature gradient whereas the electron temperature gradient modes (ETG) draw the free energy from the electron temperature gradient. Also, the trapped electron modes (TEM) are driven from electron temperature and density gradients. These instabilities are called interchange instabilities. Theoretical descriptions of such instabilities have been done in linear regimes but so far it is still not fully understood in terms of nonlinear behaviours. To palliate this lack of knowledge kinetic equations are solved numerically. These simulations are very time consuming since they are solving the distribution function evolution in 6 dimensions plus the time or in the case of gyrokinetic simulations, in 5 dimensions, the perpendicular motion around the field line being averaged on the gyromotion of the particles [115, 116, 117, 118]. In order to lower the simulation time, simulations in a reduced space around a few field lines called "*flux-tube*" are ran [119] but it relies in the local approximation which is questionable. Indeed, it consists in the assumption a homogeneous turbulence in the flux-tube which can be unverified. Calculating the momenta of the kinetic equations leads to fluid-like description of the plasma. Numerical simulations resolving these fluid equations allow to reproduce experimental features such as the profiles shapes and turbulent behaviours [120, 121, 122]. The numerical resolution is still time consuming even if the number of dimensions of the system is lowered to 3. Moreover, the simulation results interpretation can be difficult due to the presence of multiple mechanisms and the interplay between them. The reduced models give a path to low time consuming simulations conserving the main physics of selected mechanisms. In this sense, development of quasi-linear models describing the turbulence by imposed spectral shapes but with varying cross phases [58, 123] led to a local description of the turbulent transport in quantitative agreement

with experimental profiles.

Another characteristic of this edge region is the build-up of a transport barrier leading to pedestal formation. The pedestal properties such as its height and width are quantities related to the confinement level of a discharge. In a forecasting point of view, models have to predict such properties for future devices such as ITER or DEMO. A model determines the interchange stability and the Peeling Ballooning Modes destabilisation (representing the ELMs) leading to predictions for these quantities [124, 125]. This model called EPED is not able to reproduce the pedestal features in all the operational regimes. These predictions of the pedestal features do not represent the dynamics leading to this state since it only predicts the final state of equilibrium between the interchange stability and the ELMs destabilisation. Models of the transition itself have also been derived. In particular, reduced models of interplay between turbulence and sheared flows attempted to recover L-H transition features such as increase of confinement [126] or limit cycle oscillations [52, 53]. Nevertheless, such models were not able to predict transition thresholds in agreement with experimental observations. These approaches need to recover two key points : the impact of the shear on the turbulence and the flow generation by the turbulence itself. The first point has been studied theoretically through models of turbulence decorrelation by the sheared flows [31, 127, 128]. Then, more recent studies pointed out the turbulence level mitigation through a lowering of the turbulence amplitude [129, 130, 131, 132] but also from a change in the phase shift between pressure and electrostatic potential perturbations [133, 134] showing a stronger impact on the small scale structures [132]. During the last decade, works based on turbulent spectra from non-linear simulation showed that the shearing impact on the turbulence was stronger than expected [135, 136, 137, 138]. Also, studies on the interplay between turbulence and zonal flows were investigated in Gyrokinetic simulations showing ability of the turbulence to build local transport barriers [139, 140]. Moreover, studies described the flow generation by the turbulence through the Reynolds tensor [141]. This point will be one of the main objectives of the model reduction detailed in the following of this chapter. Finally, the question of the impact of the X-point position on the L-H transition has also been addressed through magnetic shear induced structure tilt generating flows through the Reynolds tensor [142, 143] recovering experimental observations on the edge rotation

profiles.

The second spatial area of interest is the scrape-off layer region. Turbulence in this region is characterised by an intermittent filamentary transport. Experimental characterisation and modelling have been intensively studied aiming at understanding the contribution of these filaments (or "blobs"). A model based on the particle drifts without considering any filament [144], the Heuristic Drift model (HD model), has been derived recovering observations in reduced transport regimes such as in H-mode. Even if the filamentary transport is reduced in such regimes, it is not proved that its contribution is negligible. Moreover, transport in all the confinement regimes seems to conserve main trends possibly indicating an universal transport feature [68]. Recent studies based on resistive turbulence considerations [145] tried to isolate the contribution of the turbulence in the SOL transport in a wide database built in AUG. They showed that when the density increases, the turbulent transport in H-mode is no more negligible [146]. More recent considerations included into the HD model taking into account collisionality effects and shearing led to a better qualitative description of the SOL transport across the confinement regimes [147]. However, this model do not find a quantitative agreement and needs to tune parameters to quantitatively match observations. A description of the turbulence and its associated transport appears necessary.

In default of modelling the turbulence features, an experimental characterisation of the filament has been managed using different diagnostics such as gas puff imaging [148, 149], fast visible camera [150, 151] or Langmuir probes [152, 153, 154]. A review of the main observations can be found in [59]. The latter system allows to measure directly the filament properties such as their amplitude, velocity, size and duty cycle applying conditional averaging methods to the measured signals. This method relies on an ad-hoc choice of the threshold in amplitude of the event considered to average, usually a few times the standard deviation of the signal. This method allows to characterise the properties of a "mean blob". Another way to study the turbulence consists in applying statistical methods to the signals building probability density functions (PDF) of the turbulence features showing impacts of large amplitude events. Both approaches showed the domination of the filament in the transport.

Attempts of modelling the turbulence features have been proposed in the last decades based on two main instabilities : the Drift Wave instability (DW) [155, 156] and the interchange instability [157]. Both instabilities can occur in the edge plasma and SOL and can be responsible of transport. Links between these models and filaments are still not fully understood and described even if it has been demonstrated that drift wave instability can generate filaments [158]. On the other hand, models of isolated filament properties have been proposed making links between their velocities and their sizes and amplitudes [159, 12]. These predictions have been recovered with numerical simulations [160, 161]. Unfortunately, no model of intermittency and amplitudes of the filaments have been developed leading to an inability to build transport models [162]. Another attempt to link filaments and transport has been driven from a statistical description of all the filament features [60, 163]. This method recovered experimental observations but relies on experimentally established distribution functions. Indeed, no theoretical predictions are given for these distribution functions preventing from extrapolating to future devices. Finally, an analytical approach based on a spectral treatment of the resistive interchange turbulence equations led to a scaling of the heat flux decay length in qualitative agreement with some experimental observations [164, 165]. It is based on the description of an unique wavenumber and an hybrid mixing length representation for the mode amplitude. In the end, plasma resistivity is considered as responsible of the parallel dynamics which is questionable in the SOL where the parallel dynamics appears strongly dominated by the sheath, at least in moderate density regimes.

In the end, no model is able to reproduce the transport in SOL of tokamak plasmas across all the operation regimes of a device. This lack of knowledge led to the use of two ways to make predictions of transport levels. The first one consists in the establishment of databases in wide plasma and machine parameter spaces in order to find scaling laws for the main transport quantities as the heat flux deposition width [64, 63, 65]. The second approach is based on numerical simulations and is used in two distinct ways : either the transport is represented by diffusive phenomena with a map of the diffusion coefficient [166, 167] or turbulent equations are solved to self-consistently reproduce the turbulent transport [120, 121, 122]. The representation of the transport by a diffusion coefficient allows to introduce experimentally or theoretically based scalings [168]. Furthermore, numerical simulations can be used to try to re-

produce experimentally observed impacts such as magnetic geometry impacts (elongation, triangularity, divertor geometry) [169, 170, 171]. Nevertheless, such simulations can be difficult to interpret. In order to better point out the underlying physics, 2D codes were developed in simplified geometries [73, 21]. Such codes showed an ability to reproduce both intermittent filaments features and exponential SOL quantities behaviours [73, 74, 75]. It inspired a work on decay length scaling fitted from simulation results in agreement with measurements in Tore Supra [75].

The lack of knowledge in understanding the turbulence and its implication in the edge plasma transport motivated to build a reduced model able to describe both parts. The work presented in this chapter aims at filling this void drawing a model of interchange turbulent spectra from which can be derived the transport observables taking into account shearing effects, magnetic geometry and sheath resistivity [172, 173, 174, 175]. Extracting Reynolds tensor expressions from this model leads to a description of the flow generation by the sheared turbulent structures. With all of these key ingredients, a representation of the edge transport is built recovering simulation results and experimental observations.

## **3.2 A transport model of interchange turbulence in a sheared flow**

This section details the derivation of a model of interplay between turbulence and a background sheared flow based on conservation equations. As a starting point, we present the paradigm proposed in this work before developing the turbulence spectra model. Then, predictions of transport observables, i.e. potential and density fluctuation levels, flux, SOL density decay length and Reynolds tensor will be deduced from this spectral model. The obtained Reynolds tensor will then be included in the poloidal momentum conservation equation to predict the flow generation by the turbulence leading to edge rotation profiles.

### **3.2.1 The Sheared Spectral Filament (SSF) model paradigm**

As introduced in the state of the art of this chapter, edge turbulent transport is characterised by intermittent filaments which are not analytically described. To palliate the fail of describing the intermittency of these structures, we propose

to apply a spectral approach to the equations. This hypothesis results in the attribution of the transport to poloidal waves. These waves can also have a radial contribution due to an introduction of the tilt due to magnetic shear and sheared flows. This spectral approach will represent the time averaged properties of the turbulence. Once the averaged spectra predictions established, we sum the contributions of the modes to the total flux, Reynolds tensor and fluctuation levels. Applying the flux model to the scrape-off layer region leads to a prediction of the density exponential decay length.

### 3.2.2 The Sheared Spectral Filament model

In order to obtain the turbulence spectra we decompose the electrostatic potential and the density in an average part and a fluctuating part composed of a sum of modes of wavenumbers  $\vec{k} = k_x \vec{e}_x + k_y \vec{e}_y$ . Here, the  $x$  direction corresponds to the radial position ( $x = \frac{r}{\rho_s}$ ) and the  $y$  one is similar to the poloidal one ( $= \frac{a\theta}{\rho_s}$ ) as in the TOKAM2D model presented in the introduction of this manuscript. Note that the radial wavenumber  $k_x$  describes the tilt of the modes and will be considered to evolve in time due to shearing effects. The average part of the density, or density background, is considered as exponentially decaying with a decay length  $\lambda$  such as in the scrape-off layer. This decay length is a result of the competition between the radial flux (from fluctuations and diffusion) and the parallel losses to the sheaths. Note that the plasma domain considered here is free of volume sources. Aiming at introducing a background sheared  $E \times B$  flow, we will impose a radial dependency of the background potential  $f(x)$  with a shearing rate  $\sigma_s$ . Density and potential fluctuations of wavenumber  $\vec{k}$  are allowed to have a phase shift  $\varphi_k$ .

$$n(x, y) = n_0 e^{-\frac{x}{\lambda}} \left( 1 + \sum_k n_k \cos(k_x x + k_y y + \varphi_k) \right) \quad (3.1)$$

$$\Phi(x, y) = \Lambda_0 + \sigma_s f(x) + \sum_k \Phi_k \cos(k_x x + k_y y) \quad (3.2)$$

These expressions are introduced in the following system of equations from

TOKAM2D :

$$(\partial_t - D_n \Delta_{\perp}) n - [\Phi, n] = S_n - \sigma_{\parallel} n e^{\Lambda - \Phi} \quad (3.3)$$

$$(\partial_t - \nu \Delta_{\perp}) \Delta_{\perp} \Phi - [\Phi, \Delta_{\perp} \Phi] = -g \frac{\partial_y n}{n} + \sigma_{\parallel} (1 - e^{\Lambda - \Phi}) \quad (3.4)$$

The background equilibrium is reached when the source of particles is compensated by the parallel losses  $\sigma_{\parallel}$  across the entire profile, setting the background density amplitude  $n_0$ . Taking into account these considerations and introducing the phase  $\Psi = \vec{k} \cdot \vec{r}$ , the system can be rewritten as :

$$\sum_{k_i} (\partial_t n_{k_i} \cos(\Psi_i + \varphi_{k_i}) - x \partial_t k_{i,x} n_{k_i} \sin(\Psi_i + \varphi_{k_i})) - [\Phi, n] = 0 \quad (3.5)$$

$$- \sum_{k_i} (\partial_t (k_i^2 \Phi_{k_i} \cos(\Psi_i)) + [\Phi, \Delta_{\perp} \Phi]) = -g \sum_{k_i} n_{k_i} \partial_y \cos(\Psi_i + \varphi_{k_i}) + \sigma_{\parallel} \sum_{k_i} \Phi_{k_i} \cos(\Phi_i) \quad (3.6)$$

In the density equation, the first left hand side term corresponds to the time derivative of the mode amplitude  $n_k$ , whereas the second term corresponds to the time derivative of the phase of the mode, which implies the time derivative of the radial wave number. This phase derivative is also present in the vorticity equation, but is kept implicit in the above notation. Second, note that the parallel loss term was omitted intentionally in equation describing the dynamics of the density perturbation. In principle, perturbations shall be damped by parallel losses, but we anticipate that this term is in fact negligible compared to the other terms of the density equation. For similar ordering motivations, we neglect the artificial diffusion and viscosity terms in both density and vorticity equations.

The Poisson bracket terms contain the underlying non-linear physics and results in the following expression for the density:

$$[\Phi, n] = n_0 e^{-\frac{x}{\lambda}} \sum_{k_i} \left[ -\sigma_s \partial_x f(x) k_{i,y} n_{k_i} \sin(\Psi_i + \varphi_{k_i}) + \frac{k_{i,y} \Phi_{k_i}}{\lambda} \sin(\Psi_i) \right. \\ \left. + \sum_{k_j} (k_{i,y} k_{j,x} - k_{i,x} k_{j,y}) n_{k_i} \Phi_{k_j} \sin(\Psi_i + \varphi_{k_i}) \sin(\Psi_j) \right]$$

The first term is the poloidal advection of the density mode by the background flow, the second term is the radial advection of the background density by the

potential mode. These two terms are linear in mode amplitude, whereas the third term gathers all the remaining non-linear couplings between potential and density modes.

A similar decomposition is done for the Poisson bracket of the vorticity equation:

$$[\Phi, \Delta\Phi] = \sum_{k_i} [\sigma_s \partial_x f(x) k_{i,y} k_i^2 \Phi_{k_i} \sin(\Psi_i) + \sum_{k_j} (k_{i,y} k_{j,x} - k_{i,x} k_{j,y}) k_j^2 \Phi_{k_i} \Phi_{k_j} \sin(\Psi_i) \sin(\Psi_j)]$$

, where the first term describes the poloidal advection of the potential mode by the background flow, and the second term gathers all non-linear mode couplings. Note that the radial advection of the background vorticity gradient by the potential mode is omitted here on purpose: we make the approximation, for now, that the spatial variation of the background flow shear is negligible on the scale of the mode.

The main difficulty in modeling turbulence is the derivation of an approximate model of the non-linear terms. In this work, we make heuristic assumptions to approximate such terms. In the density equation, we approximate the non-linear term by a term  $\sum_{k_i} k_i^2 \Phi_{k_i} n_{k_i}$  which leads to a mixing length rule for the density spectrum. This mixing length rule is observed in case of very turbulent systems. The non-linear term in the vorticity equation is approximated by a inertial-like term :  $\sum_{k_i} k_i^4 \Phi_{k_i}^2$ . These assumptions are detailed and discussed in the following. As explained later, an improved heuristic closure will be proposed for both the density and vorticity equations, based on the action of a dominant mode.

### 3.2.2.1 From isolated filaments to a description of non-linear terms : the Isolated Filament model

The approach proposed in this work to describe the non-linear term in the vorticity equation is inspired from the filamentary transport description. Indeed, the motion of the filaments is due to the charge separation induced by the diamagnetic drift of ions and electrons. When the over-pressure (or over-density) drifts outwards due to the resulting vertical electric field, the vortices remain immobile.

In order to move again, the charge separation has to occur again. This phenomenon leads to an inertial saturation of the movement of the filaments [159] (see figure 3.1).

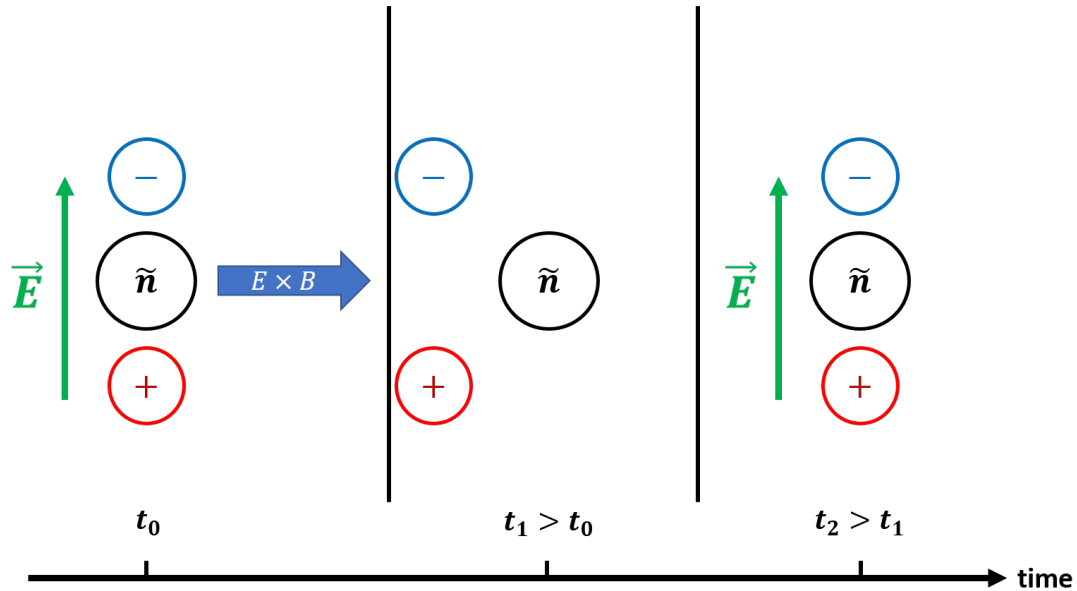


Figure 3.1: Scheme of the inertia saturation of a filament motion.

This saturation comes from a polarisation term and, consequently, is higher for higher drift velocities of the structures. It can be modelled by a restoring force with a restoring time  $\tau$  proportional to the filament size  $\delta_b$  and inversely proportional to the structure velocity  $V_b$  :  $\tau = \frac{\delta_b}{V_b}$ . We propose to extend this ordering-based method to the modes considered in this model leading to the Isolated Filament model (IF model). In this heuristic framework, we approximate the non-linear contributions by an inertial term :  $\partial_t A + [\Phi, A] \approx \frac{A_k}{\tau} = k^2 \Phi_k A_k$ . Applying this ordering considerations to the second order term in the Poisson bracket in the vorticity equation leads to the inertial saturation term  $\sum_{k_i} k_i^4 \Phi_{k_i}^2 \cos(\Phi_i)$  braking the coupling of the different modes leading to equation for single modes. We finally obtain for the vorticity equation :

$$\begin{aligned} \partial_t k_x^2 \Phi_k \cos(\Psi) - x \partial_t k_x \Phi_k \sin(\Psi) - \sigma_s \partial_r f(x) k_y k^2 \Phi_k \sin(\Psi) - k_i^4 \Phi_k^2 \cos(\Psi) = \\ - g k_y n_k \sin(\Psi + \varphi_k) + \sigma_{||} \Phi_k \cos(\Psi) \end{aligned} \quad (3.7)$$

The potential spectrum will depend on the density one. Consequently, one need to have a closure expression for the density spectrum to fully describe the turbulence behaviour.

### 3.2.2.2 The mixing length rule for the density spectrum

Applying a similar ordering approach to the continuity equation leads to a term of auto-advection of the mode at the velocity  $v_r = k_{i,y}\Phi_{k_i}$ . Again, this consideration allows to brake the mode coupling in the equation leading to individual equations for each mode. We finally obtain an equation for the mode  $k$ .

$$-x\partial_t k_x n_k \sin(\Psi + \varphi_k) = -k_y^2 n_k \Phi_k \cos(\Psi + \varphi_k) + \frac{k_y \Phi_k \sin(\Psi)}{\lambda} + \sigma_s \partial_r f(x) k_y n_k \sin(\Psi + \varphi_k) \quad (3.8)$$

Then, we need to determine the evolution of the phase shift between density and potential perturbations  $\varphi_k$ . In this work, we made the assumption that this phase shift is equal to  $\pi/2$  for all the modes. This value corresponds to the ideal interchange case and maximises the contribution of the modes to the flux. This assumption will be discussed with the simulation results in the following of the section. Taking into account this assumption the system becomes :

$$\partial_t n_k \sin(\Psi) + x\partial_t k_x n_k \cos(\Psi) = -k_y^2 n_k \Phi_k \sin(\Psi) + \frac{k_y \Phi_k \sin(\Psi)}{\lambda} - \sigma_s \partial_r f(x) k_y n_k \cos(\Psi) \quad (3.9)$$

$$(k^2 \partial_t \Phi_k + \partial_t k_x^2 \Phi_k) \cos(\Psi) - x\partial_t k_x \sin(\Psi) - k^4 \Phi_k^2 \cos(\Psi) = -g k_y n_k \cos(\Psi) + \sigma_\parallel \Phi_k \cos(\Psi) \quad (3.10)$$

Identifying the cosine terms and the sine terms in the two equations gives 3 equations : one for the mode amplitude  $n_k$ , one for the potential perturbation due to the mode  $k$   $\Phi_k$  and one for the tilt on the mode  $k_x/k_y$ .

$$0 = -k_y^2 n_k \Phi_k + \frac{k_y \Phi_k}{\lambda} \quad (3.11)$$

$$\partial_t k_x^2 \Phi_k - k^4 \Phi_k^2 = -g k_y n_k + \sigma_\parallel \Phi_k \quad (3.12)$$

$$x\partial_t k_x = \partial_r f(x) \sigma_s k_y \quad (3.13)$$

In the case without shear, the modes remain non-tilted. The radial wavenumber can be non-zero considering the magnetic shear induced tilt. In this particular case, we will neglect the magnetic shear and consider a zero-value of the radial wavenumber. We will address the impact of the magnetic shear in the sheared turbulence case. In these conditions we obtain the following expressions for the

spectra :

$$n_k = \frac{1}{\lambda k_y} \quad (3.14)$$

$$\Phi_k = \frac{\sigma_{\parallel}}{2k_y^4} \left[ -1 + \sqrt{1 + \frac{4gk_y^5 n_k}{\sigma_{\parallel}^2}} \right] \quad (3.15)$$

Replacing  $n_k$  by its expression in the potential spectrum expression (3.15) and introducing the wavenumber  $k_0 = \left( \frac{\lambda \sigma_{\parallel}^2}{4g} \right)^{1/4}$  of transition between the regime saturated by the parallel losses (low  $k_y$ ) and the regime saturated by the modes inertia (high  $k_y$ ), we finally obtain the following reduced spectral model.

$$n_k = \frac{1}{\lambda k_y} \quad (3.16)$$

$$\Phi_k = \frac{\sigma_{\parallel}}{2k_y^4} \left[ -1 + \sqrt{1 + \left( \frac{k_y}{k_0} \right)^4} \right] \quad (3.17)$$

$$k_0 = \left( \frac{\lambda \sigma_{\parallel}^2}{4g} \right)^{1/4} \quad (3.18)$$

As mentioned above, this heuristic ordering approach leads to a density spectrum expression given by a mixing length rule  $n_k = \frac{1}{\lambda k_y}$ . This is a common description expected for a strongly turbulent system [5]. The vorticity equation exhibits the driving of the turbulence by the curvature term saturated by the parallel losses and the inertia of the mode.

### 3.2.2.3 A model of turbulence without background shear : the Spectral Filament model

This description is inspired from the isolated filament model introduced just above. Usually, the filaments are plunged in a turbulent bath and interactions between filaments and vortices could also limit the motion of such structures. Indeed, in simulations we observe that the structures tend to follow the wake of the structures slightly outwards. Consequently, the filament creates vortices were other vortices are present. This will lead to a saturation of the vortex creation which could be described as an effective turbulent viscosity. Interestingly, this approach can directly be extrapolate to a spectral description. In the case

of interchange turbulence, we usually observe a dominant mode  $k_0$  exhibiting a higher growth rate. In the turbulence observed in this thesis, this mode corresponds to the higher perturbation of the potential (see figure 3.2). The resulting effective viscosity will be proportional to the potential perturbation  $\Phi_{k_0}$  induced by the dominant mode  $k_0$ . In this work, we will consider a direct proportionality with a coefficient of 1 which is in agreement with the simulation results as it will be shown in figure 3.2. These considerations end in a linear term  $\Phi_{k_0} k^4 \Phi_k$  representing the non-linear terms of the vorticity equations. Moreover, the dominant mode being faster than the others, it will be able to advect a part of the matter of larger size modes leading to a saturation of the spectra at the low wavenumbers. In order to take into account this phenomenon, we propose a heuristic model of the density spectrum keeping the simple mixing length expression. We introduce here an hybrid wavenumber  $k_{eff} = \sqrt{k_y^2 + k_0^2}$  in this mixing length rule leading to a closure of the model. This results in the following spectra expression :

$$n_k = \frac{1}{\lambda k_{eff}} = \frac{1}{\lambda k_0 \sqrt{1 + \left(\frac{k_y}{k_0}\right)^2}} \quad (3.19)$$

$$\Phi_k = \frac{g \frac{k_y}{k_0}}{\lambda \sigma_{||} \sqrt{1 + \left(\frac{k_y}{k_0}\right)^2 \left(1 + \frac{\Phi_{k_0} k_y^4}{\sigma_{||}}\right)}} \quad (3.20)$$

The expressions of  $k_0$  and  $\Phi_{k_0}$  are deduced from the equation 3.20 taken at  $k_y = k_0$  and the potential maximum value determination  $\frac{\partial \Phi_k}{\partial k}|_{k=k_0}$ . This Spectral Filament model (SF model) finally results in the following expressions :

$$n_k = \frac{1}{\lambda k_0 \sqrt{1 + \left(\frac{k_y}{k_0}\right)^2}} \quad (3.21)$$

$$\Phi_k = \frac{g \frac{k_y}{k_0}}{\lambda \sigma_{||} \sqrt{1 + \left(\frac{k_y}{k_0}\right)^2 \left(1 + \frac{1}{7} \left(\frac{k_y}{k_0}\right)^4\right)}} \quad (3.22)$$

$$k_0 = \left( \frac{0.92 \lambda \sigma_{||}^2}{4g} \right)^{1/4} \quad (3.23)$$

Interestingly, this spectrum expression as well as the mixing length expression is not depending on the density parallel loss rate. Consequently, we could

extrapolate it into the closed field line region.

The Isolated Filament model (IF model by analogy with the one in [159]) has been compared to TOKAM2D simulation results. The details of the simulation data treatment are detailed in Appendix D. In order to avoid the impact of a possible mismatch between the mixing length model and the density spectrum on the potential spectrum prediction, we predict this later using the density spectrum obtained from the simulation. This comparison points out some limitations. Figure 3.2 shows 3 discrepancies between the simulation results and the model predictions. First, the phase shift between potential and density perturbation is not exactly  $\pi/2$  but it is contained in  $[\pi/3 - \pi/2.5]$ . Nevertheless, this contribution will only have a slight impact on the flux contribution as it will be discussed in the next chapter (see section 4.3).

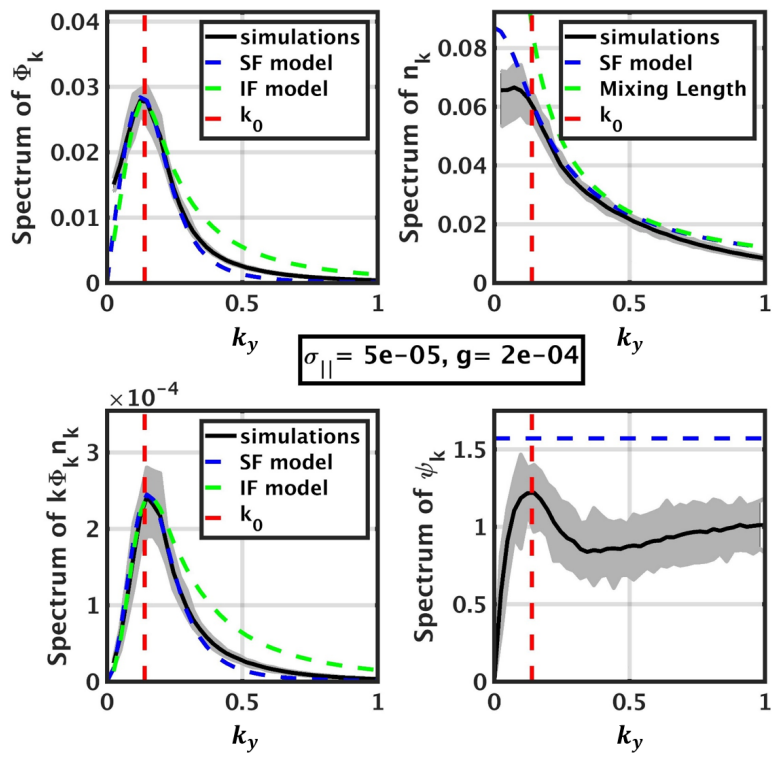


Figure 3.2: Spectra of potential (top left), density (top right), mode contribution to the flux (bottom left) and phase shift between density and potential perturbation (bottom right). Black lines are simulation results, grey areas are the time and radial variations of the poloidal spectra, green dashed lines are the isolated filament and mixing length models and blue lines are the predictions of the SF model. Red dashed lines indicate the position of the dominant wavenumber  $k_0$

Second, the density spectra exhibit an over-prediction by the model of the

low wavenumber contributions. This overestimation is also observed at the wavenumber  $k_0$  which is the characteristic mode. On the other hand, the SF model predictions are able to reproduce both spectra amplitude and shapes of the density and potential spectra. A slight over-estimation of the density spectrum is still observed but the predicted dominant mode amplitude  $n_{k_0}$  is in quantitative agreement with the simulation results.

Interestingly, the model predictions can be decomposed in a product of two terms: 1) a physical amplitude depending on the gradient length  $\lambda$ , the curvature driving coefficient  $g$  and the parallel losses rate  $\sigma_{\parallel}$  and 2) a spectral shape function of the normalised wavenumber  $u = \frac{k_y}{k_0}$ . This is convenient for the spectral integrations used to calculate transport observables as it will be seen later in this manuscript in section 3.2.2.6. This Spectral Filament model (SF model) describes the turbulent spectra in absence of background shear. The tilting equation has to be described in order to understand the impact of a background shear in the model of turbulence.

### 3.2.2.4 A model of turbulence in a homogeneous background shear : the Sheared Spectral Filament model

Aiming at understanding the impact of a background sheared flow on the turbulence we first consider a simple case of homogeneous shear rate corresponding to a parabolic background potential profile in the model  $\langle \Phi \rangle = \Lambda_0 + \frac{\sigma_s x^2}{2}$ . Introducing this expression in equation (3.13) leads to a continuous tilt of the mode.

$$\partial_t k_x = -\sigma_s k_y \quad (3.24)$$

This prediction is not verified in the simulations. Indeed, in simulations, a constant tilt of the structures is observed. We take into account this phenomenon introducing a restoring force in the model due to interchange considerations. The interchange instability tends to develop poloidal modes without tilt. It results in a restoring of the structures towards a non-tilted shape on a characteristic time  $\tau$  corresponding to the growth time of the vortices. Each mode will have a growing time  $\tau_k$  given by the time of growth of the mode vorticity due to interchange drive

:

$$\frac{k^2 \Phi_k}{\tau_k} = g k_y n_k \quad (3.25)$$

To simplify the calculations we consider that the modes contributing to the flux are concentrated around the dominant wave number and consequently, we use an unique restoring time  $\tau$  for all modes equal to the value determined for the dominant wavenumber in the case without shear.

$$\tau = \frac{k_0^2 \Phi_{k_0}}{g n_{k_0}} = 0.43 \sqrt{\frac{\lambda}{g}} \quad (3.26)$$

We introduce the interchange restoring force in equation (3.24).

$$\partial_t k_x = -\sigma_s k_y - \frac{k_x - k_x^0}{\tau} \quad (3.27)$$

Here  $k_x^0$  corresponds to a structure tilt  $\theta_x^0 = \frac{k_x^0}{k_y}$  which is not varying in time and not created by the sheared flow. Effects of magnetic shear tilt can be included in this contribution. In stationary state, the mode tilt becomes constant with the value :

$$k_x = k_x^0 - \sigma_s \tau k_y \quad (3.28)$$

This result is verified using simulations in section 3.3.2.2 on the model numerical verification. This expression can be introduced in the model of potential and density through the ratio  $k_x/k_y$  and the term related to the mode and sheared flow interaction  $\partial_t k_x \approx \frac{k_x}{\tau} = -\sigma_s k_y$ . It results in the following expressions :

$$n_k = \frac{1}{\lambda k_0 (1 + (\theta_x^0 - \sigma_s \tau)^2) \sqrt{1 + \left(\frac{k_y}{k_0}\right)^2}} \quad (3.29)$$

$$\Phi_k = \frac{g \frac{k_y}{k_0}}{\lambda \sigma_{||} (1 + (\theta_x^0 - \sigma_s \tau)^2) \left(1 + 2 \frac{\sigma_s \tau (\sigma_s \tau - \theta_x^0)}{\sigma_{||} \tau} k_y^2 + \frac{1}{7} \left(\frac{k_y}{k_0}\right)^4\right)} \quad (3.30)$$

$$k_0 = \left( \frac{0.92 \lambda \sigma_{||}^2}{4g (1 + (\theta_x^0 - \sigma_s \tau)^2)} \right)^{1/4} = 1.06 \sqrt{\sigma_{||} \tau} (1 + (\theta_x^0 - \sigma_s \tau)^2)^{-1/4} \quad (3.31)$$

It results in a model considering three effects which saturate the potential growth by the curvature drive : 1) the losses in the parallel direction, 2) the turbulent viscosity and 3) the Reynolds stress flow generation. We will distinguish two regimes : the weak shear regime in which the saturation at high wavenumbers ( $k_y \geq k_0$ ) is dominated by the turbulent viscosity and the strong shear regime in which it is the interaction with the sheared flow that dominates. In absence of magnetic shear, the transition between these two regimes occurs when the tilt of the structure reaches the condition  $\sigma_s \tau = 0.4$ . Lastly, the spectrum amplitude is lowered in both regime by the radial wavenumber creation due to the fact that the system allows to spread the spectral energy on two directions ( $k_x, k_y$ ).

### 3.2.2.5 Effect of non homogeneous shears

The effect of a homogeneous shear on the turbulence treated in the previous section might be unable to represent the real case. Indeed, the shear across the separatrix exhibits a width  $\delta_s$  of the order of the centimetre which is comparable to the structure sizes ( $\delta_b \approx 10\rho_s \approx 1cm$ ). In order to evaluate the impact of a non-homogeneous shear on the turbulence, we choose to represent the shear variation with a gate function of width  $2\delta_s$ . Taking into account the gate function  $f(x) = \frac{x^2}{2}\Pi(x, 2\delta_s)$  and the interchange restoring force in the tilt equation (3.13), we obtain :

$$x\partial_t k_x = -\sigma_s x\Pi(x, 2\delta_s) - x\frac{k_x - k_x^0}{\tau} \quad (3.32)$$

This equation is depending on the radial direction. The aim of the model driven here is to underline time averaged effects. Consequently, we propose to calculate the effective tilt of the structure averaged on a typical transport distance  $k_y^{-1}$ . Considering a stationary regime and integrating equation (3.32) in the radial direction on a distance  $k_y^{-1}$  leads to the following expression for the tilt :

$$k_x = k_x^0 - \sigma_s \tau k_y \min(1, \delta_s k_y)^2 \quad (3.33)$$

Two regimes appear : when the structure size is larger than the shear layer one, the effective tilt of the structure is lower than the case when the structure size is lower than the shear layer width. The transition between the two regime can be

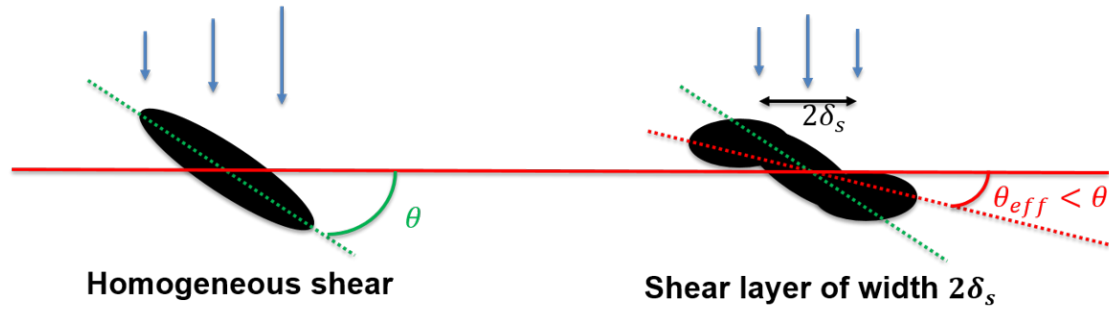


Figure 3.3: Scheme of the impact of the shear layer width on the effective tilt of the structures.

smoothed considering a lorenzian like transition.

$$k_x = k_x^0 - \sigma_s \tau k_y \frac{k_y^2 \delta_s^2}{(1 + k_y^2 \delta_s^2)} \quad (3.34)$$

Moreover, in order to simplify the integration of this term in the spectral model, we will consider the dominant wavenumber as typical radial transport length following the assumption that the important spectral contributions to the flux are close to the dominant mode one. This will be the expression which will be used in the final version of the SSF model.

$$k_x = k_x^0 - \sigma_s \tau k_y \frac{k_0^2 \delta_s^2}{(1 + k_0^2 \delta_s^2)} \quad (3.35)$$

### 3.2.2.6 From the spectra to the transport observable predictions

Since we describe the turbulent spectra interacting with a background shear flow, we can deduce the transport observables summing the contribution of all modes. This method allows to predict the radial flux  $\Gamma_r$ , the normalised fluctuation levels

of density  $\sigma_n / \langle n \rangle$  and potential  $\sigma_\Phi / T_e$  and the Reynolds tensor  $\Pi$ .

$$\Gamma_r = 8\pi^2 \langle n \rangle \int_0^{+\infty} k_y n_k \Phi_k \sin(\varphi_k) dk_y = 8\pi^2 \langle n \rangle \int_0^{+\infty} k_y n_k \Phi_k dk_y \quad (3.36)$$

$$\frac{\sigma_n}{\langle n \rangle} = \sqrt{8\pi^2 \int_0^{+\infty} n_k^2 dk_y} \quad (3.37)$$

$$\frac{\sigma_\Phi}{T_e} = \sqrt{8\pi^2 \int_0^{+\infty} \Phi_k^2 dk_y} \quad (3.38)$$

$$\Pi = 8\pi^2 \int_0^{+\infty} k_x k_y \Phi_k^2 dk_y \quad (3.39)$$

We used the phase shift between density and potential of  $\pi/2$  in the flux calculation. We also considered the parity of the spectra to change the integrals between  $-\infty$  and  $+\infty$  to the double of an integral from 0 to  $\infty$ . Inserting the density and potential spectra predictions in these expressions lead to integrals on a the normalised wavenumber  $u = \frac{k_y}{k_0}$ . Unfortunately, the term of interaction between the modes and the background shear flow keeps us from obtaining simple analytical predictions. To palliate this issue, numerical integrations at different values of  $\alpha_s = \sigma_s \tau \times (k_x^0 - \sigma_s \tau) / \sqrt{(1 + (k_x^0 - \sigma_s \tau)^2)}$  in the case of a homogeneous tilt show the evolution of these integrals with this parameter. Fitting it with second degree polynomials allows to recover well the evolution and to separate the observables dependencies with the model control parameters ( $g, \sigma_{||}$ ) and the tilt induced by the shear. Considering that the  $k_x^0$  tilt is proportional to  $k_y$ , as it is the case for the magnetic shear, we recall the tilt  $\theta_x^0 = \frac{k_x^0}{k_y}$ . We finally obtain the following expressions for the transport observables scalings :

$$\frac{\Gamma_r}{\langle n \rangle} = 41 \lambda^{-7/4} g^{3/4} \sigma_{\parallel}^{-1/2} \left( 1 + \left( \frac{k_x}{k_y} \right)^2 \right)^{-9/4} \frac{1}{(1 + 1.13\alpha_s - 0.01\alpha_s^2)} \quad (3.40)$$

$$\frac{\sigma_n}{\langle n \rangle} = 13.3 \lambda^{-9/8} g^{1/8} \sigma_{\parallel}^{-1/4} \left( 1 + \left( \frac{k_x}{k_y} \right)^2 \right)^{-7/8} \quad (3.41)$$

$$\frac{\sigma_{\Phi}}{T_e} = 5 \lambda^{-7/8} g^{7/8} \sigma_{\parallel}^{-3/4} \left( 1 + \left( \frac{k_x}{k_y} \right)^2 \right)^{-9/8} \frac{1}{(1 + 1.14\alpha_s - 0.11\alpha_s^2)} \quad (3.42)$$

$$\Pi = 17.8 \lambda^{-5/4} g^{5/4} \sigma_{\parallel}^{-1/2} \frac{k_x}{k_y} \left( 1 + \left( \frac{k_x}{k_y} \right)^2 \right)^{-11/4} \frac{1}{(1 + 1.66\alpha_s + 2.5\alpha_s^2)} \quad (3.43)$$

$$\alpha_s = \frac{\sigma_s \tau \frac{k_x^0}{k_y}}{\sqrt{\left( 1 + \left( \frac{k_x}{k_y} \right)^2 \right)}} \quad (3.44)$$

$$\frac{k_x}{k_y} = \theta_x^0 - \sigma_s \tau \frac{k_0^2 \delta_s^2}{(1 + k_0^2 \delta_s^2)} \quad (3.45)$$

Figure 3.4 shows the evolutions of the radial flux, of the dominant wavenumber and of the Reynolds tensor with the mode tilt induced by the sheared flow. The evolution of the dominant wavenumber shows the shear regime transition at the value  $\sigma_s \tau = 0.4$ . Interestingly, changing from weak to strong shear regime does not change the flux dependencies in the control parameters. This is coherent with the similar expressions of experimental scalings of energy confinement time in L-mode and H-mode [176]. In order to lower the flux by a factor of two, as it happens in the case of an L-H transition, we have to reach a tilt value of  $\sigma_s \tau = 1$ . This prediction is equivalent to a shearing rate of the order of ten kilometres per second on a centimetre. This value corresponds to the typical values of shear observed at the L-H transition. Moreover, the Reynolds tensor behaviour with structure tilt changes at the transition between weak and strong shear regime. At this transition, the lowering of the turbulence amplitude compensates the growth of the tilt leading to a decrease of the Reynolds tensor with further tilt increase.

### 3.2.2.7 Flux conservation in the scrape-off layer : predictions of the density decay length

The radial particle flux determined by the model is applied to the specific case of the scrape-off layer in which this radial flux is compensated by the parallel one

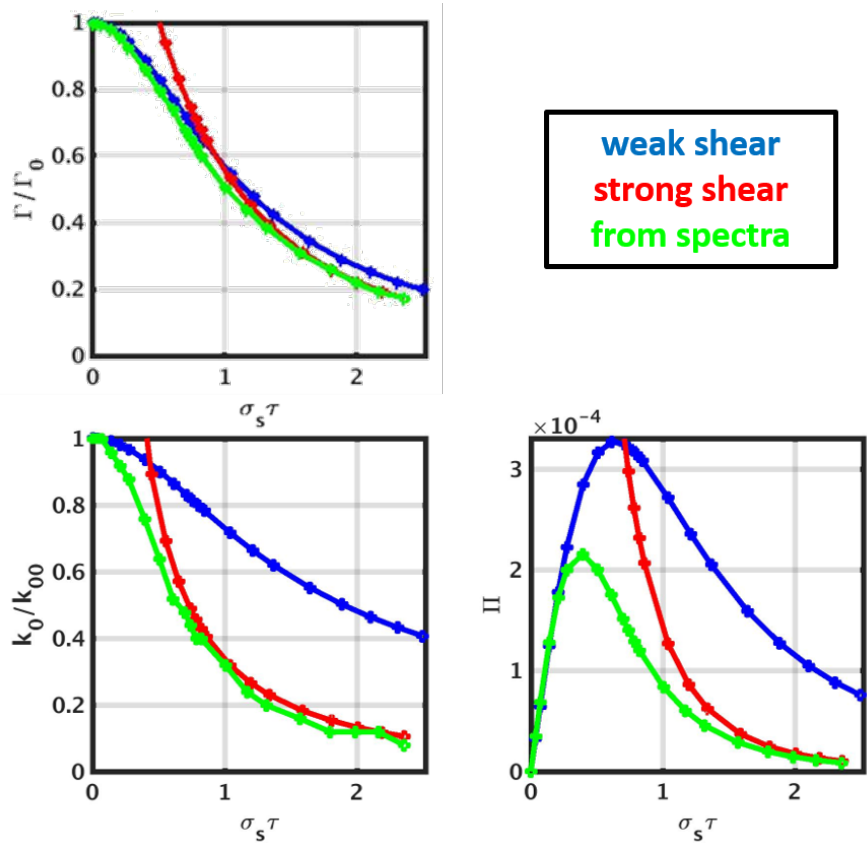


Figure 3.4: Impact of the sheared flow induced structure tilt on the transport observables : radial flux  $\Gamma_r$  (top left), dominant wavenumber  $k_0$  (bottom left) and Reynolds tensor  $\Pi$  (bottom right)

at the equilibrium when there is no particle sources or sinks in the SOL volume. This could not be the case in the divertor legs or in the case of high density regimes. These points will be discussed in the next chapter (see section 4.2).

$$\partial_r \Gamma_r + \partial_{\parallel} \Gamma_{\parallel} = 0 \quad (3.46)$$

$$\partial_r \Gamma_r = -\sigma_{\parallel} < n > \quad (3.47)$$

In order to predict density decay lengths, we need to describe the gradient of the radial flux. To that end, we assume that the only radial dependency of the flux comes from the density profile  $\partial_r \Gamma_r = -\frac{\Gamma_r}{\lambda}$ . This is consistent with eq.3.40 and the assumed shape of the background density profile. This gives a relation for the density decay length in terms of the flux predicted by the model and the

parallel loss coefficient  $\sigma_{\parallel}$ .

$$\lambda = \frac{\Gamma_r}{\sigma_{\parallel} < n >} = \frac{8\pi^2 \int_0^{+\infty} k_y \Phi_k n_k dk_y}{\sigma_{\parallel}} \quad (3.48)$$

This expression is a non-linear function of the SOL width which gives the following scaling for  $\lambda$  :

$$\lambda = 3.9 g^{3/11} \sigma_{\parallel}^{-6/11} \left( 1 + \left( \frac{k_x}{k_y} \right)^2 \right)^{-9/11} \frac{1}{(1 + 1.13\alpha_s - 0.01\alpha_s^2)^{4/11}} \quad (3.49)$$

Introducing this scaling in the flux and fluctuation levels one leads to the following scalings in the SOL :

$$\frac{\Gamma_r}{< n >} = 3.9 g^{3/11} \sigma_{\parallel}^{5/11} \left( 1 + \left( \frac{k_x}{k_y} \right)^2 \right)^{-9/11} \frac{1}{(1 + 1.13\alpha_s - 0.01\alpha_s^2)^{4/11}} \quad (3.50)$$

$$\frac{\sigma_n}{< n >} = 2.9 g^{-2/11} \sigma_{\parallel}^{4/11} \left( 1 + \left( \frac{k_x}{k_y} \right)^2 \right)^{-9/44} \frac{(1 + 1.13\alpha_s - 0.01\alpha_s^2)^{9/22}}{(1 + 1.13\alpha_s - 0.01\alpha_s^2)^{9/22}} \quad (3.51)$$

$$\frac{\sigma_{\Phi}}{T_e} = 1.7 g^{7/11} \sigma_{\parallel}^{-3/11} \left( 1 + \left( \frac{k_x}{k_y} \right)^2 \right)^{-9/22} \frac{(1 + 1.13\alpha_s - 0.01\alpha_s^2)^{9/22}}{(1 + 1.14\alpha_s - 0.11\alpha_s^2)} \quad (3.52)$$

These scalings will be compared to experimental measurements in Tore Supra in the section 3.4.3.

The impact of a sheared flow on the turbulence is described by the model. The description of the interplay between these two actors is not fully predicted since we do not predict the impact of the flow generation by the turbulence on rotation profile establishment. This key point will be the topic of the following section (section 3.2.3).

### 3.2.3 Poloidal momentum conservation

The radial shear of the poloidal rotation is at the origin of the turbulence mitigation. The shape of the radial profile of poloidal velocity results from the competition of different contributions as mentioned in the introduction of this manuscript (section 1.8). The turbulent contribution in the poloidal momentum conservation equation is deduced from the Reynolds stress predictions of the SSF model.

This contribution can be decomposed in two parts corresponding to the two structure tilt sources : the magnetic shear and the background velocity shear. The magnetic shear effect is a 3D effect which will be averaged in the parallel direction in order to be included in the model.

### 3.2.3.1 Field line average of magnetic shear tilt

In order to understand the impact of the magnetic shear on the turbulence, we describe the behaviour of a flux-tube tilted by the magnetic shear. We will consider flux-tube at the midplane of the low-field side with a circular poloidal cross-section. Following this flux-tube in the parallel direction will lead to different interceptions of the flux-tube with the poloidal plasma cross-section. The more we move off the mid-plane, the more the flux-tube will appear tilted (see figure 3.5). This effect being a 3D effect, it has to be averaged on the parallel direction to be included in the model.

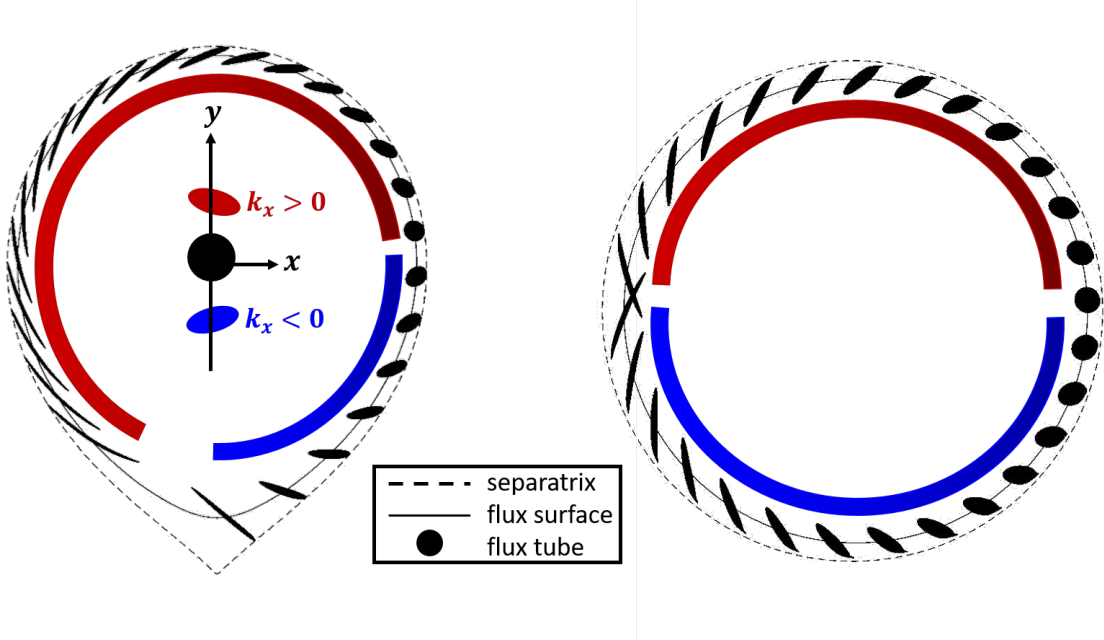


Figure 3.5: Impact of the magnetic shear on a flux tube in diverted geometry as used in [177] (left) and circular geometry (right)

In the case of an inner-wall limited circular discharge, the tilting of the flux-tubes are symmetric up-down. The parallel average of this contribution, which can be approximated by a poloidal average, will result null. The equivalence between parallel and poloidal average neglects the difference of magnetic field amplitude between the low and the high field side leading to more toroidal field lines close

to the high field side and consequently to a longer field line length in this region. This effect being of the order of the aspect ratio  $\epsilon = \frac{a}{R}$ , we will neglect it in the following work. In the case of a circular bottom-limited discharge, the average will result in a positive mean value of the tilt. The opposite result occurs in the symmetric configuration with an upper limiter. This point is more visible in diverted configuration where the symmetry is broken by the presence of the X-point. The poloidal average has to be weighted by the turbulence poloidal envelope. The ballooning feature of the turbulence can be approximated by a Gaussian envelope of width  $\Delta\theta \approx 50^\circ$  [178].

The obtained averaged value gives an effective magnetic tilt of the structures which is introduced in the radial wavenumber  $\theta_x^0$  in the SSF model. This wavenumber will be a source of Reynolds tensor which will be introduced in the flow generation model. Interestingly, the X-point position is responsible of the sign of the averaged radial wavenumber. This value will compete with the radial wavenumber created by the sheared flow. In the case of a favourable configuration, both effects add whereas in the opposite configuration they are opposite. This model of flow generation will be included in a 1D transport developed during this work.

### 3.2.3.2 A 1D transport code with sheared flows : 1DCIS (1D Code for Interchange and Shear)

In order to model the radial transport in a tokamak, we derive a model of turbulent radial flux with interplay with background sheared flows. Geometrical effects have been included in the model. From all these effects a 1D model of transport of particle and energy as well as a poloidal momentum conservation is built.

$$\partial_t n + \nabla_r (\Gamma_r n) = S_N - \sigma_{\parallel} f_{\sigma} n \quad (3.53)$$

$$\partial_t 3neT + \nabla_r (\Gamma_r 3neT) = Q - \gamma \sigma_{\parallel} f_{\sigma} 3neT \quad (3.54)$$

$$\partial_t V_{E \times B} + \nabla_r \Pi = -(\nu - \chi_{diff} \partial_r^2) (V_{E \times B} - k_{\theta} V_{*}) - \chi_{SOL} f_{\chi} (V_{E \times B} - V_{E \times B}^{SOL}) \quad (3.55)$$

where  $S_N$  is the particle source,  $Q$  is the heat source,  $\sigma_{\parallel}$  is the loss rate through the sheath,  $f_{\sigma}$  is the radial envelope of the parallel losses,  $\gamma = 5 + 2.5 \frac{T_i}{T_e} = 7.5$  is the sheath exhaust factor,  $\nu$  is the restoring force towards the neoclassical

prediction of the rotation,  $k_\theta$  is the restoring coefficient towards the diamagnetic velocity,  $\chi_{diff}$  is a viscous coefficient for viscous breaking due to small scale effects,  $\chi_{SOL}$  is a restoring force towards the rotation imposed by the sheath  $V_{E \times B}^{SOL} = \frac{-\Lambda \partial_r T}{B}$  and  $f_\chi$  is the radial envelope of this restoring force. The radial flux  $\Gamma_r$  and the Reynolds tensor are estimated from the SSF model prediction at all the radial positions. In this study, we only consider convective flux. This is consistent with the assumption of neglecting temperature fluctuations. On the other hand, such fluctuations can highly contribute to the heat transport in the closed flux region. Applying this flux model in the closed field lines can be discussed, as it will be in the discussion section of this chapter, but considering mode interferences in the high field side (as observed in the left panel of figure 3.5), we can assume that the parallel losses coefficient for the potential is comparable to the sheath one. Moreover, transport in the core can come from various instabilities. Most of these instabilities are coming from the free energy contained in the thermodynamics gradients and consequently from interchange mechanisms. The resulting flux from these instabilities would have comparable expressions as the one predicted by the SSF model. Nevertheless, this flux would be high compared to the measured one due to higher parallel losses in absence of sheath resistivity. To take it into account an envelope function  $f_g$  is added to the radial flux  $\Gamma_r$ . Another envelope  $f_k$  is attributed to the radial wavenumber induced by the magnetic shear since its non-null value comes from the X-point or the limiter presence. This model will lead to a competition between the neoclassic prediction of the rotation in the confined plasma and the turbulent flow generation.

As a first step, constant values for the neoclassical restoring force ( $\nu \approx \times 10^{-4}\omega$ ,  $k_\theta = 1$ ) have been considered in order to observe if the physics contained only in the SSF model is enough to trigger confinement transitions. Gaussian sources of particle and heat were assumed to be located at the LCFS and in the core respectively. Parabolic safety factor profiles are considered with a value of 1 at the magnetic axis. The resulting magnetic shear is constant radially with a value of  $s = \frac{r}{q} \frac{\partial q}{\partial r} = 2$ . We also neglected the momentum diffusion and imposed the parallel losses envelop equal to the SOL restoring force in the rotation equation. The machine and global plasma parameters have been taken from WEST features. Radial profiles of the envelope functions and sources are shown in figure 3.6. To understand the impact of the plasma parameters as density, magnetic field am-

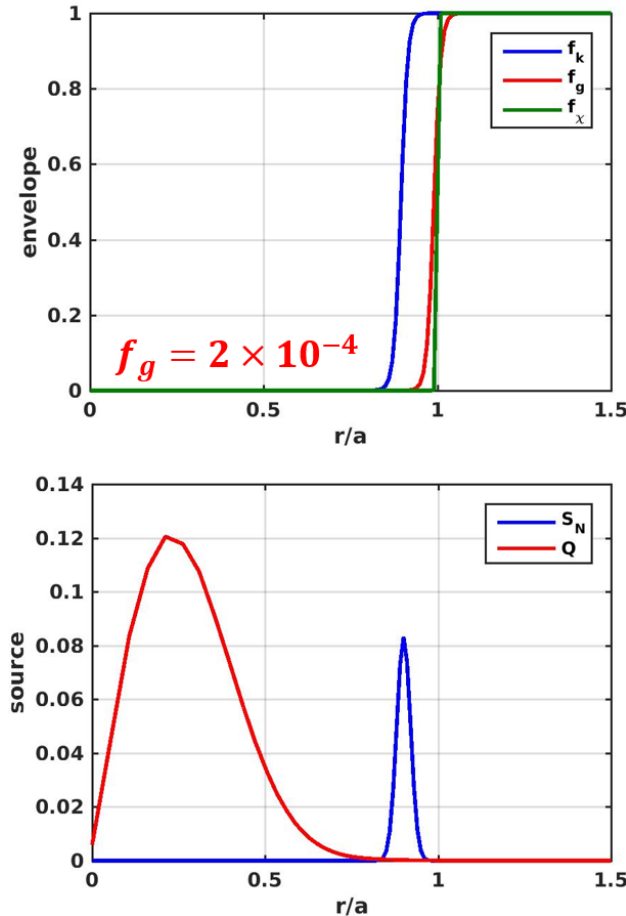


Figure 3.6: Radial profiles of the envelope functions (top) and the sources input to the 1DCIS code.

plitude, injected power and magnetic geometry, we managed scans using three values of line averaged density  $[2.5 - 3.5 - 4.5] \times 10^{19} m^{-2}$ , three values of magnetic field amplitude and six values of injected power  $[0 - 1 - 2 - 3 - 4 - 5] MW$ . The geometry has been varied in terms of X-point position : top, bottom and no X-point were considered. The density control is comparable to the one used in experiment, systematic controls of the line averaged density applied at constant time interval lead to a correction of the fuelling. So far, no model of radiation is implemented in the code. Hence, the injected power is directly the one crossing the separatrix. An example of density, temperature and rotation profiles is given figure 3.7.

The non consideration of the shear width in the approach applied here leads to an overestimation of the structure tilt in the pedestal. This approximation leads to an overestimation of the flow generation by the turbulence and of the shear impact on the turbulent flux. Nevertheless, this model was not able to demon-

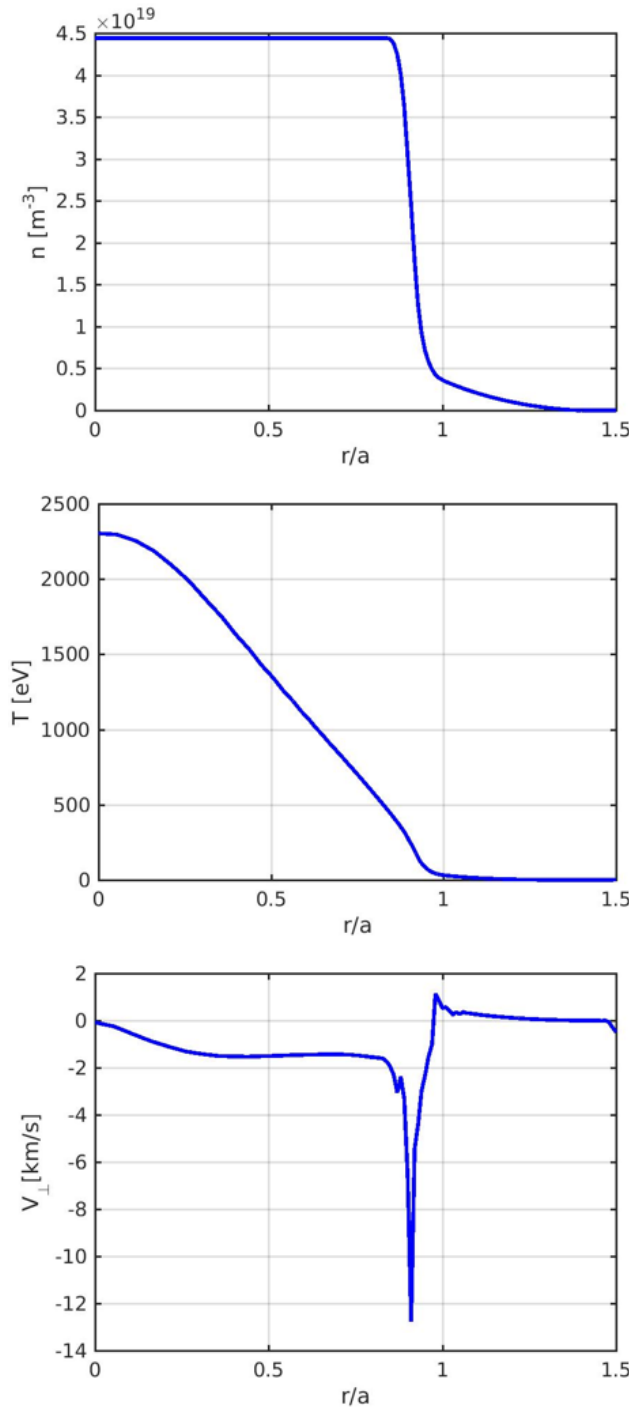


Figure 3.7: Radial profiles of the density (top), the temperature (middle) and the rotation (bottom) from a 1DCIS simulation. Case  $n_l = 3.5 \times 10^{-19} m^{-2}$ ,  $P_{inj} = 1 MW$ ,  $B = 3.7T$ , LSN configuration.

strate confinement regime transitions unlike in [126]. This model is comparable to the one developed in [54, 55]. This work showed transitions considering the neoclassical restoring force mentioned above. The radial gradient of neoclassical prediction could be necessary to induce strong rotation gradient at the edge

and generate confinement transition.

### 3.3 Verification of the model with TOKAM2D simulations

The SSF model aims at describing the edge transport by reducing the equations of interchange turbulence behaviour. It has to be verified against numerical simulations to check if it recovers the underlying physics. To that end, we ran isothermal flux-driven numerical simulations of the TOKAM2D equations with a finite elements code. In this section, we present the databases built for the verification of the model. Then, we detail the quantities used to verify the model which are the density decay lengths, the time averaged turbulent spectra, the fluctuation levels and the structure tilts. Finally, a comparison of the model predictions with the simulation results is discussed.

#### 3.3.1 Databases from TOKAM2D simulations

We built 2 databases, one including 9 cases without shear with parameters in the range of typical Tore Supra SOL parameters ( $g \in [0.1 - 10] \times 10^{-4}$  /  $\sigma_{\parallel} \in [0.1 - 10] \times 10^{-5}$ ), and one with homogeneous background shear with shear rates up to  $\sigma_s = 6 \times 10^{-3}$  corresponding to variations of velocity of a few kilometres per second on a radial distance of a centimetre. The code was not able to sustain simulations of higher shear rates with reasonable time steps. This shear is imposed by a parabolic profile of potential centred in the centre of the simulation box  $x_0$ . This second database contains 17 simulations with 4 different pairs of turbulence parameters  $[g, \sigma_{\parallel}]$ . The parameters of the simulations are summarised in table 3.1. The time is normalised to the ion cyclotron frequency. The radial and poloidal resolution normalised to the ion Larmor radius are fixed to  $\Delta_x = \Delta_y = 1$  and the box size is  $N_x \times N_y = 512 \times 256$ . The diffusion and viscous coefficients normalised to the Bohm diffusion coefficient  $D_B = \rho_s C_s$  are fixed to  $D_n = \nu = 1 \times 10^{-4}$  in order to avoid perturbations at the turbulent scales of interest ( $k_y < 3k_0$ ). This point is verified in Appendix C. The poloidal direction is periodic. A buffer zone is situated at the high radial position boundary of the simulation box. This layer is thin enough ( $\delta_{buff} = 10$ ) to not disturb the simulation results. The particle source is a Gaussian curve of width  $\delta_S = 8$  centred in  $x = 10$ .

$g[\times 10^{-4}]$	$\sigma_{\parallel}[\times 10^{-4}]$	$g[\times 10^{-4}]$	$\sigma_{\parallel}[\times 10^{-4}]$	$\sigma_s[\times 10^{-4}]$	color
40	5	8	1	0; 2.5; 5; 10; 15; 20; 30; 40	blue
8	1	1.2	0.28	0; 2.22; 4.44 ; 8.9; 13.37; 17.8	red
1.2	0.28	1.1	0.11	17.5; 25	green
1.1	0.11	1.1	0.35	63	magenta
2.6	0.35	2.6	0.35		
2	0.2	2	0.5		
2.6	1.05				

Table 3.1: TOKAM2D control parameters used to build the databases without shear (left) and with homogeneous shear (right). The color column stands for the colors of the markers of the parameter pairs  $(g, \sigma_{\parallel})$  which will be used during the comparison with the model predictions.

The simulations result in 2D maps of density and electrostatic potential exhibiting turbulent features which are tilted in presence of a background sheared flow (see figure 3.8). These mushroom-like structures result from interchange driving and move along the density gradient. These structures seem to exhibit a dominant size which adds a motivation to build a spectral model able to describe the features of a mode corresponding to this poloidal size.

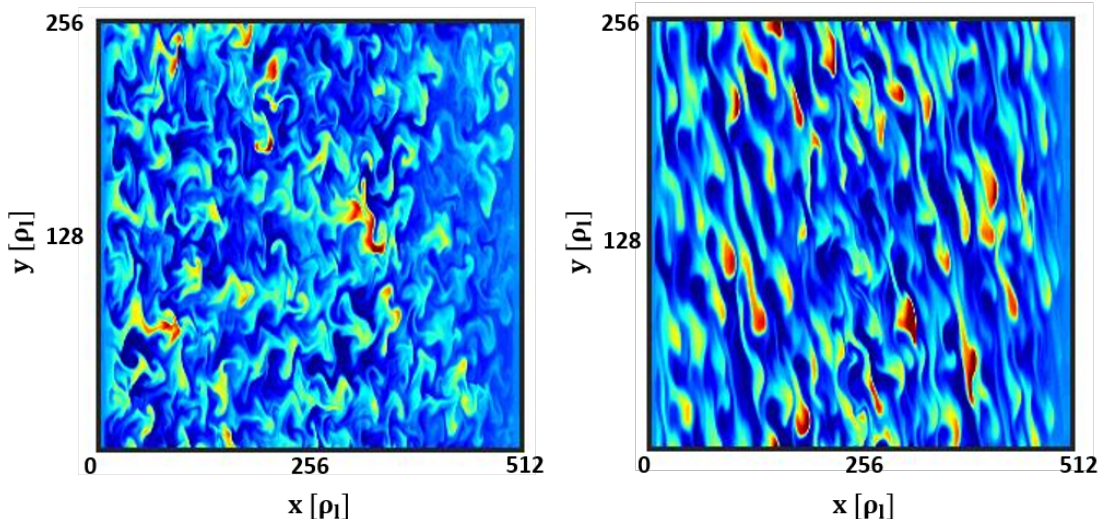


Figure 3.8: Snapshot of the density fluctuations from TOKAM2D simulation without background shear (left) and in presence of a background homogeneous shear (right)

From these 2D maps we extracted comparison points in order to verify the model

predictions as it is detailed in Appendix D. The quantities measured to verify the model predictions are :

- the **radial particle flux**  $\Gamma_r$
- the **density exponentially decaying length**  $\lambda$
- the **structure tilt** induced by the background shear flows  $\frac{k_x}{k_y}$
- the **poloidal spectra** of the electrostatic potential  $\Phi_k$  and the density  $n_k$
- the **fluctuation levels** of the density  $\sigma_n/\langle n \rangle$  and the potential  $\sigma_\Phi/\langle T_e \rangle$

### 3.3.2 Comparison of the model predictions with the simulation results

The model verification against the simulation results will be done step by step. First, we will focus on the database of simulations without background shear and then, on the one with homogeneous background shear. The comparison between model predictions and without shear simulations will start with comparisons of the model with dominant mode properties. The comparison of the predictions of the transport observables, i. e. the fluctuation levels and SOL density decay lengths, will follow right after. Next, the verification of the SSF model in the case of homogeneous background shear will start with a point on the mode tilting model. Once this point verified, we will interest in the spectra and more particularly in the properties of the dominant mode. Finally, we will compare the predictions with the measured fluctuation levels, radial particle flux and scrape-off layer width.

#### 3.3.2.1 Database without sheared flows against SF model predictions

Figure 3.9 summarises the comparison between the model predictions and the simulation results for the dominant mode features, the fluctuation levels and the density decay length. First of all, we can see that the dominant mode features are quantitatively matched against the overall database. This deeper verify the observations of figure 3.2.

This quantitative agreement between the model predictions and the simulation results is also verified for the fluctuation levels and the density decay length over

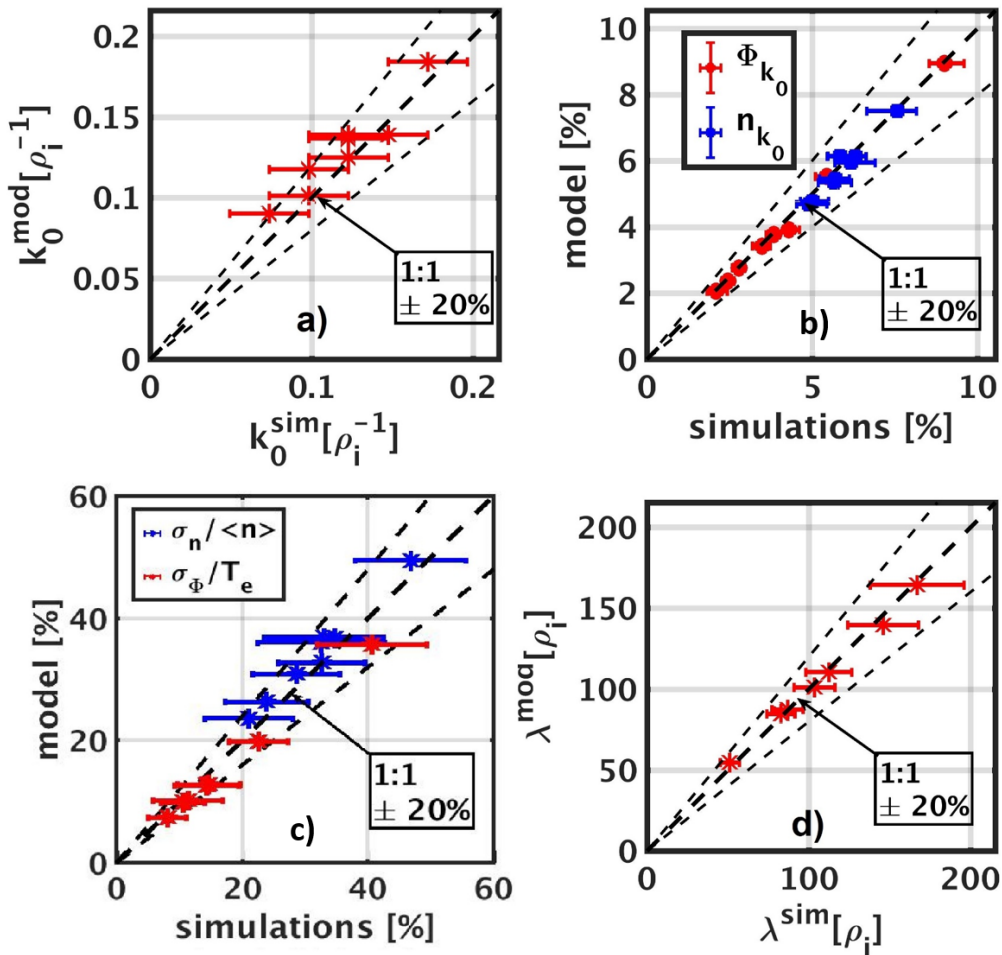


Figure 3.9: Comparison between the model predictions and the simulation results for a) the dominant wavenumber value, b) the dominant wavenumber potential and density perturbation amplitude, c) the potential and density fluctuation levels and d) the density decay length.

the whole database. The SF model is verified against experimentally relevant sets of control parameters ( $g, \sigma_{\parallel}$ ).

### 3.3.2.2 Database with homogeneous background sheared flows against SSF model predictions

In the study of the turbulence plunged in a background sheared flow, all the predictions rely on the description of the structure/mode tilt. This first step is addressed by the model of interchange restoring leading to a constant tilt. A comparison of the model predictions against the values measured in the simulations is given figure 3.10. We observe a quantitative agreement of the simulation results with the model predictions. The radial phase variation method

gives slightly higher values of the tilt than the model predictions and the 2D FFT method. Interestingly, low tilt values are more difficult to measure leading to a slight overestimation by the model. Nevertheless, the agreement remains sound against the overall database.

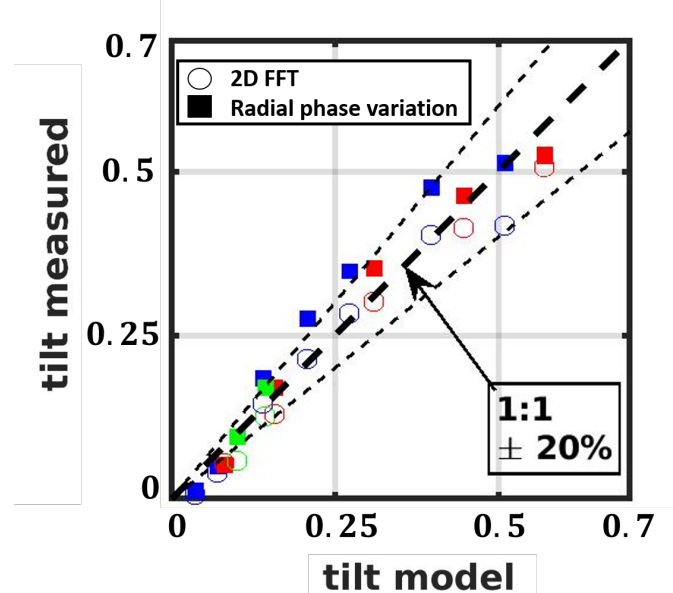


Figure 3.10: Comparison between the model predictions and the simulation results for the mode tilt. Colors correspond to different pairs of  $(g, \sigma_{\parallel})$  from table 3.1. Empty dots are obtained from the FFT2D method and the full squares from the radial phase variation.

The mode tilts will play a role in the spectral model through 2 mechanisms : 1) the lowering of the potential and density spectra due to energy spreading over the  $k_x$  values and 2) the flow generation through the Reynolds tensor. The first effect is stronger on the potential spectra than on the density ones due to the cross dependencies of the spectrum and the density decay length in the tilt of the modes. This is recovered in the simulations as observed on figure 3.11.

A comparison of the spectral properties predictions against the whole database is given figure 3.12. The model predictions are in quantitative agreement with the simulations recovering 1) the shift of the dominant wave number towards the low values, 2) the lowering of the amplitudes of the density and potential perturbations, 3) the decrease of the density decay length and 4) the density and potential fluctuation levels decrease. Strikingly, the density perturbations of the dominant mode as well as the density fluctuation level do not depends much on the shear rate amplitude. This is a consequence of the low dependency of the density spectra with the tilt of the structures.

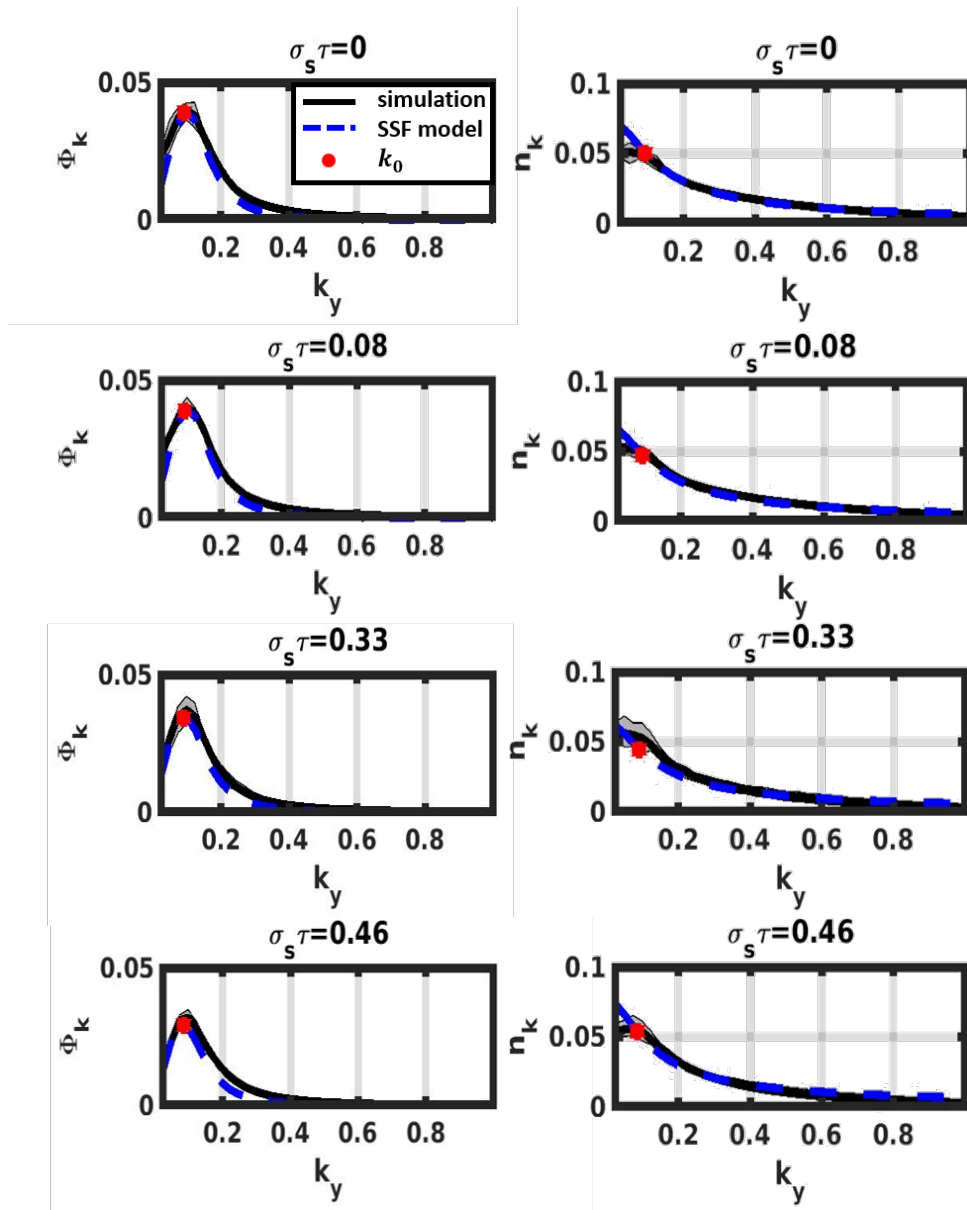


Figure 3.11: *Left* : potential spectra at different background shear rates. *Right* : density spectra at different background shear rates. Full black lines stand for simulation results, blue dashed lines for model predictions and the red dots are the model predictions at the dominant wavenumber  $k_0$ . Case [ $g = 8 \times 10^{-4}$ ,  $\sigma_{\parallel} = 1 \times 10^{-4}$ ].

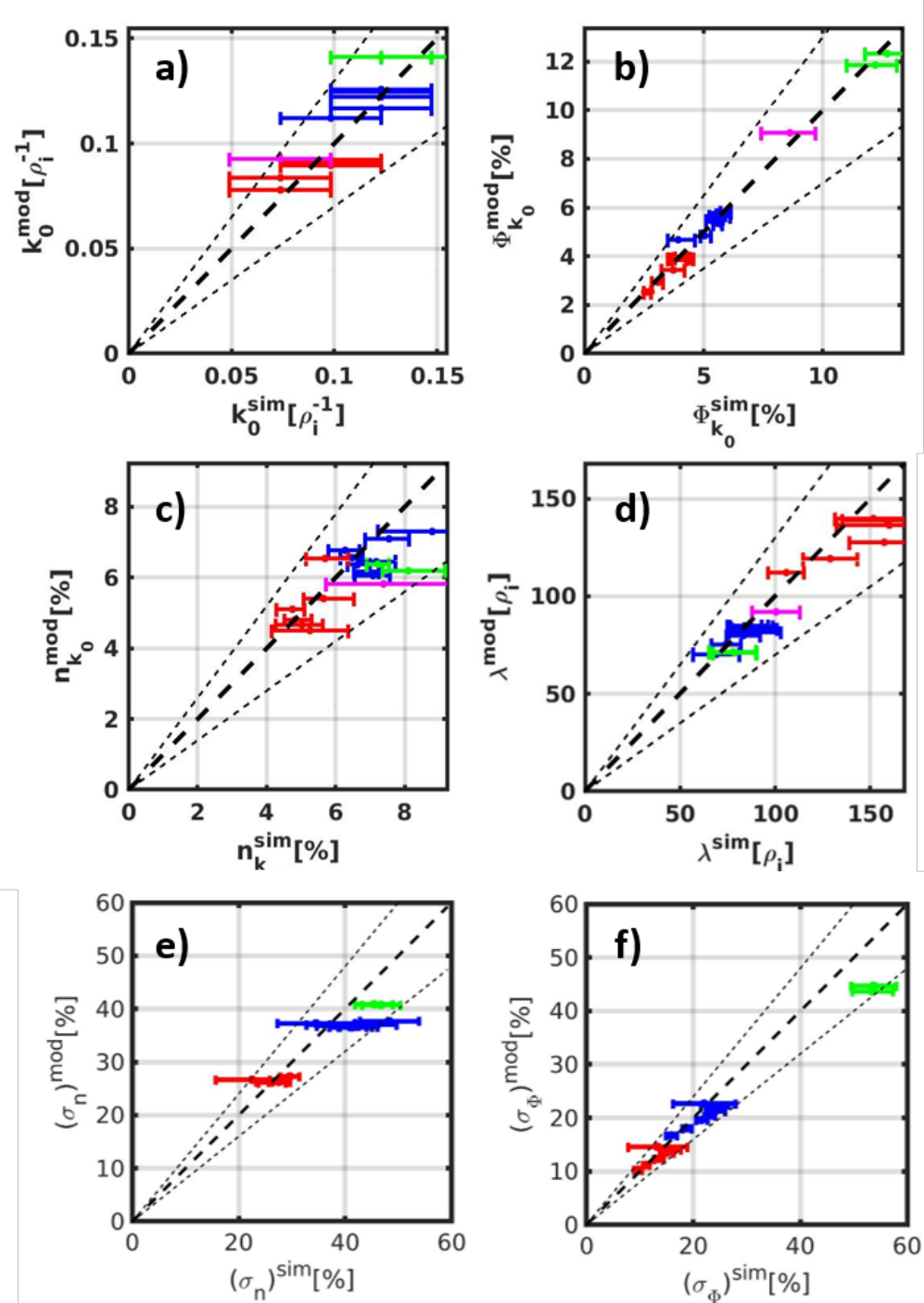


Figure 3.12: Comparison between the model predictions and the simulation results for a) the dominant mode wavenumber  $k_0$ , b) the potential perturbation at the dominant wavenumber  $\Phi_{k_0}$ , c) the density perturbation at the dominant wavenumber, d) the density decay length  $\lambda$ , e) the density fluctuation level  $\sigma_n$  and f) the potential fluctuation level  $\sigma_{\Phi}$ . Color corresponds to different pairs of  $(g, \sigma_{\parallel})$  from table 3.1.

Finally, a comparison of the measured flux normalised to the prediction of the flux in the case without shear  $\Gamma_{mod}^{ws}$  evolution with the mode tilt  $\sigma_s \tau$  with the scaling (3.50) emphasises the ability of the model to predict the turbulent particle flux in the presence of a background sheared flow (see figure 3.13).

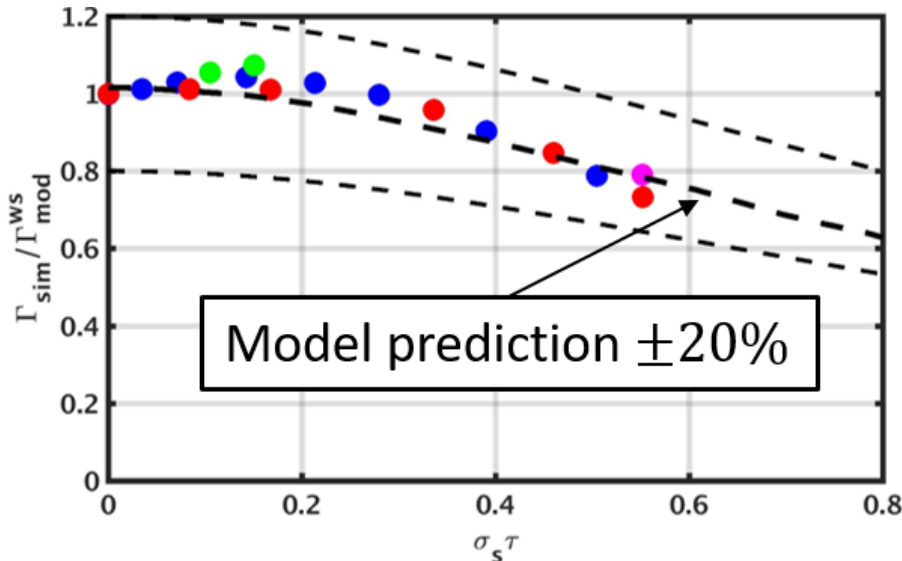


Figure 3.13: Comparison between the model predictions and the simulation results for radial flux normalised to the prediction of the flux in the case without shear  $\Gamma_{mod}^{ws}$ . Colors corresponds to different pairs of  $(g, \sigma_{||})$  from table 3.1.

These analytical predictions for the flux, density decay length, turbulence features and fluctuation levels lead to instantaneous values which presents an interesting advantage regarding the running time of simulations. Indeed, to build-up the database used to verify the model predictions, around 25000 hours of calculations have been used (this estimation does not take into account the simulations which failed).

### 3.4 Validation of the SSF model against experimental measurements

The verification of the SSF model against TOKAM2D simulations showed the ability of the model to capture the underlying physics contained in this conservation system. In order to validate the model predictions against experimental data, we need to express the control parameters  $(g, \sigma_{||})$  in terms of plasma and device parameters. This will be detailed in this section. Then a validation against measurement will be presented in 3 steps : 1) a validation of the spectral model

with spectra measured in the TJ-K torsatron, 2) a validation of the turbulence and transport observable predictions against Tore Supra Langmuir probes measurements and 3) a validation of the flow generation model against measurement in WEST.

### 3.4.1 Expressions of the control parameters ( $g$ , $\sigma_{\parallel}$ ) as functions of plasma parameters

In order to compare the model predictions with experimental measurements, we need to express the control parameters  $g$  and  $\sigma_{\parallel}$  in terms of plasma parameters. The curvature drive coefficient  $g$  is a consequence of the magnetic field curvature and depends on the scalar product of the gradient of magnetic field (major radius direction) and the orientation of the density (or pressure) gradient (structure orientation  $\vec{e}_{struct}$ )  $g = \vec{\nabla}B \cdot \vec{e}_{struct}$ . In the case of structures with circular poloidal cross sections, the direction of the structure orientation corresponds to the vector normal to the flux surfaces. As a consequence, the field line averaged curvature parameter can be written as  $g = <\frac{2\rho_s \cos(\theta)}{R}>_{\theta}$ . Nevertheless, due to magnetic shear the structures are tilted and the orientation vector is depending on the poloidal angle  $\theta$ . For a circular plasma, assuming that the Shafranov shift does not strongly impact the safety factor profile, the safety factor radial profile is parabolic. It results in a magnetic shear  $\hat{s}$  which is homogeneous all over the plasma and has a value of 2. The scalar product between the density and magnetic field gradients introduced in the curvature parameter results in  $g = <\frac{2\rho_s \cos(\theta - \arctan(\hat{s}\theta))}{R}>_{\theta} \approx 1.5 \frac{\rho_s}{R}$  (see figure 3.14).

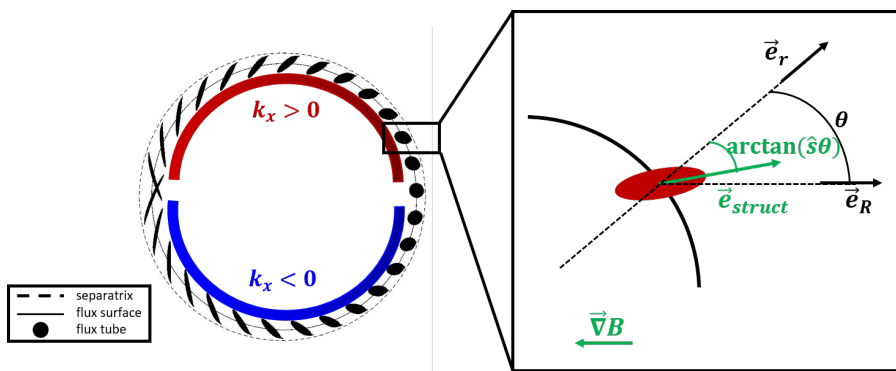


Figure 3.14: Scheme of the scalar product between the density and magnetic field gradient in a circular geometry

The parallel loss rate is given by the reconnection length  $L_{\parallel} \propto qR$  as detailed in

the introduction of the manuscript. In the case of an inner-wall limited discharge, this reconnection length corresponds to  $\pi qR$ . In consequence, both control parameters can be written as a coefficient times the ratio of the Larmor radius over the major radius of the considered device. Measuring the temperature allows to estimate the local Larmor radius and consequently calculate the control parameters.

$$g = \frac{1.5\rho_s}{R} = \frac{1.5}{RB} \frac{\sqrt{Am_p T_e (1 + T_i/T_e)}}{Ze} \quad (3.56)$$

$$\sigma_{\parallel} = \frac{\rho_s}{\pi q R} = \frac{1}{\pi q RB} \frac{\sqrt{Am_p T_e (1 + T_i/T_e)}}{Ze} \quad (3.57)$$

where  $Z$  is the ionisation degree,  $A$  is the nuclei number of the main species and  $m_p$  is the proton mass.

### 3.4.2 Validation of the spectral model against TJ-K probe measurements

The SF model is based on the prediction of the density and potential poloidal spectra. In practice, these spectra are not measurable in most of the tokamaks since it requires setup of arrays poloidally distributed and aligned on a flux surface. In addition, to measure it at the separatrix, the probes have to sustain hot temperatures and fluxes which can damage the probes. The TJ-K torsatron is a low magnetic field and low temperature device allowing to plunge probes deep into the plasma. A poloidal array of Langmuir probes designed to measure all around a flux surface is implemented (see figure 3.15) [179].

One probe over two is polarised in saturation regime and the others are polarised in floating regimes. It allows to measure both floating potential and normalised saturation current poloidal spectra. The later one can be associated to the density spectrum. The distance between two consecutive probes is 8mm. Consequently, two floating probes are separated from 16mm. The electron temperature is measured independently and is of the order of 10eV. The plasma being cold, we made the approximation of cold ions ( $T_i = 0$ ) to apply the model. No sheared flows are consider in the model applied to the data because no clear evidence of presence of such flows in the data has been observed. The safety factor considered here is the inverse of the rotational transform  $\iota$  of

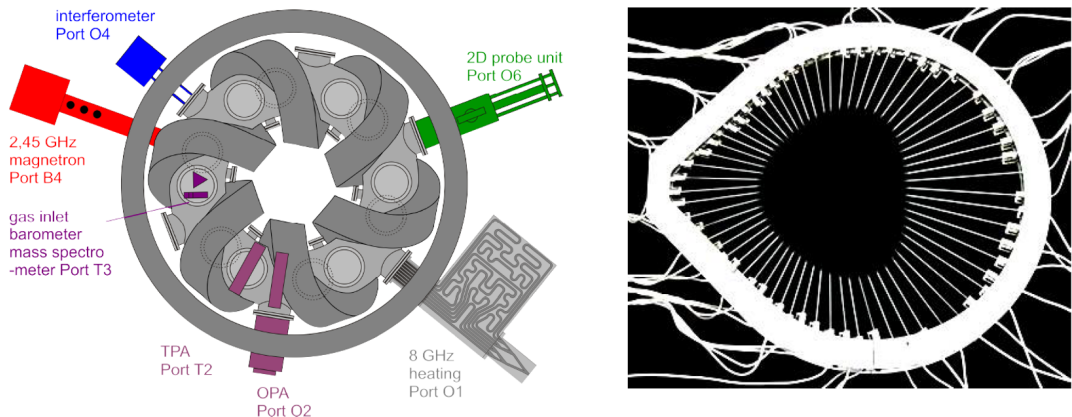


Figure 3.15: *Left* : Representation of the TJ-K torsatron. *Right* : Representation of the poloidal array of probes implemented in TJ-K.

the discharge. Table 3.2 summarises the plasma parameters of the selected measurements.

$R[m]$	$a[m]$	$q$	$B[mT]$	$T_e[eV]$	$g[\times 10^{-4}]$	$\sigma_{\parallel}[\times 10^{-4}]$
0.64	0.2	4	81.4	9	83	6.6

Table 3.2: Table of the plasma parameters of the selected shot in TJ-K

The spectra are extracted from the raw signal following the same data processing as for the simulation, namely poloidal spectra are averaged in time. A comparison between the predicted poloidal spectra of potential, density and phase shift and the experimental data is given figure 3.16 without normalising the experimental data. Strikingly, the model predictions recover the spectra shapes and amplitudes for the potential and density spectra. The Isolated Filament model seems to recover better the shape of the spectra for the high wavenumbers. It could indicate that the interaction of the modes with the dominant mode is negligible compared to the saturation due to inertia limitations of the modes. Nevertheless, both Spectral and Isolated filament models are able to describe the behaviour of the modes around the dominant mode. Interestingly, the density spectra predictions overestimates the measured contributions of low wavenumbers as it is also the case in the simulation results. In consequence, we can consider that TOKAM2D would be able to recover these experimental spectra. Finally, the phase shift between density and potential modes is close to  $\pi/2$ , at least for the modes around the dominant wavenumber. This further validates the ideal phase shift assumption. It is worth noting that the measurement presented

here were managed in the confined plasma at 15mm from the separatrix. This point seems to validate the assumption of considering reconnection lengths as parallel dynamics description. Moreover, during other experiments, the spectra shape appeared similar to the one observed here [180]. Consequently, to go further in the validation of the model, a database of TJ-K probe array measurement should be built in order to compare to model predictions.

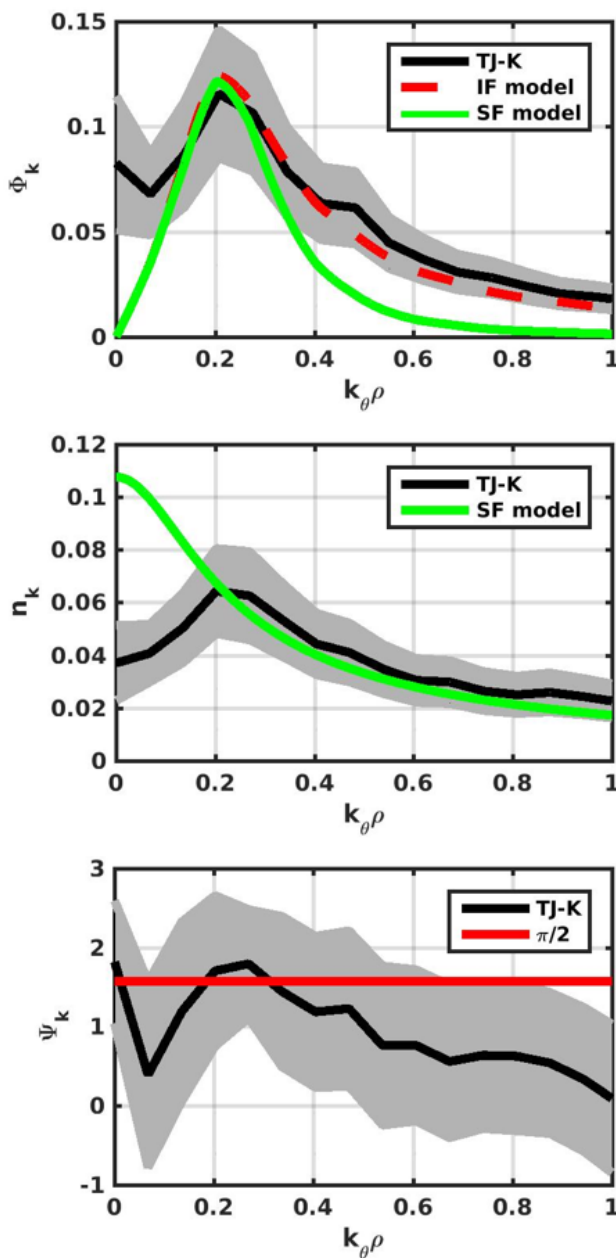


Figure 3.16: Poloidal spectra of the potential (top), the density (middle) and the phase shift between the potential and density (bottom) measured in TJK (black line and grey error bars) compared to model predictions.

### 3.4.3 Validation of the turbulence features and transport observables predictions against Tore Supra probe measurement

The next step of the validation of the SF model is the comparison of the turbulence features and the transport observable predictions against the measured one. The experimental characterisation of the turbulent properties and of the transport observable has been detailed in the previous chapter in section 2.1. No shear will be considered here because of the wideness of the temperature profiles ( $\lambda_{T_e} \approx 15\text{cm}$ ).

First, a comparison of the turbulence characteristic wavenumber and its radial velocity from  $E \times B$  convection obtained from rake probe measurements in Tore Supra against predictions of the dominant wavenumber and its velocity results in a sound agreement (see figure 3.17). It is worth noting that the model predicts time averaged mode features and not intermittent structure properties. This would indicate that the main turbulence features come from the dominant mode ones. The variation range of the measured wavenumber appears narrow (from  $5\rho_s^{-1}$  to  $10\rho_s^{-1}$  which is much lower than an order of magnitude). This would be expected from the low dependencies of the mode wavenumber with the plasma parameters as predicted by the SF model.

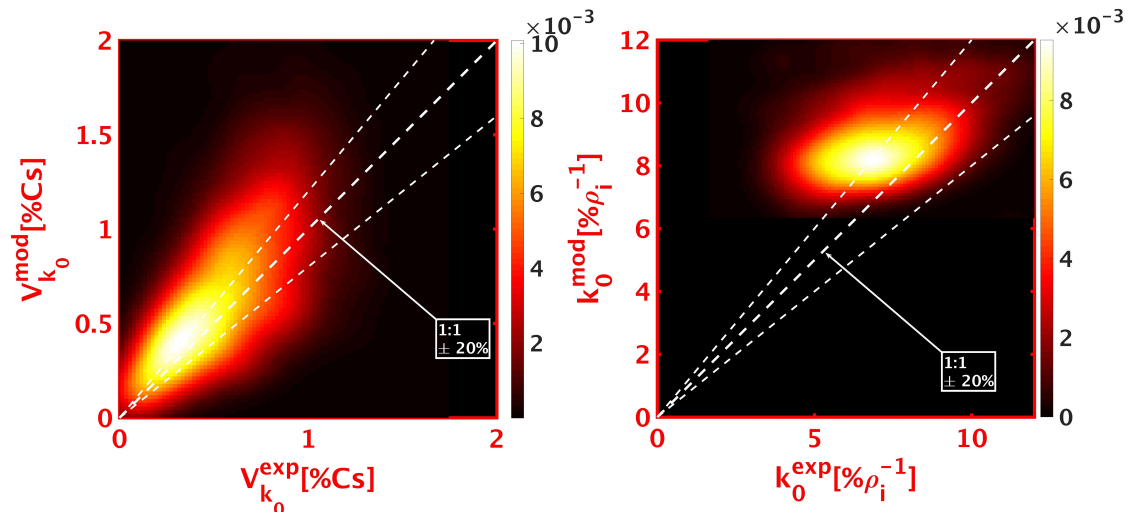


Figure 3.17: Comparison between the model predictions and the experimental measurements in Tore Supra of the dominant poloidal mode (right) and its velocity (left). The colormap represents the data point concentration.

The ability of the model to predict characteristic transport properties is further validated by the comparison of the inverse of the poloidal correlation length against the dominant mode wavenumber. Figure 3.18 illustrates this quantitative agreement.

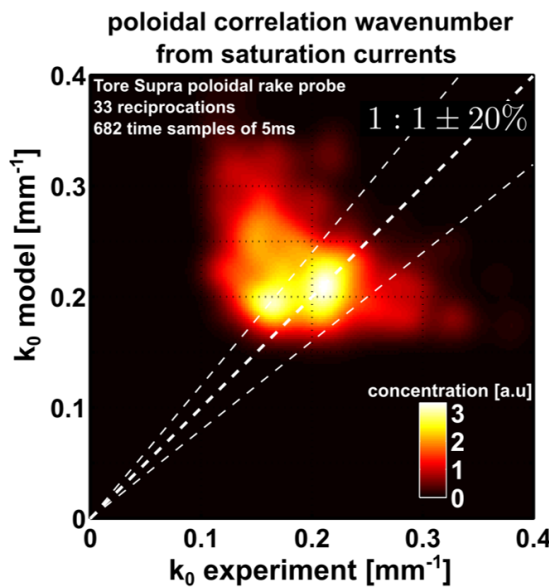


Figure 3.18: Comparison between the model predictions and the experimental measurements in Tore Supra of the dominant poloidal mode and the poloidal correlation length.

The next comparison concerns the transport observables, namely the potential and density fluctuation levels as well as the density decay length. Again, a quantitative agreement between the model predictions and the measurements is found except for the potential fluctuation level which is slightly underestimated by the model (around 15% of underestimation). This could be explained by a contribution of the electron temperature fluctuations to the total floating potential fluctuation level.

This validation against Tore Supra measurements is realised in circular limited discharges. In this configuration, plasma shaping effects could be considered negligible. A discussion about the comparison of the model predictions and experimental observations in diverted geometry is detailed later in this manuscript (section 4.1).

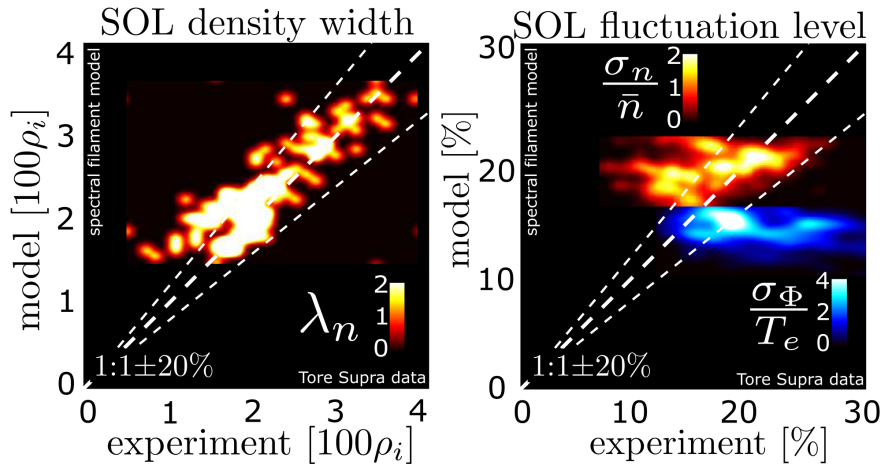


Figure 3.19: Comparison between the model predictions and the experimental measurements in Tore Supra of the density decay length (left) and the fluctuation levels of the density and of the electrostatic potential (right).

### 3.4.4 Validation of the flow generation predictions against WEST DBS measurement

The impact of the geometry on the edge rotation profiles in WEST has been observed experimentally (see section 2.2.5.2). The favourable configuration (LSN) exhibits a well in the rotation profile whereas it is not the case in the unfavourable configuration (USN). This discrepancy is blurred when the plasma current is increased. We propose an explanation of this phenomenon based on the poloidal momentum conservation including the Reynolds tensor predictions from the SSF model. To reconstruct rotation profiles from the model predictions, electron and ion temperatures are needed. Unfortunately, these physical quantities are not measured in the area of interest ( $0.8 < \rho < 1$ ). To palliate this lack, we estimated these profiles from other measurements and assumptions. First we consider modified hyperbolic tangents for the temperatures profile shapes with 4 parameters per species : the pedestal temperature  $T_{i,e}^0$ , the stiffness parameter  $\alpha_{i,e}$ , the pedestal position  $\rho_{i,e}^0$  and the pedestal width  $\Delta\rho_{i,e}$ .

$$T_{e,i} = T_{e,i}^0 (1 - \alpha_{i,e} (\rho - \rho_{i,e}^0)) \frac{1}{1 + e^{-\frac{2(\rho - \rho_{i,e}^0)}{\Delta\rho_{i,e}}}} \quad (3.58)$$

In order to determine these parameters we constrain the temperature profile using other diagnostics. First, the Electron Cyclotron Emission system gives the electron temperature for the normalised radial position under 0.8. The separatrix

electron temperature is given by the Langmuir probes and is the same for both configurations. Then we will assume that the velocity profile is given by the neo-classical prediction (an amplitude given by the ion diamagnetic drift but in the opposite direction) under  $\rho = 0.95$ . Using the density profile given by the fast sweep reflectometry system, it gives a constraint on the ion temperature profile. Finally, we impose a ratio of the ion over electron temperature at the separatrix to 2. The rotation profiles were arbitrarily shifted in order to impose a null rotation at the separatrix. This is done in order to minimise uncertainties on the radial position of the profiles due to separatrix position reconstruction. This process leads to the profiles given figure 3.20. The resulting reconstructed profiles are similar in both configurations. A study of the sensitivity of the reconstruction with the ratio of the ion over the electron temperature is presented in Appendix E. In this appendix, we also detail the fit of the experimental data with the reconstructed profiles.

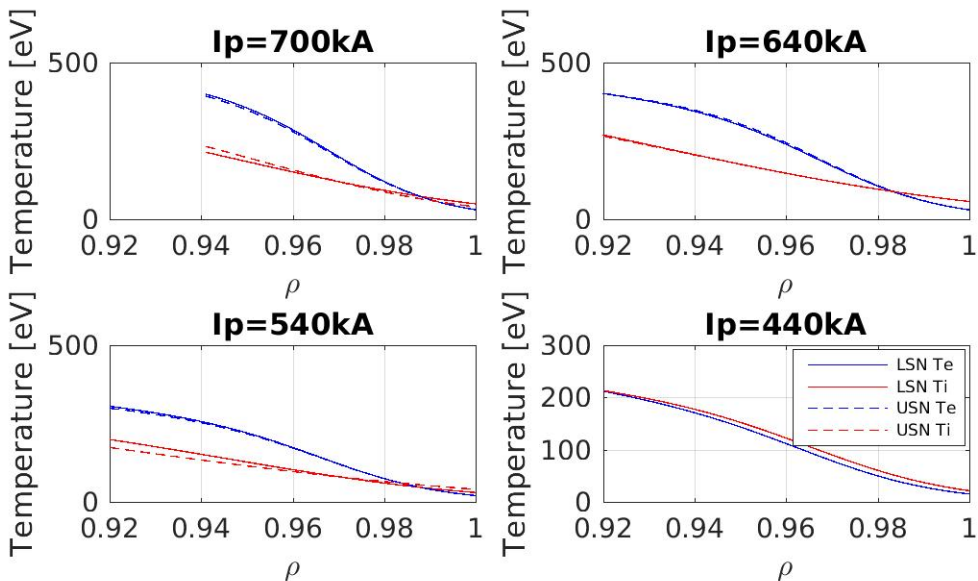


Figure 3.20: Electron (blue) and ion (red) temperature profiles reconstructed at different plasma current and in the favourable (full lines) and unfavourable (dashed lines) configurations.

Then, to calculate the structure tilt, the local shear width  $\delta_s$  has to be measured. To that end, we apply a parabolic fit ( $f = \frac{1}{2} \left( \frac{x}{\delta_s} \right)^2 + b$ ) to measure locally the parabolic width of the rotation profile  $\delta_s$  on spatial windows of width  $\delta_{rho} = 0.008$ . Finally, the last assumption consists in the profile of the tilt induced by the magnetic shear. The profile shape of this parameter is a modified hyperbolic tangent as discussed in section 3.2.3.2. We impose the position of the middle

of the pedestal of this profile as the position of the minimum of the well of the rotation profile observed in LSN. Interestingly, this position shifts slightly inwards the plasma when the plasma current decreases. This could be explained by a deeper penetration of the effect of non-null flux surface average of the mode tilt induced by the magnetic shear in lower edge gradient due to higher structure sizes and lower shearing effects which could radially decorrelate the turbulence. The width of the magnetic tilt profile remains constant between the different values of plasma current. An example of a comparison of the shear width and of the magnetic tilt between the two configurations is given figure 3.21. Taking into account these considerations and resolving the poloidal

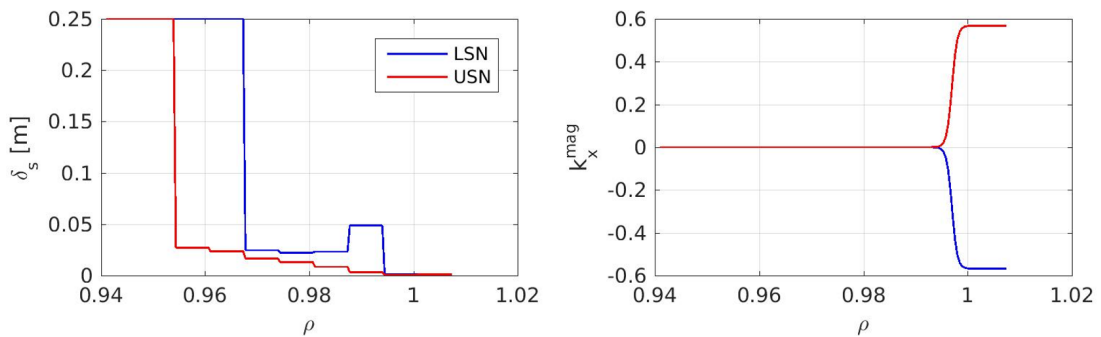


Figure 3.21: Profile of the shear width (left) and of the magnetic shear induced radial wavenumber(right) from rotation profile reconstruction for the cases at  $I_p = 700kA$ .

momentum conservation equation, we obtain the rotation profiles shown figure 3.22. This results have been obtained using the neoclassical predictions of the neoclassical restoring frequency  $\nu$ , a value of 1 for the  $K_\theta$  coefficient and a value of  $2 \times 10^{-9} m^2 s^{-1}$  for the viscosity coefficient  $\chi_{\text{diff}}$ .

Strikingly, the model recovers the discrepancy between the two configurations in terms of shape of the rotation profiles. This impact of the plasma shaping on the rotation is explained by a strong contribution of the Reynolds stress induced by the magnetic shear. An example of the Reynolds tensors coming from the magnetic shear and from the flow shear tilt is given figure 3.23. This figure shows that the major contributor to the flow generation is the radial gradient of the Reynolds stress induced by the magnetic shear (dashed lines). The opposite sign of the structure tilt induced by the magnetic shear is responsible of a slight deepening of the profile in LSN configuration and the vanish of the rotation profile well in USN seen on figure 3.22. A bump appears on USN

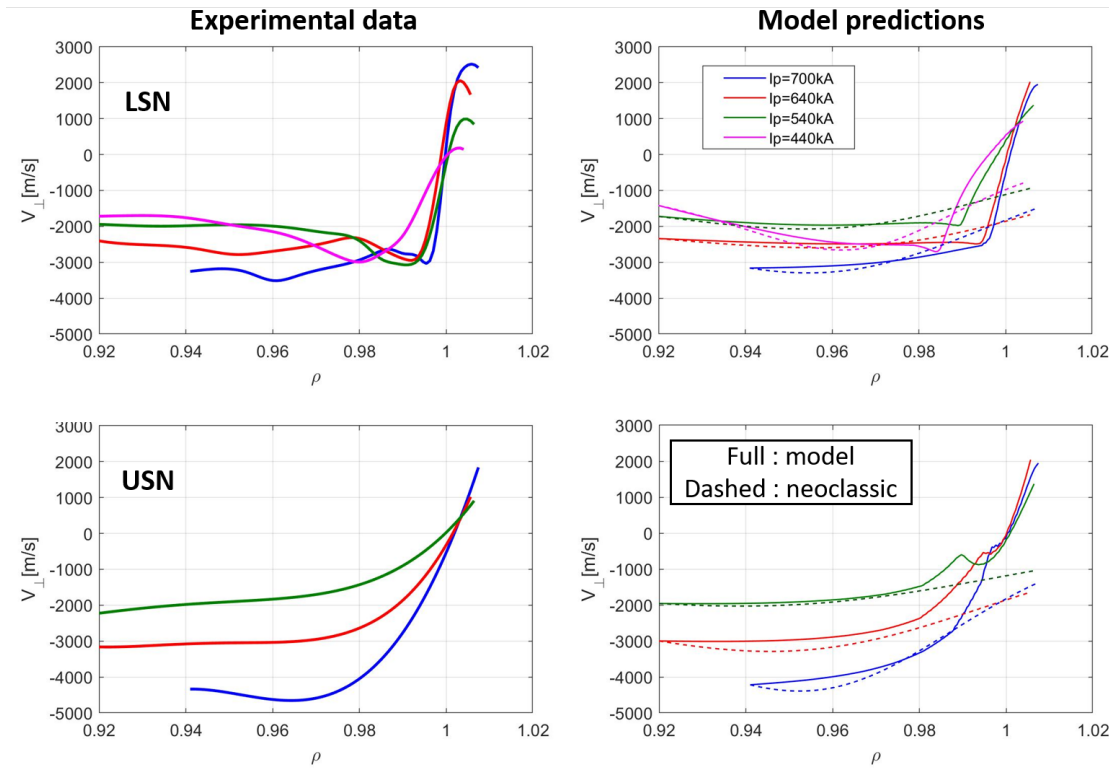


Figure 3.22: *Left* : Edge rotation profiles from DBS measurement in LSN (top) and USN (bottom) configurations (WEST #55732 and #55622 respectively). *Right* : Edge rotation profile prediction by the flow generation model. On the right plot, the full lines correspond to the model predictions and the dashed lines correspond to the neoclassical predictions.

profiles reconstruction due to the discrete evaluation of the shear width which leads to a non smooth profile of the Reynolds tensor. Unfortunately, the ion temperature profile reconstruction for the low plasma current USN case was not accurate. In consequence, no rotation profile reconstruction have been made.

The amplitude of the profiles reconstructed from the poloidal momentum conservation results from the equilibrium between the divergence of the Reynolds tensor and of the neoclassical restoring force. This is confirmed by the figure 3.24 in which we observe that the rotation generated by the Reynolds stress is damped by the viscosity to a level comparable to the neoclassical restoring force. We could interpret this viscous contribution as a lowering of the Reynolds stress which is overestimated in this study due to the underestimation of the parallel

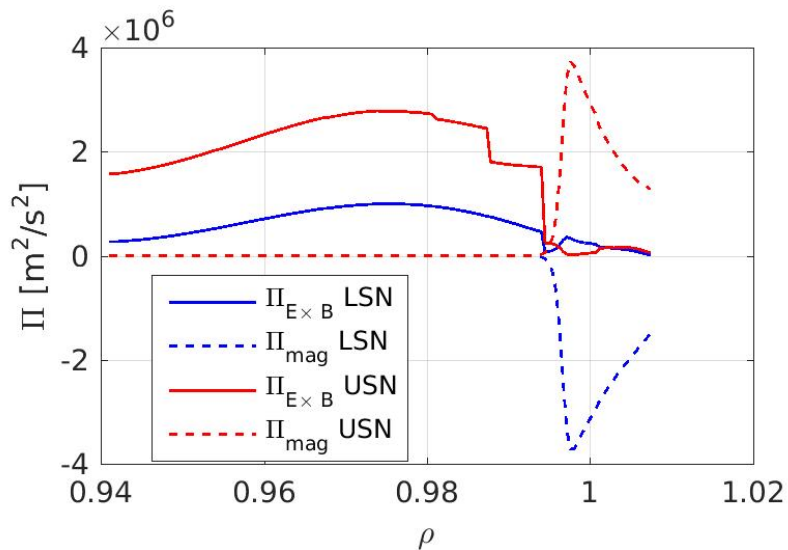


Figure 3.23: Reynolds tensor profiles for the cases at  $I_p = 700kA$ .

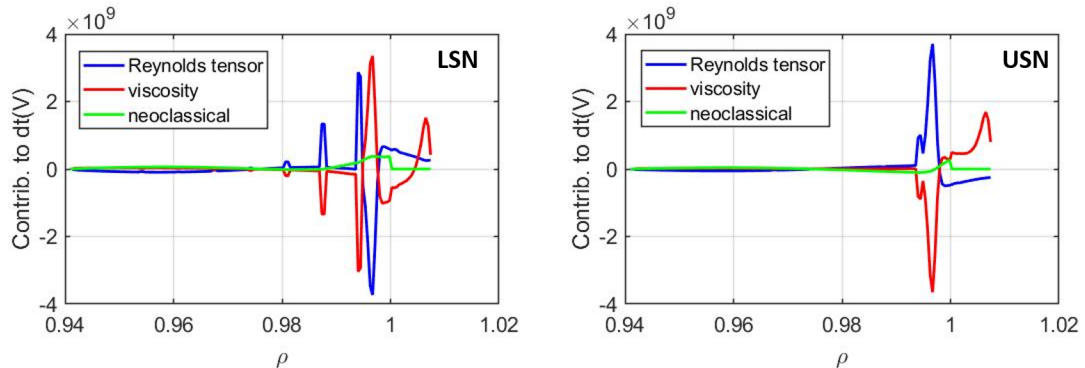


Figure 3.24: Contributions to the time evolution of the poloidal velocity (eq. 3.59) for the case  $I_p = 700kA$  in LSN configuration (left) and USN configuration (right).

losses for the electrostatic potential fluctuations.

$$\partial_t V_{E \times B} + \nabla_r \Pi = -(\nu - \chi_{diff} \partial_r^2) (V_{E \times B} - K_\theta V_*) - \chi_{SOL} f_\chi (V_{E \times B} - V_{E \times B}^{SOL}) \quad (3.59)$$

Consequently, following all of these observations, we can deduce that the shape of the tilt induced by the magnetic shear is strongly impacting the reconstructed profiles. Further investigations on the impact of the geometry on the magnetic shear tilt of the structures is discussed in the next chapter.

# **Chapter 4**

## **Discussions about the perspectives and the limits of the model**

### **Content**

---

This chapter focuses on a discussion on the model generic nature and the inclusion of more complex effects. The chapter starts on the observation of narrower SOL width in diverted geometry compared to the one observed in limited discharges. The inclusion of a plasma resistivity in the parallel dynamics description in the SOL will lead to discussions about the origin of density shoulder observations. Next, we tackle some considerations on the potential and density phase shift as well as collisionality in closed flux surfaces. Then, the magnetic topology impact on the curvature drive and the structure tilt is considered aiming at explaining the lowering of SOL width in diverted geometry. Also, the global confinement predictions from the model show an ability to recover multi-machine experimental scalings for the energy confinement time. Finally, we will present the model limits and perspectives in terms of integrated modelling.

---

A validation of the SOL model has been achieved in circular geometry. A comparison of the model predictions with reflectometry measurements of the density decay length in WEST and experimental scalings for the SOL width in L-mode and H-mode diverted discharges will be first detailed in this section. On the other hand, the model derived in this work appears generic enough to include more complex effects such as plasma shaping or collisional effects. The inclusion of these effects is presented in this chapter. The link between the spectral and the usual filament models applied to the SOL transport is discussed. The expected impacts of the electromagnetic effects on the model are also presented. An extrapolation of the flux model to the prediction of the energy confinement time is derived showing a qualitative agreement with experimental scalings. Finally, we will conclude this section on a presentation of the possible application of this model to predict main discharge features using Artificial Intelligence.

## 4.1 Model predictions against SOL width measurements in diverted plasma

It has been observed that the SOL width decreases when the magnetic configuration changes from limited to diverted [63, 64, 69]. This is recovered by 3D flux-driven numerical simulations as it can be seen figure 4.1.

In order to compare the SSF model predictions to the experimental measurements, we need to either measure the electron temperature in the SOL or introduce a scaling of the electron temperature in terms of plasma parameters in expressions (3.56) and (3.57). This scaling can be obtained using the 2 point model (2-pt model). This model will be described in the next section concerning the impact of the density on the parallel dynamics description in the SF model. The resulting scaling of the electron temperature in high recycling regime is :

$$T_e[eV] = 0.13 \left( \frac{q^2 R P_{sep}}{a \lambda_q} \right)^{2/7} \quad (4.1)$$

This scaling depends on the heat flux decay length  $\lambda_q$  and its introduction in the density decay length scaling needs to estimate  $\lambda_q$ . In the case of Tore Supra, the heat flux decay length was half of the density one. Taking it into account, neglecting the shear effects and introducing the electron temperature scaling in

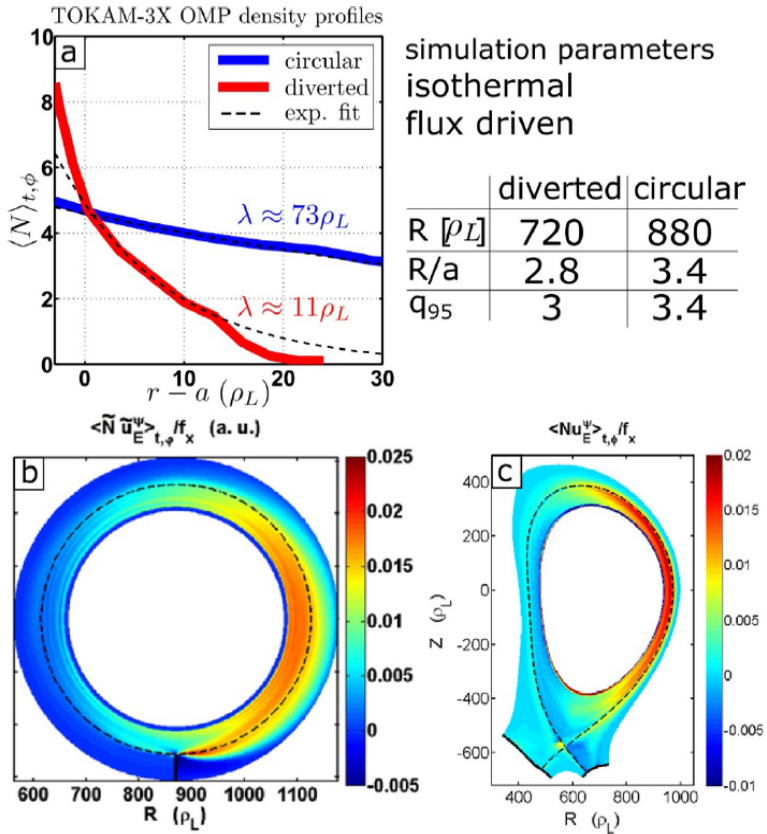


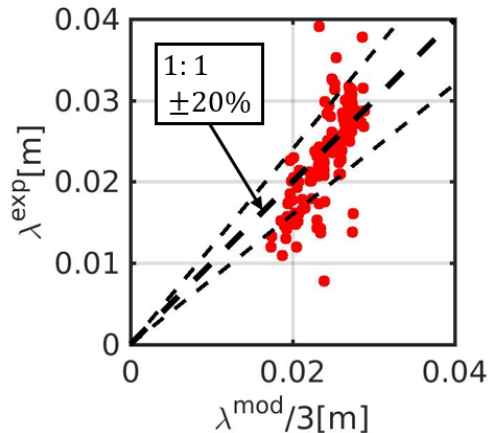
Figure 4.1: Tokam-3X isothermal simulations run with equivalent control parameters ( $\rho_s/R \approx 1/800$ ,  $q_{cyl} \approx 3$ ). 2D map of the turbulent radial particle flux, averaged along time and toroidal angle for (a) circular geometry and (b) lower single null X-point geometry. Note the strong ballooning of the particle flux, representative of interchange turbulence. (c) Average density profiles at outer midplane, illustrating the significant change of radial decay length from circular to divertor. Figure from [172].

the SOL width model prediction from equation (3.49) leads to a scaling of the SOL width in terms of plasma such as :

$$\lambda_n [mm] = 10 q_{cyl}^{0.68} B^{-0.66} R^{0.34} \left( \frac{A}{Z^2} \right)^{0.33} P_{sep}^{0.09} a^{-0.09} \quad (4.2)$$

where the magnetic field  $B$  is in Tesla, the major and minor radii  $R$  and  $a$  are in meter and the power crossing the separatrix is in Mega-watt. As a first comparison, we built a database of density decay length from the same density profiles used to build the edge rotation profiles database in WEST. To that end, we used exponential fit of the profiles between  $\rho = 1$  and  $\rho = 1.05$ . Figure 4.2 shows a qualitative agreement between the model predictions of  $\lambda$  and the experimentally measured ones, at least, for the wide SOL widths. For

the narrower SOL widths, the model overestimates the experimental values. Deeper investigations are needed to quantify the impact of the fit error bars and the density profile shapes on these discrepancies. Moreover, the model predicts SOL widths three times wider than the measured ones. This would indicate that the main physics responsible of the transport is recovered by the model but that additional effects affecting the amplitude of the predictions are missing. The SOL width scaling also recovers qualitatively the experimental scaling laws from multi-machine databases of diverted discharges in L-mode [63, 65].



The scaling obtained from the experimental data [64] is only depending on the poloidal magnetic field at the outer midplane which is not the case of the model predictions. Nonetheless, as it can be seen figure 4.3, this trend is recovered by the model predictions. The amplitude of the density decay length appears almost 20 times wider than the heat flux decay lengths in diverted H-mode discharges. It corresponds to 7 times the value in diverted geometry taking into account the factor 3 observed with the WEST database. In addition, in H-mode the strong shear layer close to the separatrix leads to a lowering of the flux, and consequently of the decay length, by a factor 2. It results in a factor of 3 – 4 between the model predictions of the density decay lengths  $\lambda_n$  and the experimental measurements of the heat flux decay lengths  $\lambda_q$  which is contained in the observed experimental range of ratio  $\lambda_n/\lambda_q$  [181]. This ratio is varying across and into the confinement regimes.

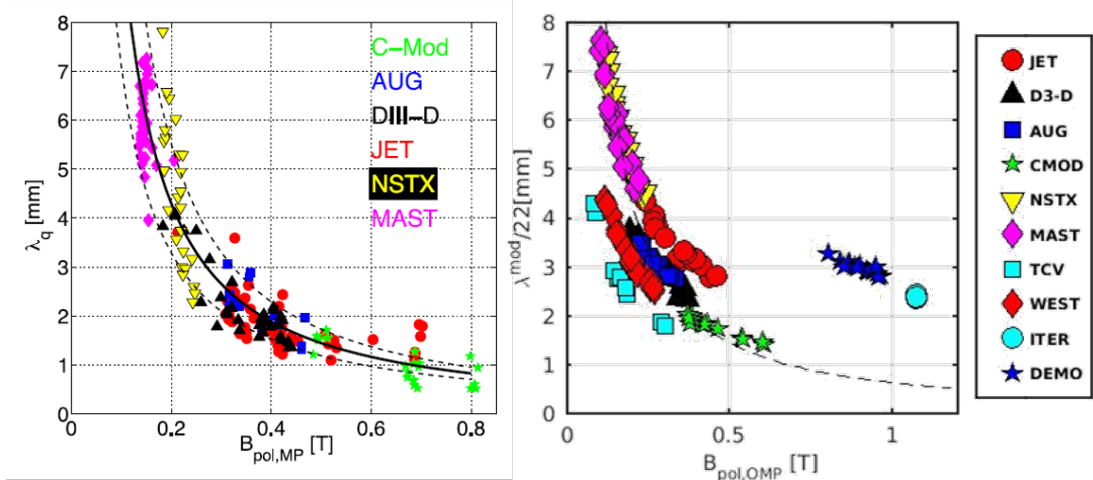


Figure 4.3: *Left* : Experimental evolution of the heat flux decay length  $\lambda_q$  in terms of the poloidal magnetic field at the outer midplane from [64]. *Right* : Predictions of the density decay length  $\lambda$  as a function of the poloidal magnetic field at the outer midplane.

The model predictions for JET discharges predicts higher values than the experimental scaling for higher values of poloidal magnetic field at the outer midplane. This trend appears also in the experimental data as it can be seen figure 4.3 on the left panel. This is due to the dependency of the scaling with the machine size. Moreover, the predictions for WEST and TCV are lower than the one predicted by the scaling. The TCV values predicted by the model are 2 times lower than the one predicted by the experimental scaling exactly as it has been recently observed [182]. Finally, the impact of the machine size on the

model predictions leads to 4 times higher values compared to the experimental scaling for the heat flux deposition length for ITER and DEMO which would help to the power exhaust without damaging the divertor tiles.

Other experiments in TCV showed an impact of the divertor leg length on the heat flux decay length in L-mode [171]. As a result, the dependency of  $\lambda_q$  with the leg length is at the power 0.45. This feature could be explained by the SSF model through the dependence of the SOL width with the parallel reconnection length. Indeed, the model predicts a SOL width such as  $\lambda_n \propto L_{\parallel}^{0.54}$ .

## 4.2 Impact of the density on the parallel dynamics description

In experiment, it has been observed that increasing the upstream density (upstream corresponding to the outer midplane) leads to a widening of the near SOL width leading to a shoulder formation [66, 67, 183]. In order to study the impact of the density in our model predictions, we focused on the parallel dynamics description. To that end, we based our study on equation (3.47) introducing a possible ionisation source in the SOL volume  $S_N$ . It results in a relation between the radial flux, the SOL width, the parallel losses and the ionisation source.

$$\lambda = \frac{\Gamma_r / \langle n \rangle}{\sigma_{\parallel} - S_N / \langle n \rangle} \quad (4.3)$$

The density impact in the model can be due to three effects : 1) a change in the parallel dynamics of the turbulence leading to an increase of the radial flux, 2) a decrease of the parallel losses for the density or 3) an increase of the ionisation source. The two first effects are addressed in this section.

As mentioned in the introduction of this manuscript, the parallel dynamics is described through a sheath resistivity model corresponding to a sheath loss rate. This loss rate corresponds to the particle exhaust at the targets. We made the assumption that the conditions are the same at the targets and at the outer midplane. This is not the case when the density increases. We can change of density regime in the conditions at the target making the electron temperature different at the upstream condition and at the target conditions. This point can

be illustrated by the 2-pt model based on conservation equations. The first considered conservation equation is the total pressure conservation. Considering the upstream condition at the stagnation point the local Mach number is null ( $M_{\parallel}^U = 0$ ). We also consider the Bohm condition at the target ( $M_{\parallel}^T = 1$ ). The exponents  $U$  and  $T$  correspond to the upstream and target conditions respectively.

$$\left( \frac{1}{2} n_e^U (C_s^U)^2 + \frac{1}{2} n_e^U (M_{\parallel}^U C_s^U)^2 \right) = \left( \frac{1}{2} n_e^T (C_s^T)^2 + \frac{1}{2} n_e^T (M_{\parallel}^T C_s^T)^2 \right) \quad (4.4)$$

$$n_e^U T_e^U \left( 1 + \frac{T_i^U}{T_e^U} \right) = 2 n_e^T T_e^T \left( 1 + \frac{T_i^T}{T_e^T} \right) \quad (4.5)$$

Neglecting energy transfer from ions to electrons along the field line we can consider the ion to electron ratio constant along a field line. This results in the relation :

$$n_e^U T_e^U = 2 n_e^T T_e^T \quad (4.6)$$

The second equation is the heat flux conservation through the separatrix. The power crossing the separatrix  $P_{SOL}$  is exhausted at the targets by the parallel flux  $q_{\parallel}$ . Considering that half of the heat goes towards each target, the power balance results in :

$$\frac{1}{2} P_{SOL} = 2\pi R \lambda_q \kappa q_{cyl} q_{\parallel} \quad (4.7)$$

The parallel flux exhaust at the target is described by :

$$q_{\parallel} = \gamma n_e^T e C_s^T T_e^T \quad (4.8)$$

where  $\gamma = 5 + 2.5 \frac{T_i}{T_e}$  is the sheath conduction coefficient. The last equation represents the heat flux flow along the field lines. Two phenomena can transport the heat along the field line : 1) the convection  $q_{\parallel}^{conv} = 2.5(1 + \frac{T_i}{T_e}) n_e e v_{\parallel} T_e$  and 2) the conduction given by the Spitzer-Härm model  $q_{\parallel}^{cond} = -3.16 n_e \frac{V_{th,e}^2}{\nu_e} \nabla_{\parallel} e T_e$  with  $V_{th,e} = \sqrt{\frac{e T_e}{m_e}}$  the electron thermal velocity and  $\nu_e = \frac{n_e e^{5/2} \ln(\Lambda)}{3(2\pi)^{3/2} \epsilon_0^2 \sqrt{(m_e) T_e^{3/2}}}$  is the electron-electron collision frequency. Both ways can be responsible of the heat transport but usually the convective contribution is neglected. We will introduce a conduction factor  $f_{cond}$  representing the fraction of the total heat flux due to the conduction transport. This results in the reduced expression for the parallel heat

flux.

$$q_{\parallel} = -f_{cond} \frac{2}{7} \kappa_0 \nabla_{\parallel} T_e^{7/2} \quad (4.9)$$

where  $\kappa_0 = -3.16 \frac{3(2\pi)^{3/2} \epsilon_0^2}{\sqrt{(eme) \ln(\Lambda)}} \approx 2000$ . After a few algebra, this system of equations results in a relation between the upstream and target temperatures.

$$\left( \frac{T_e^T}{T_e^U} \right)^{1/2} = \frac{\nu_0^*}{\nu_e^*} \left[ 1 - \left( \frac{T_e^T}{T_e^U} \right)^{7/2} \right] \quad (4.10)$$

where  $\nu_e^* = \frac{\nu_e L_{\parallel}}{V_{th,e}}$  and  $\nu_0^* = \frac{4 \times 3.16}{7 \gamma f_{cond}} \sqrt{\frac{m_i}{m_e}} \frac{1}{\sqrt{Z+\alpha}} \approx 10$ . From this relation, we deduce two regimes : 1) a low collisionality regime ( $\nu_e^* \ll \nu_0^*$ ) where  $T_e^T = \left(1 - 2 \frac{\nu_e^*}{\nu_0^*}\right) T_e^U \approx T_e^U$  and 2) a high collisionality regime ( $\nu_e^* \gg \nu_0^*$ ) where  $T_e^T = T_e^U \left(\frac{\nu_0^*}{\nu_e^*}\right)^2$ . The first regime corresponds to the assumption we made considering the temperature constant along the field line and does not affect the SSF model parallel dynamics description. The second one has to be taken into account when the density increases.

The upstream to target temperature ratio impacts the parallel coefficients in the vorticity equation  $\sigma_{\parallel}^{\Phi}$  and in the continuity equation  $\sigma_{\parallel}^n$ . The first one results from the Boltzmann description of the electrons :

$$\sigma_{\parallel} \left( 1 - e^{-\frac{(\Delta T_e^U - U)}{T_e^T}} \right) \approx \sigma_{\parallel} \frac{T_e^U}{T_e^T} \frac{\tilde{U}}{T_e^U} = \sigma_{\parallel} \frac{T_e^U}{T_e^T} \tilde{\Phi} \quad (4.11)$$

Then, the parallel loss rate comes from the integral on the parallel direction of the parallel gradient of the parallel current divided by the density :  $\frac{1}{2L_{\parallel}} \int_{-L_{\parallel}}^{+L_{\parallel}} \frac{\nabla_{\parallel} j_{\parallel}}{n} = \frac{1}{2L_{\parallel}} \left( [j_{\parallel}/n]_{-L_{\parallel}}^{+L_{\parallel}} - \int_{-L_{\parallel}}^{+L_{\parallel}} dl_{\parallel} j_{\parallel} \nabla_{\parallel} n^{-1} \right)$ . Considering the Boussinesq assumption, this term is equal to the parallel current divided by the density at the targets. This consideration is supported by the fact that in the case of a limited discharge, the density remains constant along the field lines excepted close to the targets. This assumption is also supported in the case of the 3-point model which will be detailed later in this section because we consider the X-point conditions as boundaries for our integrals. The density is expected constant from the stagnation point to the X-point location due to the absence of source or sinks. This consideration for the boundaries of the parallel integral leads to the following

parallel loss rate expression.

$$\sigma_{\parallel} = \sigma_{\parallel}^0 \left( \frac{T_e^U}{T_e^T} \right)^{-1/2} \quad (4.12)$$

where  $\sigma_{\parallel}^0$  is the rate in sheath regime. We finally obtain the expressions for the parallel loss rates :

$$\sigma_{\parallel}^n = \sigma_{\parallel}^0 \left( \frac{T_e^U}{T_e^T} \right)^{-1/2} \quad (4.13)$$

$$\sigma_{\parallel}^{\Phi} = \sigma_{\parallel}^0 \left( \frac{T_e^U}{T_e^T} \right)^{1/2} \quad (4.14)$$

Introducing these scalings in the SF model SOL predictions for the transport observables and dominant mode leads to the following expressions in terms of the sheath regime predictions characterised by a nought index:

$$\lambda = \lambda_0 \left( \frac{T_e^U}{T_e^T} \right)^{1/11} \quad (4.15)$$

$$k_0 = k_{0,0} \left( \frac{T_e^U}{T_e^T} \right)^{3/11} \quad (4.16)$$

$$\frac{\sigma_n}{\langle n \rangle} = \left( \frac{\sigma_n}{\langle n \rangle} \right)_0 \left( \frac{T_e^U}{T_e^T} \right)^{-5/22} \quad (4.17)$$

$$\frac{\sigma_{\Phi}}{T_e} = \left( \frac{\sigma_{\Phi}}{T_e} \right)_0 \left( \frac{T_e^U}{T_e^T} \right)^{-10/11} \quad (4.18)$$

These predictions are in agreement with 3D simulation results concerning the decrease of the fluctuation levels and the increase of SOL width predictions [161]. Also, this result is in agreement with the observations concerning the density shoulder. The evolutions of the SOL width, the fluctuation level, the ratio of the target temperature over the upstream one, the control parameters of the model and the normalised collisionality  $\nu_e^*/\nu_0^*$  with the power crossing the separatrix and the upstream separatrix density are presented figure 4.4. Here we supposed that the density decay length is a third of the SF model predictions as in WEST and  $\lambda_q = 0.5\lambda_n$  as in Tore Supra. The main plasma parameters are the WEST typical ones. Interestingly, the non-normalised SOL width increase for the high densities is reduced by the decrease of the Larmor radius. The parallel loss rate of the potential increases with the density due to the decrease of the target temperature.

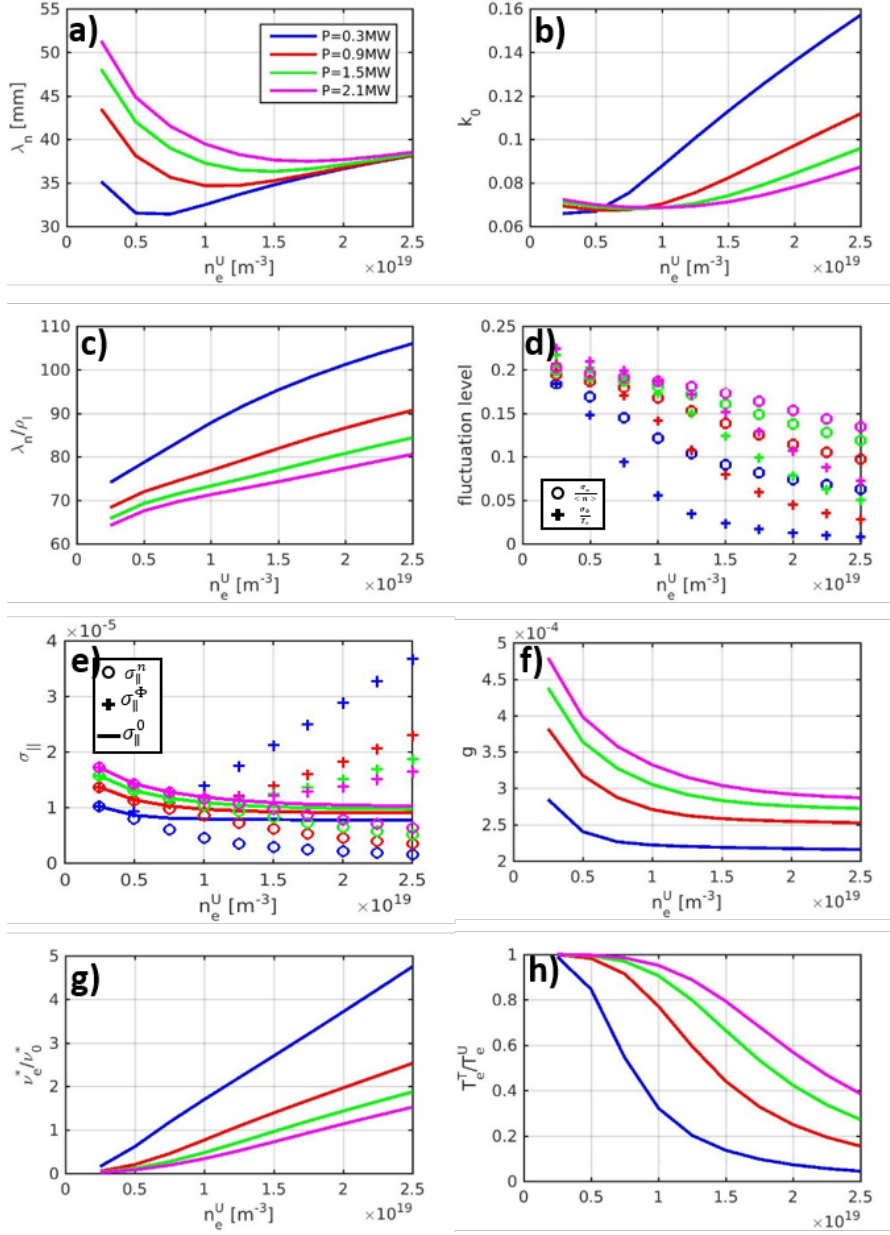


Figure 4.4: Evolution of a) the density decay length, b) the dominant mode, c) the normalised density decay length, d) the density and potential fluctuation level, e) the parallel loss rates, f) the curvature drive coefficient, g) the normalised collisionality and h) the target to upstream temperatures with the upstream density for different values of the power crossing the separatrix

This model does not make the separation between the upstream SOL and the diverted region which should be done in the presence of a strong ionisation source in the diverted SOL volume. To be consistent with the SF paradigm, we chose to apply the field line average to the upstream SOL with the X-point

conditions as boundary conditions. To express the parallel loss rate we need to estimate the parallel current perturbation at the X-point position. To that end, we will consider the perturbations of this current at the X-point location, the Ohm's law and the sheath potential imposed by the target.

$$j_{\parallel}^{\tilde{X}} = j_{\parallel}^{\tilde{X}} \quad (4.19)$$

$$= \sigma \frac{\tilde{\Phi}^X - \tilde{\Phi}^T}{L_{\parallel}^{XT}} \quad (4.20)$$

$$= en_e^T C_s^T \left( 1 - e^{\frac{\Lambda - \Phi}{T_e^T}} \right) \quad (4.21)$$

with the conductivity  $\sigma = 0.51 \frac{n_e^T Z^2 e^2}{m_e \nu_e}$ . From that, one can drive the expression of the perturbation of the parallel current at the X-point.

$$j_{\parallel}^{\tilde{X}} = Zen_e^T C_s^T \frac{\tilde{\Phi}^X}{T_e^T} \times \frac{1}{1 + \frac{0.51 L_{\parallel}^{XT} \nu_e C_s^T}{v_{th,e}^2}} \quad (4.22)$$

This last equation leads to the expression of the parallel loss parameter in the vorticity equation :

$$\sigma_{\parallel}^{\Phi} = \frac{\rho_s}{L_{\parallel}^{UX}} \left( \frac{T_e^U}{T_e^T} \right)^{1/2} \times \frac{1}{1 + \frac{0.51 L_{\parallel}^{XT} \nu_e C_s^T}{v_{th,e}^2}} \quad (4.23)$$

From this equation we can see that if we are not in a high recycling regime,  $T_e^U \approx T_e^T$  and the collisionality is low such as the parallel loss parameter is the same as the one used originally with the simple approach for the parallel dynamics.

To determine the SOL width with the SF model, the continuity equation is considered upstream and we have another parallel loss parameter for the density  $\sigma_{\parallel}^n = \frac{\rho_s}{L_{\parallel}^{UX}} Ze \frac{n_e^X}{n_e^U} C_s^X M^X$  due to the mean flow. The SSF model is now depending on target, upstream and X-point conditions which have to be determined. To that end, the same framework as the one considered for the 2-pt model is invoked using conservation equations. We have to add to the system of variables  $(n_e^U, T_e^U, n_e^T, T_e^T)$  new variables representing the conditions close to the X-point  $(n_e^X, T_e^X, M^X)$  with  $M^X = \frac{V_{\parallel}^X}{C_s^X}$  the Mach number close to the X-point.

We will also introduce the ionisation parameter  $\alpha_R$  representing the fraction of target particle flux ionised in the divertor leg volume. This parameter will contain neutral physics such as neutral sputtering from targets, the ratio between the neutrals mean free path and the distance from the target to the bulk plasma. The details of the evaluation of this parameter will be discussed later in this section.

The power balance equation is still valid since we consider no ionisation in the upstream SOL. Consequently, the heat flux through the separatrix is transported to the X-point.

$$q^X = q_0 = \frac{P_{SOL}}{4\pi R \lambda_q \frac{e\kappa}{q_{cyl}}} \quad (4.24)$$

The power flux towards the X-point will then be dissipated by two phenomena: 1) the sheath transmission at the target  $\gamma e T_e^T n_e^T C_s^T$  and 2) the ionisation power losses  $e E_i \alpha_R n_e^T C_s^T$  with  $E_i \geq 13.6\text{eV}$  the energy losses at each ionisation in eV. This value is generally higher than the ionisation energy of the Deuterium.

$$q_0 = (\gamma e T_e^T + e E_i \alpha_R) n_e^T C_s^T \quad (4.25)$$

We also consider power heat fluxes carried by conduction and not by convection. The convective contribution is also neglected in this model since we are interested in the effects at high density and high temperature parallel gradients. We consider conduction between upstream and X-point (it assumes that the ionisation in the leg is important enough to cool down X-point temperature and to lead to a domination of conductive transport). This cooling down is also assumed to be such as temperature is not too strong to have a high temperature step between X-point and target to stay in a conductive regime.

$$q_0 = \frac{2}{7} \kappa_0 \frac{(T_e^U)^{7/2} - (T_e^X)^{7/2}}{L_{||}^{UX}} \quad (4.26)$$

$$q_0 = \frac{2}{7} \kappa_0 \frac{(T_e^X)^{7/2} - (T_e^T)^{7/2}}{L_{||}^{XT}} \quad (4.27)$$

As it is the case for the total energy, the momentum flux going from X-point

$n_e^X C_s^X M^X$  towards the target plate is partially lost by ionisation in the divertor leg. The balance equation can be written as:

$$n_e^X C_s^X M^X = (1 - \alpha_R) n_e^T C_s^T \quad (4.28)$$

Finally the last equations considered here are the total pressure conservation along the field lines as presented for the 2-pt model but now with the total pressure at the X-point.

$$n_e^U T_e^U = 2n_e^T T_e^T \quad (4.29)$$

$$2n_e^T T_e^T = \left(1 + M^{X^2}\right) n_e^X T_e^X \quad (4.30)$$

Only the ionisation parameter remains unknown. It represents the fraction of neutrals ionised in the divertor leg volume. Consequently, it is a function of the ratio of the neutrals mean free path  $\lambda_{mfp}$  and the poloidal length of the leg  $L_{pol}$ . It should be 1 if  $\lambda_{mfp}$  is much lower than  $L_{pol}$  and it will lower with the increase of  $\lambda_{mfp}$ . In this study we decided to choose an inverse tangent of  $\frac{\lambda_{mfp}}{L_{pol}}$  as a function to determine  $\alpha_R$ .

$$\alpha_R = 1 - \frac{2}{\pi} \arctan \left( \frac{\lambda_{mfp}}{L_{pol}} \right) \quad (4.31)$$

We chose the factor  $\frac{2}{\pi}$  in order to have half of the neutrals ionized in the divertor leg when the mean free path is as long as the poloidal length of the leg which could be the case when we consider Gaussian distribution of mean free paths. We could choose functions as  $(1+x^a)^b$  with  $b < 0$  but for low values of  $a$  or  $b$  there is not so much difference in the results. This simple approach is a zero-order model and much complex considerations such as anisotropy of target sputtering or neutral transport in the main chamber are not considered.

The neutrals mean free path still remains non-determined. We obtain it thanks to a simple model consisting in giving to the neutrals a fraction of the ions going towards the target  $V_n = \alpha_{Vn} C_s^T$  and then considering the cross section for the ionisation of hydrogen isotopes  $\langle \sigma_{H,i} \rangle$  in  $m^3 s^{-1}$ .

$$\lambda_{mfp} = \frac{\alpha_{Vn} C_s^T}{n_e^T \langle \sigma_{H,i} \rangle} \quad (4.32)$$

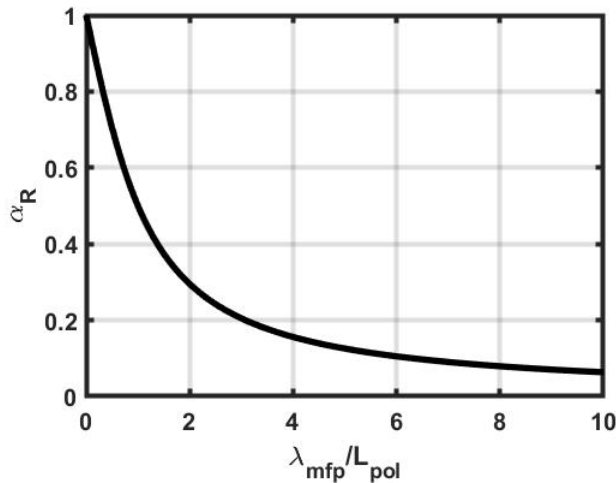


Figure 4.5: Plot of the evolution of  $\alpha_R$  with  $\frac{\lambda_{mfp}}{L_{pol}}$

Two particular cases stem from this model. In the case where  $\alpha_R \rightarrow 0$ , the ionisation in the divertor leg is very low. It could be due to low divertor density/collisionality, too short  $\lambda_q$  (leading to too much heat flux and hot divertor leg), too much power going in SOL (too hot divertor leg again) or too short divertor leg (or limited discharge). The temperature at the X-point will be close to the one at the target and so the Mach number at the X-point will be one and the conditions at the target are displaced to the X-point leading to a limited-like discharge in sheath limited regime. The case where  $\alpha_R \rightarrow 1$  corresponds to the very high recycling regime where the temperature at the target is going down due to the high ionisation rate (high density) in the divertor. It should go to the detachment regime but we do not model this phenomenon with this model because detachment is a very local phenomenon at the target.

After a few algebra, the 3-pt model set of equations can be rewritten as expressions of all the unknown quantities in terms of the ratio of the target over the

upstream temperature  $X = \frac{T_e^T}{T_e^X}$  and an equation only depending on this ratio.

$$M^X = f_1(X) = \frac{X^{1/2}}{1 - \alpha_R} \left[ 1 - \sqrt{1 - (1 - \alpha_R)^2 X^{-1}} \right] \quad (4.33)$$

$$n_e^X = f_2 = n_e^U \frac{\left[ 1 + \frac{L_{\parallel}^{UX}}{L_{\parallel}^{XT}} (1 - X^{7/2}) \right]^{2/7}}{1 + f_1(X)^2} \quad (4.34)$$

$$n_e^T = f_3(X) = \frac{f_2(X)}{2} \frac{1 + f_1(X)^2}{X} \quad (4.35)$$

$$\frac{T_e^U}{T_e^X} = f_4(X) = \frac{2f_3(X)}{n_e^u} X \quad (4.36)$$

$$T_e^T = f_5(X) \quad (4.37)$$

$$X^3 = f_5(X)^3 \frac{2}{7} \frac{(1 - \alpha_R) \kappa_0}{L_{\parallel}^{XT} f_1(X) f_2(X)} \sqrt{\frac{m_i}{Ze(1 + \alpha)}} (1 - X^{7/2}) \frac{1}{\gamma e f_5(X) + E_i \alpha_R} \quad (4.38)$$

With  $T_e^T = f_5(X)$ , the real and positive solution of

$$T_e^{T^3} + 2\beta T_e^{T^2} + \beta^2 T_e^T = \delta \quad (4.39)$$

$$\beta = \frac{E_i \alpha_R}{\gamma} \quad (4.40)$$

$$\delta = \frac{q_0^2 m_i}{f_3(X)^2 Z \gamma^2 e^3 (1 + \alpha)} \quad (4.41)$$

The coupling of this set of equation with the SF model is non linear due to the cross dependencies of the SOL width with the ionisation parameter and the different conditions at the 3 positions considered. In order to find a solution, we built a convergence algorithm solving step by step the system as following : 1) solve equation (4.38), 2) introduce  $X$  in the expression of all the parameters, 3) estimate  $\alpha_R$ , 4) determine  $\lambda_q$ , 5) solve again equation (4.38) and do it again making a loop until it converges.

In order to compare the predictions of the SSF model coupled with the 3-pt and the 2-pt model we scanned the upstream density at a constant power crossing the separatrix ( $P_{sep} = 2.1 MW$ ). Figure 4.6 shows three target condition regimes : 1) and 2) are the sheath limited and the high recycling regimes similar to the one obtained from the 2-pt model and 3) a new regime due to the increase of the resistivity in the divertor leg. This last regime is characterised by a strong

decrease of the parallel loss coefficient for the potential leading to an increase of the radial flux and of the density decay length. This point could be the origin of the density shoulder.

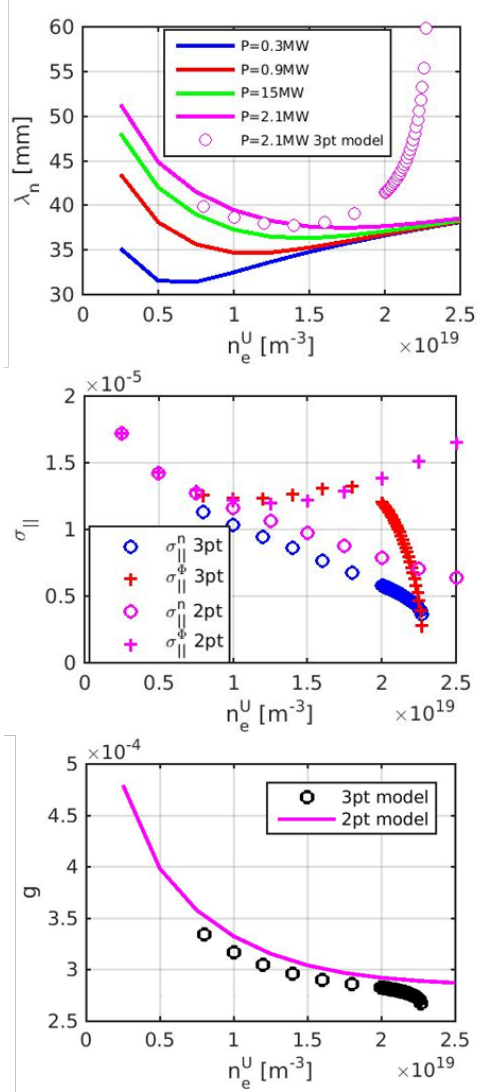


Figure 4.6: Evolution with the upstream density of a) the density decay length, b) the parallel losses coefficient  $\sigma_{||}$  and c) the curvature drive coefficient.

In order to study if this trend could be comparable to density shoulder behaviour, we managed a scan in plasma current in JET-like discharge as it has been experimentally done in [67]. We imposed a power crossing the separatrix of  $P_{sep} = 1.7MW$  and an upstream density of  $n_e^U = 0.8 \times 10^{19} m^{-3}$ . It results in a strong decrease of the density decay length when the plasma current is increased. This corresponds to a loss of the density shoulder (see figure 4.7). This regime due to resistivity could be also responsible of density limits consist-

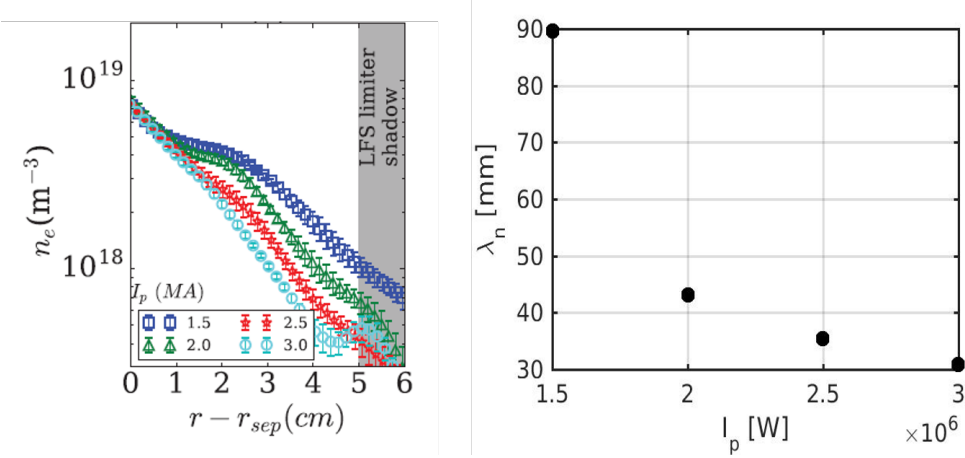


Figure 4.7: *Left* : Experimental radial profiles of the electron density measured in JET at different values of plasma current (from [67]).*Right* : Evolution of the density decay length with the plasma current predicted by the SSF model coupled with the 3pt model in JET-like discharge comparable to [67].

ing in violent plasma endings. Indeed, further increase of the upstream density leads to a strong and non-linear increase of the matter radial flux leading to an end of the discharge. This occurs when the resistive part of the parallel loss rate is high enough  $\frac{0.51 L_{\parallel}^{XT} \nu_e C_s^T}{v_{th,e}^T} \propto \frac{L_{\parallel}^{XT} n_e^T}{T_e^T} \gg 1$ . This last point shows that if we increase the ratio between the particle mean free path  $v_{th,e}/\nu_e$  over the reconnection length, we will reach the threshold in density as observed experimentally [184]. Inclusion of these effects in a transport code could help to emphasise the dynamics of such phenomena.

Another description of the parallel losses comes from the plasma resistivity in the main SOL. Indeed, if we consider that the plasma exhibits a high enough resistivity in the main SOL volume, the potential structure will have parallel gradient occurring on lower scales than the parallel reconnection length. If this condition leads to a disconnection of the filaments from the sheath targets, we could write the parallel loss rate as a resistive one given by the expression  $\sigma_{\parallel}^r = \frac{m_i}{m_e} \frac{\omega}{\nu_{ee}} \rho_s^2 k_{\parallel}^2 \approx \frac{m_i}{m_e} \frac{\omega}{\nu_{ee}} \rho_s^2 (\pi q R)^{-2}$ . Comparing this scaling to the ones predicted by the TOKAM2D or the 2-pt and 3-pt models coupled with the SSF model shows that, in current tokamak conditions, the plasma resistive loss rate is one order of magnitude lower than the sheath resistive one. This description could be more adapted to closed field lines where only modes with vortices which do not short-circuited themselves in the high-field side region can survive. In the end, even if the parallel loss rate expression in closed field line considered in

the previous sections did not take into account such resistive effects, the model dependencies in control parameters would remain the same.

### 4.3 Impact of the phase shift between potential and density fluctuations on the model predictions

As mentioned in this manuscript, we considered that the phase shift between density and potential structures is equal to the ideal interchange case one which is  $\pi/2$ . This phase shift impacts our model predictions towards two effects. The first impact comes from the curvature driving term as it can be seen in equation (3.7). The curvature term will be proportional to the sinus of the phase shift which lowers when the phase shift decreases from  $\pi/2$ . This dependency can be included in the curvature drive parameter  $g$  motivating the use of the radial envelope function in the 1DCIS code. The second impact of this phase shift is directly in the calculations of the radial flux (see equation 3.36). Again the radial flux will be directly proportional to the sinus of the phase shift. Combining both effects leads to the following scalings of the flux and the fluctuation levels :

$$\frac{\Gamma_r}{\langle n \rangle} \propto \sin(\varphi)^{7/4} \quad (4.42)$$

$$\frac{\sigma_n}{\langle n \rangle} \propto \sin(\varphi)^{1/8} \quad (4.43)$$

$$\frac{\sigma_\Phi}{T_e} \propto \sin(\varphi)^{7/8} \quad (4.44)$$

In the scrape-off layer, the SOL width resulting from the balance of the radial flux and parallel flux, this effect should impact also the density decay length in the same way as for the radial flux.

$$\lambda = \frac{\Gamma_r}{\langle n \rangle \sigma_{||}} \propto \sin(\varphi)^{7/11} \quad (4.45)$$

From this scaling, we can deduce that the phase shift observed in the simulations ( $\varphi = \pi/3$ ) would lead to less than 10% decrease of the model prediction which is negligible. It is worth noting that in this approach, we only considered a phase shift between the modes which is the same for all the modes. More complex dependencies should come from a spectrum of this phase shift and it is beyond

the scope of this work.

## 4.4 Impact of the geometry on the curvature drive coefficient $g$

The plasma shaping can also contribute to the SOL features. Especially, it has been observed experimentally that both elongation [71] and triangularity [70] can affect the SOL width. Increasing the elongation leads to a decrease of the SOL width as well as if the triangularity is increased. Negative triangularity does not seem to impact much the SOL width [70]. In the framework of the SF model, we study the impact of the elongation and the triangularity on the curvature drive coefficient  $g$ . To that end, synthetic equilibria in limited geometry with varying elongation and triangularity were built based on the analytical description of the flux surfaces [185, 186].

$$R = R_0 + \Delta_{sh} + r \cos(\theta \arcsin(\delta) \sin(\theta)) \quad (4.46)$$

$$Z = Z_0 + r\kappa \sin(\theta) \quad (4.47)$$

with  $R_0$  and  $Z_0$  the major radius and the height of the magnetic axis,  $\Delta_{sh} = a^2/R_0$  is the Shafranov shift,  $\kappa$  is the elongation and  $\delta$  is the triangularity. This analytical equilibrium can reproduce the features of plasma shaping excepted the flux expansion which could be important in the cases of high elongation, high triangularity or diverted equilibria.

A scan of the elongation and triangularity values has been managed in the ranges  $\kappa \in [1 - 1.6]$  and  $\delta \in [-0.4 - 0.4]$ . We considered WEST-like discharges with a major radius of  $R = 2.5m$ , a minor radius of  $a = 0.5m$ , a magnetic field amplitude of  $B = 3.7T$  and a safety factor parabolic profile going from 1 at the magnetic axis to 3 at the separatrix. Examples of the resulting 2D maps of the magnetic equilibria are given figure 4.8. From these equilibria, we can measure the deformation of a flux tube at different poloidal positions following the field lines of its contour. From these deformations, we can measure the poloidal and radial wavenumbers variation at the different poloidal positions as well as the scalar product of the structure orientation and the toroidal magnetic field gradient. Averaging this scalar product on the parallel direction leads to the

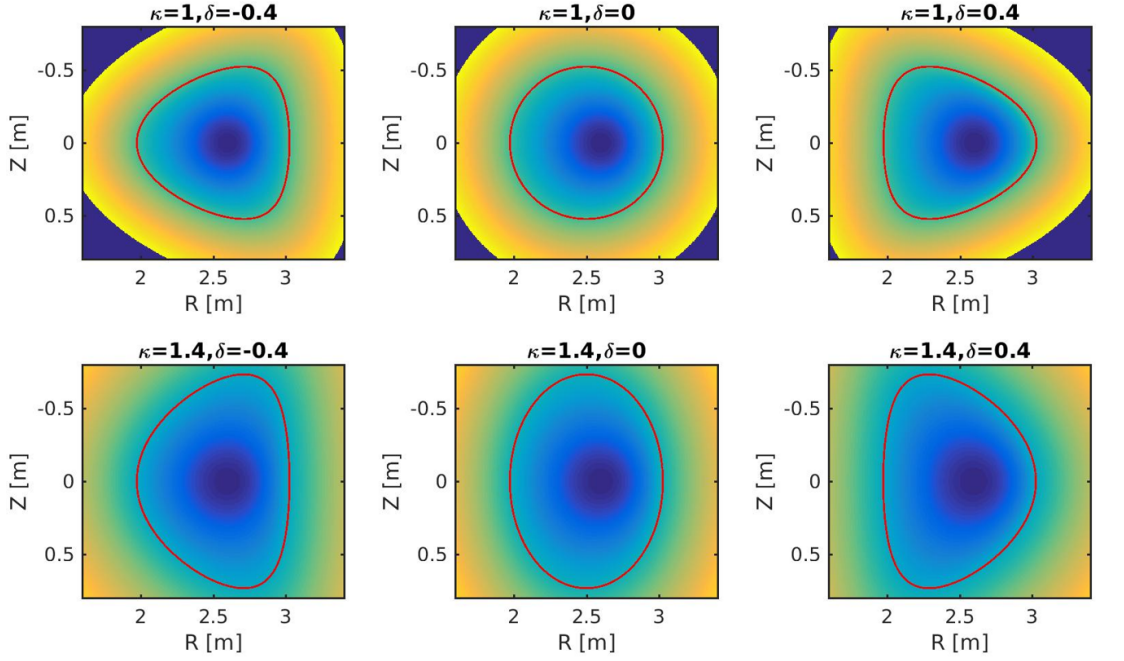


Figure 4.8: Magnetic equilibrium from the analytical expressions (4.46,4.47) for different values of elongation and triangularity. The red lines correspond to the separatrix contours.

determination of the numerical coefficient  $G_0$  in the curvature drive coefficient expression. The measure of the radial wavenumber will be discussed in the next section. In this contribution, we followed flux tubes of 5mm width situated at 1cm from the separatrix in the SOL at the low field side midplane. This flux tube size corresponds to almost  $10 - 15\rho_s$  which is of the order of the size of the  $k_0$  mode estimation in tokamak scrape-off layers.

Starting by the impact of the elongation on the curvature drive coefficient, we plotted the poloidal profile of the scalar product between the flux tube orientation and the toroidal magnetic field gradient (see figure 4.9 a) et b)). This figure shows that the elongation is responsible of a decrease of the curvature drive of the instability. This observation is in qualitative agreement with the experimental observations in TCV [71]. We also see that the analytical scaling  $G_0(\theta) = \cos(\theta - \arctan(\hat{s}\theta))$  used for the estimation of  $g$  in circular geometry is recovered by this method.

Then, we applied the same approach to the triangularity scan (see figure 4.9 c) and d)). The increase of triangularity leads to a decrease of the curvature drive

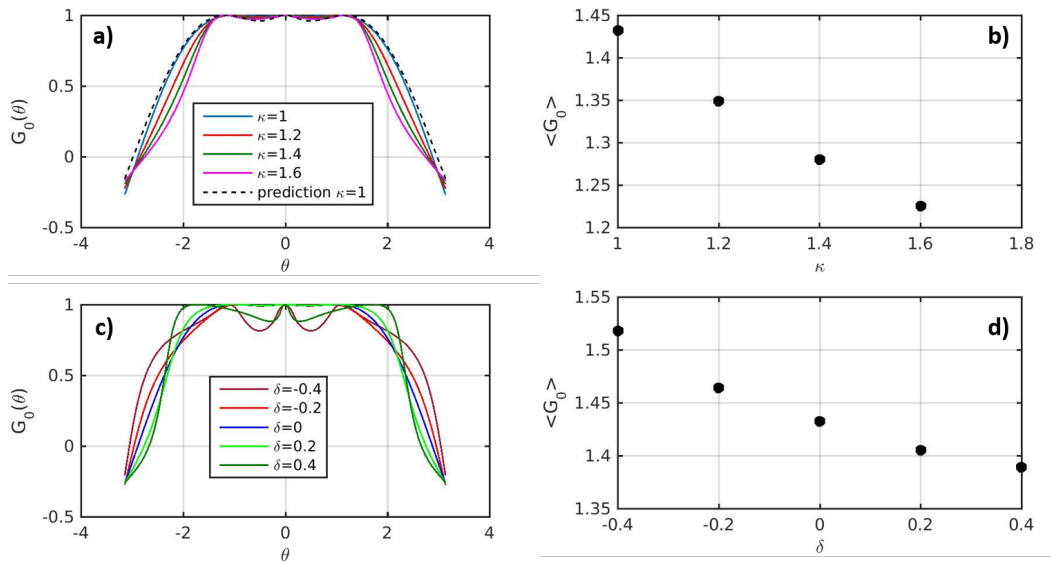


Figure 4.9: Poloidal profile of the curvature drive coefficient amplitude  $G_0$  for a) different elongations and c) different triangularities. Evolution of the averaged curvature drive coefficient amplitude  $\langle G_0 \rangle$  with b) the elongation and d) the triangularity.

and the negative triangularities lead to higher values. This is coherent with the experimental observations of [70].

Nevertheless, comparing the curvature drive coefficient amplitude  $\langle G_0 \rangle$  to the one in the circular case  $\langle G_0(\kappa = 1, \delta = 0) \rangle$  shows a low deviation reaching at the maximum 15% (see figure 4.10) which is not able to explain the experimental observations from [70, 71]. The absence of flux expansion could be responsible of this low deviation and we expect that the effects emphasised here would be enhanced considering the flux expansion.

Finally, in order to understand the impact of the diverted configuration on the curvature drive coefficient, we built an equilibrium from the analytical expression from [177]. The resulting poloidal profile bounded by the X-point position of the curvature drive coefficient amplitude appears very different from the one obtained in inner wall limited discharges (see figure 4.11). The resulting amplitude from the averaged curvature drive is 0.43 which is three times lower than the one in inner-wall limited discharges. This discrepancy leads to a lowering of the SOL width of almost 30%. This could be a part of the explanation of the SOL width lowering in diverted geometry.

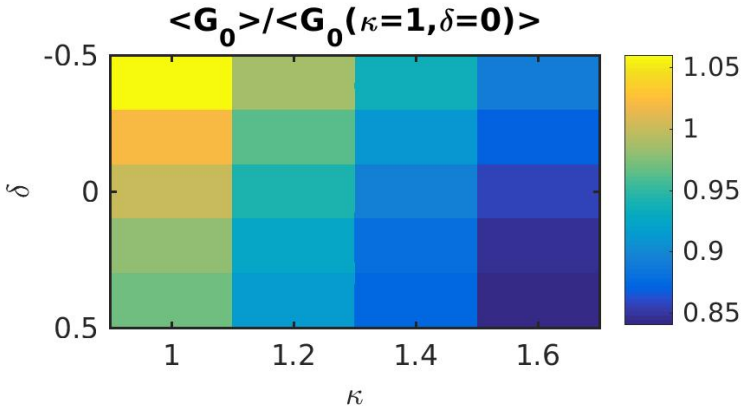


Figure 4.10: Evolution of the curvature drive amplitude  $\langle G_0 \rangle$  normalised to the one in the circular case  $\langle G_0(\kappa = 1, \delta = 0) \rangle$  with the elongation and the triangularity.

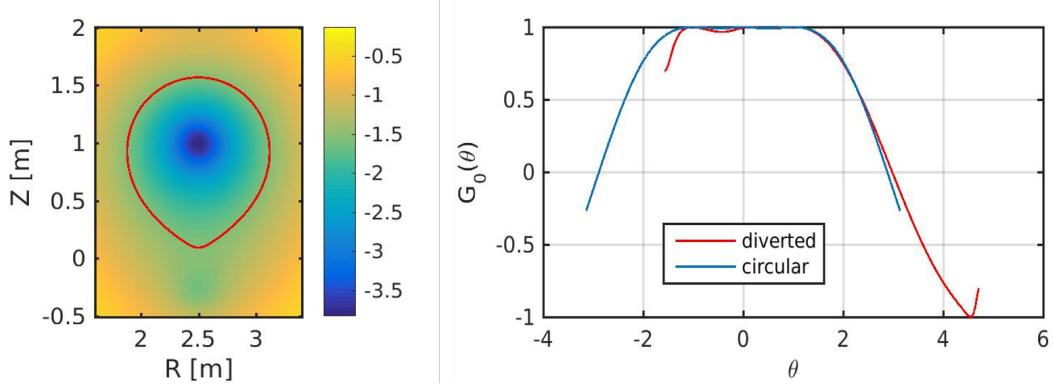


Figure 4.11: *Left* : Magnetic equilibrium in analytic diverted geometry from [177]. Red line represents the separatrix contour. *Right* : Curvature drive coefficient amplitude  $\langle G_0 \rangle$  poloidal profile.

## 4.5 Impact of the plasma shaping on the structure tilt

The scan of triangularity and elongation values can also be used to study the impact of plasma shaping on turbulence magnetic shear induced tilt measuring the flux tube inclination. The resulting evolutions of the poloidal profiles of flux tube tilt with the elongation and the triangularity is given figure 4.12. We clearly observe that both triangularity and elongation do not impact significantly the poloidal average of the flux tube tilt. Nevertheless, the elongation seems to strongly impact the tilt close in the high field side region.

On the other hand, applying the same method to the diverted analytical equilibrium leads to slightly different poloidal profiles (see figure 4.13). The difference

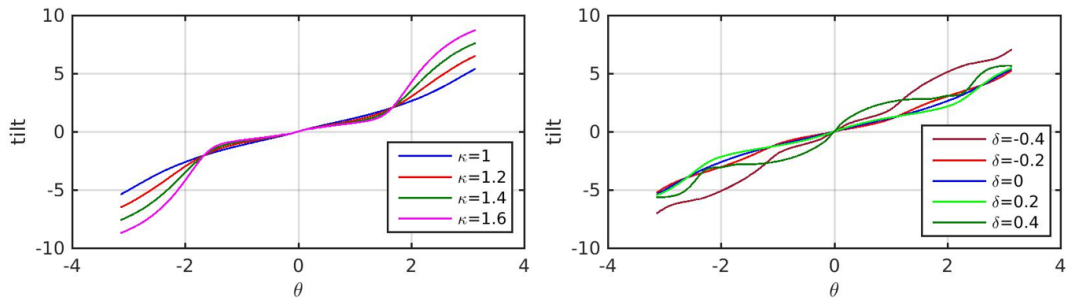


Figure 4.12: *Left* : Poloidal profiles of the flux tube tilt for different elongation amplitudes. *Right* : Poloidal profiles of the flux tube tilt for different triangularity amplitudes.

comes from the strong tilt due to the X-point presence.

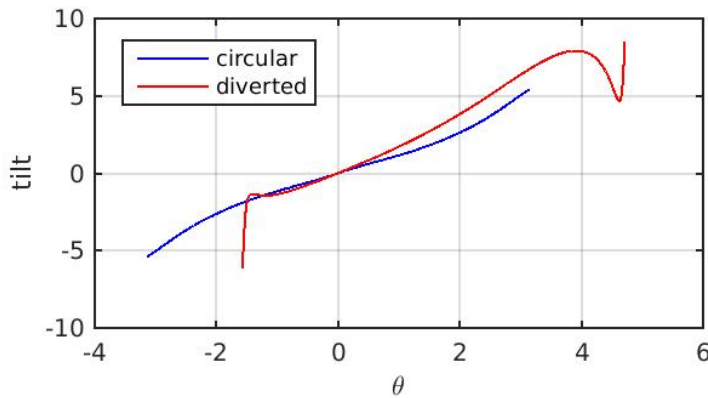


Figure 4.13: Poloidal profiles of the flux tube tilt in limited (blue line) and diverted geometry (red line).

Considering modes of wavenumber  $k\rho_s = 0.1$  at the low field side midplane and the strong tilt of the flux tube due to the X-point presence leads to values of wavenumbers close to 1. This value could be even higher with a better resolution of the equilibrium close to the X-point. At these values the modes do not have a physical meaning because their size are going under the Larmor radius. Damping phenomena should occur at such spatial scales. This point would justify the choice of cutting the poloidal distribution of the radial wavenumber at the X-point position for the determination of the averaged radial wavenumber used in the flow generation model. This method leads to tilts of around 0.5 leading to lowering of the SOL width of 15%. Considering the lowering due to the curvature drive coefficient amplitude and a parallel reconnection length from the midplane to the target equal to  $L_{\parallel} = \frac{\pi}{2}qR + L_{leg}$ , we obtain a final lowering of the SOL

width of almost 60% which is not so far from the 66% obtained from Tore Supra to WEST experimental observations. These considerations could explain the discrepancies between the SOL width values observed in limited and diverted discharges while keeping the same dependencies in the plasma parameters.

## 4.6 Impact of the electromagnetic effects on the SOL transport amplitude

In future devices, such as ITER, the separatrix plasma conditions could lead to the occurrence of electromagnetic effects. These effects would lead to a change in the parallel dynamics. Simulations of filament motion with and without electromagnetic considerations leads to a diminution of the parallel loss rate for the potential, increasing the filament growth and velocity [187]. The electromagnetic description of the turbulence is beyond the scope of this work but an attempt to include some features could be done considering the parallel transport description. Indeed, the collisionality in the divertor increases when the pressure in the leg increases leading to a possible change from electrostatic to electromagnetic parallel transport. This would be characterised by a change in the parallel velocity of transport from the electron thermal velocity to the Alfvén one. This point would change the parallel loss rate replacing the electron thermal velocity by the Alfvén one  $v_A = \sqrt{\frac{B^2}{4\pi n_e m_i}}$  in the resistive contribution to the parallel loss rate.

$$\sigma_{\parallel}^{\Phi} = \frac{\rho_s}{L_{\parallel}^{UX}} \left( \frac{T_e^U}{T_e^T} \right)^{1/2} \times \frac{1}{1 + \frac{0.51 L_{\parallel}^{XT} \nu_e C_s^T}{v_A^2}} \quad (4.48)$$

This would lead to an increase of the resistive term of the order of the ratio  $\frac{v_{th,e}}{v_A} \approx 300$  leading to a strong decrease of the loss rate as for the case of increasing density in the 3pt model. This behaviour could also explain the observations in ASDEX-Upgrade in terms of parameter space. Indeed, in this study, the density limit assessment is attributed to the transition from electrostatic to electromagnetic turbulence[188]. Further investigations are needed to adjudicate on this point.

## 4.7 Global confinement features from a generic flux model

The SF model is a transport model based on a spectral description of the turbulence. Assuming that the model is able to recover the main physics responsible of the transport, we can estimate the stored energy of a discharge  $\frac{3}{2}n_e e T_e$  from the flux predictions. Considering a typical gradient length of this order of the minor radius  $a$ , we can estimate the stored energy from the power balance equation.

$$P_{sep} = \Gamma_r^{SF} C_s T_e S \quad (4.49)$$

with  $S = 4\pi Ra$  the plasma surface in circular geometry. From this expression we can estimate a confinement time of the energy  $\tau_E$  given by the ratio of the stored energy over the injected power.

$$\tau_E = 0.007 \alpha_\tau n_{e,19}^{0.6} B[T]^{0.6} I_P[MA]^{0.2} P_{sep}[MW]^{-0.6} R[m]^{2.8} \left(\frac{a}{R}\right)^{1.9} A^{0.2} \quad (4.50)$$

with  $n_{e,19}$  the density in  $10^{19} m^{-3}$  and  $\alpha_\tau$  a coefficient taking into account the missing physics in the model such as the radial evolution of the phase shift between potential and density, the different amplitude of the potential parallel losses and shearing effects. Strikingly, comparing this scaling with experimentally based ones [176], shows a qualitative agreement in the exponents. In order to further compare these scalings, we calculated the confinement times for different devices from the synthetic database we used for the heat flux decay length estimation detailed earlier in this manuscript (see section 4.1). Plotting the comparison of the two predictions leads to a proportionality even if the dependencies in the plasma parameters are different (see figure 4.14). This could be due to cross correlations between plasma parameters. Here, an  $\alpha_\tau$  coefficient of 8 is needed to recover the experimental scaling amplitude. The proportionality between the two scalings of confinement time could indicate that the SF model is able to recover the main transport features in a tokamak discharge considering interchange driven turbulence.

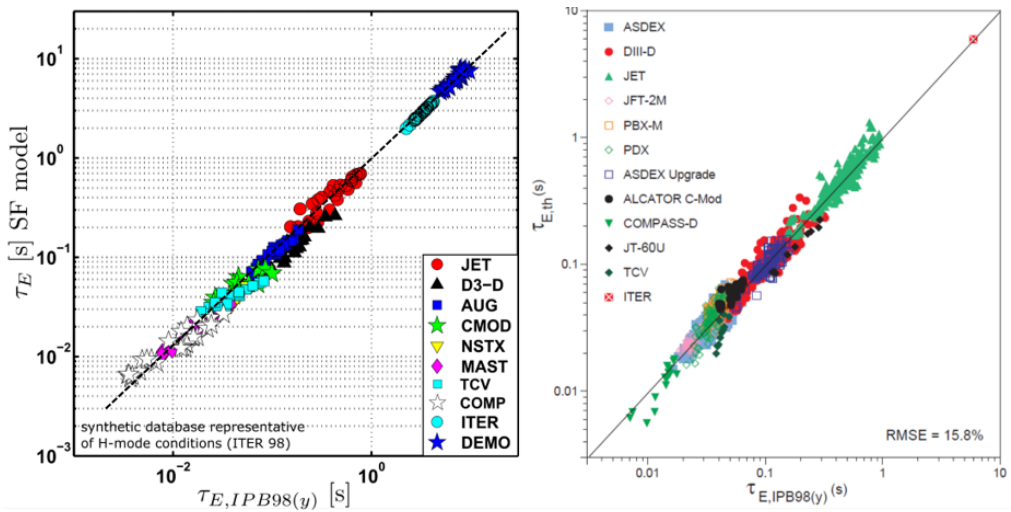


Figure 4.14: *Left* : Comparison between the predictions of the SF model and the experimental scaling from [176] for the energy confinement time. *Right* : Same comparison between the experimental data and the experimental scaling (from [176]).

## 4.8 The link between the spectral model and blob description

As mentioned in the state of the art of this chapter, the SOL transport is usually characterised by filaments. These filaments exhibits an intermittent behaviour. The model presented here is based on time averaged turbulent spectra. The link between both description is not trivial. On the other hand, recent developments based on statistical description of filament features has been managed [60]. Assuming that the main features of the turbulence come from the dominant mode properties, we could estimate the mean value of the distribution functions of the different filament features. Moreover, the momenta of those distribution functions could be also estimated by summing the mode contributions as it has been done in the model derived in this work to estimate the fluctuation levels. The amplitude of the filaments would not be recovered by the SF model due to the time average. However, we could only have an estimation of the product of the mean filament amplitude times the duty cycle of the turbulence.

We could also consider the filaments as constructive interferences of modes described by the SF model. This point of view is comparable to the one described in [158] invoking such interferences to generate filaments from drift wave instabil-

ties. Further investigations on how the modes could interfere to build filaments should be managed.

## 4.9 Towards a 0D model for main confinement features

The main objective of the transport modelling established here is to predict the main confinement features of discharges only knowing the discharge parameters. A first step has been carried with the 1DCIS model and the different geometrical and collisional considerations impacts on the model predictions in this work. Nevertheless, some uncertainties on turbulence features in the closed field lines keep us from fully predicting the main confinement features. This physics is the one included in the radial envelopes used in the 1DCIS code. An interesting step would be the use of Artificial Intelligence to determine these envelope features using neural networks. Establishing a database from the experimental data and inputting it in a learning system could lead to estimations of the parametric dependencies of the coefficient of the modified hyperbolic tangent used to build these envelopes. It would result in a 0D code able to reconstruct global transport features such as the radial profiles and confinement times but also the rotation profiles and the turbulence properties.



# **Chapter 5**

## **Conclusion**

The magnetic fusion device performances are strongly dependent on the edge particle and energy transport features since these fluxes constitute the main losses of the confined plasma and dictates the heat and matter deposition behaviour on the vessel wall. The origin of this transport is found in an important turbulent activity across the boundary of the confined plasma region responsible of this confinement degradation. Fortunately, this transport appears lowered in increased confinement regimes. This turbulence mitigation is attributed to an interplay with strongly sheared flows at the periphery of the plasma leading to the build-up of a transport barrier. This barrier establishment is not fully understood and represents one of the main research topics of the fusion domain. Moreover, both turbulence behaviour and flow generation have been observed to be highly impacted by the plasma shaping. These complex geometrical actuators being very hard to model or to simulate, our main understanding of their effects comes from experimental observations. These lacks of knowledge make difficult the predictions for future devices such as ITER or DEMO leading to the use of experimentally based scaling laws extracted from measurement in the current tokamaks.

In this thesis, we investigate the edge turbulent transport description and its interplay with edge flows. To that end, an experimental characterisation and theoretical developments have been managed in order to better describe both turbulence features and edge rotation profile establishment. From these frames, we aimed at predicting particle deposition width, turbulence features and flow generation mechanisms. In particular, we highlighted the strong impact of the edge plasma conditions such as magnetic topology and density

regimes on these different points. It results in an analytical model of turbulent transport offering the ability of predicting all of these features finding quantitative agreements with measurement in different devices such as TJ-K, WEST or Tore Supra as well as with experimental scaling laws.

In the first instance, we managed an experimental characterisation of the SOL turbulence features as well as the resulting transport using Langmuir probes in Tore Supra. This diagnostic offers a good enough time resolution to characterise transport observables such as fluctuation levels as well as the density exponentially decaying radial profiles. This effort results in a database containing enough statistics to validate model predictions made in this work. We also characterised the rotation profiles at the periphery of the confined region with Doppler Back Scattering measurements in the WEST tokamak. A systematic study of these measurements in various conditions led to the highlight of the effects of heating power injection, edge density and magnetic topology on the edge rotation radial profiles amplitude and shapes. The most significant result coming from this study is the strong effect of the plasma shaping, in particular the position of the X-point (either at the top or the bottom of the plasma) on the presence and the depth of a well in the profile responsible of the main local shearing rate amplitude. Also, the first characterisations of H-mode assessment in WEST have been documented in this thesis again showing impacts of the magnetic topology on both the assessment to the increased confinement regime and the confinement quality itself.

Then, a theoretical framework has been established based on time averaged turbulent spectra of the electrostatic potential and the density in the case of interchange turbulence. This paradigm offers an alternative description of the edge turbulent features to the intermittent filamentary point of view. This description includes the interplay of the turbulence with background sheared flows through the turbulence saturation by the flow and the flow generation from the turbulent Reynolds tensor. From this spectral model, we derived predictions for the main transport observables such as the potential and density fluctuation levels and the radial particle flux which are only depending on three parameters : 1) the curvature drive  $g$ , 2) the parallel loss rate  $\sigma_{\parallel}$  due to the current flowing through the sheath at the plasma-wall interaction area and 3) the shearing rate  $\sigma_s$ . Applying this flux model in the opened field lines region results in a

prediction of the SOL density decay length  $\lambda$ . The next step was the inclusion of magnetic shear and shear layer width in the mode tilt model to build a relevant model of turbulence mitigation and flow generation for the plasma periphery region.

Next, this model is verified against a set of 2D flux-driven isothermal simulations using the TOKAM2D code. It results in a quantitative agreement between the mode tilt, the density and potential spectra as well as the transport observables predictions against almost 25 simulations with and without background sheared flows. We conclude on a successful verification of the analytical model. Afterwards, a step by step validation of the model against experimental measurement has been achieved. First, the spectra predictions have been able to reproduce the one measured in the TJ-K torsatron. Second, the transport observables and turbulence features measured in Tore Supra are in quantitative agreement with the model predictions. Finally, the impact of the magnetic topology on the edge rotation profiles measured in WEST is recovered by a model based on the competition between the turbulent flow generation and the neoclassical force recalling the edge velocity towards the neoclassical predictions.

The SOL transport model derived in this thesis is based on simple considerations of the magnetic geometry and density regimes. Nevertheless, it is able to recover qualitatively the experimental scalings of the SOL width and the one measured in WEST with an overestimation of their amplitudes. Furthermore, the model predictions for the SOL width in H-mode of large future devices (ITER and DEMO) are wider than the experimentally based even if we apply a numerical lowering factor to the amplitude to recover the current device measurement. Recent measurement of this SOL width in TCV appeared lower than the established scaling which is also reproduced by the model predictions. Another interesting point comes from the generic feature of the model which allows to include more complex effects in the control parameters  $g$  and  $\sigma_{\parallel}$  such as impact of the magnetic geometry or the density regimes in the parallel dynamics description. Considering the magnetic topology effects on the control parameters results in the recovering of the lowering of the SOL width amplitude occurring when the configuration goes from the limited to the diverted one. The development of a 3-point model for the main conservation relations in the SOL including a simple recycling description allows to include complex collisional

physics offering the ability to recover experimental observations as density shoulder.

The theoretical framework proposed in this work is a first step towards a 0D predictive model of the main confinement and power/particle exhaust features. At the moment, some questions on the applicability of the model are still pending. In particular, the application of the model to the confined region is questionable. Indeed, even if the main instabilities occurring in tokamak plasmas are coming from the interchange mechanisms, complex saturation mechanisms are not taken into accounts such as mode coupling with trapped electrons in Trapped Electron Modes turbulence. Also, the model being isothermal and electrostatic, it neglects the contributions of temperature fluctuations as well as electromagnetic effects which both play a critical role in the closed flux surfaces region. Moreover, the parallel description proposed here is based on the presence of a sheath at the plasma-wall interaction region boundary. In the closed field line regions, resonance and collisional considerations should be involved in the parallel dynamics. However, applying the flux model to the confined plasma allows to build a scaling of the energy confinement time in agreement with the one based on experimental measurement across the overall panel of current magnetic devices. Assuming that the model is able to recover the main physics, radial envelope functions for the control parameters could be estimated thanks to neural networks to palliate this lack of knowledge and predict discharge properties from the plasma and machine parameters.

# **Appendices**



# Appendix A

## Flux divergence ordering

We want to determine which term of the particle flux divergence is dominating in the continuity equation. First, we consider that  $E \times B$  and diamagnetic drift velocities are first order perturbations due to their proportionality to simple gradients of potential or pressure. The polarisation drift velocity being of second order in perturbation, it can be neglected in the particle flux contributions. We recall the drift velocities expressions in terms :

$$\vec{v}_{E \times B} = \frac{\vec{E} \times \vec{B}}{B^2} \quad (\text{A.1})$$

$$\vec{v}_* = \frac{\vec{B} \times \vec{\nabla} p}{nqB^2} \quad (\text{A.2})$$

$$\vec{v}_{pol} = \frac{-m}{qB^2} \left[ \partial_t + (\vec{v}_{E \times B} + \vec{v}_*) \cdot \vec{\nabla} \right] \vec{\nabla} U \quad (\text{A.3})$$

where  $U$  is the electrostatic potential. The perpendicular particle flux divergence reads :

$$\vec{\nabla}_\perp (n(\vec{v}_{E \times B} + \vec{v}_*)) = (\vec{v}_{E \times B} + \vec{v}_*) \vec{\nabla}_\perp n + n \vec{\nabla}_\perp (\vec{v}_{E \times B} + \vec{v}_*) \quad (\text{A.4})$$

$$= \vec{v}_{E \times B} \vec{\nabla}_\perp n + n \vec{\nabla}_\perp (\vec{v}_{E \times B} + \vec{v}_*) \quad (\text{A.5})$$

In order to determine the hierarchy of importance of each term of the flux divergence, we will compare it to the first term corresponding to the  $E \times B$  advection

on the density gradient. To do it we will use the relation :

$$\vec{\nabla} \cdot \left( \frac{\vec{\nabla} f \times \vec{B}}{B^2} \right) = \vec{\nabla} \times \vec{\nabla} f \cdot \frac{\vec{B}}{B^2} - \vec{\nabla} f \cdot \vec{\nabla} \left( \frac{\vec{B}}{B^2} \right) \quad (\text{A.6})$$

$$= -\vec{\nabla} f \cdot \vec{\nabla} \left( \frac{\vec{B}}{B^2} \right) \quad (\text{A.7})$$

$$= -\vec{\nabla} f \cdot \left( \frac{1}{B^2} \vec{\nabla} \times \vec{B} + \vec{B} \times \vec{\nabla} \left( \frac{1}{B^2} \right) \right) \quad (\text{A.8})$$

$$(\text{A.9})$$

Using Maxwell-Ampère's law, we finally obtain :

$$\vec{\nabla} \cdot \left( \frac{\vec{\nabla} f \times \vec{B}}{B^2} \right) = -\vec{B} \cdot \left( \vec{\nabla} \left( \frac{1}{B^2} \right) \times \vec{\nabla} f \right) - \frac{\mu_0}{B^2} \vec{j} \cdot \vec{\nabla} f \quad (\text{A.10})$$

Both  $E \times B$  and diamagnetic drift divergences can be written as eq:[A.10](#). It leads to the same demonstration for both term replacing the  $f$  function by  $U$  or either by  $n$  ( $p$  in an isothermal model). Thus, using  $\vec{j} \times \vec{B} = \vec{\nabla} p$  we obtain:

$$\left| \frac{n \vec{\nabla}_\perp \cdot \vec{v}_{E \times B}}{\vec{v}_{E \times B} \cdot \vec{\nabla}_\perp n} \right| = \left| \frac{n \vec{B} \cdot \left( \vec{\nabla} \left( \frac{1}{B^2} \right) \times \vec{\nabla} U \right)}{\vec{v}_{E \times B} \cdot \vec{\nabla}_\perp n} \right| + \left| \frac{\frac{\mu_0}{B^2} \vec{j} \cdot \vec{\nabla} U}{\vec{v}_{E \times B} \cdot \vec{\nabla}_\perp n} \right| \quad (\text{A.11})$$

$$\approx \left| \frac{n \nabla U / RB}{n \nabla U / BL_n} \right| + \left| \frac{n \mu_0 \nabla U \nabla p / R^3}{n \nabla U / BL_n} \right| \quad (\text{A.12})$$

$$\approx \frac{L_n}{R} + \beta \quad (\text{A.13})$$

In a typical tokamak discharge  $L_n/R$  is about  $(1-10) \times 10^{-3}$  in the scrape-off layer and  $\beta$  values are about  $(1-1000) \times 10^{-6}$ . We can consider that the contributions of the drift velocity divergences are negligible.

# Appendix B

## Curvature parameter $G$ derivation in circular geometry

We will consider toroidal concentric flux surfaces. We will calculate the field line average of the curvature term in the case of inner-wall limited discharges. In this case, the field lines go from the outer mid-plane to the targets situated at the angles  $\pm\Delta\theta = \pm\pi$ . In this case, the coordinates  $(r, \alpha = q\theta - \varphi)$  represent a field line. We also define the curvilinear coordinate along this field line  $z = \int_0^\theta Rq d\theta'$ . In the large aspect ratio limit ( $r/R_0 \ll 1$ ), we can write this coordinate as  $z \approx qR_0\theta$ . Using this relation, we can change of coordinate system from the usual system  $(r, \theta, \varphi)$  to  $(r^*, \alpha, z)$ .

$$\begin{cases} r^* = r \\ \alpha = q\theta - \varphi \\ z = qR_0\theta \end{cases} \longleftrightarrow \begin{cases} r = r^* \\ \theta = z/(qR_0) \\ \varphi = z/R_0 - \alpha \end{cases}$$

The partial derivative in the usual coordinate system can be rewritten in terms of the ones in the field line coordinates and of the magnetic shear  $\hat{s} = \frac{r}{q} \frac{dq}{dr}$ .

$$\begin{cases} \partial_r = \partial_{r^*} + \frac{\hat{s}z}{R_0r^*}\partial_\alpha + \frac{\hat{s}z}{r^*}\partial_z \\ \partial_\theta = q\partial_\alpha + qR_0\partial_z \\ \partial_\varphi = -\partial_\alpha \end{cases}$$

Considering  $r^*$  and  $\alpha$  constant along a field line, the average of a function  $A$  along a field line of length  $2L_\parallel = \Delta\theta qR_0$  in the new coordinate system is given

by :

$$\langle A \rangle_{FL} = \frac{1}{2\Delta\theta q R_0} \int_{-\Delta\theta q R_0}^{\Delta\theta q R_0} A dz \quad (\text{B.1})$$

The field line averaged curvature term  $\langle [n, B^{-1}] \rangle_{FL}$  can be deduced from the partial derivatives, the major radius expression  $R = R_0 + r \cos(\theta)$  and the expression (B.1). Considering that the density and its radial and poloidal gradients are constant along the field lines ( $\partial_z n = 0$ ,  $\partial_z(\partial_r n) = 0$  and  $\partial_z(\partial_\theta n) = 0$ ) so  $q\partial_\alpha n \approx \partial_\theta n$  and that the magnetic field amplitude is given by  $B = \frac{B_0 R_0}{R}$ , this average results in :

$$\langle [n, B^{-1}] \rangle_{FL} = \frac{1}{B_0 R_0} \langle [n, R] \rangle_{FL} \quad (\text{B.2})$$

$$= -\frac{1}{B_0 R_0} \left\langle \sin(\theta) \partial_r + \frac{\cos(\theta)}{r} \partial_\theta \right\rangle_{FL} n \quad (\text{B.3})$$

$$= -\frac{1}{B_0 R_0} \left\langle \sin(\theta) \left( \partial_{r^*} + \frac{\hat{s} q \theta}{r^*} \partial_\alpha \right) + \frac{q \cos(\theta)}{r^*} \partial_\alpha \right\rangle_{FL} n \quad (\text{B.4})$$

$$= \frac{1}{B_0 R_0 r} \frac{(1 + \hat{s}) \sin(\Delta\theta) - \hat{s} \Delta\theta \cos(\Delta\theta)}{\Delta\theta} q \partial_\alpha n \quad (\text{B.5})$$

$$= \frac{\hat{s}}{B_0 R_0 r} q \partial_\alpha n \quad (\text{B.6})$$

$$= \frac{\hat{s}}{B_0 R_0 r} \partial_\theta n \quad (\text{B.7})$$

We finally obtain that in the case of circular inner-wall limited discharges the parameter  $G_0$  is equal to the magnetic shear.

## Appendix C

# Study of the impact of the viscous and diffusive parameters on the TOKAM2D simulations for the model verification

The model developed in this work is based on a spectral approach of the TOKAM2D equations. We assumed that the diffusive and the viscous terms, characterised by the coefficient  $D$  and  $\nu$  respectively, are negligible. Including these effects in the equation of the SSF model leads to the following system :

$$\partial_t(k^2\Phi_k) + k^4\Phi_{k_0}\Phi_k + \nu k^4\Phi_k = gk_y n_k \quad (\text{C.1})$$

$$\partial_t n_k + k^2 n_k \Phi_k + D k^2 n_k = \frac{k_y \Phi_k}{\lambda} \quad (\text{C.2})$$

We clearly see that the viscous term is negligible only if the coefficient  $\nu$  is well lower than the potential perturbation of the dominant mode which is responsible of the turbulent viscosity. This condition is also valid for the diffusive term considering that the modes of interest are close to the dominant mode. The dominant mode potential perturbation  $\Phi_{k_0}$  are of the order of  $10^{-2}$ . To avoid the impact of the diffusive and viscous terms we imposed coefficients of the order of  $10^{-4}$ .

In numerical simulations, these coefficients can be enhanced due to numerical noise. Aiming at evaluating the effective values of these coefficients, we realised

a dedicated simulation with the curvature drive and the parallel losses coefficient  $g$  and  $\sigma_{\parallel}$  set at low values ( $10^{-9}$ ). We imposed a poloidal mode of wavenumber  $k_y = 0.15$  and amplitude  $10^{-3}$  on both potential and density maps (see figure C.1) in order to study its amplitude time evolution. The mode wavenumber has been chosen to be close to the typical  $k_0$  values in edge plasma. This evolution will be characterised by decaying exponential with characteristic times  $\tau_{\Phi} = (\nu k_y^2)^{-1}$  and  $\tau_n = (D k_y^2)^{-1}$  for the potential and density perturbations respectively.

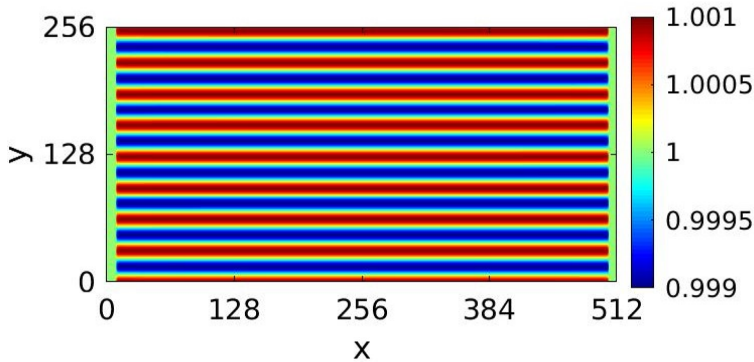


Figure C.1: 2D map of the density exhibiting the imposed mode  $k_y = 0.15$ .

The simulation results do exhibit a time decaying exponential evolution of the mode amplitude (see figure C.2) characterised by effective viscous and diffusive coefficients  $\nu_{eff} = 1.05 \times 10^{-4}$  and  $D_{eff} = 1.07 \times 10^{-4}$  which are close to the ones imposed to the code. Consequently, we can fairly consider that their impact is negligible in our simulation results and that these simulations are relevant for the model verification.

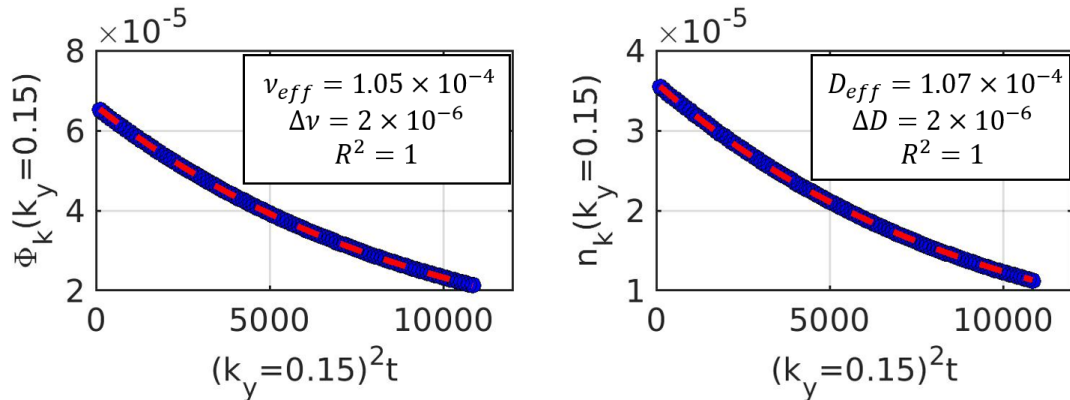


Figure C.2: Time evolution of the density and potential mode  $k_y = 0.15$  from the simulation results showing the exponential fit applied to extract the effective  $\nu$  and  $D$  coefficients.

# **Appendix D**

## **Extracting turbulence features and transport observables from the simulation results**

In order to verify the model, we need to compare its predictions with simulation quantities. This verification will be managed step by step. First, we will measure the density decay lengths from the radial profiles. A characterisation of the structure tilt will then be exposed. Furthermore, turbulent poloidal spectra of potential and density will be obtained applying Fourier transform to the simulation data. We will interest particularly in the dominant mode features. Once the spectral model is validated, a measuring method of fluctuation levels predicted by the model will be shown.

### **D.1 Electrostatic potential, density and particle flux radial profiles**

TOKAM2D simulations are flux-driven. At the beginning the density map is homogeneous and the source starts to increase locally the density. This increase creates a radial density gradient which reaches a threshold. At this point, turbulence starts to develop enough to transport the matter further. This radial transport is balanced by the parallel losses and it leads to a filling of the box reaching an equilibrium. The data process applied in this work starts when this equilibrium is reached. This point is achieved when the mean density in the box is stationary (see figure D.1).

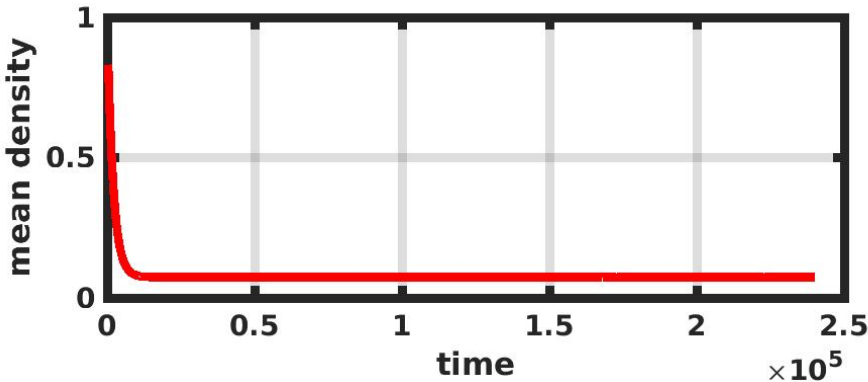


Figure D.1: Time evolution of the mean density in the simulation box

In order to describe the turbulence features with enough statistics, we keep maps in steady-state on 1000 time steps with time steps high enough to describe turbulent oscillations of the mean density.

Averaging the 2D maps on the poloidal direction and on the time window defined above, we built radial profiles of potential, density and radial particle flux normalised to the density  $\langle \Gamma_r \rangle / \langle n \rangle = \langle -n\partial_y \Phi \rangle / \langle n \rangle$ . Examples of these profiles in simulations with and without background sheared flow is given in figure D.2. We can see that the potential imposed in the simulations remains unchanged in average. The density profile exhibits an exponential behaviour as expected. The radial flux is almost constant in a wide radial range  $x \in [30 - 400]$ . It slightly decay at the high radial positions. This point validates the local transport assumption  $\partial_r \Gamma_r = -\Gamma_r/\lambda$  meaning that the only radial dependency of the flux comes from the density profile. In order to build averaged poloidal spectra, we chose radial intervals to apply poloidal Fourier transform before averaging them. The radial interval in simulations without shear is  $x \in [50 - 200]$  due to the constant feature of the normalised radial flux and the distance from the buffer zone and particle source. In the simulations with homogeneous background shear, we chose symmetric intervals around the centre of the imposed potential profile ( $x \in [150 - 350]$ ) to avoid possible impacts of asymmetric flows  $\sigma_s(x - x_0)$ . The treatment used to build the spectra will be detailed further in the manuscript (section D.2).

To evaluate the density decay lengths, exponential fit have been applied on the density profiles in the radial interval defined above at each time step. Then,

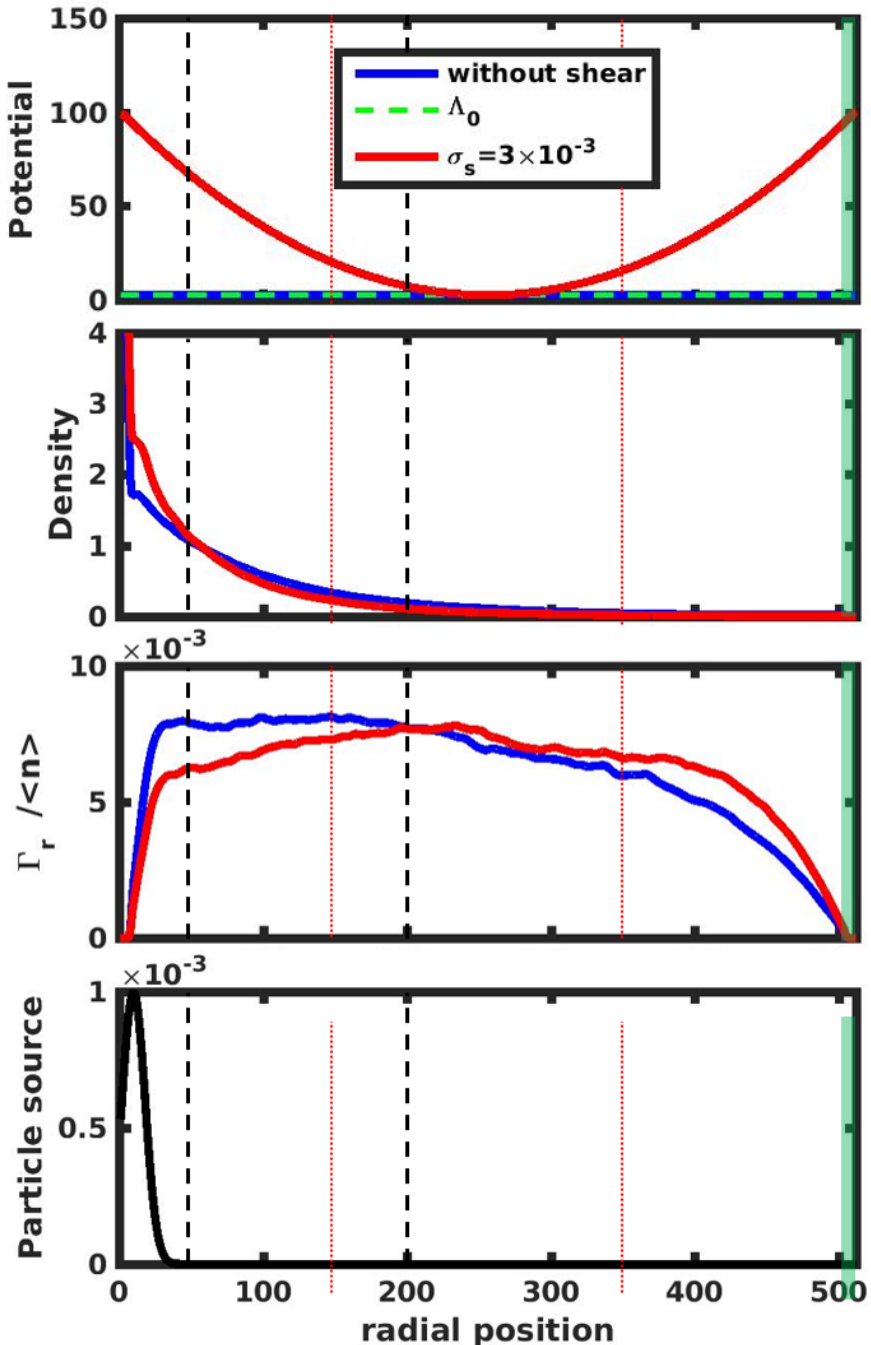


Figure D.2: Radial profiles from TOKAM2D simulations from the top to bottom : electrostatic potential, density, particle flux, particle source. Blue lines represent a case without shear ( $[g = 8 \times 10^{-4}, \sigma_{\parallel} = 1 \times 10^{-4}]$ ) and red lines the same case with a homogeneous shear rate  $\sigma_s = 3 \times 10^{-3}$ . Black dashed lines corresponds to the zone of spectra extraction in the case without shear whereas red dotted lines corresponds to the one for the cases with shear. The green area at the right boundary is the buffer zone.

the retained value of this decay length is the average of the measured values. The standard deviation is chosen as an estimation of the uncertainties since the

probability density function of the values of  $\lambda$  is close to a Gaussian distribution. An example of these fits is given figure D.3. The obtained averaged value will be compared to the model predictions in the attributed sections (sections 3.3.2.1 and 3.3.2.2).

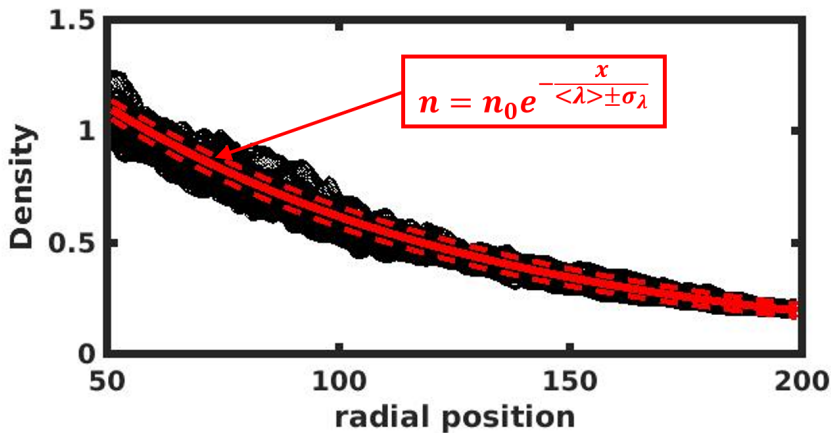


Figure D.3: Radial profiles of the density in black lines. Fit with time averaged decay length in full red line. Red dashed lines represent the profiles deviating from the averaged decay length by a standard deviation. ( $g = 8 \times 10^{-4}$ ,  $\sigma_{\parallel} = 1 \times 10^{-4}$ ,  $\langle \lambda \rangle = 85$  and  $\sigma_{\lambda} = 5.4$ )

## D.2 Poloidal spectra of the density and electrostatic potential

The SSF model is based on the prediction of the density and potential poloidal spectra. The first step in the validation of the model is to verify that the model recovers the spectra extracted from the simulations 2D map. The paradigm of the model is based on time averaged spectra corresponding to a mean turbulence. To follow this point of view, the poloidal spectra are measured in the simulation in the radial intervals mentioned above and then, they are time averaged. An example of the measured spectra is given figure 3.2 in a case without background sheared flow. The grey areas represent the uncertainties on the spectra at each poloidal wavenumber. The probability density function of the spectra at each mode are not Gaussian-like but corresponds to flat curves. The errorbars have been chosen as the maximum and minimum values at each wavenumber.

In order to verify the model against the whole database, comparison points have been chosen as the dominant wave number  $k_0$  and the potential and density perturbation  $\Phi_{k_0}$  and  $n_{k_0}$  represented by the red dot on figure 3.2. These values are compared against the model predictions in the dedicated sections of this manuscript (sections 3.3.2.1 and 3.3.2.2). The uncertainties on the potential and density perturbations are described in the previous paragraph. Concerning the uncertainty on the dominant mode wavenumber, it is imposed by the box size of the simulation  $\Delta k_y = \frac{2\pi}{N_y}$ .

### D.3 Structure tilt characterisation

In the case of turbulence plunged in a background sheared flow, the spectral model needs the description of the tilt of the structure. This inclination has been probed in the simulation results using two methods. The first one consists in a 2D Fourier transform and the second one is based on the radial variation of the phase of the turbulent perturbations. Both are retained in the final database.

- **2D Fourier transform :** We obtained 2D spectra applying a Fourier transform in the radial and poloidal directions at all the time steps of the simulation results. Then we time averaged these 2D maps in wavenumbers according to the SSF model paradigm. In the case of a simulation without background sheared flow, this spectrum is composed of two lobes centered on the  $k_x$  axis. Introducing the background sheared flows leads to the tilt of the structure which is observed on the 2D map in the Fourier space  $(k_x, k_y)$  as an elongation of the lobe following a linear curve of slope given by the tilt  $\frac{k_x}{k_y}$  (see figure D.4). Aiming at measuring this tilt, two ways can be used. First, extracting the value of the radial wavenumber corresponding to the maximum value of the spectrum at a given poloidal wavenumber and dividing it by the poloidal wavenumber. The second one is similar and consists in fitting the radial spectrum with a function to extract the maximum position. These two methods would give equivalent results but the second one is hard to manage due to the complex shape of the spectrum in radial wavenumber. The first method will be retained for the comparison with the model predictions. Examples of  $(k_x, k_y)$  maps of the 2D Fourier transform in the cases with and without background sheared flow are given figure D.4. A radial spectrum is also given in example showing a complex shape.

Interestingly, the potential and density 2D spectra exhibit different tilt with a stronger tilt of the density spectrum. This could be due to a mode envelope contribution  $n_k = n_k^0 \cos(\Lambda_x) \cos(k_x x + k_y y + \varphi_k)$  giving an effective tilt which is the sum of  $k_x$  and  $\Lambda_x$ . Consequently, the relevant value of  $k_x/k_y$  will come from the potential spectrum.

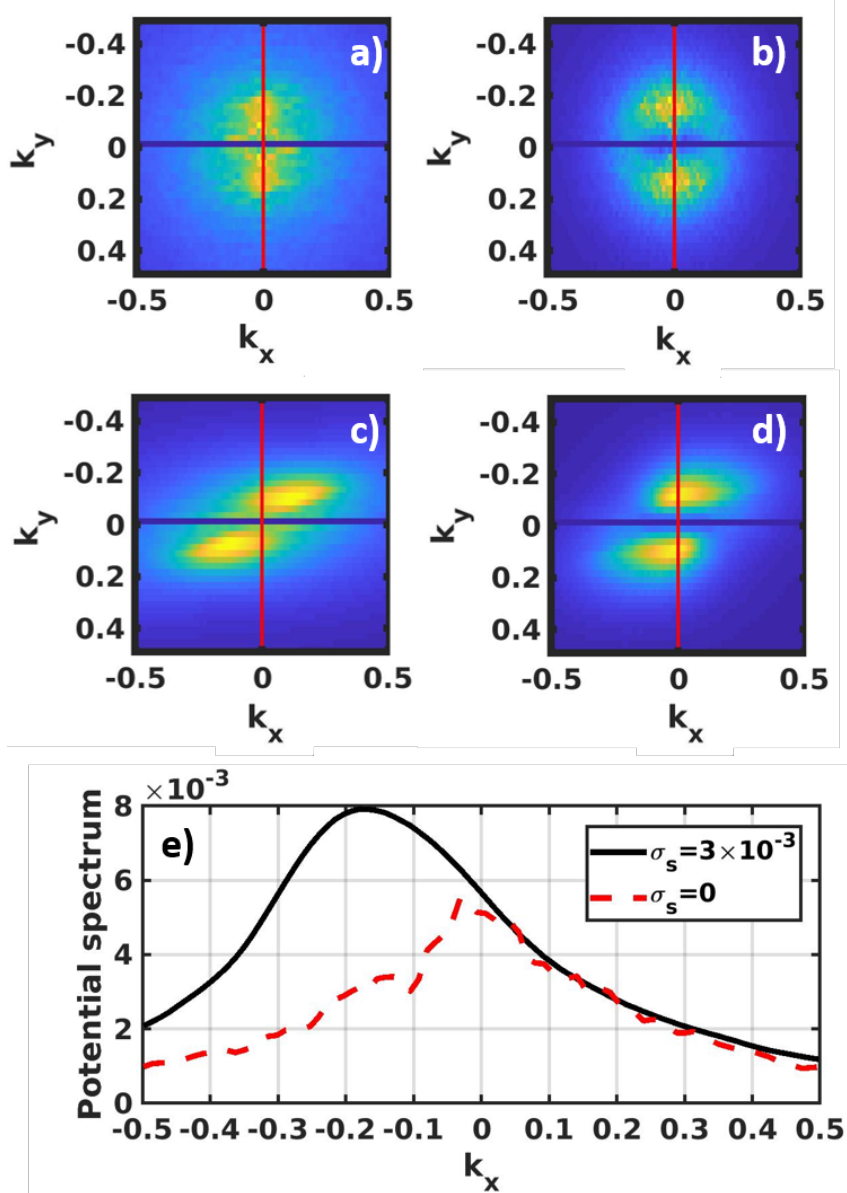


Figure D.4: a) 2D Fourier transform of the density without background sheared flow, b) 2D Fourier transform of the potential without background sheared flow, c) 2D Fourier transform of the density in presence of a background sheared flow, d) 2D Fourier transform of the potential with background sheared flow and e)  $k_x$  spectrum of the potential with (black full line) and without (red dashed line) shear at  $k_y = 0.11$ . Vertical red lines represents the  $k_y = 0$  axis. Case  $[g = 8 \times 10^{-4}, \sigma_{\parallel} = 1 \times 10^{-4}], \sigma_s = [0, 3] \times 10^{-3}$ .

- **Radial phase variation method :** Another way to probe the tilt of the modes is based on the spatial variation of the perturbation phase. Indeed, the perturbation can be written as  $\tilde{\Phi} = \tilde{\Phi}_0 e^{i(k_x x + k_y y)}$ . Locally, the radial variation of the phase of the mode  $k_y$  will be proportional to  $k_x$ . The difference between the phase at the position  $x + \Delta x$  and the one at the position  $x$  is  $k_x \Delta x$ . Applying a poloidal Fourier transform and measuring the slope of the radial variation of the phase is a direct measurement of the radial wavenumber. This method will be constrained at the high values of the poloidal wavenumber due to the fact that the structure of size lower than the minimum poloidal step do not have physical meaning. Another constraint occurs at the low  $k_y$  values. The wavenumbers of sizes higher than a poloidal size will have too low values to measure a  $k_x$  value which are lower than the  $k_y$  ones in our simulations. Averaging the ratio  $k_x/k_y$  in the relevant range of poloidal will lead to a measure of the tilt of the mode and will be compared to the model predictions. In order to have a good precision of this probing process, we time averaged the radial phase variation at different position of the box and we averaged it on the positions for all the poloidal modes. An example of the radial variation of the phase is given figure D.5 underlying the linear feature of the radial profile of the phase.

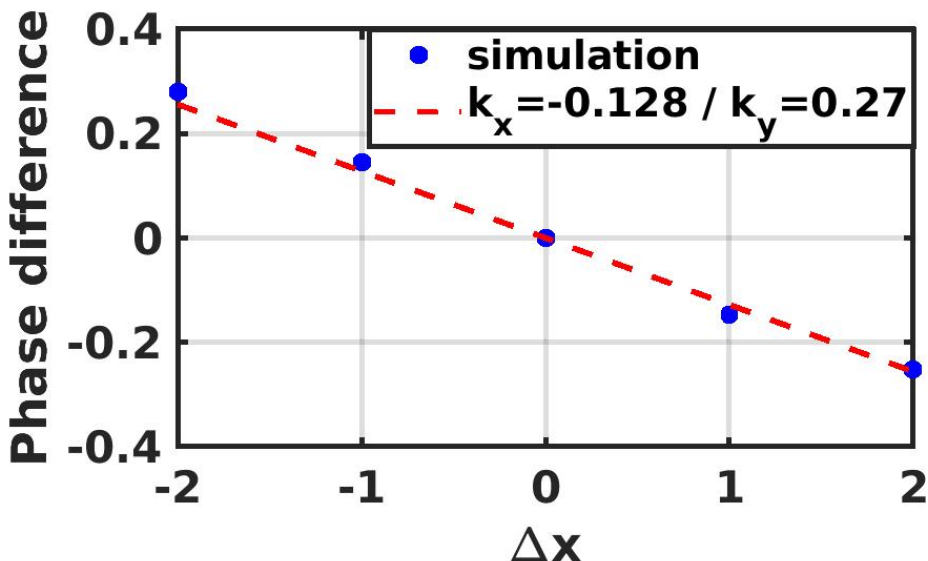


Figure D.5: Radial variation of the perturbation phase of the  $k_y = 0.27$  mode from the simulation results (blue dots) linearly fitted to get the radial wavenumber value (red dashed line). Case [ $g = 8 \times 10^{-4}$ ,  $\sigma_{\parallel} = 1 \times 10^{-4}$ ],  $\sigma_s = 3 \times 10^{-3}$ .

## D.4 Fluctuation levels measurement

Finally, the last transport observable predicted by the model are the potential and density fluctuation levels. To extract it from the simulation results, we measured the standard deviations in time of both quantities in the radial intervals defined earlier and in poloidal coordinates between 30 and 220. The fluctuation level which will be compared to the model predictions is the average of these values and the uncertainty is the standard deviation obtained from the 2D map. This uncertainty is justified, as for the density decay length, by Gaussian-like distribution functions.

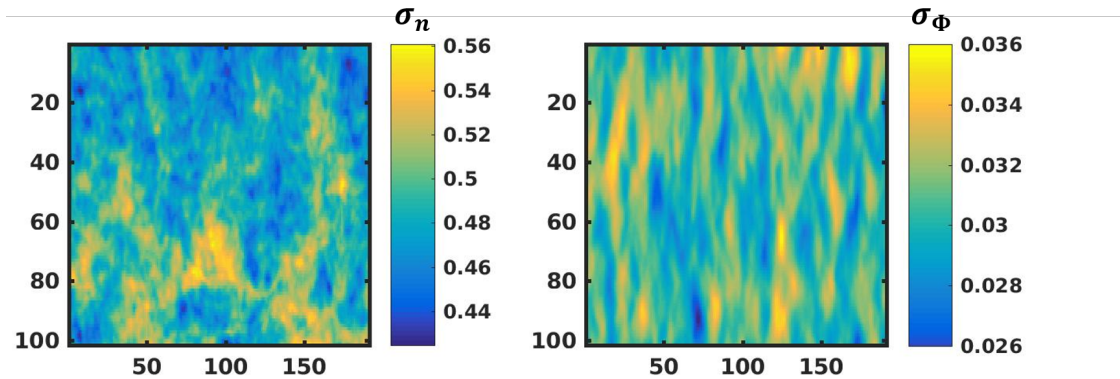


Figure D.6: 2D maps of the fluctuation levels of density (left) and electrostatic potential (right). Case  $[g = 2.6 \times 10^{-4}, \sigma_{\parallel} = 1.05 \times 10^{-4}, \sigma_s = 0]$

# Appendix E

## Ion and electron radial profiles reconstruction

In order to apply the model of flow generation by the turbulence and input it into the poloidal momentum conservation, we need to reconstruct electron and ion temperature profiles. To that end, we constrained the parameters of modified hyperbolic tangent with the experimental data. The electron temperature is constrained with the ECE data between  $\rho = 0.6$  and  $\rho = 0.9$  and by the temperature at the separatrix given by the Langmuir probes. The ion temperature is constrained by the ion temperature at the separatrix corresponding to the one of the electrons multiplied by a coefficient. The impact of this coefficient on the resulting profiles will be discussed later in this appendix. The ion temperature radial profile is also constrained using the DBS velocity measurements. We assume that under  $\rho = 0.95$ , the rotation profile is given by the neoclassical prediction. This process leads to the ion and electron temperature profiles given figure 3.20. Figure E.1 shows the comparison between the ECE data and the reconstructed electron temperature profiles as well as the comparison between the neoclassical prediction of the velocity from the ion temperature reconstruction against velocity profiles from DBS reflectometry measurements. It shows that the reconstructed profiles quantitatively agree with the experimental data except in the case of low plasma current and USN configuration where the neoclassical prediction of the velocity does not agree with the profile measured by DBS reflectometry. This last point will not be included in the validation of the model prediction of flow generation by the turbulence.

The reconstruction of the temperature profiles is using a coefficient for the ratio of the ion to the electron temperature at the separatrix. In order to understand

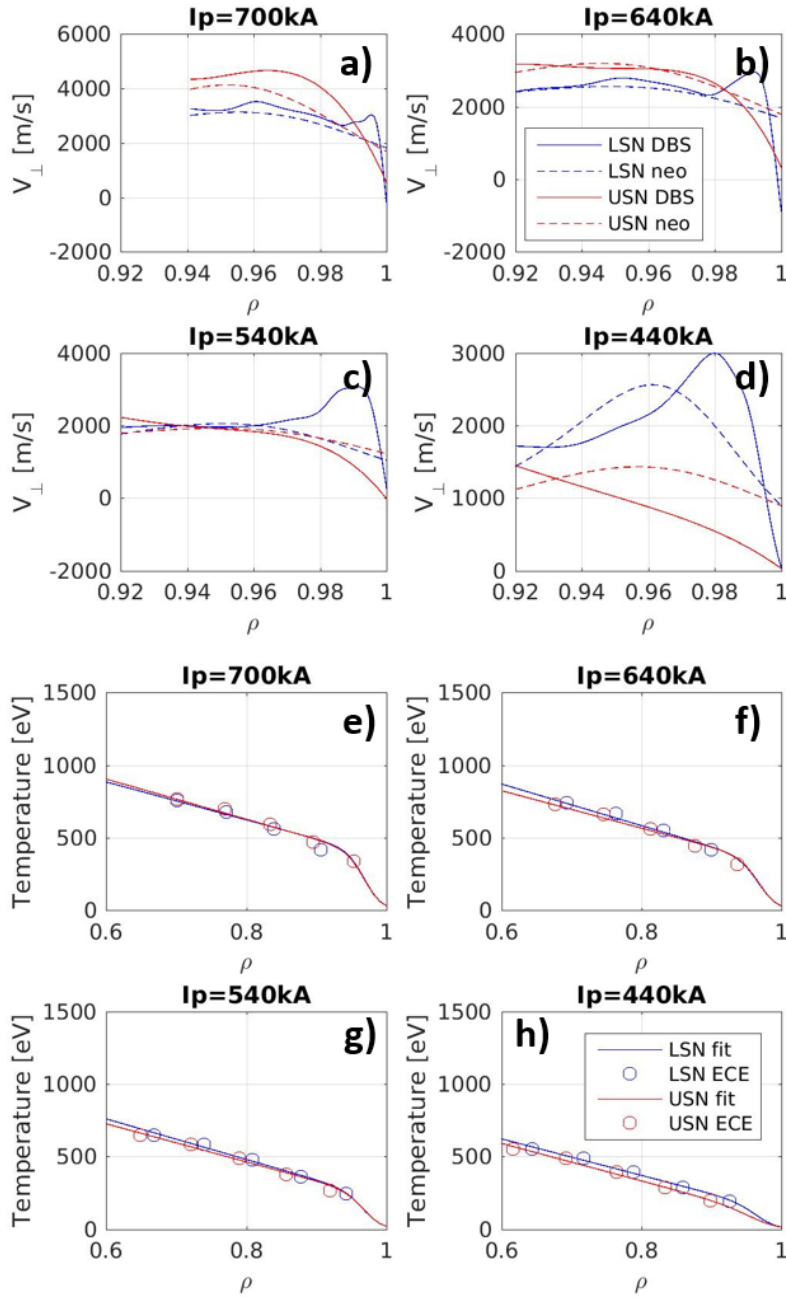


Figure E.1: a)-d) Comparison of the edge rotation profiles measured by DBS reflectometry against neoclassical prediction from the ion temperature profile reconstruction. e)-h) Comparison of the edge temperature profiles measured with the ECE system and the electron temperature profiles reconstructed. The different figures correspond to different plasma current in USN (WEST #55622) and LSN (WEST #55732) configurations.

its impact on the profile reconstruction, we managed a scan in the range of experimental values  $T_i/T_e \in [1 - 2.5]$ . The resulting temperature profiles are given figure E.2. This scan gives an estimation of the uncertainty on the reconstruction

of the ion temperature profiles. We observe a vertical shift of the profiles towards the increasing values (increase of 10% between the minimum and the maximum ion to electron temperature ratio value at the separatrix) when the temperature ratio is increased at the separatrix. The profiles shape remains conserved except in certain cases at low temperature ratio at the separatrix. It is probably due to a starting parameter range for the regression which is not wide enough. Nevertheless, in the case of the comparison managed in this work, this starting parameter range is wide enough, the  $T_i/T_e$  ratio is high enough and the values around are also coherent.

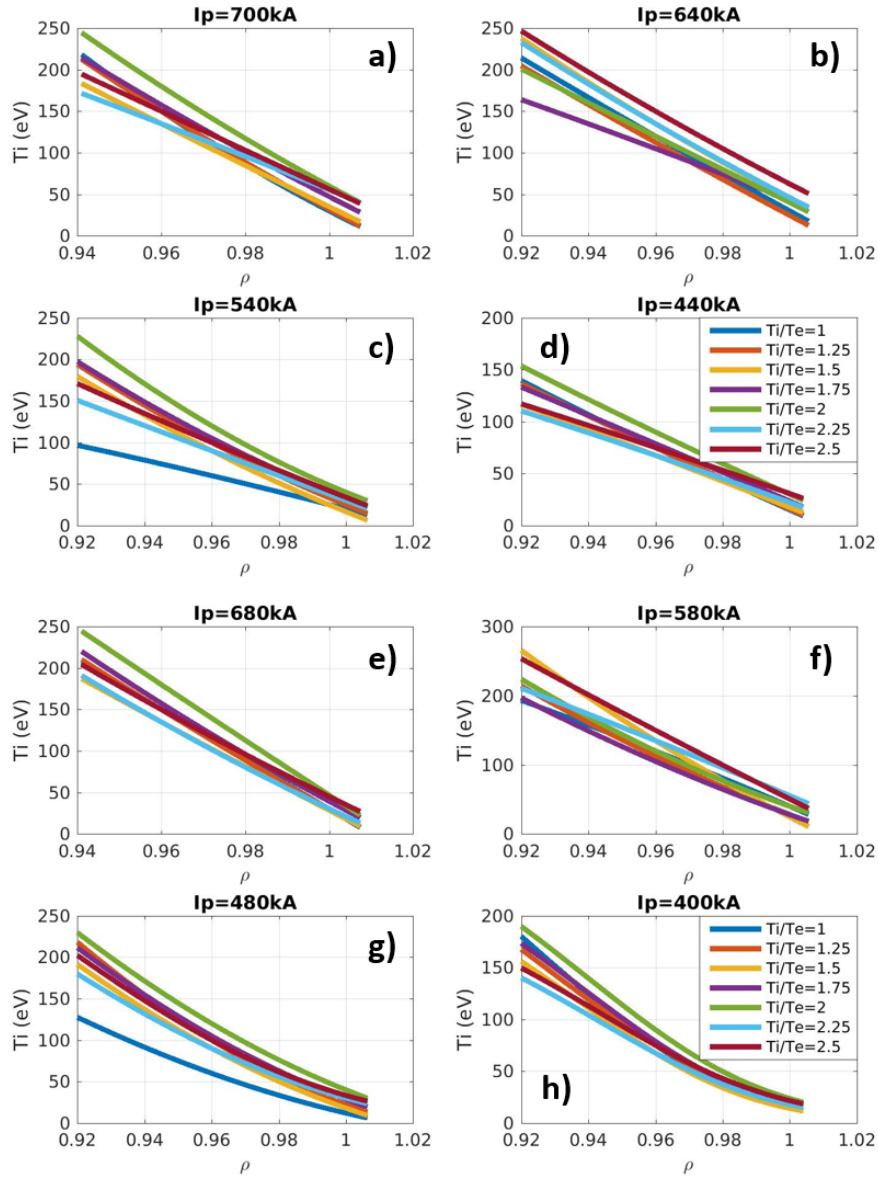


Figure E.2: a)-d) Ion temperature profiles reconstructed at different ion to electron temperature ratio in LSN (WEST #55732). e)-h) Ion temperature profiles reconstructed at different ion to electron temperature ratio in USN (WEST #55622).

# Bibliography

- [1] Jeffrey P. Freidberg. *Plasma Physics and Fusion Energy*. Cambridge University Press, 2007.
- [2] J D Lawson. Some criteria for a power producing thermonuclear reactor. *Proceedings of the Physical Society. Section B*, 70(1):6–10, jan 1957.
- [3] P. R. Thomas, P. Andrew, B. Balet, D. Bartlett, J. Bull, B. de Esch, A. Gibson, C. Gowers, H. Guo, G. Huysmans, T. Jones, M. Keilhacker, R. Koenig, M. Lennholm, P. Lomas, A. Maas, F. Marcus, F. Nave, V. Parail, F. Rimini, J. Strachan, K-D. Zastrow, and N. Zornig. Observation of alpha heating in jet dt plasmas. *Phys. Rev. Lett.*, 80:5548–5551, Jun 1998.
- [4] ITER website. <https://www.iter.org>.
- [5] J Wesson. *Tokamaks*. Oxford University Press, 2004.
- [6] Richard F. Post. Magnetic mirror fusion systems: Characteristics and distinctive features. *UNT Digital Library*, August 1987.
- [7] A. Dinklage, C.D. Beidler, P. Helander, G. Fuchert, H. Maaßberg, K. Rahbarnia, K. Sunn Pedersen, Y. Turkin, R. C. Wolf, A. Alonso, T. Andreeva, B. Blackwell, S. Bozhenkov, B. Buttenschön, A. Czarnecka, F. Effenberg, Y. Feng, J. Geiger, M. Hirsch, U. Höfel, M. Jakubowski, T. Klinger, J. Knauer, G. Kocsis, A. Krämer-Flecken, M. Kubkowska, A. Langenberg, H. P. Laqua, N. Marushchenko, A. Mollén, U. Neuner, H. Niemann, E. Pasch, N. Pablant, L. Rudischhauser, H. M. Smith, O. Schmitz, T. Stange, T. Szepesi, G. Weir, T. Windisch, G. A. Wurden, and Z. Zhang. Magnetic configuration effects on the wendelstein 7-x stellarator. *Nature Phys*, 14:855–860, 2018.
- [8] Jeffrey P. Freidberg. *Ideal MHD*. Cambridge University Press, 2014.
- [9] J. F. Drake, Y. T. Lau, P. N. Guzdar, A. B. Hassam, S. V. Novakovski, B. Rogers, and A. Zeiler. Local negative shear and the formation of transport barriers. *Phys. Rev. Lett.*, 77:494–497, Jul 1996.
- [10] V. D. Shafranov. Plasma Equilibrium in a Magnetic Field. *Reviews of*

- Plasma Physics*, 2:103, January 1966.
- [11] D. Carralero, P. Manz, L. Aho-Mantila, G. Birkenmeier, M. Brix, M. Groth, H. W. Müller, U. Stroth, N. Vianello, and E. Wolfrum. Experimental validation of a filament transport model in turbulent magnetized plasmas. *Phys. Rev. Lett.*, 115:215002, Nov 2015.
  - [12] J. R. Myra, D. A. Russell, and D. A. D'Ippolito. Collisionality and magnetic geometry effects on tokamak edge turbulent transport. i. a two-region model with application to blobs. *Physics of Plasmas*, 13(11):112502, 2006.
  - [13] F. L. Hinton and R. D. Hazeltine. Theory of plasma transport in toroidal confinement systems. *Rev. Mod. Phys.*, 48:239–308, Apr 1976.
  - [14] Per Helander and Dieter J. Sigmar. *Collisional transport in magnetized plasmas*. 2002.
  - [15] F Wagner and U Stroth. Transport in toroidal devices-the experimentalist's view. *Plasma Physics and Controlled Fusion*, 35(10):1321–1371, oct 1993.
  - [16] Paulett C. Liewer. Measurements of microturbulence in tokamaks and comparisons with theories of turbulence and anomalous transport. *Nuclear Fusion*, 25(5):543–621, may 1985.
  - [17] A. J. Wootton, B. A. Carreras, H. Matsumoto, K. McGuire, W. A. Peebles, Ch. P. Ritz, P. W. Terry, and S. J. Zweben. Fluctuations and anomalous transport in tokamaks. *Physics of Fluids B: Plasma Physics*, 2(12):2879–2903, 1990.
  - [18] X. Garbet. Instabilités, turbulence et transport dans un plasma magnétisé. HDR, 2001.
  - [19] P. C. Stangeby. *The Plasma Boundary of Magnetic Fusion Devices*. 2000.
  - [20] Yanick Sarazin. *Etude de la turbulence de bord dans les plasmas de tokamaks*. PhD thesis, 1997. Thèse de doctorat dirigée par Pelletier, Guy Physique Université Joseph Fourier (Grenoble) 1997.
  - [21] Y. Sarazin and Ph. Ghendrih. Intermittent particle transport in two-dimensional edge turbulence. *Physics of Plasmas*, 5(12):4214–4228, 1998.
  - [22] F. L. Hinton and C. W. Horton. Amplitude limitation of a collisional drift wave instability. *The Physics of Fluids*, 14(1):116–123, 1971.
  - [23] M. Kocan, R.A. Pitts, G. Arnoux, I. Balboa, P.C. de Vries, R. Dejarnac, I. Furno, R.J. Goldston, Y. Gribov, J. Horacek, M. Komm, B. Labit, B. LaBombard, C.J. Lasnier, R. Mitteau, F. Nespoli, D. Pace, R. Panek,

- P.C. Stangeby, J.L. Terry, C. Tsui, and P. Vondracek. Impact of a narrow limiter SOL heat flux channel on the ITER first wall panel shaping. *Nuclear Fusion*, 55(3):033019, feb 2015.
- [24] D. D. Ryutov. Geometrical properties of a “snowflake” divertor. *Physics of Plasmas*, 14(6):064502, 2007.
- [25] O Pan, T Lunt, M Wischmeier, and D Coster and. SOLPS simulations of detachment in a snowflake configuration for the future upper divertor in ASDEX upgrade. *Plasma Physics and Controlled Fusion*, 60(8):085005, jun 2018.
- [26] B. Covele, M. Kotschenreuther, S. Mahajan, P. Valanju, A. Leonard, J. Watkins, M. Makowski, M. Fenstermacher, and H. Si. Increased heat dissipation with the x-divertor geometry facilitating detachment onset at lower density in DIII-d. *Nuclear Fusion*, 57(8):086017, jun 2017.
- [27] F. Wagner, G. Becker, K. Behringer, D. Campbell, A. Eberhagen, W. Engelhardt, G. Fussmann, O. Gehre, J. Gernhardt, G. v. Gierke, G. Haas, M. Huang, F. Karger, M. Keilhacker, O. Klüber, M. Kornherr, K. Lackner, G. Lisitano, G. G. Lister, H. M. Mayer, D. Meisel, E. R. Müller, H. Murrmann, H. Niedermeyer, W. Poschenrieder, H. Rapp, H. Röhr, F. Schneider, G. Siller, E. Speth, A. Stäbler, K. H. Steuer, G. Venus, O. Vollmer, and Z. Yü. Regime of improved confinement and high beta in neutral-beam-heated divertor discharges of the asdex tokamak. *Phys. Rev. Lett.*, 49:1408–1412, Nov 1982.
- [28] G. T. Hoang, C. Bourdelle, X. Garbet, G. Antar, R. V. Budny, T. Aniel, V. Basiuk, A. Bécoulet, P. Devynck, J. Lasalle, G. Martin, F. Saint-Laurent, and the Tore Supra Team. Internal transport barrier with ion-cyclotron-resonance minority heating on tore supra. *Phys. Rev. Lett.*, 84:4593–4596, May 2000.
- [29] D Frigione, L Garzotti, C. D Challis, M. De Baar, P. De Vries, M Brix, X Garbet, N Hawkes, A Thyagaraja, L Zabeo, and JET EFDA contributors. Pellet injection and high density ITB formation in JET advanced tokamak plasmas. *Nuclear Fusion*, 47(2):74–84, jan 2007.
- [30] Y. Ma, J.W. Hughes, A.E. Hubbard, B. LaBombard, R.M. Churchill, T. Golfinopolous, N. Tsujii, and E.S. Marmar. Scaling of h-mode threshold power and I-h edge conditions with favourable ion grad-bdrift in alcator c-mod tokamak. *Nuclear Fusion*, 52(2):023010, jan 2012.
- [31] H. Biglari, P. H. Diamond, and P. W. Terry. Influence of sheared poloidal

- rotation on edge turbulence. *Physics of Fluids B: Plasma Physics*, 2(1):1–4, 1990.
- [32] Keith H. Burrell. Tests of causality: Experimental evidence that sheared  $\mathbf{e} \times \mathbf{b}$  flow alters turbulence and transport in tokamaks. *Physics of Plasmas*, 6(12):4418–4435, 1999.
- [33] J Schirmer, G.D Conway, H Zohm, W Suttrop, and the ASDEX Upgrade Team. The radial electric field and its associated shear in the ASDEX upgrade tokamak. *Nuclear Fusion*, 46(9):S780–S791, aug 2006.
- [34] Y R Martin, T Takizuka, and the ITPA CDBM H-mode Threshold Data Group. Power requirement for accessing the h-mode in ITER. *Journal of Physics: Conference Series*, 123:012033, jul 2008.
- [35] C. Bourdelle. Staged approach towards physics-based I-h transition models. *Nuclear Fusion*, 60(10):102002, sep 2020.
- [36] F. Ryter, L. Barrera Orte, B. Kurzan, R.M. McDermott, G. Tardini, E. Viezzer, M. Bernert, and R. Fischer and. Experimental evidence for the key role of the ion heat channel in the physics of the I-h transition. *Nuclear Fusion*, 54(8):083003, may 2014.
- [37] M. Schmidtmayr, J.W. Hughes, F. Ryter, E. Wolfrum, N. Cao, A.J. Creely, N. Howard, A.E. Hubbard, Y. Lin, M.L. Reinke, J.E. Rice, E.A. Tolman, S. Wukitch, Y. Ma, and and. Investigation of the critical edge ion heat flux for I-h transitions in alcator c-mod and its dependence on BT. *Nuclear Fusion*, 58(5):056003, mar 2018.
- [38] P. Gohil, T.E. Evans, M.E. Fenstermacher, J.R. Ferron, T.H. Osborne, J.M. Park, O. Schmitz, J.T. Scoville, and E.A. Unterberg. L-h transition studies on DIII-d to determine h-mode access for operational scenarios in ITER. *Nuclear Fusion*, 51(10):103020, aug 2011.
- [39] Y Andrew, T M Biewer, K Crombe, D Keeling, E de la Luna, C Giroud, N C Hawkes, M Kempenaars, A Korotkov, A Meigs, Y R Martin, A Murari, I Nunes, R Sartori, and T Tala and. H-mode access on JET and implications for ITER. *Nuclear Fusion*, 50(12):124053, nov 2008.
- [40] B. LaBombard, J. E. Rice, A. E. Hubbard, J. W. Hughes, M. Greenwald, R. S. Granetz, J. H. Irby, Y. Lin, B. Lipschultz, E. S. Marmar, K. Marr, D. Mossessian, R. Parker, W. Rowan, N. Smick, J. A. Snipes, J. L. Terry, S. M. Wolfe, and S. J. Wukitch. Transport-driven scrape-off layer flows and the x-point dependence of the I-h power threshold in alcator c-mod. *Physics of Plasmas*, 12(5):056111, 2005.

- [41] A. Marinoni, M. E. Austin, A. W. Hyatt, M. L. Walker, J. Candy, C. Chrystal, C. J. Lasnier, G. R. McKee, T. Odstrčil, C. C. Petty, M. Porkolab, J. C. Rost, O. Sauter, S. P. Smith, G. M. Staebler, C. Sung, K. E. Thome, A. D. Turnbull, and L. Zeng. H-mode grade confinement in I-mode edge plasmas at negative triangularity on dIII-D. *Physics of Plasmas*, 26(4):042515, 2019.
- [42] I. Cziegler, P. H. Diamond, N. Fedorczak, P. Manz, G. R. Tynan, M. Xu, R. M. Churchill, A. E. Hubbard, B. Lipschultz, J. M. Sierchio, J. L. Terry, and C. Theiler. Fluctuating zonal flows in the i-mode regime in alcator c-mod. *Physics of Plasmas*, 20(5):055904, 2013.
- [43] T. Happel, P. Manz, F. Ryter, P. Hennequin, A. Hetzenegger, G.D. Conway, L. Guimarais, C. Honoré, U. Stroth, and E. Viezzer and. Turbulence intermittency linked to the weakly coherent mode in ASDEX upgrade i-mode plasmas. *Nuclear Fusion*, 56(6):064004, may 2016.
- [44] P. Manz, P. Lauber, V.E. Nikolaeva, T. Happel, F. Ryter, G. Birkenmeier, A. Bogomolov, G.D. Conway, M.E. Manso, M. Maraschek, D. Prisiazhniuk, and E. Viezzer. Geodesic oscillations and the weakly coherent mode in the i-mode of ASDEX upgrade. *Nuclear Fusion*, 55(8):083004, jun 2015.
- [45] E. Viezzer. Access and sustainment of naturally ELM-free and small-ELM regimes. *Nuclear Fusion*, 58(11):115002, sep 2018.
- [46] E. Trier, L.-G. Eriksson, P. Hennequin, C. Fenzi, C. Bourdelle, G. Falchetto, X. Garbet, T. Aniel, F. Clairet, and R. Sabot. Radial electric field measurement in a tokamak with magnetic field ripple. *Nuclear Fusion*, 48(9):092001, aug 2008.
- [47] C. Fenzi, X. Garbet, E. Trier, P. Hennequin, C. Bourdelle, T. Aniel, G. Colledani, P. Devynck, C. Gil, Ö. Gürcan, L. Manenc, M. Schneider, and J.-L. Segui and. On plasma rotation with toroidal magnetic field ripple and no external momentum input. *Nuclear Fusion*, 51(10):103038, sep 2011.
- [48] T. Kobayashi. The physics of the mean and oscillating radial electric field in the I-h transition: the driving nature and turbulent transport suppression mechanism. *Nuclear Fusion*, 60(9):095001, jul 2020.
- [49] K. C. Shaing. An estimate of the ion orbit loss rate in tokamaks. *Physics of Fluids B: Plasma Physics*, 4(10):3310–3315, 1992.
- [50] J. S. deGrassie, J. A. Boedo, and B. A. Grierson. Thermal ion orbit loss and radial electric field in dIII-D. *Physics of Plasmas*, 22(8):080701, 2015.
- [51] Robert W. Brzozowski, Frank Jenko, Roberto Bilato, and Marco Cavedon.

- A geometric model of ion orbit loss under the influence of a radial electric field. *Physics of Plasmas*, 26(4):042511, 2019.
- [52] Eun-jin Kim and P. H. Diamond. Dynamics of zonal flow saturation in strong collisionless drift wave turbulence. *Physics of Plasmas*, 9(11):4530–4539, 2002.
- [53] K. Miki, P. H. Diamond, S. H. Hahn, W. W. Xiao, Ö. D. Gürcan, and G. R. Tynan. Physics of stimulated  $l \rightarrow h$  transitions. *Phys. Rev. Lett.*, 110:195002, May 2013.
- [54] L. Chôné, P. Beyer, Y. Sarazin, G. Fuhr, C. Bourdelle, and S. Benkadda. L-h transition dynamics in fluid turbulence simulations with neoclassical force balance. *Physics of Plasmas*, 21(7):070702, 2014.
- [55] L. Chôné, P. Beyer, Y. Sarazin, G. Fuhr, C. Bourdelle, and S. Benkadda. Mechanisms and dynamics of the external transport barrier formation in non-linear plasma edge simulations. 55(7):073010, jun 2015.
- [56] U Stroth, P Manz, and M Ramisch. On the interaction of turbulence and flows in toroidal plasmas. *Plasma Physics and Controlled Fusion*, 53(2):024006, jan 2011.
- [57] X. Garbet, J. Abiteboul, E. Trier, Ö. Gürcan, Y. Sarazin, A. Smolyakov, S. Allfrey, C. Bourdelle, C. Fenzi, V. Grandgirard, P. Ghendrih, and P. Hennequin. Entropy production rate in tokamaks with nonaxisymmetric magnetic fields. *Physics of Plasmas*, 17(7):072505, 2010.
- [58] C. Bourdelle, X. Garbet, F. Imbeaux, A. Casati, N. Dubuit, R. Guirlet, and T. Parisot. A new gyrokinetic quasilinear transport model applied to particle transport in tokamak plasmas. *Physics of Plasmas*, 14(11):112501, 2007.
- [59] D. A. D'Ippolito, J. R. Myra, and S. J. Zweben. Convective transport by intermittent blob-filaments: Comparison of theory and experiment. *Physics of Plasmas*, 18(6):060501, 2011.
- [60] O. E. Garcia. Stochastic modeling of intermittent scrape-off layer plasma fluctuations. *Phys. Rev. Lett.*, 108:265001, Jun 2012.
- [61] F.D. Halpern and P. Ricci. Velocity shear, turbulent saturation, and steep plasma gradients in the scrape-off layer of inner-wall limited tokamaks. *Nuclear Fusion*, 57(3):034001, dec 2016.
- [62] J. R. Myra, D. A. Russell, and S. J. Zweben. Theory based scaling of edge turbulence and implications for the scrape-off layer width. *Physics of Plasmas*, 23(11):112502, 2016.

- [63] A. Scarabosio, T. Eich, A. Herrmann, and B. Sieglin. Outer target heat fluxes and power decay length scaling in I-mode plasmas at jet and aug. *Journal of Nuclear Materials*, 438:S426–S430, 2013. Proceedings of the 20th International Conference on Plasma-Surface Interactions in Controlled Fusion Devices.
- [64] T. Eich, A.W. Leonard, R.A. Pitts, W. Fundamenski, R.J. Goldston, T.K. Gray, A. Herrmann, A. Kirk, A. Kallenbach, O. Kardaun, A.S. Kukushkin, B. LaBombard, R. Maingi, M.A. Makowski, A. Scarabosio, B. Sieglin, J. Terry, A. Thornton, and and. Scaling of the tokamak near the scrape-off layer h-mode power width and implications for ITER. *Nuclear Fusion*, 53(9):093031, aug 2013.
- [65] J Horacek, R A Pitts, J Adamek, G Arnoux, J-G Bak, S Brezinsek, M Dimtrova, R J Goldston, J P Gunn, J Havlicek, S-H Hong, F Janky, B LaBombard, S Marsen, G Maddaluno, L Nie, V Pericoli, Tsv Popov, R Panek, D Rudakov, J Seidl, D S Seo, M Shimada, C Silva, P C Stangeby, B Viola, P Vondracek, H Wang, G S Xu, and Y Xu and. Multi-machine scaling of the main SOL parallel heat flux width in tokamak limiter plasmas. *Plasma Physics and Controlled Fusion*, 58(7):074005, may 2016.
- [66] D. Carralero, J. Madsen, S.A. Artene, M. Bernert, G. Birkenmeier, T. Eich, G. Fuchert, F. Laggner, V. Naulin, P. Manz, N. Vianello, and E. Wolfrum. A study on the density shoulder formation in the sol of h-mode plasmas. *Nuclear Materials and Energy*, 12:1189–1193, 2017. Proceedings of the 22nd International Conference on Plasma Surface Interactions 2016, 22nd PSI.
- [67] A. Wynn, B. Lipschultz, I. Cziegler, J. Harrison, A. Jaervinen, G. F. Matthews, J. Schmitz, B. Tal, M. Brix, C. Guillemaut, D. Frigione, A. Huber, E. Joffrin, U. Kruzei, F. Militello, A. Nielsen, N.R. Walkden, and S. Wiesen and. Investigation into the formation of the scrape-off layer density shoulder in JET ITER-like wall I-mode and h-mode plasmas. *Nuclear Fusion*, 58(5):056001, feb 2018.
- [68] D. Brunner, B. LaBombard, A.Q. Kuang, and J.L. Terry. High-resolution heat flux width measurements at reactor-level magnetic fields and observation of a unified width scaling across confinement regimes in the alcator c-mod tokamak. *Nuclear Fusion*, 58(9):094002, jul 2018.
- [69] D.L. Rudakov, J.A. Boedo, R.A. Pitts, G.L. Jackson, C.J. Lasnier, A.W. Leonard, R.A. Moyer, P.C. Stangeby, G.R. Tynan, and J.G. Watkins. Sol

- width in limited versus diverted discharges in diii-d. *Journal of Nuclear Materials*, 415(1, Supplement):S387–S390, 2011. Proceedings of the 19th International Conference on Plasma-Surface Interactions in Controlled Fusion.
- [70] M Faitsch, R Maurizio, A Gallo, S Coda, T Eich, B Labit, A Merle, H Reimerdes, B Sieglin, C Theiler, et al. Dependence of the I-mode scrape-off layer power fall-off length on the upper triangularity in tcv. *Plasma Physics and Controlled Fusion*, 60(4):045010, 2018.
- [71] Federico Nespoli, Benoît Labit, Ivo Furno, Jan Horacek, CK Tsui, JA Boedo, Roberto Maurizio, Holger Reimerdes, C Theiler, Paolo Ricci, et al. Understanding and suppressing the near scrape-off layer heat flux feature in inboard-limited plasmas in tcv. *Nuclear Fusion*, 57(12):126029, 2017.
- [72] S. Tsuji, K. Ushigusa, Y. Ikeda, T. Imai, T. Itami, M. Nemoto, K. Nagashima, Y. Koide, Y. Kawano, T. Fukuda, T. Kondoh, M. Shimada, H. Nakamura, O. Naito, H. Yoshida, T. Nishitani, H. Kubo, K. Tobita, Y. Kusama, S. Ishida, M. Sato, N. Isei, T. Sugie, N. Miya, R. Yoshino, and K. Uehara. Observation of the limiter h mode in the jt-60 tokamak with lower-hybrid current drive. *Phys. Rev. Lett.*, 64:1023–1026, Feb 1990.
- [73] A. H. Nielsen, M. Jens, G. S. Xu, N. Volker, Jens Juul Rasmussen, and Yan Ning. 2d fluid simulations of interchange turbulence with ion dynamics. volume 37D. European Physical Society, 2013. 40th European Physical Society Conference on Plasma Physics, 40th EPS ; Conference date: 01-07-2013 Through 05-07-2013.
- [74] N. Fedorczak, J.P. Gunn, N. Nace, A. Gallo, C. Baudoin, H. Bufferand, G. Ciraolo, Th. Eich, Ph. Ghendrih, and P. Tamain. Width of turbulent sol in circular plasmas: A theoretical model validated on experiments in tore supra tokamak. *Nuclear Materials and Energy*, 12:838–843, 2017. Proceedings of the 22nd International Conference on Plasma Surface Interactions 2016, 22nd PSI.
- [75] N. Fedorczak, A. Gallo, P. Tamain, H. Bufferand, G. Ciraolo, and Ph. Ghendrih. On the dynamics of blobs in scrape-off layer plasma: Model validation from two-dimensional simulations and experiments in tore supra. *Contributions to Plasma Physics*, 58(6-8):471–477, 2018.
- [76] H. Bufferand, B. Bensiali, J. Bucalossi, G. Ciraolo, P. Genesio, Ph. Ghendrih, Y. Marandet, A. Paredes, F. Schwander, E. Serre, and P. Tamain.

- Near wall plasma simulation using penalization technique with the transport code soledge2d-eirene. *Journal of Nuclear Materials*, 438:S445–S448, 2013. Proceedings of the 20th International Conference on Plasma-Surface Interactions in Controlled Fusion Devices.
- [77] I. H. Hutchinson. Ion collection by probes in strong magnetic fields with plasma flow. *Phys. Rev. A*, 37:4358–4366, Jun 1988.
  - [78] M Kočan, J P Gunn, J-Y Pascal, G Bonhomme, C Fenzi, E Gauthier, and J-L Segui. Edge ion-to-electron temperature ratio in the tore supra tokamak. *Plasma Physics and Controlled Fusion*, 50(12):125009, nov 2008.
  - [79] B. LaBombard. An interpretation of fluctuation induced transport derived from electrostatic probe measurements. *Physics of Plasmas*, 9(4):1300–1311, 2002.
  - [80] N. Fedorczak. *Experimental investigation of turbulent transport at the edge of a tokamak plasma*. PhD dissertation, 2010.
  - [81] R Kumar and S.K Saha. Temperature fluctuations and turbulent transport at the edge of the SINP tokamak. *Nuclear Fusion*, 43(7):622–628, jul 2003.
  - [82] J. A. Boedo, D. L. Rudakov, R. A. Moyer, G. R. McKee, R. J. Colchin, M. J. Schaffer, P. G. Stangeby, W. P. West, S. L. Allen, T. E. Evans, R. J. Fonck, E. M. Hollmann, S. Krasheninnikov, A. W. Leonard, W. Nevins, M. A. Mahdavi, G. D. Porter, G. R. Tynan, D. G. Whyte, and X. Xu. Transport by intermittency in the boundary of the dIII-D tokamak. *Physics of Plasmas*, 10(5):1670–1677, 2003.
  - [83] D. L. Rudakov, J. A. Boedo, R. A. Moyer, S. Krasheninnikov, A. W. Leonard, M. A. Mahdavi, G. R. McKee, G. D. Porter, P. C. Stangeby, J. G. Watkins, W. P. West, D. G. Whyte, and G. Antar. Fluctuation-driven transport in the DIII-D boundary. *Plasma Physics and Controlled Fusion*, 44(6):717–731, June 2002.
  - [84] F. Clairet, C. Bottreau, A. Medvedeva, D. Molina, G. D. Conway, A. Silva, and U. Stroth.  $1\mu s$  broadband frequency sweeping reflectometry for plasma density and fluctuation profile measurements. *Review of Scientific Instruments*, 88(11):113506, 2017.
  - [85] R. Nazikian and E. Mazzucato. Reflectometer measurements of density fluctuations in tokamak plasmas (invited). *Review of Scientific Instruments*, 66(1):392–398, 1995.
  - [86] M Hirsch, E Holzhauer, J Baldzuhn, B Kurzan, and B Scott. Doppler reflec-

- tometry for the investigation of propagating density perturbations. *Plasma Physics and Controlled Fusion*, 43(12):1641–1660, oct 2001.
- [87] M Hirsch and E Holzhauer. Doppler reflectometry with optimized temporal resolution for the measurement of turbulence and its propagation velocity. *Plasma Physics and Controlled Fusion*, 46(4):593–609, mar 2004.
- [88] P Hennequin, C Honoré, A Truc, A Quéméneur, C Fenzi-Bonizec, C Bourdelle, X Garbet, G.T Hoang, and the Tore Supra team. Fluctuation spectra and velocity profile from doppler backscattering on tore supra. *Nuclear Fusion*, 46(9):S771–S779, aug 2006.
- [89] G D Conway, J Schirmer, S Klenge, W Suttrop, E Holzhauer, and the AS-DEX Upgrade Team. Plasma rotation profile measurements using doppler reflectometry. *Plasma Physics and Controlled Fusion*, 46(6):951–970, apr 2004.
- [90] L. Vermare, P. Hennequin, Ö. D. Gürcan, C. Bourdelle, F. Clairet, X. Garbet, and R. Sabot. Impact of collisionality on fluctuation characteristics of micro-turbulence. *Physics of Plasmas*, 18(1):012306, 2011.
- [91] C Honoré, P Hennequin, A Truc, and A Quéméneur. Quasi-optical gaussian beam tracing to evaluate doppler backscattering conditions. *Nuclear Fusion*, 46(9):S809–S815, aug 2006.
- [92] T.H. Stix. *Waves in Plasmas*. Am. Inst. of Phys., 1992.
- [93] Steven Weinberg. Eikonal method in magnetohydrodynamics. *Phys. Rev.*, 126:1899–1909, Jun 1962.
- [94] P. Hennequin, C. Honoré, A. Truc, A. Quéméneur, N. Lemoine, J.-M. Chareau, and R. Sabot. Doppler backscattering system for measuring fluctuations and their perpendicular velocity on tore supra. *Review of Scientific Instruments*, 75(10):3881–3883, 2004.
- [95] R. Schmidt. Multiple emitter location and signal parameter estimation. *IEEE Transactions on Antennas and Propagation*, 34(3):276–280, 1986.
- [96] L. Vermare, P. Hennequin, Ö.D. Gürcan, and the Tore Supra Team. Detection of geodesic acoustic mode oscillations, using multiple signal classification analysis of doppler backscattering signal on tore supra. 52(6):063008, apr 2012.
- [97] B Chouli, C Fenzi, X Garbet, C Bourdelle, J Decker, T Aniel, J-F Artaud, V Basiuk, F Clairet, G Colledani, R Dumont, D Elbeze, C Gil, P Lotte, and Y Sarazin and. Co- and counter-current rotation in tore supra lower hybrid current drive plasmas. *Plasma Physics and Controlled Fusion*,

- 56(9):095018, jul 2014.
- [98] B Chouli, C Fenzi, X Garbet, C Bourdelle, Y Sarazin, J Rice, T Aniel, J-F Artaud, B Baiocchi, V Basiuk, P Cottier, J Decker, F Imbeaux, M Irishkin, D Mazon, and M Schneider and. Investigations of LHCD induced plasma rotation in tore supra. *Plasma Physics and Controlled Fusion*, 57(12):125007, oct 2015.
- [99] R. Varennes, L. Vermare, X. Garbet, Y. Sarazin, V Grandirard, G. Dif-Pradalier, D. Zarzoso, K. Obrejan, M. Peret, Ph. Ghendrih, and E. Bourne. Impact of non-axisymmetric magnetic field perturbations on flows. In *25th EU-US TTF Conference*, 2021.
- [100] Pascale Hennequin, Laure Vermare, N. Fedorczak, J. Bernardo, Özgür D. Gürcan, Elisée Trier, C. Fenzi, J. Gunn, P. Monier-Garbet, R. Ghendrih, and X. Garbet. The effect of SOL flows on edge and core radial electric field and rotation in Tore Supra. In *37th EPS Conference on Plasma Physics*, number P1.1040, Dublin, Ireland, June 2010.
- [101] A V Chankin, E Delabie, G Corrigan, D Harting, C F Maggi, and H Meyer and. EDGE2d-EIRENE modelling of near SOL e r: possible impact on the h-mode power threshold. *Plasma Physics and Controlled Fusion*, 59(4):045012, mar 2017.
- [102] H. Bufferand, G. Ciraolo, Y. Marandet, J. Bucalossi, Ph. Ghendrih, J. Gunn, N. Mellet, P. Tamain, R. Leybros, N. Fedorczak, F. Schwander, and E. Serre. Numerical modelling for divertor design of the WEST device with a focus on plasma–wall interactions. *Nuclear Fusion*, 55(5):053025, apr 2015.
- [103] C.F. Maggi. Progress in understanding the physics of the h-mode pedestal and ELM dynamics. *Nuclear Fusion*, 50(6):066001, may 2010.
- [104] L. Vermare, P. Hennequin, C. Honoré, M. Peret, G. Dif-Pradalier, X. Garbet, J. Gunn, C. Bourdelle, F. Clairet, J. Morales, R. Dumont, M. Goniche, P. Maget, R. Varennes, and the WEST Team. Formation of the radial electric field profile in the WEST tokamak. *Nuclear Fusion*, 62(2):026002, dec 2021.
- [105] T. Putterich. In *ITPA Transport and confinement*, June 2020.
- [106] F. Clairet, C. Bottreau, J. M. Chareau, M. Paume, and R Sabot. Edge density profile measurements by x-mode reflectometry on tore supra, Oct 2000.
- [107] R. J. Groebner and T. H. Osborne. Scaling studies of the high mode

- pedestal. *Physics of Plasmas*, 5(5):1800–1806, 1998.
- [108] V Ostuni, J Morales, C Bourdelle, J-F Artaud, P Manas, R Dumont, N Fedorczak, M Goniche, P Maget, and Y Sarazin. Confinement properties in the large aspect ratio, full tungsten environment of the WEST tokamak. 25th Joint EU-US TTF Meeting - EU-US Transport Task Force, September 2021. Poster.
- [109] A. Loarte, J. W. Hughes, M. L. Reinke, J. L. Terry, B. LaBombard, D. Brunner, M. Greenwald, B. Lipschultz, Y. Ma, S. Wukitch, and S. Wolfe. High confinement/high radiated power h-mode experiments in alcator c-mod and consequences for international thermonuclear experimental reactor (iter) qdt=10 operation. *Physics of Plasmas*, 18(5):056105, 2011.
- [110] C. Bourdelle, C.F. Maggi, L. Chôné, P. Beyer, J. Citrin, N. Fedorczak, X. Garbet, A. Loarte, F. Millitello, M. Romanelli, and Y. Sarazin and. L to h mode transition: on the role of zeff. *Nuclear Fusion*, 54(2):022001, jan 2014.
- [111] A.E. Hubbard, T. Osborne, F. Ryter, M. Austin, L. Barrera Orte, R.M. Churchill, I. Cziegler, M. Fenstermacher, R. Fischer, S. Gerhardt, R. Groebner, P. Gohil, T. Happel, J.W. Hughes, A. Loarte, R. Maingi, P. Manz, A. Marinoni, E.S. Marmar, R.M. McDermott, G. McKee, T.L. Rhodes, J.E. Rice, L. Schmitz, C. Theiler, E. Viezzer, J.R. Walk, A. White, D. Whyte, S. Wolfe, E. Wolfrum, and Z. Yan and. Multi-device studies of pedestal physics and confinement in the i-mode regime. *Nuclear Fusion*, 56(8):086003, jul 2016.
- [112] G. S. Xu, B. N. Wan, H. Q. Wang, H. Y. Guo, H. L. Zhao, A. D. Liu, V. Naulin, P. H. Diamond, G. R. Tynan, M. Xu, R. Chen, M. Jiang, P. Liu, N. Yan, W. Zhang, L. Wang, S. C. Liu, and S. Y. Ding. First evidence of the role of zonal flows for the  $l-h$  transition at marginal input power in the east tokamak. *Phys. Rev. Lett.*, 107:125001, Sep 2011.
- [113] L. Schmitz, L. Zeng, T. L. Rhodes, J. C. Hillesheim, E. J. Doyle, R. J. Groebner, W. A. Peebles, K. H. Burrell, and G. Wang. Role of zonal flow predator-prey oscillations in triggering the transition to h-mode confinement. *Phys. Rev. Lett.*, 108:155002, Apr 2012.
- [114] J. Cheng, J. Q. Dong, K. Itoh, L. W. Yan, M. Xu, K. J. Zhao, W. Y. Hong, Z. H. Huang, X. Q. Ji, W. L. Zhong, D. L. Yu, S.-I. Itoh, L. Nie, D. F. Kong, T. Lan, A. D. Liu, X. L. Zou, Q. W. Yang, X. T. Ding, X. R. Duan, and Yong Liu. Dynamics of low-intermediate-high-confinement transitions in toroidal

- plasmas. *Phys. Rev. Lett.*, 110:265002, Jun 2013.
- [115] A. J. Brizard and T. S. Hahm. Foundations of nonlinear gyrokinetic theory. *Rev. Mod. Phys.*, 79:421–468, Apr 2007.
- [116] W. W. Lee. Gyrokinetic approach in particle simulation. *The Physics of Fluids*, 26(2):556–562, 1983.
- [117] Zebin Li, Guoya Sun, Ihor Holod, Yong Xiao, Wenlu Zhang, and Zhihong Lin. GTC simulation of ideal ballooning mode in tokamak plasmas. *Plasma Science and Technology*, 15(6):499–505, jun 2013.
- [118] V. Grandgirard, J. Abiteboul, J. Bigot, T. Cartier-Michaud, N. Crouseilles, G. Dif-Pradalier, Ch. Ehrlacher, D. Esteve, X. Garbet, Ph. Ghendrih, G. Latu, M. Mehrenberger, C. Norscini, Ch. Passeron, F. Rozar, Y. Sarazin, E. Sonnendrücker, A. Strugarek, and D. Zarzoso. A 5d gyrokinetic full-f global semi-lagrangian code for flux-driven ion turbulence simulations. *Computer Physics Communications*, 207:35–68, 2016.
- [119] J. Candy and R.E. Waltz. An eulerian gyrokinetic-maxwell solver. *Journal of Computational Physics*, 186(2):545–581, 2003.
- [120] P. Tamain, H. Bufferand, G. Ciraolo, C. Colin, D. Galassi, Ph. Ghendrih, F. Schwander, and E. Serre. The tokam3x code for edge turbulence fluid simulations of tokamak plasmas in versatile magnetic geometries. *Journal of Computational Physics*, 321:606–623, 2016.
- [121] F.D. Halpern, P. Ricci, S. Jolliet, J. Loizu, J. Morales, A. Mosetto, F. Musil, F. Riva, T.M. Tran, and C. Wersal. The gbs code for tokamak scrape-off layer simulations. *Journal of Computational Physics*, 315:388–408, 2016.
- [122] P Ricci, F D Halpern, S Jolliet, J Loizu, A Mosetto, A Fasoli, I Furno, and C Theiler. Simulation of plasma turbulence in scrape-off layer conditions: the GBS code, simulation results and code validation. *Plasma Physics and Controlled Fusion*, 54(12):124047, nov 2012.
- [123] G. M. Staebler, J. E. Kinsey, and R. E. Waltz. A theory-based transport model with comprehensive physics. *Physics of Plasmas*, 14(5):055909, 2007.
- [124] P. B. Snyder, R. J. Groebner, A. W. Leonard, T. H. Osborne, and H. R. Wilson. Development and validation of a predictive model for the pedestal height. *Physics of Plasmas*, 16(5):056118, 2009.
- [125] P. B. Snyder, T. H. Osborne, K. H. Burrell, R. J. Groebner, A. W. Leonard, R. Nazikian, D. M. Orlov, O. Schmitz, M. R. Wade, and H. R. Wilson. The eped pedestal model and edge localized mode-suppressed regimes:

- Studies of quiescent h-mode and development of a model for edge localized mode suppression via resonant magnetic perturbations. *Physics of Plasmas*, 19(5):056115, 2012.
- [126] F. L. Hinton and G. M. Staebler. Particle and energy confinement bifurcation in tokamaks. *Physics of Fluids B: Plasma Physics*, 5(4):1281–1288, 1993.
- [127] K. C. Shaing and E. C. Crume. Bifurcation theory of poloidal rotation in tokamaks: A model for I-h transition. *Phys. Rev. Lett.*, 63:2369–2372, Nov 1989.
- [128] M Tendler. Different scenarios of transitions into improved confinement modes. *Plasma Physics and Controlled Fusion*, 39(12B):B371–B382, dec 1997.
- [129] H. Sugama and M. Wakatani. Radial electric field effect on resistive interchange modes. *Physics of Fluids B: Plasma Physics*, 3(4):1110–1112, 1991.
- [130] X.-H. Wang, P. H. Diamond, and M. N. Rosenbluth. Stability of ion-temperature-gradient-driven modes in the presence of sheared poloidal flows. *Physics of Fluids B: Plasma Physics*, 4(8):2402–2413, 1992.
- [131] G. R. Tynan, R. A. Moyer, M. J. Burin, and C. Holland. On the nonlinear turbulent dynamics of shear-flow decorrelation and zonal flow generation. *Physics of Plasmas*, 8(6):2691–2699, 2001.
- [132] Ö. D. Gürcan. Effect of sheared flow on the growth rate and turbulence decorrelation. *Phys. Rev. Lett.*, 109:155006, Oct 2012.
- [133] B. A. Carreras, V. E. Lynch, L. Garcia, and P. H. Diamond. Resistive pressure-gradient-driven turbulence with self-consistent flow profile evolution. *Physics of Fluids B: Plasma Physics*, 5(5):1491–1505, 1993.
- [134] A S Ware, P W Terry, P H Diamond, and B A Carreras. Transport reduction via shear flow modification of the cross phase. *Plasma Physics and Controlled Fusion*, 38(8):1343–1347, aug 1996.
- [135] G.M. Staebler, J. Candy, R.E. Waltz, J.E. Kinsey, and W.M. Solomon. A new paradigm for  $\mathbf{E} \times \mathbf{v}$  velocity shear suppression of gyro-kinetic turbulence and the momentum pinch. *Nuclear Fusion*, 53(11):113017, sep 2013.
- [136] G. M. Staebler, R. E. Waltz, J. Candy, and J. E. Kinsey. New paradigm for suppression of gyrokinetic turbulence by velocity shear. *Phys. Rev. Lett.*, 110:055003, Jan 2013.
- [137] J. E. Kinsey, R. E. Waltz, and J. Candy. Nonlinear gyrokinetic turbulence

- simulations of  $e \times b$  shear quenching of transport. *Physics of Plasmas*, 12(6):062302, 2005.
- [138] C. F. Figarella, S. Benkadda, P. Beyer, X. Garbet, and I. Voitsekhovitch. Transport reduction by rotation shear in tokamak-edge turbulence. *Phys. Rev. Lett.*, 90:015002, Jan 2003.
- [139] G. Dif-Pradalier, P. H. Diamond, V. Grandgirard, Y. Sarazin, J. Abiteboul, X. Garbet, Ph. Ghendrih, A. Strugarek, S. Ku, and C. S. Chang. On the validity of the local diffusive paradigm in turbulent plasma transport. *Phys. Rev. E*, 82:025401, Aug 2010.
- [140] G. Dif-Pradalier, G. Hornung, Ph. Ghendrih, Y. Sarazin, F. Clairet, L. Vermare, P. H. Diamond, J. Abiteboul, T. Cartier-Michaud, C. Ehrlacher, D. Estève, X. Garbet, V. Grandgirard, Ö. D. Gürcan, P. Hennequin, Y. Kotsuga, G. Latu, P. Maget, P. Morel, C. Norscini, R. Sabot, and A. Storelli. Finding the elusive  $E \times B$  staircase in magnetized plasmas. *Phys. Rev. Lett.*, 114:085004, Feb 2015.
- [141] Ö. D. Gürcan, P. H. Diamond, T. S. Hahm, and R. Singh. Intrinsic rotation and electric field shear. *Physics of Plasmas*, 14(4):042306, 2007.
- [142] N Fedorczak, Ph Ghendrih, P Hennequin, G R Tynan, P H Diamond, and P Manz. Dynamics of tilted eddies in a transversal flow at the edge of tokamak plasmas and the consequences for I-h transition. *Plasma Physics and Controlled Fusion*, 55(12):124024, nov 2013.
- [143] N Fedorczak, P Manz, S Chakraborty Thakur, M Xu, and G R Tynan. Zonal flow shear amplification by depletion of anisotropic potential eddies in a magnetized plasma: idealized models and laboratory experiment. *Plasma Physics and Controlled Fusion*, 55(2):025011, jan 2013.
- [144] R.J. Goldston. Heuristic drift-based model of the power scrape-off width in low-gas-puff h-mode tokamaks. *Nuclear Fusion*, 52(1):013009, dec 2011.
- [145] A. Zeiler, D. Biskamp, J. F. Drake, and B. N. Rogers. Transition from resistive ballooning to  $\eta_i$  driven turbulence in tokamaks. *Physics of Plasmas*, 5(7):2654–2663, 1998.
- [146] T. Eich, P. Manz, R.J. Goldston, P. Hennequin, P. David, M. Faitsch, B. Kurzan, B. Sieglin, E. Wolfrum, and and. Turbulence driven widening of the near-SOL power width in ASDEX upgrade h-mode discharges. *Nuclear Fusion*, 60(5):056016, apr 2020.
- [147] A.O. Brown and R.J. Goldston. Generalization of the heuristic drift sol model for finite collisionality and effect on flow shearing rate vs. inter-

- change growth rate. *Nuclear Materials and Energy*, 27:101002, 2021.
- [148] S. J. Zweben, D. P. Stotler, J. L. Terry, B. LaBombard, M. Greenwald, M. Mutterspaugh, C. S. Pitcher, K. Hallatschek, R. J. Maqueda, B. Rogers, J. L. Lowrance, V. J. Mastrocola, and G. F. Renda. Edge turbulence imaging in the alcator c-mod tokamak. *Physics of Plasmas*, 9(5):1981–1989, 2002.
- [149] M. Agostini, S. J. Zweben, R. Cavazzana, P. Scarin, G. Serianni, R. J. Maqueda, and D. P. Stotler. Study of statistical properties of edge turbulence in the national spherical torus experiment with the gas puff imaging diagnostic. *Physics of Plasmas*, 14(10):102305, 2007.
- [150] A Kirk, N Ben Ayed, G Counsell, B Dudson, T Eich, A Herrmann, B Koch, R Martin, A Meakins, S Saarelma, R Scannell, S Tallents, M Walsh, H R Wilson, and the MAST team. Filament structures at the plasma edge on MAST. *Plasma Physics and Controlled Fusion*, 48(12B):B433–B441, nov 2006.
- [151] O. Grulke, J. L. Terry, B. LaBombard, and S. J. Zweben. Radially propagating fluctuation structures in the scrape-off layer of alcator c-mod. *Physics of Plasmas*, 13(1):012306, 2006.
- [152] J. A. Boedo, D. Rudakov, R. Moyer, S. Krasheninnikov, D. Whyte, G. McKee, G. Tynan, M. Schaffer, P. Stangeby, P. West, S. Allen, T. Evans, R. Fonck, E. Hollmann, A. Leonard, A. Mahdavi, G. Porter, M. Tillack, and G. Antar. Transport by intermittent convection in the boundary of the dIII-D tokamak. *Physics of Plasmas*, 8(11):4826–4833, 2001.
- [153] P. Devynck, P. Ghendrih, and Y. Sarazin. The origin of the long time correlations of the density fluctuations in the scrape-off layer of the tore supra tokamak. *Physics of Plasmas*, 12(5):050702, 2005.
- [154] N. Fedorczak, J.P. Gunn, Ph. Ghendrih, P. Monier-Garbet, and A. Pocheau. Flow generation and intermittent transport in the scrape-off-layer of the tore supra tokamak. *Journal of Nuclear Materials*, 390-391:368–371, 2009. Proceedings of the 18th International Conference on Plasma-Surface Interactions in Controlled Fusion Device.
- [155] Akira Hasegawa and Kunioki Mima. Pseudo-three-dimensional turbulence in magnetized nonuniform plasma. *The Physics of Fluids*, 21(1):87–92, 1978.
- [156] Akira Hasegawa and Masahiro Wakatani. Plasma edge turbulence. *Phys. Rev. Lett.*, 50:682–686, Feb 1983.

- [157] Bruce D. Scott. Drift wave versus interchange turbulence in tokamak geometry: Linear versus nonlinear mode structure. *Physics of Plasmas*, 12(6):062314, 2005.
- [158] S.I. Krasheninnikov. On the origin of plasma density blobs. *Physics Letters A*, 380(46):3905–3907, 2016.
- [159] S.I. Krasheninnikov. On scrape off layer plasma transport. *Physics Letters A*, 283(5):368–370, 2001.
- [160] Federico Nespoli, Patrick Tamain, Nicolas Fedorczak, Hugo Bufferand, Guido Ciraolo, Philippe Ghendrih, Davide Galassi, Raffaele Tatali, Eric Serre, and Yannick Marandet. Filament dynamics in presence of X-point in turbulence simulations. In *APS Division of Plasma Physics Meeting Abstracts*, volume 2019 of *APS Meeting Abstracts*, page UP10.013, January 2019.
- [161] R. Tatali, E. Serre, P. Tamain, D. Galassi, P. Ghendrih, F. Nespoli, H. Bufferand, T. Cartier-Michaud, and G. Ciraolo. Impact of collisionality on turbulence in the edge of tokamak plasma using 3d global simulations. *Nuclear Fusion*, 61(5):056002, mar 2021.
- [162] Ph. Ghendrih, Y. Sarazin, G. Falchetto, X. Garbet, V. Grandgirard, M. Ottaviani, P. Kaw, P. Beyer, and S. Benkadda. Scaling intermittent cross-field particle flux to iter. 20 IAEA fusion energy conference 2004, France, 2004. PLASMA PHYSICS AND FUSION TECHNOLOGY.
- [163] F. Militello, T. Farley, K. Mukhi, N. Walkden, and J. T. Omotani. A two-dimensional statistical framework connecting thermodynamic profiles with filaments in the scrape off layer and application to experiments. *Physics of Plasmas*, 25(5):056112, 2018.
- [164] F.D. Halpern, P. Ricci, B. Labit, I. Furno, S. Jolliet, J. Loizu, A. Mosetto, G. Arnoux, J.P. Gunn, J. Horacek, M. Kočan, B. LaBombard, and C. Silva and. Theory-based scaling of the SOL width in circular limited tokamak plasmas. *Nuclear Fusion*, 53(12):122001, nov 2013.
- [165] F D Halpern, J Horacek, R A Pitts, and P Ricci. A theoretical interpretation of the main scrape-off layer heat-flux width scaling for tokamak inner-wall limited plasmas. *Plasma Physics and Controlled Fusion*, 58(8):084003, jul 2016.
- [166] E. Serre, H. Bufferand, A. Paredes, F. Schwander, G. Ciraolo, Ph. Ghendrih, and P. Tamain. Numerical modeling of the impact of geometry and wall components on transport in the tokamak edge. *Contributions to*

- Plasma Physics*, 52(5-6):401–405, 2012.
- [167] H. Bufferand, C. Baudoin, J. Bucalossi, G. Ciraolo, J. Denis, N. Fedorczak, D. Galassi, Ph. Ghendrih, R. Leybros, Y. Marandet, N. Mellet, J. Morales, N. Nace, E. Serre, P. Tamain, and M. Valentiniuzzi. Implementation of drift velocities and currents in soledge2d–eirene. *Nuclear Materials and Energy*, 12:852–857, 2017. Proceedings of the 22nd International Conference on Plasma Surface Interactions 2016, 22nd PSI.
- [168] S. Baschetti, H. Bufferand, G. Ciraolo, P. Ghendrih, A. Gallo, E. Serre, and and. Study of the role of the magnetic configuration in a  $k-\epsilon$  model for anomalous transport in tokamaks. *Journal of Physics: Conference Series*, 1125:012001, nov 2018.
- [169] E. Laribi, E. Serre, P. Tamain, and H. Yang. Impact of negative triangularity on edge plasma transport and turbulence in TOKAM3X simulations. *Nuclear Materials and Energy*, page 101012, April 2021.
- [170] A Gallo, N Fedorczak, S Elmore, R Maurizio, H Reimerdes, C Theiler, C K Tsui, J A Boedo, M Faitsch, H Bufferand, G Ciraolo, D Galassi, P Ghendrih, M Valentiniuzzi, P Tamain, and and. Impact of the plasma geometry on divertor power exhaust: experimental evidence from TCV and simulations with SolEdge2d and TOKAM3x. *Plasma Physics and Controlled Fusion*, 60(1):014007, oct 2017.
- [171] R. Maurizio, S. Elmore, N. Fedorczak, A. Gallo, H. Reimerdes, B. Labit, C. Theiler, C.K. Tsui, W.A.J. Vijvers, and and. Divertor power load studies for attached I-mode single-null plasmas in TCV. *Nuclear Fusion*, 58(1):016052, dec 2017.
- [172] N. Fedorczak, M. Peret, H. Bufferand, G. Ciraolo, Ph. Ghendrih, and P. Tamain. A spectral filament model for turbulent transport and scrape off layer width in circular geometry. *Nuclear Materials and Energy*, 19:433–439, 2019.
- [173] M. Peret, N. Fedorczak, P. Tamain, Ph. Ghendrih, L. Vermare, Tore Supra, and WEST Teams. A spectral model for interchange transport in tokamak scrape-off layers. 61(4):046045, mar 2021.
- [174] Mathieu Peret, Nicolas Fedorczak, Laure Vermare, M Ramisch, and B Schmid. A model of interchange turbulent transport across separatrix with sheared flows. 25th Joint EU-US TTF Meeting - the EU-US Transport Task Force, September 2021. Poster.
- [175] M. Peret and al. submitted. *Physics of Plasmas*, 2021.

- [176] ITER Physics Expert Group on Confin Transport, ITER Physics Expert Group on Confin Database, and ITER Physics Basis Editors. Chapter 2: Plasma confinement and transport. *Nuclear Fusion*, 39(12):2175–2249, dec 1999.
- [177] A Loarte and P.J Harbour. Effect of the magnetic flux geometry of a poloidal divertor on the profiles and parameters at the target. *Nuclear Fusion*, 32(4):681–686, apr 1992.
- [178] N. Fedorczak, J.P. Gunn, Ph. Ghendrih, G. Ciraolo, H. Bufferand, L. Isoardi, P. Tamain, and P. Monier-Garbet. Experimental investigation on the poloidal extent of the turbulent radial flux in tokamak scrape-off layer. *Journal of Nuclear Materials*, 415(1, Supplement):S467–S470, 2011. Proceedings of the 19th International Conference on Plasma-Surface Interactions in Controlled Fusion.
- [179] G Birkenmeier, M Ramisch, G Fuchert, A Köhn, B Nold, and U Stroth. Spatial structure of drift-wave turbulence and transport in a stellarator. *Plasma Physics and Controlled Fusion*, 55(1):015003, nov 2012.
- [180] G. Birkenmeier, M. Ramisch, B. Schmid, and U. Stroth. Experimental evidence of turbulent transport regulation by zonal flows. *Phys. Rev. Lett.*, 110:145004, Apr 2013.
- [181] D Silvagni, T Eich, M Faitsch, T Happel, B Sieglin, P David, D Nille, L Gil, U Stroth, and and. Scrape-off layer (SOL) power width scaling and correlation between SOL and pedestal gradients across l, i and h-mode plasmas at ASDEX upgrade. *Plasma Physics and Controlled Fusion*, 62(4):045015, feb 2020.
- [182] R. Maurizio, B.P. Duval, B. Labit, H. Reimerdes, M. Faitsch, M. Komm, U. Sheikh, C. Theiler, and the TCV team and. H-mode scrape-off layer power width in the TCV tokamak. *Nuclear Fusion*, 61(2):024003, jan 2021.
- [183] D.L Rudakov, J.A Boedo, R.A Moyer, P.C Stangeby, J.G Watkins, D.G Whyte, L Zeng, N.H Brooks, R.P Doerner, T.E Evans, M.E Fenstermacher, M Groth, E.M Hollmann, S.I Krasheninnikov, C.J Lasnier, A.W Leonard, M.A Mahdavi, G.R McKee, A.G McLean, A.Yu Pigarov, W.R Wampler, G Wang, W.P West, and C.P.C Wong. Far SOL transport and main wall plasma interaction in DIII-d. *Nuclear Fusion*, 45(12):1589–1599, nov 2005.
- [184] B. LaBombard, R. L. Boivin, M. Greenwald, J. Hughes, B. Lipschultz, D. Mossessian, C. S. Pitcher, J. L. Terry, and S. J. Zweben. Particle transport in the scrape-off layer and its relationship to discharge density limit in

- alcator c-mod. *Physics of Plasmas*, 8(5):2107–2117, 2001.
- [185] R. L. Miller, M. S. Chu, J. M. Greene, Y. R. Lin-Liu, and R. E. Waltz. Non-circular, finite aspect ratio, local equilibrium model. *Physics of Plasmas*, 5(4):973–978, 1998.
- [186] J.-M. Moret, S. Franke, H. Weisen, M. Anton, R. Behn, B. P. Duval, F. Hofmann, B. Joye, Y. Martin, C. Nieswand, Z. A. Pietrzyk, and W. van Toledo. Influence of plasma shape on transport in the tcv tokamak. *Phys. Rev. Lett.*, 79:2057–2060, Sep 1997.
- [187] Wonjae Lee, Maxim V. Umansky, J. R. Angus, and Sergei I. Krasheninnikov. Electromagnetic effects on dynamics of high-beta filamentary structures. *Physics of Plasmas*, 22(1):012505, 2015.
- [188] Thomas Eich and Peter Manz. The separatrix operational space of asdex upgrade due to interchange-drift-alfvén turbulence. *Nuclear Fusion*, 2021.



## DOCTORAL SCHOOL

**Titre :** Pousser la physique des barrières de transport jusqu'au mur : comment les conditions aux limites impactent-elles le confinement dans les tokamaks?

**Mots clés :** fusion nucléaire, tokamaks, turbulence plasma, barrières de transport, géométrie magnétique

**Résumé :** Ce travail est dédié à la compréhension de la formation des barrières de transport à la périphérie des plasmas de fusion confinés par champ magnétique. Deux axes principaux ont été suivis. Une caractérisation expérimentale des profils de rotation par réflectométrie Doppler a été effectuée dans le tokamak WEST en parallèle du développement d'un modèle de transport impliquant une description spectrale de la turbulence et de son interaction avec des écoulements cisailés. Cette étude est appliquée à la région de bord faisant la jonction entre le plasma de cœur où ont lieu les réactions de fusion et la région d'interaction avec la paroi où le plasma dépose les particules et l'énergie sur le mur. L'établissement de barrières de transport dans cette région est attribué à la génération d'un écoulement fortement cisaiillé atténuant la turbulence. Les observations expérimentales montrent que cet établissement est sensible aux conditions du plasma de bord notamment à la configuration magnétique, tels que la présence et la position d'un point X (point où le champ magnétique poloidal est nul) ainsi qu'à l'amplitude de la densité locale.

Une caractérisation expérimentale des profils de rotation au bord du plasma dans des conditions variées montre les impacts de l'injection de puissance de chauffage, de la configuration magnétique ainsi que de la densité sur l'amplitude et la forme des profils. En particulier, la topologie magnétique, au travers de la position du point X, en haut ou en bas du plasma, est à l'origine de l'absence ou de la présence d'un puit dans le profil. Cette différence s'estompe lorsque le courant plasma est augmenté. De plus, les premières études de l'accès à un mode de confinement amélioré dans WEST mettent en évidence des profils de rotation records. De manière intéressante, la configuration point X haut, usuellement défavorable à la transition, présente des profondeurs de puit plus importantes que dans la configuration symétrique

en présentant cependant un gradient moins fort des profils de densité. Dans l'objectif de comprendre ces observations, une approche théorique a été développée pour décrire à la fois la turbulence et son interaction avec des écoulements cisaiillés. Une approche spectrale a été appliquée aux équations décrivant la turbulence d'interchange plongée dans un écoulement de fond cisaiillé. Ce point de départ permet de prédire à la fois des observables du transport (flux, niveaux de fluctuation) et le tenseur de Reynolds permettant la génération d'écoulement. Appliquée à la zone d'interaction avec la paroi, cette description permet de prédire les longueurs caractéristiques de dépôt de particules sur le mur. De plus, ce modèle est suffisamment générique pour permettre d'y inclure des effets plus complexes comme ceux de la collisionnalité et de la géométrie. En effet, il ne dépend que de trois paramètres de contrôle : la courbure dépendant de la géométrie, la dynamique parallèle aux lignes de champs qui est fonction de la géométrie et de la densité et l'inclinaison des structures par l'écoulement de fond cisaiillé ou le cisaillement magnétique. Ces effets sont étudiés au regard de l'impact de la forme du plasma et de la densité sur ces paramètres. Ce modèle a été vérifié avec des simulations 2D forcées par le flux avec des paramètres de contrôle dans l'espace des valeurs mesurées dans l'expérience. De surcroît, une comparaison des prédictions analytiques avec les mesures ont montré trois étapes de validation : 1) les spectres turbulents mesurés dans le torsatron TJ-K sont reproduits par les prédictions, 2) les propriétés de la turbulence ainsi que les longueurs de décroissance des profils de densité mesurés dans Tore Supra sont en accord quantitatif avec celles données par le modèle et 3) le modèle de génération d'écoulement par la turbulence reproduit les observations expérimentales concernant l'impact de la géométrie et du courant plasma.

**Title :** Pushing the physics of edge transport barriers towards the wall : how do boundary conditions impact confinement transitions in tokamaks?

**Keywords :** nuclear fusion, tokamaks, plasma turbulence, transport barriers, magnetic geometry

**Abstract :** This work deals with the understanding of transport barrier establishment in the edge of magnetically confined fusion plasmas. To that end, two main axis were explored. First, an experimental characterisation of the rotation profiles by Doppler Back-Scattering reflectometry (DBS) have been performed in the WEST tokamak. On the other hand, a theoretical development of transport models implying a spectral description of the turbulence and its interplay with sheared flows have been developed. In fact, tokamak plasmas can be decomposed in three regions of interest : a confined core region where the fusion reactions take place, a plasma-wall interaction region where the plasma intercepts the wall leading to power and particle exhaust and a transition region between the two firsts called edge region. The establishment of a transport barrier in this latter is attributed to the generation of a strongly sheared flow leading to a mitigation of the turbulence. Experimentally, the build up of the barrier appeared very sensitive to edge plasma conditions such as the magnetic configuration, i.e. the existence and the position of an X-point (where the poloidal magnetic field is null) as well as edge density amplitude.

An experimental characterisation of edge rotation profiles has been managed in various plasma conditions showing impacts of heating power injection, magnetic geometry and density on both profiles amplitude and shape. In particular, the magnetic topology of the plasma appeared strongly influencing the rotation behaviour. The X-point position, i. e. symmetrically in the top or the bottom part of the plasma corresponding to the so-called unfavourable and favourable configurations, induces the presence or the absence of rotation well at the confined plasma boundary. This discrepancy becomes blurred when the plasma current increases. Moreover, the first observations of an increased confinement regime in the WEST tokamak show edge velocity records. Interestingly, a deeper well in the rotation profile is observed in

unfavourable configuration even if the density profile exhibits a slightly weaker gradient at the edge (or a weaker pedestal).

Aiming at understanding these features, a theoretical development has been derived to describe both transport and sheared flow/turbulence interplay. A spectral approach of the edge turbulent equations led to a description of all the features of the interchange turbulence plunged into a background sheared flow. From this starting point, a reconstruction of the principal transport observables such as fluctuation levels, fluxes or flow generation through the Reynolds stress creation is driven. Applied to the plasma-wall interaction region, this model gives predictions for particle exhaust characteristic width. Interestingly, the model remains simple enough to include more complex geometric and collisional effects. Indeed, this turbulence description only depends on three control parameters : the curvature drive depending on the geometry, the parallel dynamics features depending on both geometry and density conditions and the structure tilt due to magnetic and background flow shear. These effects are investigated and discussed regarding the impacts of plasma shaping and edge density on these control parameters. Then, this model has been verified against a broad set of 2D flux-driven simulations with control parameters in the range of the experimental ones. Furthermore, a comparison of the model predictions with experimental data revealed three validation steps. First, the model recovers turbulent spectra measured in the TJ-K torsatron. Then, comparing the predictions with turbulent features and background density profile decay lengths measured with Langmuir probes in Tore Supra results in a sound quantitative agreement. Finally, the model of flow generation by the turbulence recovers the experimental observations mentioned above concerning the impact of the magnetic geometry and the plasma current.

